

Universiteit
Leiden
The Netherlands

Facets of radio-loud AGN evolution : a LOFAR surveys perspective

Williams, W.L.

Citation

Williams, W. L. (2015, December 10). *Facets of radio-loud AGN evolution : a LOFAR surveys perspective*. *PhD Thesis*. Retrieved from https://hdl.handle.net/1887/37016

Version:	Not Applicable (or Unknown)
License:	Leiden University Non-exclusive license
Downloaded from:	https://hdl.handle.net/1887/37016

Note: To cite this publication please use the final published version (if applicable).

Cover Page



Universiteit Leiden



The handle http://hdl.handle.net/1887/37016 holds various files of this Leiden University dissertation.

Author: Williams, Wendy L.
Title: Facets of radio-loud AGN evolution : a LOFAR surveys perspective
Issue Date: 2015-12-10

Facets of radio-loud AGN evolution

a LOFAR surveys perspective

Wendy L. Williams

© 2015 Wendy L. Williams

ISBN:

Cover: LOFAR 150 MHz image of the Boötes field with an artistic impression of source J142912+332634.

Facets of radio-loud AGN evolution

a LOFAR surveys perspective

Proefschrift

ter verkrijging van
de graad van Doctor aan de Universiteit Leiden,
op gezag van Rector Magnificus prof. mr. C.J.J.M. Stolker,
volgens besluit van het College voor Promoties
te verdedigen op donderdag 10 december 2015
klokke 10:00 uur

door

Wendy L. Williams
geboren te Johannesburg, Zuid-Afrika
in 1986

Promotiecommissie

Promotor:	Prof. dr. Huub Röttgering	Leiden University
Co-Promotor:	Dr. Reinout van Weeren	Harvard-Smithsonian Center for Astrophysics
Overige leden:	Prof. dr. Philip Best	University of Edinburgh
	Dr. Jarle Brinchmann	Leiden University
	Prof. dr. Marijn Franx	Leiden University
	Prof. dr. Michael Garrett	ASTRON/Leiden University
	Prof. dr. George Miley	Leiden University
	Dr. Raffaella Morganti	ASTRON/University of Grongingen

For my parents.

For my part I know nothing with any certainty,
but the sight of the stars makes me dream.
Vincent Van Gogh

Contents

1 Introduction **1**
- 1.1 Active Galactic Nuclei . . . 1
  - 1.1.1 Accretion Modes . . . 2
  - 1.1.2 Radio AGN . . . 4
  - 1.1.3 Feedback Processes . . . 6
- 1.2 Low Frequency Radio Astronomy . . . 7
- 1.3 This Thesis . . . 9
- 1.4 Future Prospects . . . 10

2 The Two-meter Radio Mini Survey **13**
- 2.1 Introduction . . . 14
- 2.2 Observations and Data Reduction . . . 15
  - 2.2.1 Observations . . . 15
  - 2.2.2 Data Reduction . . . 17
- 2.3 Source Detection and Characterisation . . . 20
  - 2.3.1 Detection . . . 20
  - 2.3.2 Resolved Sources . . . 23
  - 2.3.3 Completeness and Reliability . . . 23
  - 2.3.4 Astrometric and Flux Uncertainties . . . 26
  - 2.3.5 Diffuse Sources . . . 29
- 2.4 Analysis . . . 29
  - 2.4.1 Source Counts . . . 30
  - 2.4.2 Spectral Index Distributions . . . 33
- 2.5 Conclusion . . . 35
- 2.A Selected Radio Images . . . 39
  - 2.A.1 Note on source J144102+3530 . . . 39

3 LOFAR LBA 3C 295 and Boötes **43**
- 3.1 Introduction . . . 44
- 3.2 Observations & data reduction . . . 45
  - 3.2.1 Data reduction . . . 45
  - 3.2.2 Imaging and CLEANing . . . 50
- 3.3 Results . . . 51
  - 3.3.1 Source detection . . . 56
  - 3.3.2 Astrometric uncertainties . . . 56
  - 3.3.3 Flux density uncertainties . . . 59
  - 3.3.4 Completeness and reliability . . . 61
- 3.4 Analysis . . . 63

3.4.1 Source counts . . . 63
3.4.2 Spectral indices . . . 67
3.4.3 Ultra-steep spectrum sources . . . 70
3.5 Conclusions . . . 73
3.A Extended sources at 62 MHz . . . 75
3.B SED & photo-z fitting results . . . 80
3.C Source counts at 62 MHz for the Boötes field and 3C 295 fields . . . 84

4 LOFAR HBA Boötes **85**
4.1 Introduction . . . 86
4.2 Observations . . . 87
4.3 Data Reduction . . . 88
4.3.1 Direction-independent calibration . . . 90
4.3.2 Directional calibration – 'Facet' scheme . . . 95
4.4 Final Image and Catalogue . . . 101
4.4.1 Source Detection and Characterisation . . . 102
4.4.2 Astrometric and Flux Density Uncertainties . . . 102
4.4.3 Reliability . . . 109
4.4.4 Resolved Sources . . . 109
4.4.5 Source Catalogue . . . 112
4.5 Results . . . 113
4.5.1 Spectral Index Distributions . . . 113
4.5.2 Source Counts . . . 115
4.6 Conclusion . . . 121
4.A Postage stamp images . . . 122
4.B Source size distribution . . . 122

5 Radio-AGN Feedback **129**
5.1 Introduction . . . 130
5.2 Radio-Loud AGN Samples . . . 131
5.2.1 Local SDSS Sample . . . 132
5.2.2 Distant VLA-COSMOS Sample . . . 132
5.3 The Stellar-Mass dependent Luminosity Function . . . 133
5.3.1 The Luminosity Function . . . 133
5.3.2 Space Density Evolution . . . 136
5.4 The Radio-Loud Fraction . . . 136
5.4.1 The Stellar Mass Function . . . 138
5.4.2 The Radio-Loud Fraction . . . 138
5.5 Interpretation . . . 139
5.6 Summary and Conclusions . . . 142

6 Radio AGN in the Boötes field **143**
6.1 Introduction . . . 144
6.2 Radio Data . . . 145
6.3 Multiwavelength Data . . . 146
6.3.1 Combined Photometry Catalogue . . . 146
6.3.2 Additional Multiwavelength Surveys . . . 147

6.3.3 The AGN and Galaxy Evolution Survey . . . 148
6.4 SED fitting . . . 148
6.4.1 Photometric Redshifts . . . 148
6.4.2 Stellar Masses, Star Formation Rates and Rest-frame Colours . . . 151
6.5 Optical identification of Radio Sources . . . 152
6.5.1 Visual Classification . . . 152
6.5.2 Likelihood Ratio . . . 153
6.5.3 Match Results . . . 154
6.5.4 Contamination . . . 155
6.6 Properties of Radio Sources . . . 155
6.6.1 Local Reference Sample . . . 155
6.6.2 Subsample Selection . . . 157
6.6.3 IR SED fitting . . . 157
6.6.4 Star Formation contribution . . . 159
6.6.5 Colour-mass distribution . . . 161
6.6.6 Radio-loud fraction . . . 167
6.7 Conclusion . . . 169
6.7.1 Future work . . . 169
6.A Radio-Optical Matches . . . 171
6.B Example SED fits . . . 171

Bibliography **179**

Summary **189**

Samenvatting **195**

Publications **201**

Curriculum Vitae **203**

Acknowledgements **205**

CHAPTER 1

Introduction

1.1 Active Galactic Nuclei

Just over fifty years ago, Schmidt (1963) associated the radio source, 3C273, with an optically unresolved source at the then extreme redshift, of $z \approx 0.158$. This was shortly followed by the discovery of a population of such quasi-stellar radio sources (quasars) at even higher redshifts and a similar population of quasi-stellar galaxies (Sandage 1965). It is now understood that the fundamental property of these sources, called Active Galactic Nuclei (AGN), is that they are powered by gas falling into the relativistically-deep potential well of black holes with masses of millions to billions that of the Sun. Such supermassive black holes (SMBHs) lie at or near the centres of (probably) all galaxies. The observational characteristics of traditional AGN are diverse and may include an incredibly high luminosity, emission on very small angular scales, broadened emission lines, variability, radio emission, the presence of jets, and polarised emission. Compared to a normal galaxy, a typical AGN may have excess ultraviolet, infra-red and X-ray emission resulting in a flat broadband spectrum. However, any given AGN may exhibit only a selection of these features and different classifications of AGN over the years have created a 'zoo' of objects. Over the past fifty years our understanding of AGN has been built up into a unified model in which, the observed features are heavily dependent on viewing angle, the mass of the central black hole and the accretion rate of the black hole (e.g. Antonucci 1993).

Up to the eighties, these AGN were merely interesting laboratories for the study of extremely high-energy physical processes, and their role in the evolution of galaxies was not yet realised. However, the accumulation of observational evidence, while still largely indirect, has led to the now widely accepted notion that AGN play a crucial role in the evolution of galaxies and are necessary to produce the observed properties of galaxies in the contemporary Universe. Firstly, AGN are more numerous than originally thought, with many more weaker AGN. This leads us to understand that they play an important role in the life-cycle of galaxies. Secondly, the growth of galaxies, as traced by their star formation histories, and the growth of SMBHs, traced by AGN, are remarkably similar. Both show an increase to $z \approx 1$, with a peak at $z \approx 2 - 3$ (e.g. Shankar et al. 2009). Moreover, the masses of the SMBHs in massive galaxies are correlated with various properties of their hosts. These properties include the galaxy luminosities (e.g. Kormendy & Richstone 1995; Marconi & Hunt 2003; Gültekin et al. 2009), the galaxy bulge masses (e.g. Magorrian et al. 1998; McLure & Dunlop 2002) and the velocity dispersions (e.g. Ferrarese & Merritt 2000; Gebhardt et al. 2000; Merritt & Ferrarese 2001). Finally, the anti-hierarchical

evolution of AGN (e.g. Miyaji et al. 2000; Hasinger et al. 2005; Bongiorno et al. 2007; Rigby et al. 2011), i.e. the fact that the space density of low-luminosity AGN peaks around z < 1 and that of high-luminosity AGN peaks around $z \approx 2$, is very similar to the cosmic downsizing of star-forming galaxies (e.g. Cowie et al. 1996; Menci et al. 2008; Fontanot et al. 2009) and spheroidal galaxies (e.g. Cimatti et al. 2006).

At least out to $z \approx 2$, galaxies are observed to have a clear bi-modal distribution (Kauffmann et al. 2008; Blanton et al. 2003c; Baldry et al. 2004). The first population is that of blue galaxies. These tend to have lower stellar masses (M_*) and have high star formation rates (SFR). In general more massive blue galaxies have higher SFR. The second population is called red and dead, owing to their minimal star formation activity. These are preferentially more massive galaxies. Broadly, galaxy evolution can be sketched as the following (e.g. Lilly et al. 2013): a galaxy starts its life on the blue star-forming sequence and it gradually gains mass by accreting gas from the cosmic web and via mergers with other galaxies. At some point, star formation ceases when its supply of gas becomes cut off, in a poorly understood process called quenching, and the galaxy evolves onto the red sequence. Red galaxies usually only increase in mass through further mergers. Numerical and semi-analytical models of the formation and evolution of galaxies show that additional processes are necessary to explain the present day massive galaxy population. In particular AGN provide a means to either heat or eject the surrounding gas and prevent further star formation from cold gas.

1.1.1 Accretion Modes

Over the last decade a more complete picture has emerged of the population of AGN in the present-day Universe. In this picture, the AGN population is split in two categories, with the division between them based on their accretion rates and distinct in the SMBH and host galaxy properties. In the first class, the dominant energy output is in the form of electromagnetic radiation from the efficient conversion of potential energy when gas is accreted by the SMBH. This is referred to as the 'radiative-mode'. Historically, they have been called Seyferts or QSOs depending on their luminosity. The second class produces little electromagnetic radiation and the energy output is primarily in the form of bulk kinetic energy carried by collimated jets. Consequently, these are usually referred to as 'jet-mode' AGN. A schematic overview of the two classes is shown in Fig. 1.1 and their observational characteristics and fuelling mechanisms are described in the following sections.

Radiative-mode

In these AGN, inflow on to the SMBH occurs via a geometrically thin, optically thick accretion disk (Shakura & Sunyaev 1973). Thermal continuum emission from the accretion disk is produced spanning from the extreme ultraviolet (UV) through the optical. A corona of hot gas produces X-ray emission through Compton scattering of light from the disk. Radiation from the disk and corona heats and photoionises gas in the vicinity. Closer to the SMBH, where the velocity dispersion of the gas is a few thousands km/s, this produces broad emission lines in the UV, optical and near-infrared (NIR). More tenuous gas at greater distances, results in both forbidden and permitted emission lines, with narrower linewidths (hundreds of km/s). These give rise to, respectively, the broad-line region (BLR) and narrow-line region (NLR). The presence of a larger-scale dusty molecular gas structure may, in some cases, inhibit views of certain emission by absorbing soft X-ray, UV and visual light. This dusty structure re-radiates the ab-

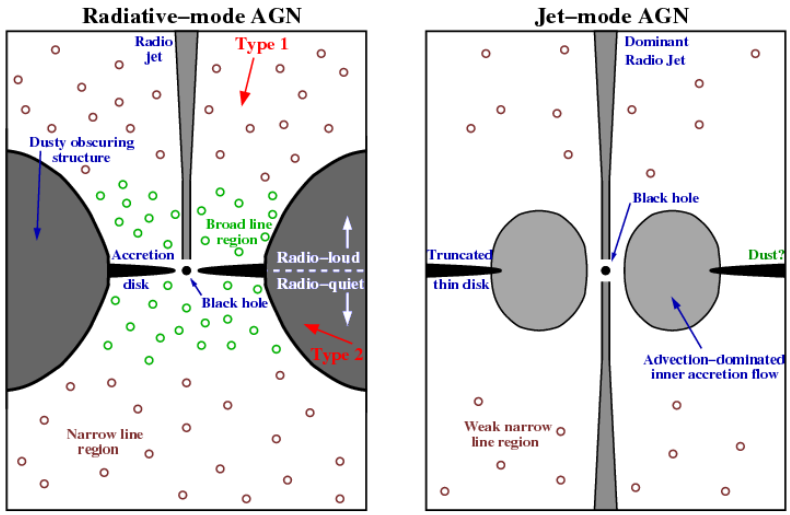


Figure 1.1: Schematic drawings of the central engines of AGN in the radiative mode (*left*) and jet mode (*right*). Radiative-mode AGN have a geometrically thin, optically thick accretion disk, illuminating the broad- and narrow-line regions with UV radiation. At some viewing angles, a dusty, obscuring structure may inhibit the view of the accretion disk and broad-line region (Type 2 AGN). While at other angles, these features are visible (Type 1 AGN). A small fraction of these sources produce powerful radio jets. Jet-mode AGN lack the accretion disk, having instead a geometrically thick ADAF. Radio jets release the majority of the energy output in the form of bulk kinetic energy. (Image reproduced from Heckman & Best 2014).

sorbed light as thermal emission in the mid-infrared (MIR). In the unified models (e.g. Barthel 1989; Antonucci 1993; Urry & Padovani 1995), the angle at which the source is viewed results in different features being seen. Sources which are not obscured have been referred to as Type 1, while obscured sources are called Type 2 and may lack broad emission lines, soft X-ray emission and optical emission from the disk. In some cases, even the hard X-ray emission can be obscured. A small fraction of these sources produce collimated jets, leading to radio emission. The key observation that led to the adoption of unified models for powerful radio galaxies and radio-loud quasars was that all quasars appear to be beamed towards us (Barthel 1989). These sources have been called quasi-stellar objects (QSOs) or Seyferts, depending on the luminosities. The nomenclature for this mode includes 'Quasar mode', 'cold mode', 'fast-accretor', 'high excitation', or 'strong-lined'. Radio sources in the radiative-mode have been found to be typically hosted by lower mass, bluer galaxies in less dense environments (e.g. Tasse et al. 2008b; Janssen et al. 2012).

The most widely suggested triggering mechanism for radiative-mode AGN activity is through major mergers or strong tidal interactions (e.g. Kauffmann & Haehnelt 2000; Hopkins & Beacom 2006; Hopkins et al. 2008). Mergers are indeed known to trigger starbursts (e.g. Larson & Tinsley 1978). However, there is contradictory evidence which suggests that there is no enhanced AGN activity in mergers identified either by galaxies with close companions (e.g. Li et al. 2008) or through their morphology (e.g. Reichard et al. 2009). Another proposed fuelling mechanism is through secular processes (disc instabilities, minor mergers, recycled gas from dying stars, galaxy bars etc.), in particular for low-luminosity AGN (e.g. Genzel et al. 2008; Johansson et al. 2009; Ciotti et al. 2010). It remains clear, however, that what is needed to produce radiative-mode

AGN activity is an abundant central supply of cold dense gas (e.g. Larson 2010).

Jet-mode

The second class of AGN either lack or have a truncated accretion disk. Instead, accretion occurs on timescales shorter than the radiative cooling time by means of a geometrically thick structure. Gas is accreted in advection dominated or radiatively inefficient accretion flows (ADAFs or RIAFs, e.g. Narayan & Yi 1994, 1995; Quataert 2001; Narayan 2005; Ho 2008). This results in two-sided relativistic jets, which may extend from a few parsecs to megaparsec scales. These sources do not show the luminous narrow lines expected in the framework of AGN unification (e.g. Hine & Longair 1979; Laing et al. 1994; Jackson & Rawlings 1997). They also lack the expected infrared emission from a dusty torus (e.g. Whysong & Antonucci 2004; Ogle et al. 2006) and do not show accretion related X-ray emission (Hardcastle et al. 2006; Evans et al. 2006). They lack the strong emission lines of the radiative-mode AGN, but may exhibit some weak narrow lines (called LINERs). Jet-mode AGN nomenclature includes 'radiatively inefficient', 'radio-mode', 'hot-mode', 'weak lined', 'slow-accretor', and 'low excitation'. Best et al. (2005a) showed that jet-mode radio galaxies are hosted by fundamentally different galaxies: higher mass, redder and occurring in more dense environments. This mode in particular provides a direct feedback connection between the AGN and its hot gas fuel supply in the manner of work done by the expanding radio lobes on the hot intra-cluster gas.

The fuel source of jet-mode AGN has been argued to be hot gas (e.g. Hardcastle et al. 2007). The source of this hot gas has long been postulated to be shed from old stars (e.g. David et al. 1987; Norman & Scoville 1988; Ciotti & Ostriker 1997; Kauffmann & Heckman 2009). These sources are generally found to be in massive galaxies in the centres of groups and clusters, whose hot gaseous X-ray emitting haloes provide a source of fuel.

1.1.2 Radio AGN

Radio continuum observations are an important means to find AGN, particularly those in the jet-mode. Also, because the dusty obscuring structure is transparent to the radio, radio-emitting Type 2 radiative-mode AGN are detectable in radio surveys. As with studying AGN at other wavelengths, radio observations have their problems. These include complications in identifying the optical host galaxies, because the jet emission and source are not coincident, and confirmation that the radio emission is indeed from the AGN instead of star formation processes. Radio-loud objects are notably important to our understanding of AGN. Despite the fact that they constitute only a small fraction of the overall population, it is during this phase that the impact of the AGN on their surrounding environment (through the production of jets and large-scale outflows and shocks) can be most directly observed and measured (e.g. Kraft et al. 2003; Cattaneo & Best 2009; Croston et al. 2011). Moreover, radio galaxies make up over 30 per cent of the massive galaxy population, and it is likely that all massive galaxies go through a radio-loud phase, as the activity is expected to be cyclical (e.g. Best et al. 2005b; Saikia & Jamrozy 2009).

The radio emission from AGN is synchrotron radiation, arising from relativistic electrons spiralling around magnetic field lines, both of which likely originate near the central SMBH (Rees 1978; Blandford & Payne 1982). The exact mechanism responsible for the production of relativistic jets in some AGN are not understood due to the low resolution of current observations, which cannot provide enough evidence to favour one of the various theoretical models of jet production over the many that exist. Indeed, much progress has been made in semi-analytical

models and magneto-hydrodynamic simulations of jets since black holes were first postulated to be a source of high energy particle jets (e.g. Blandford & Znajek 1977; Williams 1995; Falcke 1996; Vlahakis & Königl 2003; Polko et al. 2010). However, the synchrotron emission is well understood and has a characteristic power-law spectral shape, $S_\nu \propto \nu^\alpha$ over decades in frequency (e.g. Klamer et al. 2006), where the spectral index, α, is typically ≈ -0.8 (e.g. De Breuck et al. 2000). Thus, radio observations of AGN can benefit from the increased brightness towards lower observing frequencies. At the lowest frequencies though the spectrum flattens due to synchrotron self-absorption or free-free absorption Rybicki & Lightman (1979). At lower frequencies, the lower relativistic energy of the emitting particles results in a longer synchrotron lifetime. The observed, as opposed to intrinsic, duty cycle[1] of radio activity is thus longer. A small population of sources have ultra-steep spectra (USS; $\alpha \lesssim -1.3$). It has long been realised that in flux-limited radio surveys, sources with the steepest spectra are systematically at higher redshifts (e.g. Tielens et al. 1979; Blumenthal & Miley 1979). Selection of such sources has resulted in the discovery of the most distant radio galaxies (Miley & De Breuck 2008).

Historically, radio loud resolved jet-dominated sources have been separated in two classes, largely defined by their apparent morphology, Farnaroff-Riley class I and II (Fanaroff & Riley 1974). FRI, or edge-darkened, sources tend to display luminosities which peak close to the galaxy core, and may include disturbed or anisotropic radio structures. FRII, or edge-brightened, sources have well defined morphologies, with clear lobes and outer hotspots, and jets that are more collimated in general than FRIs. Both FRIs and FRIIs span a wide range in radio luminosity with significant overlap. However there is a rough critical power, $P_{1.4\mathrm{GHz}} \approx 10^{24}\,\mathrm{W\,Hz^{-1}}$, above which most sources are FRII and below which most are FRI (Best 2009; Gendre et al. 2010). The most popular interpretation of the difference between FRI and FRIIs is that it can be explained by the density of the Intergalactic Medium (IGM) in which they exist. Jets produced by the central engine will be disrupted, and reach very much shorter distances due to entrainment (mixing) of the surrounding medium in regions of high density IGM, producing FRIs. The denser the environment, the more powerful the jet is needed to be in order to prevent disruption, and produce a classic FRII. However, the reasons for the divide may not be solely confined to this simple idea, as FRIIs have been found in clusters, i.e. regions of high density IGM (e.g. Wan & Daly 1996).

An alternative scheme is to separate radio AGN by their accretion types, which are more directly linked with their feedback modes. Indeed, there two distinct populations revealed by radio surveys. The first is associated with strong classical QSOs (i.e. radiative-mode), historically called 'high excitation radio galaxies' (HERGs). The second is a population of weak LINER-like sources (i.e. jet-mode), called 'low excitation radio galaxies' (e.g. Hine & Longair 1979; Laing et al. 1994). In the local Universe it has been shown by Best & Heckman (2012), that 95 per cent of low-luminosity radio AGN ($P_{1.4\mathrm{GHz}} \lesssim 10^{25}\,\mathrm{W\,Hz^{-1}}$) are jet-mode LERGs, while radiative-mode HERGs start to dominate at high powers ($P_{1.4\mathrm{GHz}} \gtrsim 10^{26}\,\mathrm{W\,Hz^{-1}}$). Because of the similar limiting power, there is some overlap between the FR classification Gendre et al. (2013), but it is not one-to-one with samples of jet-mode FRIIs (e.g. Laing et al. 1994) and a small population of radiative-mode FRIs (e.g. Heywood et al. 2007).

Radio samples derived from large spectroscopic surveys provide an excellent means to study the radio AGN population in the two modes. Such samples have reinforced the idea that LERGs or jet-mode sources are hosted predominantly by red massive ellipticals at the centres of groups or clusters, while HERGs or radiative mode radio sources are hosted by bluer star-forming galaxies

[1] i.e. the observed ratio in time between when the radio source is 'on' to when it is 'off.'

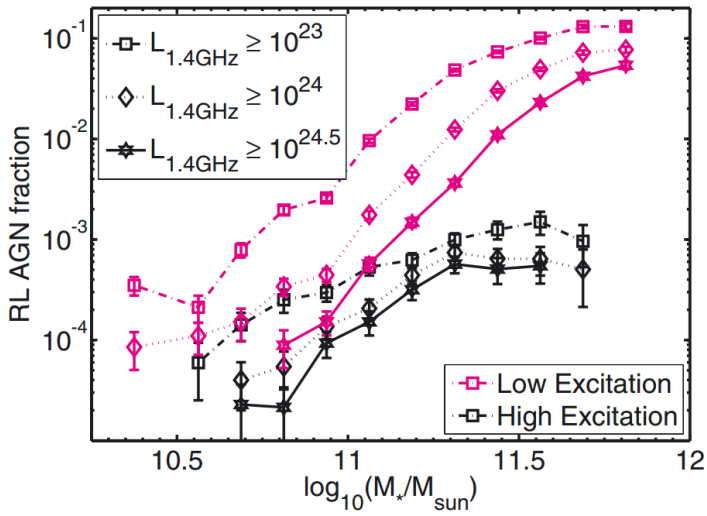


Figure 1.2: The fraction of radio AGN as a function of their host galaxy stellar mass. Low excitation, or jet-mode, sources show a much flatter dependence on stellar mass than high excitation, or radiative-mode, sources. Largely independent of the radio-power cutoff. (reproduced from Janssen et al. 2012).

(e.g. Best & Heckman 2012; Janssen et al. 2012; Gürkan et al. 2014). In particular, studies by Best & Heckman (2012) used such a sample to derive the Eddington ratios for the radio sources in the radiative and jet-modes by calculating the total jet energy output in the form of mechanical energy and the total bolometric radiative luminosity. They find that the two populations are distinct in their Eddington-scaled accretion rates, with the jet-modes sources accreting at $<$ 1 per cent of the Eddington rate, and radiative-mode sources accreting at $1 - 10$ per cent of the Eddington rate. Similarly, Janssen et al. (2012) show that the prevalence of radio AGN activity as a function of host stellar mass and colour is different for HERGs and LERGS. In particular, the fraction of LERGs is a much steeper function of host stellar mass ($f_{\rm LERG} \propto M_*^{2.5}$) than for HERGs ($f_{\rm HERG} \propto M_*^{2.5}$). This is shown in Fig. 1.2.

1.1.3 Feedback Processes

To explain the observed co-evolution of black holes and their hosts, theoretical models invoke 'feedback' between the SMBH and the gas and dust within the host galaxy (e.g. Granato et al. 2004; Springel et al. 2005; Croton et al. 2006; Hopkins et al. 2006; Sijacki et al. 2009; Cen & Chisari 2011). Models often represent the effects of feedback in two ways, denoted 'quasar mode' and 'radio mode' (e.g. Croton et al. 2006), related to the accretion modes described above. In the quasar mode, energy is released as winds driven by the radiative output of AGN. The radiation interacts with gas and dust in the host galaxy. The resulting winds can expel gas from the galaxy, thus stopping the accretion of matter on to the black hole and further quenching star formation (e.g. Page et al. 2012). However, studies of X-ray luminous AGN do not show any evidence for this (e.g. Harrison et al. 2012). In radio-mode feedback, the jets may play an important role in the evolution of the host galaxy by heating up the cold gas and suppressing star formation (e.g. Best et al. 2005a; Hardcastle et al. 2013). In the most dramatic scenario, the jets can expel the

molecular gas from the host galaxy. Radio-mode feedback has been widely used in simulations as a mechanism usually to prevent the overproduction of stars in massive galaxies, to produce the observed 'red and dead' galaxies (e.g. Bower et al. 2006; Werner et al. 2014). However, a positive radio-mode feedback has also been suggested (e.g. Silk & Nusser 2010; Gaibler et al. 2012; Kalfountzou et al. 2012). In this 'jet-induced star formation', the radio jets drive shocks in the interstellar medium which enhance the star formation, which has already been observed (e.g. Blanco et al. 1975; van Breugel et al. 1985; McCarthy et al. 1987; Chambers et al. 1987; Eales & Rawlings 1990; Best et al. 1998; Inskip et al. 2005).

1.2 Low Frequency Radio Astronomy

In 1931 astronomy was revolutionised with the first major extension of observations beyond the optical, near-ultraviolet and near-infrared. This occurred when Jansky (1933) made the first serendipitous discovery of a source of extra-terrestrial emission using an antenna operating at radio frequencies of 20.5 MHz. This emission, designated Sagittarius A, is now known to originate from the Galactic centre. Shortly thereafter Reber (1940) detailed the first radio map of the Galactic plane and large portions of the sky with observations at 160 MHz. Among the first important scientific discoveries was that of the first extragalactic radio source, Cygnus A, (Baade & Minkowski 1954) and that of the first QSO, 3C283, (Schmidt 1963).

Radio astronomy developed rapidly in the early years, with significant early technological milestones achieved with the first astronomical observations with a two-element radio interferometer (Ryle & Vonberg 1946) and the first use of earth rotation synthesis (Ryle 1962). During this time several low frequency surveys were conducted with the Cambridge interferometry 3C, 4C, 6C and 7C at 159, 178, 151 and 151 MHz, respectively (Edge et al. 1959; Bennett 1962; Pilkington & Scott 1965; Gower et al. 1967; Hales et al. 1988, 2007) building up the ever larger samples radio sources leading to greater understanding in particular of quasars and AGN. While many of the earliest radio telescopes operated at low frequencies ($\lesssim$ 200 MHz), the development over the past fifty years has largely been towards higher frequencies ($\gtrsim$ 1400 MHz) in the pursuit of higher sensitivities and higher angular resolution.

The last decade has seen a substantial growth in the number and diversity of radio synthesis telescopes being constructed, as a lead up to the Square Kilometre Array (SKA; Schilizzi 2005). Examples include the Expanded Very Large Array (EVLA; Perley et al. 2004), the Australian Square Kilometre Array Pathfinder (ASKAP; Johnston et al. 2007), and the Karoo Array Telescope (MeerKAT). Additionally, faster computers mean it is now possible to correlate signals from hundreds to thousands of individual antennae, making it possible to build large arrays of dipoles. This has led to a rejuvenation in low-frequency radio astronomy with several new arrays being built, including the Long Wavelength Array (LWA; Taylor 2007), the Murchison Widefield Array (MWA; Lonsdale et al. 2009; Tingay et al. 2013), and the Low Frequency Array (LOFAR; van Haarlem et al. 2013).

LOFAR is a new low frequency radio telescope in the Netherlands and surrounding European countries. Its revolutionary design makes use of phased arrays instead of the traditional and expensive dishes, which are turned into a real telescope electronically. The array is composed of several 'stations' each containing a number of simple dipoles. There are two types of dipole antennas, one for the Low Band Array (LBA) operating at 10–80 MHz and one for the High Band Array (HBA) operating in the 110–240 MHz range. The Dutch part of the array consists of 37 stations going out to 80 km. The array is extended to baselines of up to 1200 km with a



Figure 1.3: The LOFAR superterp near Exloo, Netherlands, showing several stations with both HBA and LBA antennae (*left*). Individual LBA (*top right*) and HBA (*bottom right*). (credit LOFAR/ASTRON).

further eight stations in a number of other European countries. The signals from the antennas are digital, meaning that many beams or pointings can be formed simultaneously. This, combined with its large instantaneous field-of-view, makes LOFAR an extremely efficient instrument for surveying large areas of the sky. The electronic nature of the beams makes LOFAR highly flexible. In terms of frequencies, a total bandwidth of up to 95 MHz is available. The Dutch array provides resolutions of a few tens of arcsec at 60 MHz and a few arcsec 150 MHz, unprecedented for these frequencies. The inclusion of international baselines gives sub-arcsecond resolution in both the low and high bands. Fig. 1.3 shows an image of the central collection of six stations, the 'superterp', and close-up images of individual LBA and HBA dipoles.

These telescopes bring both new scientific and new technical challenges. These challenges include developing new theories to describe effects which were previously ignored and algorithms to solve the resulting equations. This requires a significant increase in the performance of these algorithms in order to produce the best possible sensitivity and dynamic range. Practically, the new instruments demand the ability to handle the large increase (of factors of hundreds or thousands) in data volume, which in turn requires high performance computing and faster calibration and imaging algorithms. Radio astronomy has progressed significantly since the first radio images of the sky were made. In particular in the area of calibration, whereby instrumental and ionospheric effects are corrected for. The first major advance in calibration was the introduction of self-calibration (e.g. Pearson & Readhead 1984), which allows one correction per antenna per polarisation. Low frequency observations necessarily lead to wide fields of view and greater effects of the ionosphere. This requires corrections to be made which vary across the field-of-view. In recent years, significant progress has been made in the field of direction-dependent calibration, including field-based calibration (Cotton et al. 2004), Source Peeling and atmospheric modelling (SPAM Intema et al. 2009; Intema 2014) and SAGECal (Yatawatta et al. 2013; Kazemi et al. 2011). Additionally, high performance algorithms to solve the calibration equations have been developed such as Statistically Efficient and Fast Calibration (stefcal; Salvini & Wijnholds 2014) and the use of Kalman filters (e.g. Smirnov & Tasse 2015). Improvements in imaging

techniques have also been needed as some of the assumptions made in early radio imaging break down. These include techniques such as w-projection (Cornwell et al. 2008) and A-projection (Bhatnagar et al. 2008) in imaging, and the development of new imaging software which take these into account (e.g. Tasse et al. 2013).

1.3 This Thesis

One of the most fundamental issues in understanding the role of AGN in galaxy formation is the need to accurately measure the cosmic evolution of quasar activity and the accretion history of the Universe, and to compare this with the build-up of the stellar populations of galaxies: do black holes and their host galaxies grow coevally, or does one precede the other? what is the primary mode of black hole growth? The majority of the growth of SMBHs and the stellar component of galaxies occurs between redshifts of about 0.5 and 2. Their present day growth is an order of magnitude lower than it was at their peak. To properly understand the detailed process of galaxy formation and evolution the physical processes involved in 'AGN feedback' need to be identified and quantified. Current radio and spectroscopic surveys have greatly increased our understanding of the contemporary population of AGN. While these sources contain a fossil record of their histories, to fully quantify the effect of AGN, it is necessary to extend such work back to earlier cosmic epochs where the AGN and star-formation activity of the Universe peaked. With the more powerful radio telescopes now available, it is now becoming possible to directly study the AGN population at these redshifts. To this end, in this thesis we aim to answer the following:

1. How does the relationship between galaxy mass and radio AGN fraction, i.e. the radio source duty cycle, evolve with redshift?
2. How does the radio AGN population evolve with redshift?
3. What is relationship between host galaxy properties and radio AGN at redshift $0.5 \lesssim z \lesssim 2$?

In this thesis the redshift evolution of radio-loud AGN is studied. The main tool for these studies is deep, high-resolution, low frequency imaging of fields with excellent complementary data. The first part of this thesis (Chapters 1 to 3) uses the most advanced calibration techniques to provide low-frequency radio images using the GMRT and LOFAR. The latter part of the thesis (Chapters 4 and 5) combine radio samples with optical data to study host galaxy properties of radio-loud AGN over cosmic time.

Chapter 2 presents a wide area, deep, high-resolution 153 MHz GMRT observations of the NOAO Boötes field (Jannuzi & Dey 1999). This extragalactic deep field has been extensively studied at optical, ultraviolet and mid-infrared wavelengths. The low frequency radio data have been calibrated for direction-dependent ionospheric effects with the SPAM package (Intema et al. 2009). The GMRT mosaic image includes seven pointings, covering a total of 30 square degrees, at a resolution of 25 arcsec and achieves an rms noise of $2-5$ mJy beam^{-1}. The extracted source catalogue contains 1289, of which 453 are resolved. Monte-Carlo routines for determining the completeness and reliability of radio catalogues are developed. Euclidean-normalized differential source counts and spectral index distributions were calculated.

In **Chapter 3** we present the first LOFAR Low Band Antenna (LBA) observations of the Boötes and 3C 295 fields at 34, 46, and 62 MHz, covering an area of 17 to 52 square degrees. The images presented are the deepest images ever obtained in this frequency range at noise levels of 12, 8, and 5 mJy beam^{-1} in the three frequency bands. Source extraction yielded 300–400

sources in each of the images. Source counts are again derived with the 62 MHz source counts agree with previous GMRT 153 MHz and VLA 74 MHz differential source counts, scaling with a spectral index of -0.7. The lower frequency 34 MHz source counts, suggest that the average spectral index of radio sources flattens towards lower frequencies. The average spectral index of sources between 34 and 1400 MHz also shows a spectral flattening. A sample of ultra-steep spectrum (USS; $\alpha < -1.1$) radio sources is selected in the Boötes field from the spectral indices computed between 62 MHz, 153 MHz and 1.4 GHz, making use of the higher frequency data available in this field. These USS sources are likely to be associated with massive high redshift radio galaxies and the derived photometric redshifts show they are located in the $0.7 \lesssim z \lesssim 2.5$ range.

The first LOFAR, $130 - 169$ MHz, High Band Antenna (HBA) deep field observations of the Boötes field are presented in **Chapter 4**. The 19 square degree image, has a rms noise of $\approx 120 - 150$ μJy beam^{-1} and resolution of 5.6×7.4 arcsec, at least an order of magnitude deeper and $3 - 5$ times higher in resolution than that achieved with the GMRT observations in Chapter 1. Particular care is taken in the calibration of this data, making use of an advanced direction-dependent calibration scheme. The resulting radio source catalogue contains 5 652 sources. Differential source counts which are an order of magnitude lower in flux density than previously done are presented. The counts show a flattening at $\lesssim 10$ mJy with the rise of the low flux density star forming galaxies.

Chapter 5 is a study of the evolution of the fraction of radio-loud AGN as a function of their host stellar mass and shows how the fraction of low mass galaxies hosting high power radio-loud AGN increases with redshift. This is done by combining radio and optical data with one sample in the local universe, $0.01 < z \leqslant 0.3$, and a second sample at higher redshifts, $0.5 < z \leqslant 2$. An increase of more than an order of magnitude in the fraction of lower mass ($M_* < 10^{10.75}$ $M_\odot$) galaxies hosting radio-loud AGN is observed. On the other hand the fraction of high mass galaxies hosting radio-loud AGN remains more or less constant out to redshifts of 1–2. An increase in cold or radiative mode accretion with increasing cold gas supply at earlier epochs is responsible for the rising population of low mass radio-loud AGN.

In **Chapter 6** a further study of the redshift evolution of radio AGN as a function of the properties of their galaxy hosts is made. This uses the LOFAR data of the Boötes field from Chapter 3. The optical-infrared data is used to compile a catalogue of galaxies with photometric redshifts, stellar masses and rest-frame colours. We use this to study the host galaxies of high power $P_{1.4\,\mathrm{GHz}} > 10^{25}\,\mathrm{W\,Hz^{-1}}$ radio sources at intermediate redshifts, $0.5 \leqslant z < 2$. We also attempt to determine the mid-infrared AGN contribution to classify the radio-sources as HERGs and LERGs on the basis of photometry. We show that the fraction of HERGs and the fraction of blue radio AGN increases with redshift.

1.4 Future Prospects

The future is bright for radio AGN evolution studies. The current LOFAR surveys are already providing larger, higher redshift samples, such as those presented in this thesis. Soon, other continuum surveys to be performed with instruments such as APERTIF and the new JVLA will provide complementary higher frequency information. Deeper photometric surveys are also currently underway or in planning, including PanSTARRS. New multi-object survey spectrographs, such as WEAVE (Dalton et al. 2012) on the 4.2-m William Herschel Telescope (WHT), will provide much larger samples at high redshifts. WEAVE-LOFAR is a planned follow-up survey

that will provide the primary source of spectroscopic information for the LOFAR surveys. In particular, WEAVE will provide spectra for $\approx 10^7$ objects at $z > 2$ using Ly_α emission over $10,000$ square degrees. Spectra are required for much more than simply estimating redshifts; they allow for the robust decomposition between star forming galaxies and AGN, and between accretion modes in the AGN. Spectra also permit the measurement of velocity dispersions, estimates of metallicities and virial black hole masses. For many galaxies, metallicities and stellar velocity dispersions will provide further important information on the chemistry and dynamical mass of systems and their evolution, and the accretion mechanism for radio AGN can be determined, all crucial ingredients in galaxy formation and evolution models. Many thousands of WEAVE-LOFAR spectra will thus provide an important step forward in understanding the feedback processes in AGN.

Looking further ahead, the field is poised for another revolution, in terms of ground-breaking depth and area covered by future optical imaging and spectroscopic surveys (e.g. LSST, Euclid, 4MOST, MOONS). Finally, AGN and galaxy evolution studies also form an important part of the science case for the SKA (Kapinska et al. 2015).

CHAPTER 2

T-RaMiSu: The Two-meter Radio Mini Survey I. The Boötes Field

We present wide area, deep, high-resolution 153 MHz GMRT observations of the NOAO Boötes field, adding to the extensive, multi-wavelength data of this region. The observations, data reduction, and catalogue construction and description are described here. The seven pointings produced a final mosaic covering 30 square degrees with a resolution of 25 arcsec. The rms noise is 2 mJy beam^{-1} in the centre of the image, rising to $4-5$ mJy beam^{-1} on the edges, with an average of 3 mJy beam^{-1}. Seventy-five per cent of the area has an rms<4 mJy beam^{-1}. The extracted source catalogue contains 1289 sources detected at 5σ, of which 453 are resolved. We estimate the catalogue to be 92 per cent reliable and 95 per cent complete at an integrated flux density limit of 14 mJy. The flux densities and astrometry have been corrected for systematic errors. We calculate the differential source counts which are in good agreement with those in the literature and provide an important step forward in quantifying the source counts at these low frequencies and low flux densities. The GMRT 153 MHz sources have been matched to the 1.4 GHz NVSS and 327 MHz WENSS catalogues and spectral indices were derived.

Williams, W. L., Intema, H. T. and Röttgering, H. J. A.
A&A, 549, A55 (2013)

2.1 Introduction

Deep low-frequency radio surveys provide unique data which will help resolve many questions related to the formation and evolution of massive galaxies, quasars and galaxy clusters. Until now, such surveys have largely been limited by the corrupting influence of the ionosphere on the visibility data, but new techniques allow for the correction for these effects (e.g. Cotton et al. 2004; Intema et al. 2009). Recently deep ($0.7 - 2\,\mathrm{mJy\,beam^{-1}}$) images have been made, in particular with the Giant Metrewave Radio Telescope (GMRT, e.g. Ananthakrishnan 2005) at 153 MHz (e.g. Ishwara-Chandra & Marathe 2007; Sirothia et al. 2009; Ishwara-Chandra et al. 2010). These observations can be used to study:

Luminous radio sources at $z > 4$ – High redshift radio galaxies (HzRGs, e.g. Miley & De Breuck 2008) provide a unique way to study the evolution of the most massive galaxies in the Universe. One of the most efficient ways of identifying these sources is to search for ultra-steep spectrum (USS) radio sources with $\alpha \lesssim -1$, $S_\nu \propto \nu^\alpha$ (Roettgering et al. 1997; De Breuck et al. 2002). Low frequency observations provide an easy way of identifying USS sources and extending these observations to lower flux density limits increases the distance to which these HzRGs can be identified. Surveying larger areas increases the probability of locating these rare sources.

Distant starburst galaxies – The local radio-IR correlation for star forming galaxies is very tight, and seems to hold at high redshift (Kovács et al. 2006). However, the physical processes involved are poorly understood and only models that carefully fine-tune the time scales for the heating of the dust, the formation of supernovae, and the acceleration, diffusion and decay of the relativistic electrons can reproduce the correlation. The low-frequency spectral shape of galaxies reveals information about the amount of free-free absorption and relating this to the dust content, size, mass, total amount of star formation and environment of the galaxies will further constrain the radio-IR models. To date, however, few galaxies have been well studied at low frequencies and those that have, show a diverse range of spectral shapes (e.g. Clemens et al. 2010).

Faint peaked spectrum sources – Young radio-loud AGN are ideal objects to study the onset and early evolution of classical double radio sources. They usually have synchrotron self-absorbed spectra and compact radio morphologies. Relative number statistics have indicated that these radio sources must be significantly more powerful at young ages, which may be preceded by a period of luminosity increase (e.g. Snellen et al. 2003). Multi-epoch VLBI observations of individual Gigahertz Peaked Spectrum and Compact Symmetric Objects indicate dynamical ages in the range of a few hundred to a few thousand years (e.g Polatidis & Conway 2003). Since the peak of these sources shifts to lower observed frequencies at higher redshift, low frequency observations, combined with multi-wavelength data, can identify these faint peakers and establish whether they are less luminous or at very high redshift and have different host properties (masses, starformation rates).

The accretion modes of radio sources – Radio galaxies and radio loud quasars have been studied extensively in order to reveal the details of the relationship between Active Galactic Nuclei (AGN) and their host galaxies, in particular how their interaction affects their evolution. The expanding jets of radio-loud AGN provide a mechanism for the transfer of energy to the intracluster medium and prevent the catastrophic cooling and formation of too-massive elliptical galaxies (Fabian et al. 2006; Best et al. 2006, 2007; Croton et al. 2006; Bower et al. 2006), but the accretion and feedback processes and how they evolve over cosmic time are not fully understood. It is known that the fraction of massive galaxies which are radio-loud at $z \approx 0.5$ is about the same

as observed locally ($z \approx 0.1$, Best et al. 2005b), while for less massive galaxies ($< 10^{10.5} M_{\odot}$), it is an order of magnitude larger. Studies of these AGN show two different types: a 'hot' mode where radiatively inefficient accretion occurs from hot halo gas onto massive galaxies, and a 'cold' mode where cold gas from major mergers drives high accretion rates. The strong evolution in the radio luminosity function is thus a result of less massive galaxies experiencing more mergers and being more active at high z. A full understanding of the different AGN populations, their distribution in luminosity and host galaxy properties, and particularly their cosmic evolution, is important for AGN and galaxy evolutionary models. Differences in their host galaxy populations will provide insight into the triggering mechanisms for radio activity as well as the effect of radio feedback.

In this paper we present wide, deep, high-resolution observations of the NOAO Boötes extragalactic field at 153 MHz taken with the GMRT. An initial, very deep, ≈ 1 mJy beam^{-1} rms, 153 MHz GMRT map of this field was presented by Intema et al. (2011). Here we present additional pointings around this map effectively tripling the size of the surveyed area at a slightly higher noise level. The Boötes field is part of the NOAO Deep Wide Field Survey (NDWFS; Jannuzi & Dey 1999) and covers ≈ 9 deg^2 in the optical and near infra-red B_W, R, I and K bands. There is a wealth of additional complementary data available for this field, including X-ray (Murray et al. 2005; Kenter et al. 2005), UV (GALEX; Martin et al. 2003), and mid infrared (Eisenhardt et al. 2004; Martin et al. 2003). The region has also been surveyed at radio wavelengths with the WSRT at 1.4 GHz (de Vries et al. 2002), the VLA at 1.4 GHz (Higdon et al. 2005) and 325 MHz (Croft et al. 2008). Recently, the AGN and Galaxy Evolution Survey (AGES) has provided redshifts for 23 745 galaxies and AGN across 7.7 deg^2 of the Boötes field (Kochanek et al. 2012). This unique rich multiwavelength dataset, combined with the new low frequency radio data presented here, will be valuable in improving our understanding of the above-mentioned key topics in astrophysics.

The observations presented here are the first part of the Two-meter Radio Mini Survey (T-RaMiSu), consisting of two 153 MHz mosaics of similar area and depth. The second mosaic, centered on the galaxy cluster Abell 2256, will be presented by Intema et. al (in prep).

This paper is structured as follows. In Sect. 2.2 we describe the GMRT observations of the extended region around the NOAO Boötes field. We describe the techniques employed to achieve the deepest possible images. Our data reduction relies on the ionospheric calibration with the SPAM package (Intema et al. 2009). In Sect. 2.3 we describe the source detection method and the compilation of a source catalogue. This section also includes a discussion of the completeness and reliability of the catalogue and an analysis of the quality of the catalogue. The source counts and spectral index distributions are presented in Sect. 2.4. Finally, Sect. 2.5 summarises and concludes this work.

2.2 Observations and Data Reduction

2.2.1 Observations

The central Boötes field was previously observed with the GMRT from $3-4$ June 2005 (Intema et al. 2011). We use the data from a single day of this observing run, combined with new observations of six flanking fields taken during $3-6$ June 2006 with the GMRT at 153 MHz. Data from the first day only of the first observing run, 3 June, was used as the RFI situation was marginally better on this day and the length of a single day's observation, 359 min, compares well with that of the new observations of the flanking fields, 205 min, which leads to a more uniform mosaic. Table 2.1 lists the observational parameters used, highlighting any differences between

Table 2.1: GMRT observation parameters for the Boötes field.

Parameter	Central	Flanking
Observation Dates	3 June 2005	3-6 June 2006
Pointings	Boötes	Boötes A-F
Primary Calibrator	3C 48	3C 48
Total Time on Calibrator	20 min	51 min
Secondary Calibrator	3C 286	3C 286
Total Time on Calibrator	9×10 min	10×4.5 min (per day)
Cadence	50 min	30 min
Total Time on Target	359 min	205 min (per pointing)
Integration time		16.9 s
Polarisations		RR,LL
Channels		128
Channel Width		62.5 kHz
Total Bandwidth		8.0 MHz
Central Frequency		153 MHz

Table 2.2: Pointing centres of the Boötes central and flanking fields.

Field	RA (J2000)	DEC (J2000)
Boötes	14:32:05.75	+34:16:47.5
Boötes A	14:32:05.75	+36:06:47.5
Boötes B	14:24:19.53	+35:10:52.5
Boötes C	14:24:29.58	+33:20:54.5
Boötes D	14:32:05.75	+32:26:47.5
Boötes E	14:39:41.92	+33:20:54.5
Boötes F	14:39:51.97	+35:10:52.5

the two sets of observations. The flanking fields are arranged on a hexagonal grid with a radius of 110arcmin just beyond the half power point of the primary beam of the GMRT at 153 MHz ($\theta_{\rm FWHM} \approx 3^\circ$); Table 2.2 gives the central coordinates of each pointing. Typically $26-27$ of the 30 antennas were available during each observing run. 3C 48 and 3C 286 were observed as phase, bandpass and flux density calibrators. For each of the four days, the target fields were observed in sets of ≈ 4.5 min each, followed by a calibrator observation (3C 286) of ≈ 4.5 min. 3C 48 was observed at the beginning or end of each day for $\approx 20-30$ min. The frequent (≈ 30 min interval) calibrator observations of 3C 286 provide a means to track changes in the GMRT system, RFI and ionospheric conditions, and flux density scale. The short target field observations spread over each night of observing provides fairly uniform uv-coverage.

2.2.2 Data Reduction

The data for the central pointing was re-reduced in the same manner as the new flanking fields in order to allow for consistent integration into a single mosaic. The data reduction consisted of two stages: 'traditional calibration' followed by directional-dependent ionospheric phase calibration, both of which were implemented in Python using the ParselTongue (Kettenis et al. 2006) interface to the Astronomical Image Processing System package (AIPS; Greisen 1998). Ionospheric calibration was done with the 'Source Peeling and Atmospheric Modelling' ParselTongue-based Python module (SPAM; Intema et al. 2009).

The data for each day were calibrated separately. The flux density scale was set and initial amplitude, phase and bandpass calibration were done using 3C 48. 3C 48 is brighter than 3C 286 and provides a better determination of the bandpass. In order to reduce the data volume, the LL and RR polarisations were combined as Stokes I and every 5 channels were combined to form 18 channels of width 0.3125 MHz yielding an effective bandwidth of 5.625 MHz. After this calibration, the uv-data from all four days for each target, were combined.

Initial imaging of each target field was done after a phase-only calibration against a model field constructed from NVSS sources within each field. Table 2.3 lists the important imaging parameters. The calibration was then improved by several rounds of phase-only self-calibration followed by one round of amplitude and phase self-calibration where gain solutions were determined on a longer time-scale than the phase-only solutions. Excessive visibilities were determined from the model-subtracted data and were removed. Additional automated removal of bad data causing ripples in the image plane was done by Fourier transforming the model-subtracted images and identifying and removing extraneous peaks in the uv-plane. Further, persistent RFI was flagged and low level RFI modelled and subtracted using the LowFRFI[1] routine in ObitTalk (Cotton 2008). After self-calibration the rms noise in the inner half of the primary beam area was 2.5 mJy beam^{-1} in the central field and $3.5-5$ mJy beam^{-1} in the flanking fields, with the local noise increasing $2-3$ times near the brightest sources. Note, the presence of extremely bright sources with peak flux densities of the order of $5-8$ Jy beam^{-1} prior to primary beam correction in flanking fields D through F resulted in the slightly higher overall noise in these fields.

Significant artefacts, however, remained in all fields near bright sources. To reduce these we applied the SPAM algorithm on the self-calibrated data. The SPAM parameters are listed in the bottom part of Table 2.3 which include the number of ionospheric layers modeled and their heights and relative weights, the slope of the assumed power law function of phase structure resulting from turbulence (γ) and the number of free parameters in the fit (see Intema et al. 2009, for a more detailed description of the meaning of these parameters). Three iterations of peeling were done: in the first we only applied the peeling solutions to the peeled sources and in the final two we fitted an ionospheric phase screen to the peeling solutions. Up to 20 sources with flux densities above 0.4 Jy (not corrected for primary beam effects) were peeled in the final stage in each field. The screen was made up of two equally-weighted turbulent layers at 250 and 350 km. SPAM also allowed for the determination of and correction for antenna-based phase discontinuities.

In order to have a homogeneous point spread functions in all pointings, final images were made with a circular restoring beam of radius 25 arcsec and a pixel size of 3.8 arcsec. The flux density scales of the central and flanking fields were scaled up by 60 per cent and 30 per cent respectively based on information from 3C 286 (discussed in Sect. 2.3.4). In the final individual field images, the rms noise in the central half of the primary beam area before primary beam

[1] Obit Development Memo Series # 16 see `http://www.cv.nrao.edu/~bcotton/Obit.html`

Table 2.3: Final CLEAN (top) and SPAM (bottom) parameters for individual Boötes fields.

Parameter	Value
Widefield imaging	polyhedron facet-based[a]
	multi-frequency synthesis[b]
Deconvolution	Cotton-Schwab CLEAN[c]
field size	4°
facets	85
facet size	32.4arcmin
facet separation	26.4arcmin
Weighting	Robust[e] -0.5[d]
`uvbxfn`, `uvbox`	4, 1
CLEAN box threshold	$5\,\sigma$
CLEAN depth	$3\,\sigma$
Pixel size	3.8 arcsec
Restoring beam	25 arcsec circular[d]
SPAM calibration cycles	3
Peeled sources	20[f]
Layer heights (weights)	250 km (0.5)
	350 km (0.5)
Turbulence parameter γ	$5/3$[g]
Model parameters	$\leqslant 20$
Reference catalogue	NVSS[h]

[a]Perley (1989); Cornwell & Perley (1992)
[b]Conway et al. (1990)
[c]Schwab (1984); Cotton (1999); Cornwell et al. (1999)
[d]Final imaging parameters
[e]Briggs (1995)
[f]14 for field F
[g]pure Kolmogorov turbulence
[h]Condon et al. (1994, 1998)

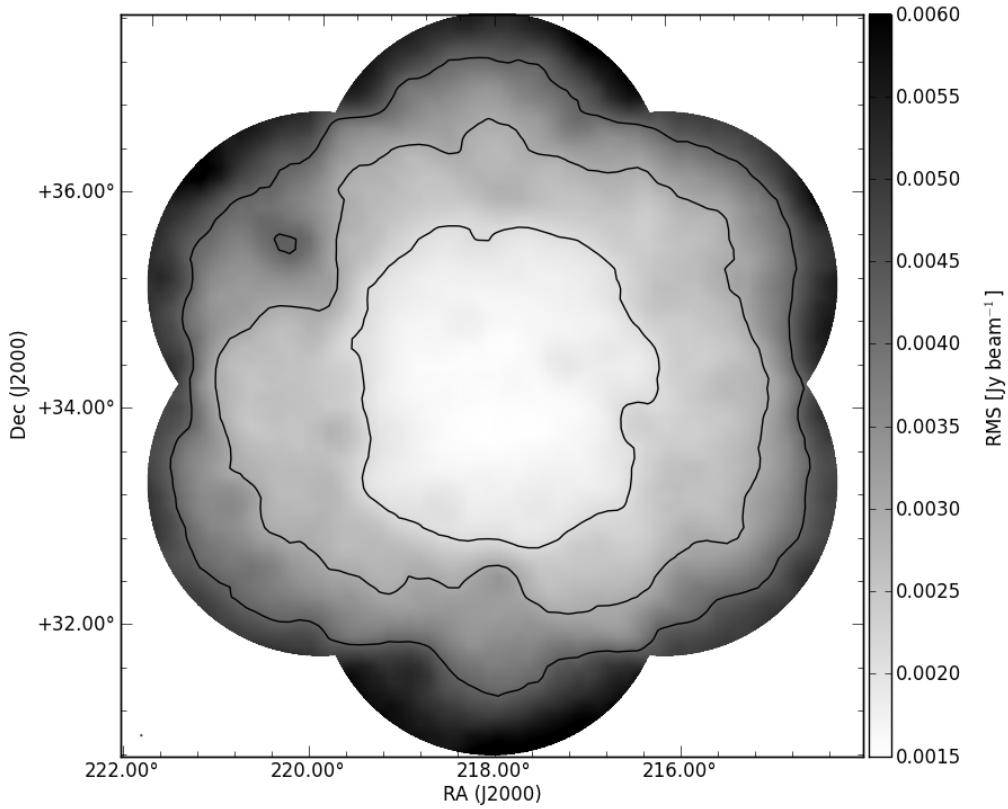


Figure 2.1: Greyscale map showing the local rms noise measured in the mosaic image. The greyscale shows the rms noise from $0.5\sigma_{\rm avg}$ to $2\sigma_{\rm avg}$, where $\sigma_{\rm avg} = 3.0\,{\rm mJy\,beam^{-1}}$ is the approximate rms in the mosaic centre. The contours are plotted at $[1/\sqrt{2}, 1, \sqrt{2}] \times \sigma_{\rm avg}$. Peaks in the local noise coincide with the locations of bright sources.

correction was $1.8\,\mathrm{mJy\,beam^{-1}}$ in the central field and $2.5 - 2.7\,\mathrm{mJy\,beam^{-1}}$ respectively in the flanking fields. This is $3 - 5$ times the theoretical noise, similar to the factor above thermal noise obtained by deeper single pointing of Intema et al. (2011). The seven pointings were each corrected for the primary beam of the GMRT up to a radius of $1.6°$, where the primary beam correction factor drops to 40 per cent of its central value, and were then mosaicked together by weighting the final image by the inverse of the square of the rms noise of each individual pointing. Figure 2.1 illustrates the variation in rms noise across the mosaic which is shown in entirety in Fig. 2.2. The noise level is smooth and around $2\,\mathrm{mJy\,beam^{-1}}$ across the interior of the map, and increases towards the edges to about $4 - 5\,\mathrm{mJy\,beam^{-1}}$. The average noise in the final mosaic is $3.0\,\mathrm{mJy\,beam^{-1}}$, with 49 per cent under $3\,\mathrm{mJy\,beam^{-1}}$ and 74 per cent under $4\,\mathrm{mJy\,beam^{-1}}$. A small portion of the mosaic covering the inner square degree is shown in Fig. 2.3 to illustrate the resolution and quality of the map. There remain some phase artefacts visible around the brightest sources, which have not been entirely removed during peeling. It is possible that some artefacts are caused by elevation-dependent pointing errors, since each pointing was observed in a series of scans with varying elevations (Tasse et al. 2007; Mohan et al. 2001; Chandra et al. 2004).

2.3 Source Detection and Characterisation

2.3.1 Detection

We used the PyBDSM package[1] to detect and characterise sources in the mosaic image. PyBDSM identifies islands of contiguous emission by identifying all pixels greater than the pixel threshold and adding each of these pixels to an island of contiguous pixels exceeding the island threshold. Each island is fit with one or more Gaussians which are subsequently grouped into sources. Sources are classified as 'S' for single sources, 'M' for multiple-Gaussian sources and 'C' for components of a multi-source island. From the fitted parameters the deconvolved sizes are computed assuming the theoretical beam. Errors on the fitted parameters are computed following Condon (1997). Prior to source detection the local background rms is determined by measuring the pixel statistics within a sliding box. For determining the rms background in our map we used a box size of 100 pixels to capture the variation in local noise around the brightest sources. We used a pixel threshold of $5\sigma_L$ and an island threshold of $3\sigma_L$. In generating a source list we allowed all Gaussians in each island to be grouped into a single source. PyBDSM detected 1296 sources from 1578 Gaussians fitted to 1301 islands, of which 1073 were single-component 'S' sources. Based on visual inspection a small number of sources were removed as they were false, or bad, detections on the edge of the image.

The final catalogue consists of 1289 sources between 4.1 mJy and 7.3 Jy and is available as part of the online version of this article and from the CDS[2]. The flux scales of the individual pointings were adjusted prior to mosaicing as described in Sect. 2.3.4 and the astrometry in the catalogue has been corrected for a systematic offset also described in Sect. 2.3.4. A sample of the catalogue is shown in Table 2.4 where the columns are:
Column (1) Source name,
Columns (2,3) flux-weighted position right ascension, RA, and uncertainty,
Columns (4,5) flux-weighted position declination, DEC, and uncertainty,
Column (6) integrated source flux density and uncertainty,

[1] `http://home.strw.leidenuniv.nl/~mohan/anaamika`
[2] `http://cdsweb.u-strasborg.fr/`

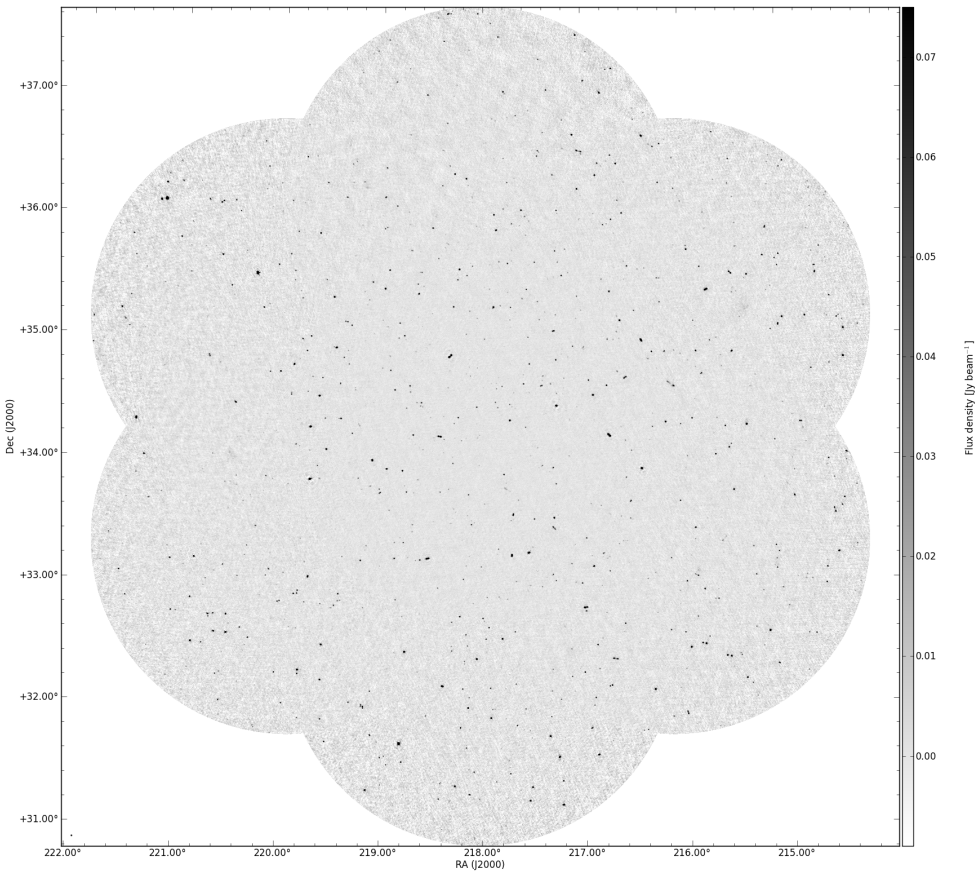


Figure 2.2: Greyscale map showing the entire mosaic. The image covers 30 square degrees. The greyscale shows the flux density from $-3\sigma_{\mathrm{avg}}$ to $25\sigma_{\mathrm{avg}}$ where $\sigma_{\mathrm{avg}} = 3.0\,\mathrm{mJy\,beam}^{-1}$ is the average rms across the entire mosaic.

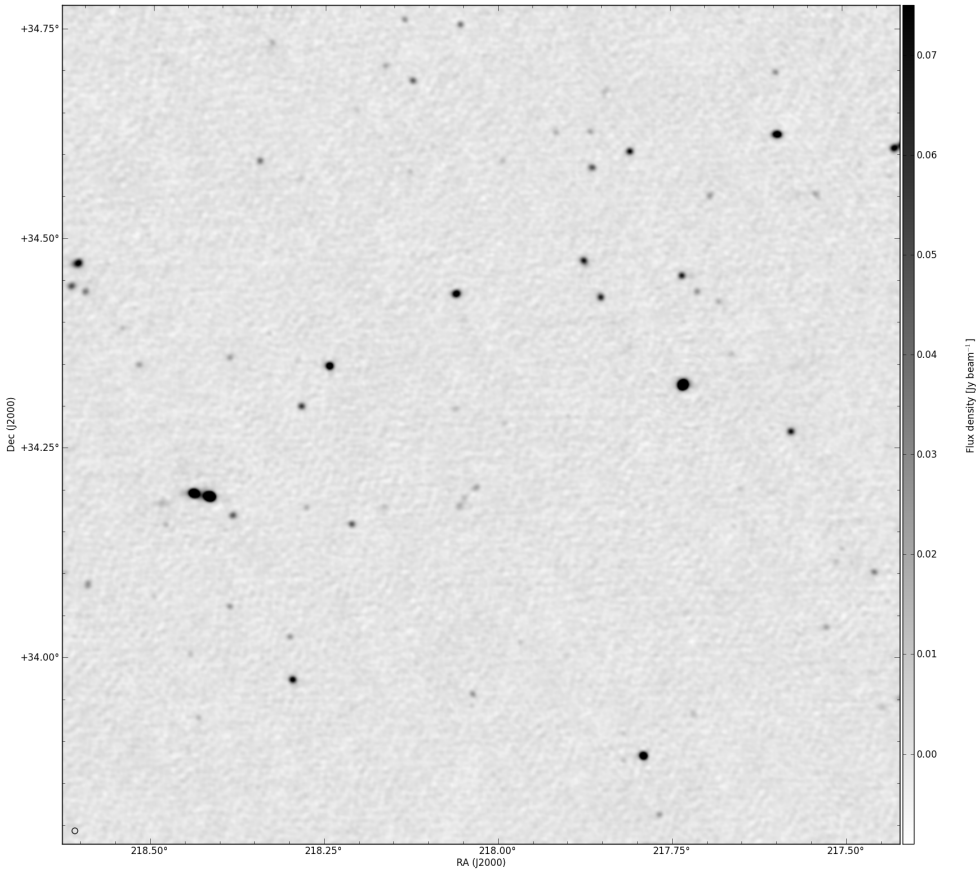


Figure 2.3: Zoom-in of the central part of the mosaic. The image covers 1 square degree. The greyscale shows the flux density from $-3\sigma_{\mathrm{avg}}$ to $25\sigma_{\mathrm{avg}}$ where $\sigma_{\mathrm{avg}} = 3.0\,\mathrm{mJy\,beam}^{-1}$ is the average rms across the entire mosaic.

Column (7) peak flux density and uncertainty,
Columns (8,9,10) fitted parameters: deconvolved major- and minor-axes, and position angle, for extended sources,
Column (11) local rms noise, and
Column (12) the number of Gaussians fitted to the source.
Extended sources are classified as such based on the ratio between the integrated and peak flux densities (see Sect. 2.3.2). Unresolved sources have a '-' listed for all their fitted shape parameters (semi-major and -minor axes and position angle) or for only the semi-minor axis where the source is resolved in one direction. For extended sources consisting of multiple Gaussians, the fitted parameters for each Gaussian are given on separate lines in the table, listed as 'a', 'b', etc. Images of the 25 brightest sources are shown in Appendix 2.A.

2.3.2 Resolved Sources

In the presence of no noise, the extendedness of a source can simply be determined from the ratio of the integrated flux density to the peak flux density, $S_i/S_p > 1$. However, since the errors on S_i and S_p are correlated, the S_i/S_p distribution is skewed, particularly at low signal-to-noise. To determine an upper envelope of this distribution, we performed a Monte-Carlo simulation in which we generated 25 random fields containing $\approx 10\,000$ randomly positioned point sources with peak flux densities between 0.1σ and 20σ, where σ was taken to be $3\,\mathrm{mJy\,beam^{-1}}$. The source flux densities are drawn randomly from the source count distribution, $dN/dS \propto S^{-1.6}$ (Sect. 2.4.1). We neglect the deviation of the true source counts from a power law slope at high fluxes as there are very few sources at these fluxes. The rms noise map for these fields was taken from the central 4000×4000 pixel^2 of the residual mosaic. Source detection was performed in the same manner described in Sect. 2.3.1, thus only ≈ 750 sources in each field satisfy the detection criterion of peak flux density $> 5\sigma$. The S_i/S_p distribution produced from the Monte-Carlo simulation is plotted in the *top* panel of Fig. 2.4. To determine the 95 per cent envelope, a curve was fit to the 95th percentile of 20 logarithmic bins across signal-to-noise ratio. The fitted envelope is characterised by:

$$S_i/S_p = 1 + \left\{ (0.01 \pm 0.02)^2 + (3.58 \pm 0.10)^2 \left(\sigma_L/S_p\right)^2 \right\}^{0.5}.$$

The measured distribution of S_i/S_p as a function of signal-to-noise ratio is shown in the *bottom* panel of Fig. 2.4. The line shows the upper envelope from the Monte-Carlo simulation. Of the 453 sources that lie above this line (35 per cent of all 1289 sources), approximately 41, i.e. 9 per cent, are not truly extended and merely lie above the line by chance. However, all these sources above the line are listed in the catalogue as extended and the measured deconvolved FWHM major and minor axes are given.

2.3.3 Completeness and Reliability

To quantify the completeness and reliability of the catalogue, we performed a similar Monte-Carlo simulation to that described in the previous section. However, in this case approximately 25 per cent of the artificial sources inserted into the noise map were extended sources – Gaussians with FWHM larger than the beamsize. This allows for a better estimate of the completeness and reliability in terms of integrated flux densities.

The completeness of a catalogue represents the probability that all sources above a given flux density are detected. We have estimated this by plotting the fraction of detected sources in our

Table 2.4: Sample of the GMRT 153 MHz combined source and Gaussian-component catalogue.

Source ID	RA	σ_{RA}	DEC	σ_{DEC}	S_i	S_p	a[a]	b[a]	ϕ[a]	rms	$N_{\rm gauss}$[b]
	[deg]	[arcsec]	[deg]	[arcsec]	[mJy]	[mJy beam^{-1}]	[arcsec]	[arcsec]	[deg]	[mJy beam^{-1}]	
(1)	(2)	(3)	(4)	(5)	(6)	(7)	(8)	(9)	(10)	(11)	(12)
J144733+3507	221.88796	0.9	35.13126	1.5	158 ± 33	69 ± 15	38.3 ± 3.4	19.3 ± 1.9	5 ± 6	5.4	1
J144658+3308	221.74358	2.9	33.14058	1.1	42 ± 13	20 ± 6				4.9	2
a	221.74843	2.8	33.14096	1.8	19 ± 8	19 ± 5	-	-	-		
b	221.73914	2.8	33.14001	2.6	23 ± 8	18 ± 5	15.9 ± 6.8	9.5 ± 5.6	56 ± 90		
J144705+3442	221.77266	1.8	34.71605	1.6	32 ± 9	27 ± 7	-	-	-	4.7	1
J144706+3457	221.77552	1.4	34.95096	1.5	25 ± 9	28 ± 7	-	-	-	5.0	1
J144645+3330	221.69153	1.8	33.50822	1.4	31 ± 9	29 ± 7	-	-	-	4.8	1
J144640+3322	221.66919	0.9	33.36920	0.8	72 ± 16	62 ± 13	-	-	-	4.9	1
J144646+3440	221.69543	1.5	34.67482	1.1	29 ± 9	32 ± 8	-	-	-	5.1	1
J144648+3546	221.70230	1.9	35.77421	1.4	19 ± 8	25 ± 6	-	-	-	5.0	1
J144613+3303	221.55831	0.7	33.06494	0.6	169 ± 35	131 ± 27	-	-	-	5.0	-
J144638+3553	221.65996	2.1	35.88845	2.3	37 ± 11	27 ± 7	-	-	-	5.7	1
J144626+3512	221.61124	1.0	35.20927	0.7	314 ± 65	244 ± 50	-	-	-	7.5	-
J144619+3425	221.58123	3.2	34.42447	2.4	46 ± 12	26 ± 7	-	-	-	5.5	1
J144606+3316	221.52865	2.9	33.26922	2.2	20 ± 7	17 ± 5	-	-	-	4.2	1
J144557+3251	221.49062	0.6	32.86032	0.5	122 ± 26	111 ± 23	-	-	-	5.0	1
J144555+3237	221.48098	2.4	32.62328	3.6	24 ± 7	17 ± 5	-	-	-	4.4	1
J144617+3506	221.57405	1.1	35.11639	1.3	158 ± 34	75 ± 16				5.3	2
a	221.57091	0.9	35.11314	0.7	93 ± 20	78 ± 16	15.3 ± 1.8	5.6 ± 1.4	72 ± 16		
b	221.57923	1.4	35.12223	2.1	65 ± 15	38 ± 9	29.4 ± 5.1	10.6 ± 2.8	12 ± 14		
J144602+3339	221.50949	2.1	33.66347	1.3	42 ± 10	27 ± 6	29.3 ± 5.3	-	64 ± 11	3.8	1
J144607+3503	221.52967	1.2	35.05975	0.6	81 ± 18	62 ± 13	-	-	178 ± 6	4.8	1

[a] Parameters are given for extended sources to which Gaussian components were successfully fit.

[b] A '-' indicates a poor Gaussian fit. In these cases the total flux density quoted is the total flux density in the source island.

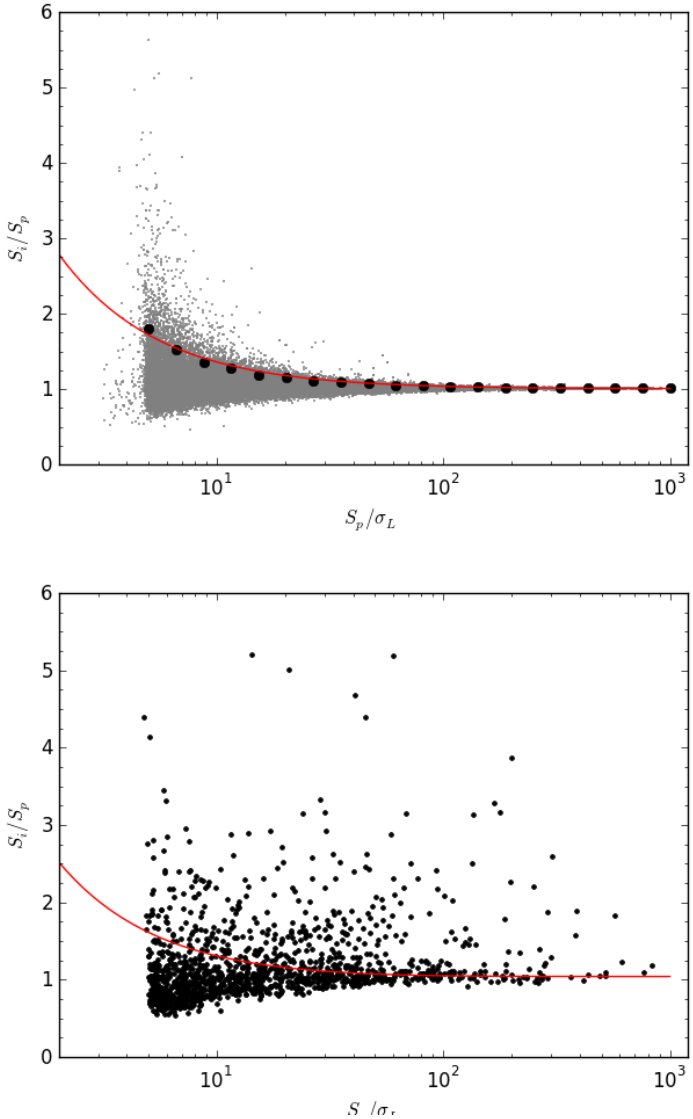


Figure 2.4: *Top* The simulated ratio of integrated to peak flux density as a function of signal-to-noise ratio for sources from the 25 Monte-Carlo simulations. For 20 logarithmic bins in signal-to-noise ratio, the black points show the threshold below which 95 per cent of the sources lie in that bin. The red line shows a fit to this upper envelope. *Bottom* The measured ratio of integrated to peak flux density as a function of signal-to-noise ratio. The line shows the upper envelope containing 95 per cent of the unresolved sources as determined from Monte-Carlo simulations.

MC simulation as a function of integrated flux density (*top* panel of Fig. 2.5), i.e. the fraction of input sources that have a catalogued flux density using the same detection parameters. Due to the variation in rms across the image, the detection fraction has been multiplied by the fraction of the total 30 deg^2 area in which the source can be detected. The completeness at a given flux density is determined by integrating the detected fraction upwards from a given flux density limit and is plotted as a function of integrated flux density in the *bottom* panel of Fig. 2.5. We thus estimate that the catalogue is 95 per cent complete above a peak flux density of 14 mJy.

The reliability of the catalogue indicates the probability that all sources above a given flux density are real. In the *top* panel of Fig. 2.6, the false detection rate FDR, i.e. the fraction of catalogued sources that do not have an input source, is plotted as a function of the integrated flux density. Integrating up from a given detection limit and multiplying by the normalised source flux distribution, we can determine an estimate of the overall FDR or reliability, $R = 1 - FDR$, of the catalogue. The reliability is plotted as a function of integrated flux density limit in the *bottom* panel of Fig. 2.6. For a 14 mJy detection threshold, the reliability is 92 per cent.

2.3.4 Astrometric and Flux Uncertainties

Errors in the phase calibration introduce uncertainties in the source positions. To assess these uncertainties and determine any systematic offsets we selected a sample of sources with peak flux densities at least $10\sigma_L$. We searched for 1.4 GHz NVSS (Condon et al. 1998) sources within 45 arcsec of these targets. 745 matches were found. From this sample, we measured a small offset of $(\Delta\alpha, \Delta\delta) = (0.44\,\text{arcsec}, -0.21\,\text{arcsec})$, which is of the order of the pixel size of the 153 MHz observations and the NVSS accuracy (≈ 1 arcsec). A correction for this offset has been applied to all sources in the catalogue. The scatter in the offsets between the GMRT and NVSS positions is a combination of noise-independent calibration errors, ϵ, in both the GMRT and NVSS data as well as a noise-dependent error, σ, from position determination via Gaussian-fitting:

$$\sigma^2 = \epsilon^2_{\text{GMRT}} + \epsilon^2_{\text{NVSS}} + \sigma^2_{\text{GMRT}} + \sigma^2_{\text{NVSS}}$$

The NVSS calibration errors are $(\epsilon_\alpha, \epsilon_\delta)_{\text{NVSS}} = (0.45\,\text{arcsec}, 0.56\,\text{arcsec})$ (Condon et al. 1998). To separate the noise-dependent and -independent uncertainties we select from the above sample only the NVSS sources with position errors of less than 0.6 arcsec and measure a scatter of $(\sigma_\alpha, \sigma_\delta)_{\text{GMRT}} = (0.67\,\text{arcsec}, 0.65\,\text{arcsec})$. For this very high signal-to-noise sub-sample of 107 sources the noise-dependent fit errors for both the GMRT and NVSS can safely be assumed to be small so we determine the GMRT calibration errors to be $(\epsilon_\alpha, \epsilon_\delta)_{\text{GMRT}} = (0.50\,\text{arcsec}, 0.32\,\text{arcsec})$. These are added quadratically to the Gaussian-fit position uncertainties in the catalogue.

Similarly, in addition to the noise-dependent Gaussian fitting uncertainties on the fluxes (Condon 1997), the uncertainty in the measured flux densities all consists of a noise-independent component. The uncertainty introduced through transferring the flux density scale from the calibrator to the target fields is the main such uncertainty and depends on a number of factors: (i) the data quality, (ii) the accuracy of the model, and (iii) differences in observing conditions between the calibrator and target.

Like the target data, the calibrator data is adversely affected by RFI and the ionosphere. The RFI conditions of the flanking field observations were similar to those when the central pointing data were taken, however, the ionosphere was not as calm. Following Intema et al. (2011) we adopt a slightly inflated, ad-hoc amplitude uncertainty of ≈ 4 per cent due to RFI and ionospheric effects.

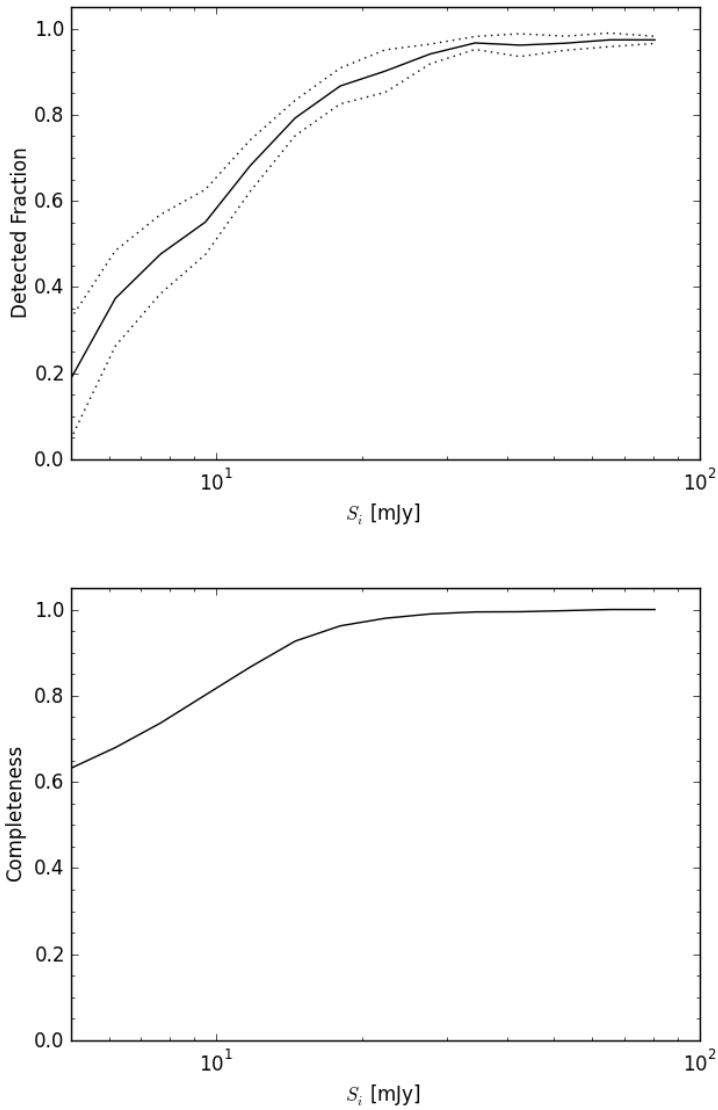


Figure 2.5: *Top* Fraction of sources detected as a function of integrated flux density to local noise ratio calculated from 25 Monte-Carlo simulations. The solid line shows the mean of all 25 randomly generated fields and the two dotted lines show the 1σ uncertainty. *Bottom* Estimated completeness of the catalogue as a function of integrated flux density limit accounting for the varying sensitivity across the field of view.

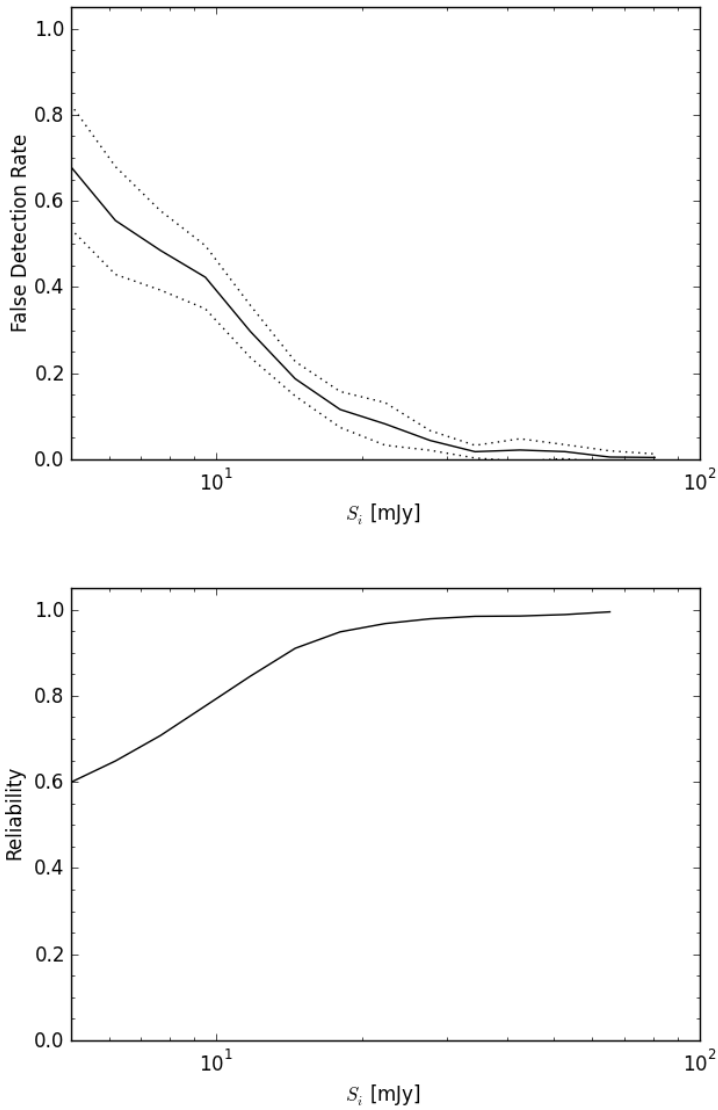


Figure 2.6: *Top* False detection rate as a function of peak flux density to local signal-to-noise ratio calculated from 25 Monte-Carlo simulations. The solid line shows the mean of all 25 randomly generated fields and the two dotted lines show the 1σ uncertainty. *Bottom* Estimated reliability of the catalogue as a function of integrated flux density limit accounting for the varying sensitivity across the field of view.

The calibrator model is of a point source whose flux density at 153 MHz is predicted from the Perley-Taylor model based on flux density measurements at many frequencies. 3C 48 is a point source of 64.4 Jy at 153 MHz. Intema et al. (2011) provide an improved model for 3C 286, a point source of 31.01 Jy at 153 MHz, and estimate a flux density uncertainty of 5 per cent. The large field of view, however, means that there are other fainter sources present in the calibrator field. For similar duration observations of 3C 286 Intema et al. (2011) set an upper limit of 1 per cent on the flux density uncertainty. Since 3C 48 is about a factor of two brighter, we estimate that the flux density uncertainty due to additional sources in the 3C 48 field is also at most 1 per cent.

Individual antennas are sensitive to the galactic diffuse radio emission which varies across the sky and so may be different for the calibrator and target fields thereby introducing an offset to the flux density scale as well as additional uncertainty. However, since the GMRT does not measure the sky temperature, we require external information to take this into account. Following Tasse et al. (2007) and Intema et al. (2011) we determine the mean off-source sky-temperature from the Haslam et al. (1982) all-sky radio maps at 408 MHz: both the Boötes and 3C 286 fields have sky temperatures of $\approx 20 \pm 1$ K. Using the equation from Tasse et al. (2007), this implies that no offset in the flux density scale is required for 3C 286 and we estimate a gain uncertainty of 2 per cent. However, the sky temperature near the primary calibrator 3C 48 is 24 ± 1 K which implies a flux density correction of 0.92 with an estimated uncertainty of 8 per cent. Since the flux density scale is linear, this offset is applied post hoc to the measured flux densities.

Prior to combining the individual pointings, we compared the measured primary beam-corrected flux densities of sources in the overlapping regions (approximately $110 - 150$ sources per region) and found those in the flanking fields to be consistently higher by 30 ± 5 per cent. To investigate this we made images after calibration using 3C 286 as the primary calibrator. This yielded consistent fluxes between the central and flanking fields. It is likely that significant time-dependent changes in the GMRT systems over the course of each observing night were captured by the regular (each 30 min) observations of 3C 286. We thus used the 3C 286-calibrated images to derive a correction to the flux density scales of the flanking fields, a factor of 1.3, before combining the individual pointings. The uncertainty of this correction is 10 per cent.

The total estimated uncertainty in transferring the flux density scale is of the order of 20 per cent which we add quadratically to the measured Gaussian fit uncertainty for each source. Comparison of the flux density of bright sources measured in the individual pointings after the above correction shows good agreement between the flux density scales of the individual pointings and the measured scatter is ≈ 16 per cent, which also includes a contribution by the noise-dependent terms.

2.3.5 Diffuse Sources

We have identified two faint diffuse sources in the final mosaic which were not detected by PyBDSM as their peak flux densities are too low. Postage stamps of these two sources are shown in Fig. 2.7. The first, D1, is located at RA = 14:21:32, DEC = +35:12:12. This source has previously detected in WENSS by Delain & Rudnick (2006) who have associated it with a galaxy group at $z = 0.01$. The second diffuse source, D2, is located at RA = 14:41:56, DEC = +34:01:34.

2.4 Analysis

The 1289 sources in the catalogue provide a statistically significant sample across three orders of magnitude in flux density from 4 mJy to 7 Jy. In this section we present the derived 153 MHz

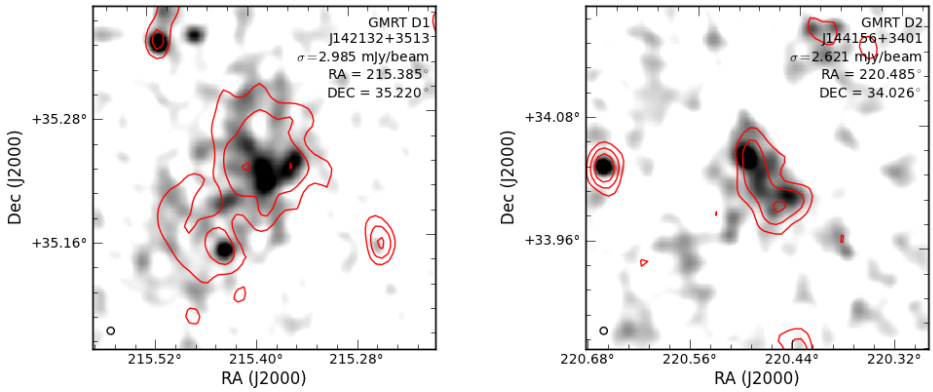


Figure 2.7: Postage stamps showing D1, RA = 14:21:32, DEC = +35:12:12 (*left*) and D2, RA=14:41:56, DEC=+34:01:34 (*right*). The greyscale goes from 0.5σ to 5σ and the images have been smoothed with a Gaussian of 50 arcsec. WENSS contours are overlaid at $[1.5, 3.0, 10.0] \times \sigma_L$ where σ_L is the local *rms* in the WENSS images – $3.5\,\mathrm{mJy\,beam^{-1}}$ and $3.7\,\mathrm{mJy\,beam^{-1}}$ respectively for D1 and D2.

source counts and spectral index distributions based on matching these sources to catalogues at 1.4 GHz and 320 MHz.

2.4.1 Source Counts

The Euclidean-normalized differential source counts are shown in Fig. 2.8. Due to the large variation in rms across the mosaic, the sources are not uniformly detected across the image, i.e. faint sources can only be detected in a smaller area in the inner part of the image. We therefore weight each source by the inverse of the area in which it can be detected (e.g. Windhorst et al. 1985), which also accounts for the varying detection area within a given flux density bin. Accurate derivation of the source counts is complicated by a number of effects. In general, noise can scatter sources into adjacent bins, most noticably at low flux densities. A positive bias is introduced by the enhancement of weak sources by random noise peaks (Eddington bias). Furthermore, low surface brightness extended sources can be missed as their peak flux densities fall below the detection limit. We have used our Monte-Carlo simulations to estimate the combined contribution of these effects and derive a correction factor to the observed source counts. Errors on the final normalised source counts are propagated from the errors on the correction factors and the Poisson errors (Gehrels 1986) on the raw counts per bin. The flux density bins start at three times the average rms, 15 mJy, and increase in factors of $2^{1/4}$, $2^{1/2}$ or 2 chosen to provide source counts of $60 - 80$ in most, except for the highest, flux density bins. Table 2.5 lists (i) the flux density bins, (ii) the central flux density of the bin, (iii) the raw counts, (iv) the effective detection areas for sources at the lower and upper limits of the flux density bin, (v) the effective area corresponding to the bin centre, (vi) the mean weight of the sources in the bin, (vii) the correction factor, and (viii) the corrected normalised source counts.

We have compared our source counts with the little observational data available at this frequency. Our source counts agree well with those derived by Intema et al. (2011) for the central field. Since their image is approximately three times deeper than our mosaic, the good agreement at low flux densities lends credance to our correction factors. The recent source counts from Ghosh et al. (2012) and those by Ishwara-Chandra et al. (2010) for a smaller, slightly shal-

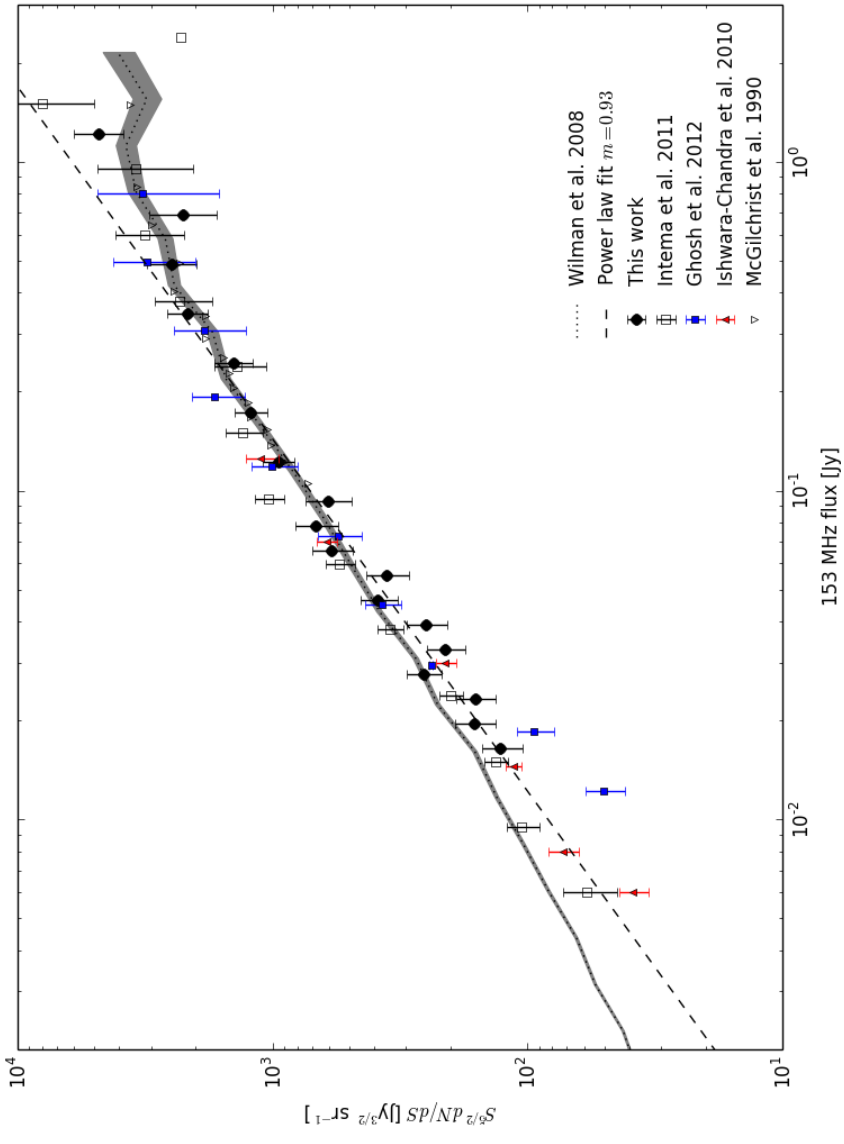


Figure 2.8: Euclidean-normalized differential source counts for the GMRT $153\,\mathrm{MHz}$ catalogue (filled black circles) in 18 logarithmic flux density bins between $15\,\mathrm{mJy}$ and $6.5\,\mathrm{Jy}$. For comparison we have plotted the $153\,\mathrm{MHz}$ source counts from Intema et al. (2011) (open squares) for the central Böotes pointing, from Ghosh et al. (2012) (blue filled squares) and from Ishwara-Chandra et al. (2010) (red filled triangles), as well as the $151\,\mathrm{MHz}$ source counts from McGilchrist et al. (1990) for part of the 7C catalogue (open inverted triangles). Also shown is a source count model by Wilman et al. (2008) (dotted line with shaded area indicating the 1σ errors) and a power law fitted between $150 - 400\,\mathrm{mJy}$ (dashed line) which has a slope of 0.93 ± 0.04.

Table 2.5: Euclidean-normalized differential source counts for the GMRT 153 MHz catalogue.

S Range [Jy]	S_c [Jy]	Raw Counts	Area [deg^2]	$A(S_c)$ [deg^2]	$\langle W \rangle$	Correction	Normalised counts [Jy$^{3/2}$ sr^{-1}]
$0.015 - 0.018$	0.016	$70.0^{+9.4}_{-8.3}$	$17.1 - 22.1$	19.7	0.80	1.14 ± 0.15	127^{+24}_{-22}
$0.018 - 0.021$	0.020	$68.0^{+9.3}_{-8.2}$	$22.1 - 26.5$	24.4	0.83	1.11 ± 0.14	162^{+30}_{-28}
$0.021 - 0.025$	0.023	$66.0^{+9.2}_{-8.1}$	$26.5 - 30.5$	28.7	0.91	1.06 ± 0.13	160^{+30}_{-28}
$0.025 - 0.030$	0.028	$86.0^{+10.3}_{-9.3}$	$30.5 - 32.9$	32.1	0.93	1.00 ± 0.11	256^{+42}_{-40}
$0.030 - 0.036$	0.033	$62.0^{+8.9}_{-7.9}$	$32.9 - 33.3$	33.2	0.96	0.94 ± 0.10	210^{+38}_{-35}
$0.036 - 0.042$	0.039	$58.0^{+8.7}_{-7.6}$	...	33.3	0.95	0.90 ± 0.11	249^{+47}_{-44}
$0.042 - 0.050$	0.046	$74.0^{+9.6}_{-8.6}$	...	33.3	0.99	0.91 ± 0.11	386^{+68}_{-64}
$0.050 - 0.060$	0.055	$51.0^{+8.2}_{-7.1}$	...	33.3	0.99	0.93 ± 0.11	357^{+71}_{-65}
$0.060 - 0.071$	0.066	$64.0^{+9.0}_{-8.0}$	...	33.3	0.99	0.95 ± 0.12	588^{+112}_{-105}
$0.071 - 0.085$	0.078	$57.0^{+8.6}_{-7.5}$	...	33.3	1.00	0.96 ± 0.13	680^{+137}_{-127}
$0.085 - 0.101$	0.093	$39.0^{+7.3}_{-6.2}$	...	33.3	1.00	0.96 ± 0.11	606^{+133}_{-119}
$0.101 - 0.143$	0.122	$81.0^{+10.0}_{-9.0}$	...	33.3	1.00	0.96 ± 0.07	951^{+136}_{-126}
$0.143 - 0.202$	0.172	$61.0^{+8.9}_{-7.8}$	...	33.3	1.00	0.97 ± 0.05	1218^{+187}_{-167}
$0.202 - 0.285$	0.244	$42.0^{+7.5}_{-6.5}$	...	33.3	1.00	0.98 ± 0.05	1423^{+265}_{-229}
$0.285 - 0.404$	0.345	$38.0^{+7.2}_{-6.1}$	...	33.3	1.00	0.98 ± 0.04	2160^{+422}_{-362}
$0.404 - 0.571$	0.487	$26.0^{+6.2}_{-5.1}$	...	33.3	1.00	0.98 ± 0.05	2496^{+606}_{-502}
$0.571 - 0.807$	0.689	$14.0^{+4.8}_{-3.7}$	...	33.3	1.00	0.98 ± 0.05	2257^{+790}_{-608}
$0.807 - 1.615$	1.211	$25.0^{+6.1}_{-5.0}$	...	33.3	1.00	0.98 ± 0.04	4807^{+1182}_{-971}
$1.615 - 6.458$	4.036	$9.0^{+4.1}_{-2.9}$	...	33.3	1.00	0.99 ± 0.01	5925^{+2715}_{-1936}

lower GMRT field also agree well with our data, except the Ghosh et al. (2012) counts deviate at low flux densities, becoming increasingly lower. At the high flux end, the 7C 151 MHz source counts (McGilchrist et al. 1990) match our counts well. We have fit a power law over the flux density range $15-400$ mJy and obtain a slope of 0.93 ± 0.04 which is consistent with, but slightly steeper than, the 0.91 obtained by Intema et al. (2011) across the same flux density range. Likewise, it is consistent with the value of 1.01 found by Ishwara-Chandra et al. (2010), but is slightly shallower. The source counts derived from the small sample of George & Stevens (2008) (not plotted) are fit by a single power law with a slope of 0.72, but their deviation is probably due to poor statistics. Model source counts have been derived by Wilman et al. (2008) for the 151 MHz source population predicted from the extrapolated radio luminosity functions of different radio sources in a ΛCDM framework. The Wilman et al. (2008) model catalogue has been corrected with their recommended post-processing, which effectively reduces the source count slightly at low flux densities. The dominant source population at flux densities above ≈ 200 mJy is that of FRII radio sources. Only below this flux density does the FRI population begin to dominate. There is a general agreement between our data and this model which has an approximate power-law slope of 0.79 between 10 and 400 mJy. At low flux densities it is likely that the Wilman et al. (2008) counts slightly overestimate the true counts due to double counting of hybrid AGN-star forming galaxies.

2.4.2 Spectral Index Distributions

While deep 1.4 GHz data exists for the Boötes Field (de Vries et al. 2002), this only covers the central 7 deg^2. This data was used in Intema et al. (2011) in a 153 MHz flux-limited spectral index analysis. However, we choose to compare our source list to the NVSS 1.4 GHz catalogue (Condon et al. 1994) which covers our entire survey area at a comparable resolution. We searched for NVSS counterparts within 45 arcsec of each GMRT source. Despite the relatively small difference in resolution between the NVSS (45 arcsec) and the GMRT (25 arcsec) data, a small number of GMRT sources (9 pairs) were matched the same NVSS source. Also, due to differences in the grouping of components into sources, we merged 16 pairs of NVSS sources which matched a single GMRT source. Sources were merged by summing their total flux densities. A spectral index was calculated for each GMRT source based on the combined flux density of merged sources.

We matched 1134 NVSS sources to 1127 GMRT sources and then used this matched subsample to compute the spectral index[1] distribution which is shown in Fig. 2.9. The flux density limit of 2.5 mJy at 1.4 GHz biases the detection of 1.4 GHz counterparts to fainter 153 MHz sources to those with flatter spectra. 168 GMRT sources have no match in NVSS. These are consistent with having steeper spectral indices below the diagonal line in Fig. 2.9 and we therefore provide an an upper limit to the spectral index given the NVSS flux density limit. The mean spectral index is -0.87 ± 0.01, calculated using the Kaplan-Meier estimator (KM; e.g. Feigelson & Nelson 1985) to account for the upper limits. This value is comparable to those found by Intema et al. (2011), -0.79, Ishwara-Chandra & Marathe (2007), -0.85, Sirothia et al. (2009), -0.82, and Ishwara-Chandra et al. (2010), -0.78. By considering the KM mean spectral index within 5 logarithmic flux density bins between 85 mJy and 1 Jy (overplotted in Fig. 2.9 and listed in Table 2.6), we find a gradual steepening of the spectral index with increasing flux density, from ≈ -0.84 at ≈ 30 mJy to ≈ -0.97 at $F \gtrsim 600$ mJy. This trend is still clear if the first flux density bin is ignored (i.e. considering $F \gtrsim 40$ mJy) assuming that this bin remains biased by

[1]The spectral index is defined as $S_\nu \propto \nu^\alpha$

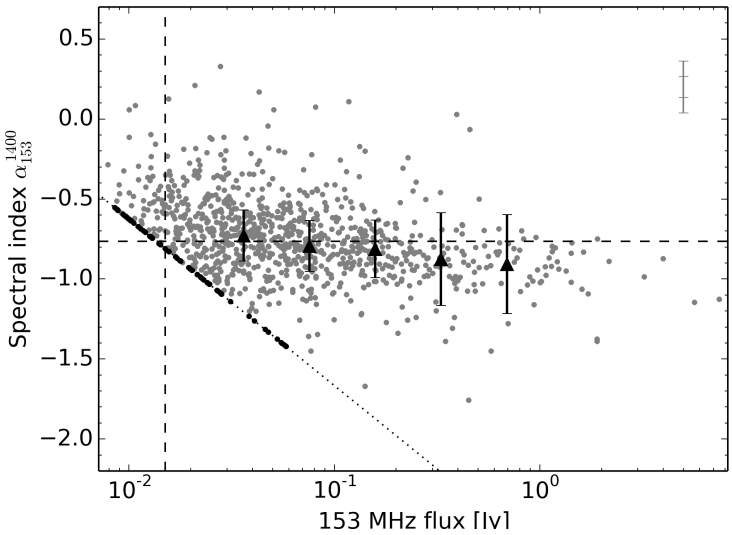


Figure 2.9: Spectral index, α_{153}^{1400}, distribution of sources matched between 1.4 GHz and 153 MHz (grey points). The difference in resolution is 45 arcsec (NVSS) and 25 arcsec (GMRT) and multiple GMRT matches to a single NVSS source have been merged into one. The vertical line shows $5\sigma_{\rm avg}$, where $\sigma_{\rm avg}$ is the average rms noise in the GMRT mosaic. The diagonal dotted line indicates the incompleteness limit due to the sensitivity of NVSS and sources with upper limits are plotted as black points along this line. The horizontal dashed line shows the KM mean spectral index of -0.87 ± 0.01 accounting for upper limits. The large black triangles show the mean spectral index in 5 logarithmic bins. Error bars on individual points are not plotted for clarity, but a single bar in the top right indicates the maximum and minumum errors in the dataset.

the upper limits. This is consistent with what is found in the literature (e.g. Ishwara-Chandra et al. 2010; Tasse et al. 2006; Cohen et al. 2004; de Vries et al. 2002). Since it appears that there is no spectral steepening or flattening due to redshifted curved spectra (Bornancini et al. 2010), this flattening is likely due to a correlation between source luminosity and spectral index ($P - \alpha$), which is known to exist for FRII radio galaxies (e.g. Blundell et al. 1999). According to the models of Wilman et al. (2008), the observed 153 MHz source population is dominated by FRII galaxies at these flux density levels ($\gtrsim 20$ mJy).

We also compared our source list to WENSS at 327 MHz (Rengelink et al. 1997), noting that the errors in this spectral index are much greater due to the smaller difference in frequency. The WENSS beam is 54×54 arcsec/ $\sin\delta$, or 54×96 arcsec at the declination of the Boötes field. We thus searched for WENSS counterparts within 96 arcsec of each GMRT source. Of the 1289 GMRT sources we matched 689 to 675 WENSS sources. The 14 pairs of GMRT sources within the beam of a single WENSS source were combined as described in the previous paragraph and spectral indices determined for each based on the combined flux density. A visual check led to the removal of 12 misidentified or confused sources. The resulting spectral index distribution for α_{153}^{327} is shown in Fig. 2.10. Once again there is a bias towards flatter or inverted spectra at low 153 MHz flux densities due to the WENSS flux density limit of 18 mJy at 327 MHz. We provide upper limits to the spectral indices given the WENSS flux density limit for the 576 GMRT sources with that have WENSS flux densities below the WENSS detection limit

Table 2.6: Binned median spectral indices between the GMRT at 153 MHz and NVSS at 1.4 GHz and WENSS at 327 MHz).

	NVSS α_{153}^{1400}		WENSS α_{153}^{327}	
Bin Centre	Counts	KM Mean	Counts	KM Mean
[mJy]	(Upper limits)	Spectral Index	(Upper limits)	Spectral Index
36	275(10)	-0.835 ± 0.015	-	-
76	213(7)	-0.909 ± 0.017	209(16)	-0.940 ± 0.031
158	143	-0.922 ± 0.018	140	-0.752 ± 0.028
331	71	-0.972 ± 0.029	72	-0.792 ± 0.028
692	28	-0.970 ± 0.028	32	-0.845 ± 0.033

and thus should have spectral indices are steeper than the diagonal line in Fig. 2.10. The KM mean spectral index in this case is -0.84 ± 0.02 (taking into account the upper limits) and is slightly shallower than that observed between 153 and 1400 MHz. The KM mean spectral indices measured in 4 flux density bins are also listed in Table 2.6. There is, however, no clear trend with flux density observed, although there is an indication of a slight flattening of the average radio spectrum if the first flux bin is excluded. This may be due to the fact that α_{153}^{327} is less robust due to the small frequency difference and the errors on the individual measurements are higher.

Around 50 per cent of our sources have data at three frequencies (1400, 327, and 153 MHz), thus we have not attempted to fit or locate peaks in the radio spectra. Instead we show a radio 'colour-colour' plot, Fig. 2.11, comparing the spectral indices α_{153}^{1400} and α_{153}^{327}. The line illustrates where the two spectral indices are equal. Here we have plotted separately bright 153 MHz sources, above 0.1 Jy beam^{-1}, as these sources have smaller errors on their spectral indices and are not affected by incompleteness at the other two frequencies (see Figs. 2.9 and 2.10). In general there is a flattening of the average radio spectrum toward lower frequencies, as the majority of points fall above the line. It is likely that this observed turnover in the spectra at low frequencies is due synchrotron self-absorption. We also plot the distribution of the difference in spectral indices, $\alpha_{153}^{1400} - \alpha_{153}^{327}$, Fig. 2.12, which shows a mean value of -0.25 for only bright sources and and -0.2 for all sources.

Finally, we have also compared our source list to VLSS at 74 MHz (Cohen et al. 2007), again noting that the errors in this spectral index will be much greater due to the smaller difference in frequency. VLSS has a resolution of 80 arcsec so we searched for VLSS sources within this radius of each GMRT source. 58 GMRT sources were matched to 55 VLSS sources. The resulting spectral index distribution is shown in Fig. 2.13. In this case these is a bias towards steeper spectra at low 153 MHz flux densities due to the VLSS flux density limit of 0.5 Jy at 74 MHz. The KM mean spectral index in this case is -0.55 which was calculated for sources with GMRT fluxes above 0.5 Jy.

2.5 Conclusion

We have presented the results from a $\approx$30 square degree, high resolution (25 arcsec) radio survey at 153 MHz centred on the NOAO Boötes field. We have employed the SPAM ionospheric calibration scheme to achieve an rms noise in the 7 pointing mosaicked image of $\approx 2 - 4$ mJy

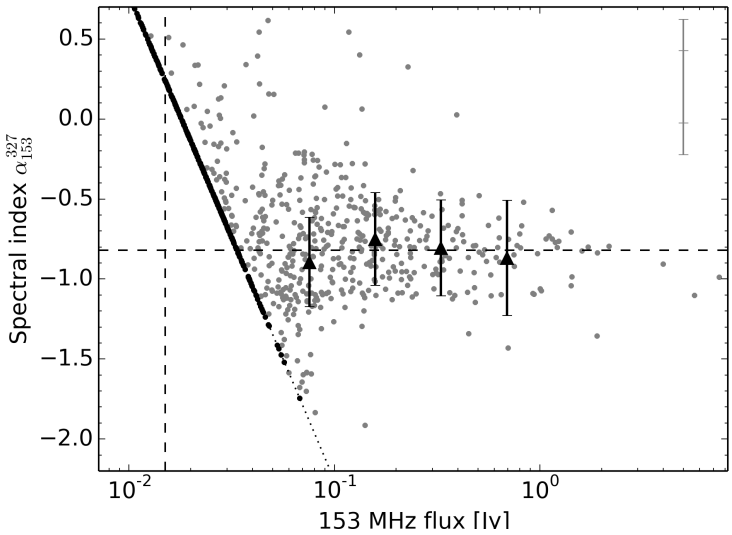


Figure 2.10: Spectral index, α_{153}^{327}, distribution between $327\,\mathrm{MHz}$ and $153\,\mathrm{MHz}$ (grey points). The difference in resolution is 54×96 arcsec (WENSS) and 25 arcsec (GMRT) and multiple GMRT matches to a single WENSS source have been merged. The vertical line shows $5\sigma_{\mathrm{avg}}$, where σ_{avg} is the average rms noise in the GMRT mosaic. The diagonal dotted line indicates the incompleteness limit due to the sensitivity of WENSS. The horizontal dashed line shows the KM mean spectral index of -0.84 ± 0.02 which takes the upper limits into account. The large black triangles show the median spectral index in 4 logarithmic bins. Error bars on individual points are not plotted for clarity, but a single bar in the top right indicates the maximum and minumum errors in the dataset.

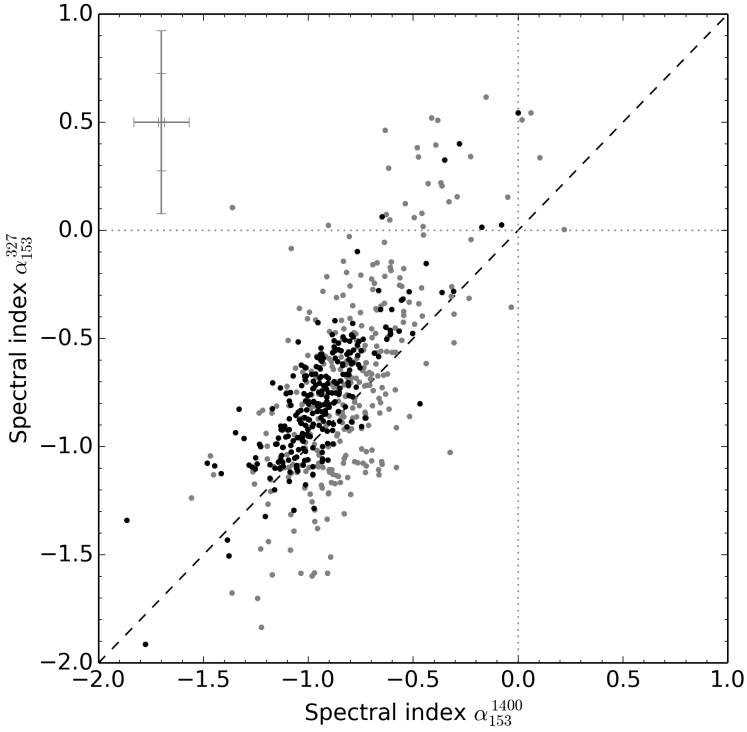


Figure 2.11: Comparison between α_{327}^{1400} and α_{153}^{327}. The black dashed line indicates where the spectral index is the same in both regions of the spectrum. Sources with GMRT fluxes above 0.1 Jy beam^{-1} are plotted in black and fainter sources are plotted in grey. Error bars on individual points are not plotted for clarity, but a single error bar in the top left indicates the maximum and minumum errors in the dataset.

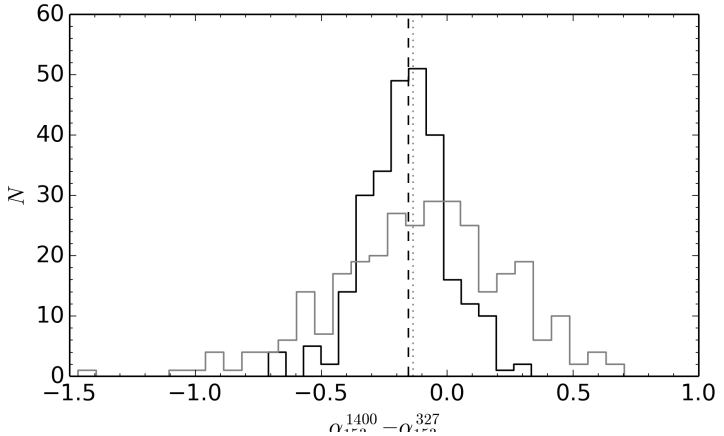


Figure 2.12: Comparison between α_{153}^{1400} and α_{153}^{327}: histogram of $\alpha_{153}^{1400} - \alpha_{153}^{327}$. Again, the histogram for bright GMRT sources is plotted in black and for fainter sources in grey. The dashed black line shows the mean value of -0.25 and the grey dotted line, the mean value of -0.2, for bright and all sources respectively. indicating that the majority of sources have flattened spectra at low frequencies.

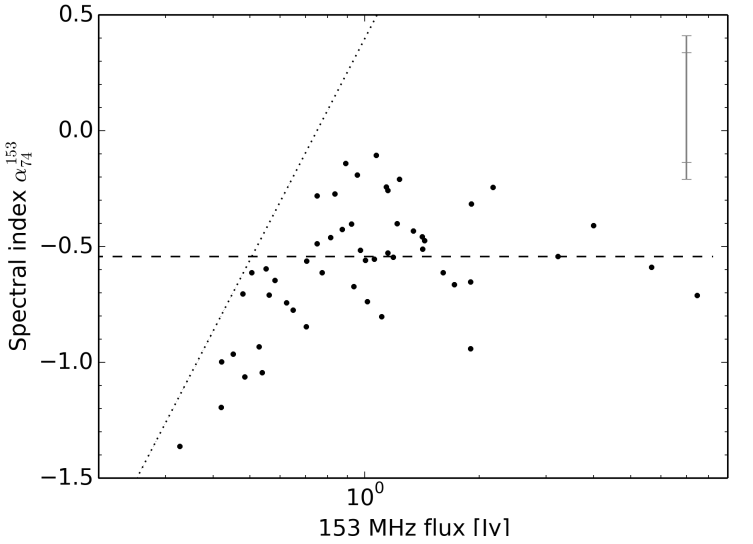


Figure 2.13: Spectral index distribution between 74 MHz and 153 MHz. The difference in resolution is 80 arcsec (VLSS) and the 25 arcsec (GMRT) and multiple GMRT matches to a single VLSS source have been merged into one. The vertical line shows $5\sigma_{\rm avg}$, where $\sigma_{\rm avg}$ is the average rms noise in the GMRT mosaic. The diagonal dotted line indicates the incompleteness limit due to the sensitivity of VLSS. The horizontal dashed line shows the KM mean spectral index of -0.55. Error bars on individual points are not plotted for clarity, but a single bar in the top right indicates the maximum and minumum errors in the dataset.

beam^{-1}. The source catalogue contains 1289 sources between 4.1 mJy and 7.3 Jy detected at 5 times the local noise. We estimate the catalogue to be 92 per cent reliable and 95 per cent complete to an integrated flux density of 14 mJy. The catalogue has been corrected for systematic errors on both the astrometry and flux density scales.

We have analysed the source population by investigating the source counts and by identifying counterparts within the 1.4 GHz NVSS and 327 MHz WENSS surveys and have computed the spectral index distributions of these sources. Understanding the low frequency, low flux source population is of particular importance to Epoch of Reionization projects (e.g. Ghosh et al. 2012, and references therein) where good models of the foregrounds are needed.

In the near future, this data will be combined with the existing multi-wavelength data covering the NOAO Boötes field and we will study the properties of radio galaxies as a function of various multi-wavelength parameters across a range of cosmic time. Further investigation of the spectral indices will be done and can be used to identify USS sources as well as high redshift gigahertz peaked spectrum (GPS) sources.

Acknowledgements

The authors thank the anonymous referee for their useful comments, which have improved this manuscript. We also acknowledge the staff of the GMRT that made these observations possible. GMRT is run by the National Centre for Radio Astrophysics of the Tata Institute of Fundamental Research. This publication made use of data from the Very Large Array, operated by the National Radio astronomy Observatory. The National Radio Astronomy Observatory is a facility of the National Science Foundation operated under cooperative agreement by Associated Universities, Inc.

Appendix

2.A Selected Radio Images

Figure 2.A.2 shows the 25 brightest sources in the catalogue, excluding the second brightest source which is described below (see also Fig. 2.A.1).

2.A.1 Note on source J144102+3530

Figure 2.A.1 shows GMRT postage stamp of the second brightest source in the catalogue. Also shown is the FIRST image (Becker et al. 1995) of this source which shows that most of the structure seen in the GMRT image is in fact real. Only the extension to the North-West in the GMRT image has no clear match in the FIRST image and may be due to deconvolution errors.

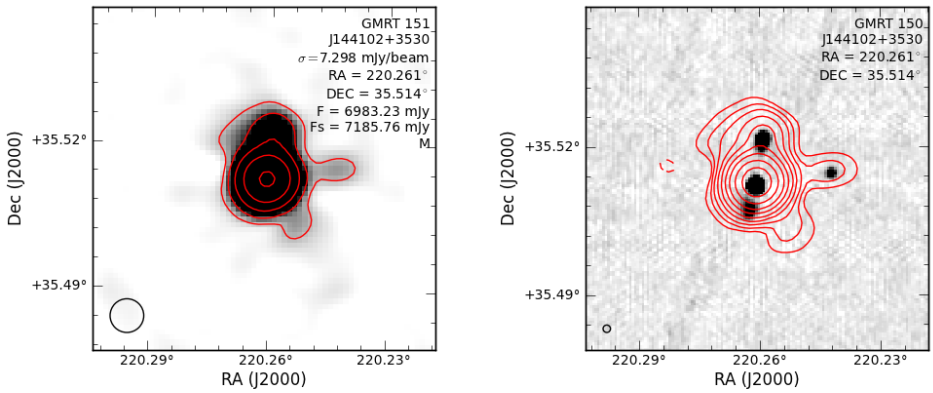


Figure 2.A.1: The second brightest source in the $153\,\mathrm{MHz}$ catalogue: *left* GMRT image and *right* FIRST image with GMRT contours. In both images the GMRT countours are plotted in red at intervals of $3\sigma \times [-\sqrt{3}, \sqrt{3}, \sqrt{10}, \sqrt{30}, \sqrt{100}, \ldots]$ and the greyscale goes from 1σ to 30σ.

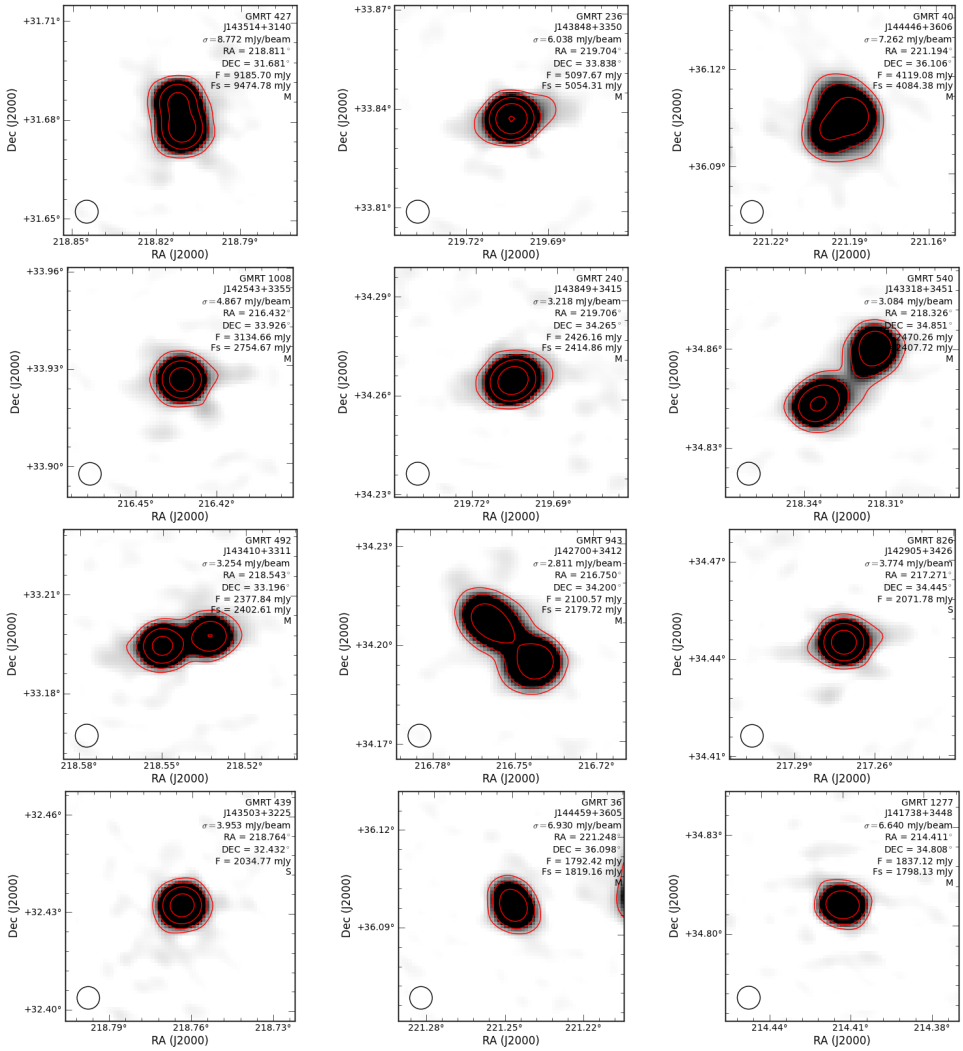


Figure 2.A.2: The 25 brightest 153 MHz radio sources (exluding J144102+3530). Countours are plotted in red at intervals of $3\sigma \times (-\sqrt{3}, \sqrt{3}, \sqrt{10}, \sqrt{30}, \sqrt{100}, \ldots)$ and the greyscale goes from 1σ to 30σ. The text in each image lists the local rms noise, the source coordinates and total flux, density and the source type ('S' or 'M'). The beamsize is shown in the bottom left corner.

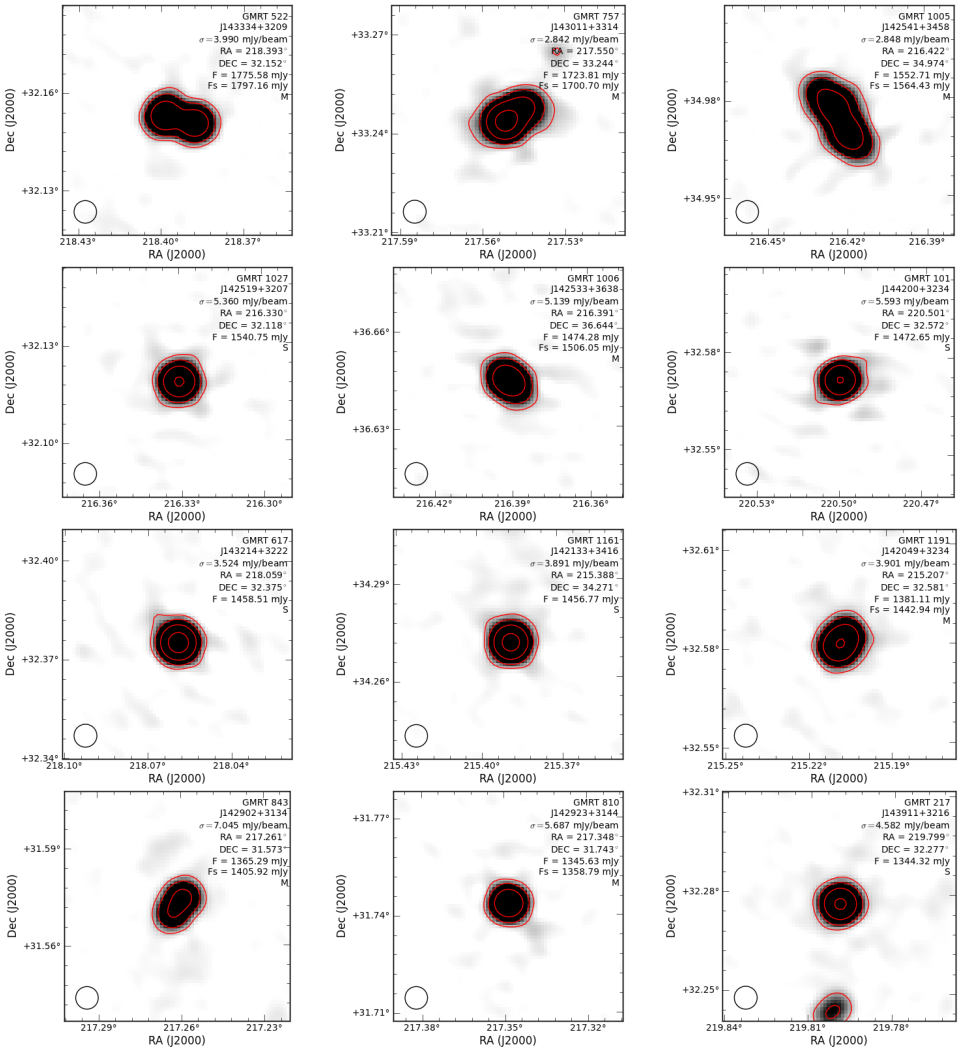


Figure 2.A.2: Continued.

CHAPTER 3

LOFAR Low-band antenna observations of the 3C 295 and Boötes fields: source counts and Ultra-Steep Spectrum sources

We present LOFAR Low Band observations of the Boötes and 3C 295 fields. Our images made at 34, 46, and 62 MHz reach noise levels of 12, 8, and 5 mJy beam^{-1}, making them the deepest images ever obtained in this frequency range. In total, we detect between 300 and 400 sources in each of these images, covering an area of 17 to 52 deg^2. From the observations we derive Euclidean-normalized differential source counts. The 62 MHz source counts agree with previous GMRT 153 MHz and VLA 74 MHz differential source counts, scaling with a spectral index of -0.7. We find that a spectral index scaling of -0.5 is required to match up the LOFAR 34 MHz source counts. This result is also in agreement with source counts from the 38 MHz 8C survey, indicating that the average spectral index of radio sources flattens towards lower frequencies. We also find evidence for spectral flattening using the individual flux measurements of sources between 34 and 1400 MHz and by calculating the spectral index averaged over the source population. To select ultra-steep spectrum ($\alpha < -1.1$) radio sources, that could be associated with massive high redshift radio galaxies, we compute spectral indices between 62 MHz, 153 MHz and 1.4 GHz for sources in the Boötes field. We cross-correlate these radio sources with optical and infrared catalogues and fit the spectral energy distribution to obtain photometric redshifts. We find that most of these ultra-steep spectrum sources are located in the $0.7 \lesssim z \lesssim 2.5$ range.

van Weeren, R. J., Williams, W. L., Tasse, C., et al.
ApJ, 793, 82 (2014)

3.1 Introduction

Low-frequency surveys of the sky are an important tool to address various open questions in astrophysics ranging from the evolution of galaxies, active galactic nuclei (AGN), galaxy clusters, to pulsars. The half power beam width (HPBW) of radio telescopes scales with wavelength, making low-frequency radio observations ($\lesssim$ 300 MHz) an efficient way to carry out large-area surveys. In addition, these observations take advantage of the steep synchrotron spectra ($F_\nu \propto \nu^\alpha$, with α the spectral index) of many extragalactic radio sources, with the flux densities increasing towards lower frequencies.

Low-frequency observations are particularly important to locate distant high-redshift radio galaxies (HzRG). Empirically it has been found that the radio spectral index correlates with the redshift of host galaxies, with the steepest spectra corresponding to the highest redshifts. Therefore massive high-redshift galaxies can be found by selecting radio sources with ultra-steep radio spectra (USS), especially in combination with an optical or near-IR magnitude cut (e.g., De Breuck et al. 2000; Miley & De Breuck 2008; Ker et al. 2012). However, USS sources are rare so large surveys are needed to find them. The fraction of USS sources with $\alpha^{1400}_{\approx 350} < -1.3$ is about 0.5 per cent (De Breuck et al. 2000). Deep observations at $\lesssim$ 150 MHz have the potential to detect sources with $\alpha \lesssim -2$, because these sources become too faint to be detected in sensitive high-frequency observations.

Radio sources in the last stages of the AGN evolution (both short and long-lived) are also most efficiently selected at low-frequencies. These relic or dying radio sources have steep and curved radio spectra due to synchrotron and inverse Compton losses as the central energy supply has been switched off (e.g., Parma et al. 2007; Kunert-Bajraszewska et al. 2010; Murgia et al. 2011).

Recently, most deep low-frequency surveys have been carried out with the GMRT at around 150 MHz (e.g., Ishwara-Chandra & Marathe 2007; Sirothia et al. 2009; Ishwara-Chandra et al. 2010; Intema et al. 2011; Williams et al. 2013). These surveys reach a rms noise level of the order of a mJy per beam. Below 100 MHz, there are no radio surveys that reach a similar depth. Cohen et al. (2004) carried out a 165 deg^2 74 MHz survey with a central noise of 24 mJy beam^{-1} at a resolution of 25 arcsec. Tasse et al. (2006) surveyed the XMM-LSS field at 74 MHz with a resolution of 30 arcsec, covering an area of 132 deg^2. The median rms noise over the field was 32 mJy beam^{-1}. Larger, but shallower surveys below 100 MHz, are the 74 MHz VLSS (Cohen et al. 2007; Lane et al. 2014) and 38 MHz (Hales et al. 1995; Rees 1990) surveys.

The LOw Frequency ARray (LOFAR) is a new generation radio telescope operating at 10–240 MHz (van Haarlem et al. 2013). With its multi-beaming capabilities, high-spatial resolution, and large fractional bandwidth, it is an ideal instrument to carry out large surveys. Here we report on the first LOFAR Low Band Antenna commissioning observations of the Boötes and the 3C 295 fields (which includes the Groth Strip). Both the Boötes field and the Groth Strip have been extensively studied at higher radio frequencies and other parts of the electromagnetic spectrum. For the Boötes field, observations have been carried out at 153 MHz (Intema et al. 2011; Williams et al. 2013), 325 MHz (Croft et al. 2008), 1.4 GHz (de Vries et al. 2002; Higdon et al. 2005), and 3.1 GHz (Croft et al. 2013). The Groth strip has been observed at 1.4 GHz (Ivison et al. 2007).

The outline of this paper is as follows. The observations and data reduction are described in Sect. 3.2. The results and analysis are presented in Sects. 3.3 and 3.4. This is followed by the conclusions in Sect. 3.5. All coordinates and images use the J2000 coordinate system.

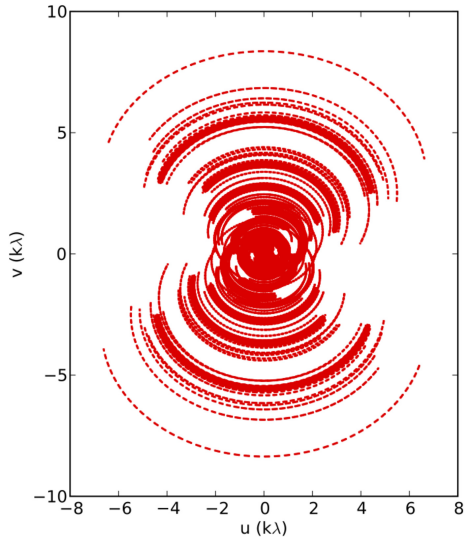


Figure 3.1: UV-coverage of the 3C 295 observations. The relatively large fractional bandwidth fills the uv-plane radially (not shown in the figure).

3.2 Observations & data reduction

The Boötes and 3C 295 fields were simultaneously observed on April 12, 2012 as part of a multi-beam observation with the LOFAR Low Band Antenna (LBA) stations. The idea behind the multi-beam setup is that we use the 3C 295 observations as a calibrator field to transfer the gain amplitudes to the (target) Boötes field. The total integration time on both fields was 10.25 hr. An overview of the observations is given in Table 3.1. Complete frequency coverage was obtained between 54 and 70 MHz for both fields, while non-contiguous frequency coverage was obtained between 30 and 54 MHz for the 3C 295 only. All four correlation products were recorded. By default, the frequency band was divided into subbands, each 195.3125 kHz wide. Each subband was further divided in 64 channels and the integration time was 1 s.

Nine Dutch remote stations were used, and 22 core stations, giving baselines that range between 90 m and 80 km. The resulting uv-coverage is displayed in Fig. 3.1. The LBA_OUTER configuration was used. In the LBA_OUTER configuration 48 LBA antennas are used, located mostly in the outer part of the stations (which have diameters of about 81 m). This increases the sidelobe levels for the station beams, but reduces the field of view (FoV) with respect to other station antenna configurations available. The HPBW is about 3.6°, 4.8°, and 7.2° at 60, 45, and 30 MHz, respectively. It should be noted though that the station beams are complex-valued, time and direction dependent, and differ from station to station.

3.2.1 Data reduction

Our data reduction broadly consists of the following steps: (1) flagging, (2) bright off-axis source removal, (3) averaging, (4) solving for the 3C 295 complex gains (in a circular basis to deal with differential Faraday Rotation), (5) transfer of the amplitude solutions from 3C 295 to the Boötes

Table 3.1: LBA Observations

Observations ID	L56691
Pointing centre 3C 295	14:11:20.9, +52:13:55
Pointing centre Boötes	14:32:03.0, +34:16:33
Integration time	1 s
Observation date	12 April, 2012
Total on-source time	10.25 hr
Correlations	XX, XY, YX, YY
Frequency setup	54–70 MHz[a] full coverage
	40–54 MHz[b] 25 subbands*
	30–40 MHz[c] 21 subbands*
Bandwidth	16 MHz[a], 4.9 MHz[b], 4.1 MHz[c]
Bandwidth per subband	195.3125 kHz
Channels per subband	64

[a] 54–70 MHz Boötes and 3C 295 fields
[b] 40–54 MHz 3C 295 field
[c] 30–44 MHz 3C 295 field
* subbands are more or less evenly distributed within this frequency range, the total bandwidth is reported in Table 3.2

field, and (6) phase-only calibration of the Bootes field against a GMRT model, and (7) imaging of the 3C 295 field and Boötes fields. All calibration steps are performed with the BlackBoard Selfcal (BBS) software system (Pandey et al. 2009). Below these steps are explained in more detail.

Flagging, bright off-axis source removal, and averaging

The first step in the reduction consisted of the automatic flagging of radio frequency interference (RFI) using the AOFlagger (Offringa et al. 2010, 2012). The first and last three channels of each subband were also flagged. Typically about 2 per cent of the data was flagged as RFI in the 50 to 70 MHz range. Between 30 and 40 MHz this percentage increases by a factor of $\approx$ 2–3 (see Offringa et al. 2013, for an overview of the LOFAR RFI environment). About a dozen subbands were lost due to failures of the data storage system.

A next step consisted of the removal of the bright 'A-team' radio sources Cas A and Cyg A. These sources have integrated flux densities of 18 and 17 kJy at 74 MHz, respectively. Although they are located outside the main FoV, they are sufficiently bright to prevent proper calibration and imaging of sources in the central part of the FoV if detected in the secondary lobes of the beam. The amplitudes of these off-axis sources are strongly modulated as they move in and out of the station beam sidelobes. These sources were removed with the 'demixing' method described by van der Tol et al. (2007) and which is part of the standard LOFAR pre-processing pipeline (Heald et al. 2010). For the models of Cas A and Cyg A we took the clean component models at 74 MHz from Very Large Array (VLA) A-array[1] observations (Kassim et al. 2007) with a

[1] http://lwa.nrl.navy.mil/tutorial/

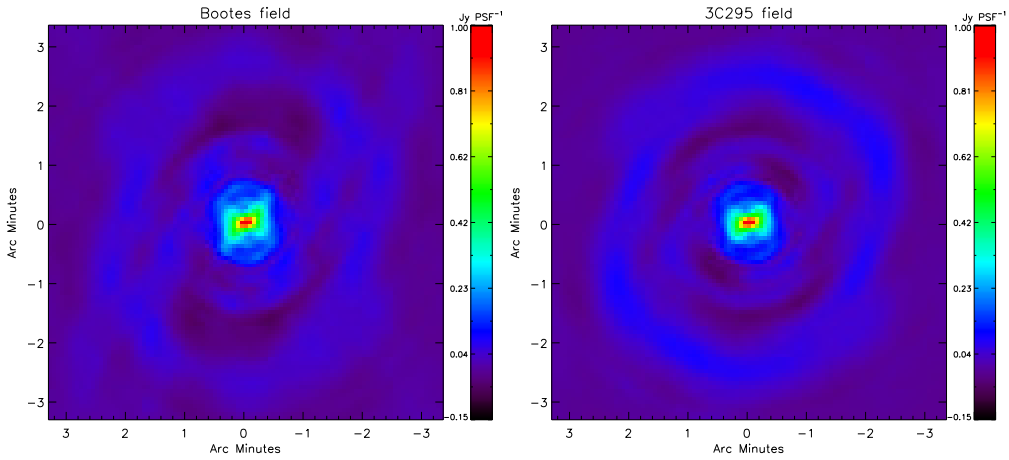


Figure 3.2: Point Spread Functions for the Boötes (*left*) and 3C 295 (*right*) images covering the 54–70 MHz frequency range.

resolution of 25 arcsec. After flagging and subtracting out Cas A and Cyg A, we averaged the data in time to 5 s and one channel per subband. The time resolution is set by the requirement to avoid decorrelation due to rapid ionospheric phase variations. At large radial distances from the field centre there is some bandwidth smearing. At the HPBW, the source width increases by a factor of ≈ 1.2 at 62 MHz and a factor of ≈ 1.9 at 34 MHz, due to this effect.

3C 295 field

The primary calibrator 3C 295 has a sufficiently high flux density that it dominates the total flux in the main FoV. 3C 295 consists of two main source components (e.g., Perley & Taylor 1991) and has an angular size of only $\approx$ 5 arcsec. Given that our longest baseline is $\approx$ 80 km (corresponding to a resolution of about 10 arcsec), we used a simple two CLEAN component model for the source. The integrated flux density of the source is given by the model of Scaife & Heald (2012).

Before calibrating, we converted the linear XX, XY, YX, YY correlations ($V_{\rm XY}$) to circular RR, RL, LR, LL correlations $V_{\rm RL}$ using the transformation described by Hamaker & Bregman (1996)

$$V_{\rm RL} = C_A V_{\rm XY} C_A^* \,, \tag{3.1}$$

with

$$C_A = \frac{1}{\sqrt{2}} \begin{pmatrix} 1 & i \\ 1 & -i \end{pmatrix} \,. \tag{3.2}$$

This transformation was done via a PYTHON script. The effects of the station beams[1] were taken out as well in the direction of 3C 295 with BBS. This is needed because the LBA stations

[1]The station beam model is derived using the dipole beam model based on the interpolation of electromagnetic simulations of the LBA dipole beam response, and the dipole locations within a station (Hamaker & Bregman 1996).

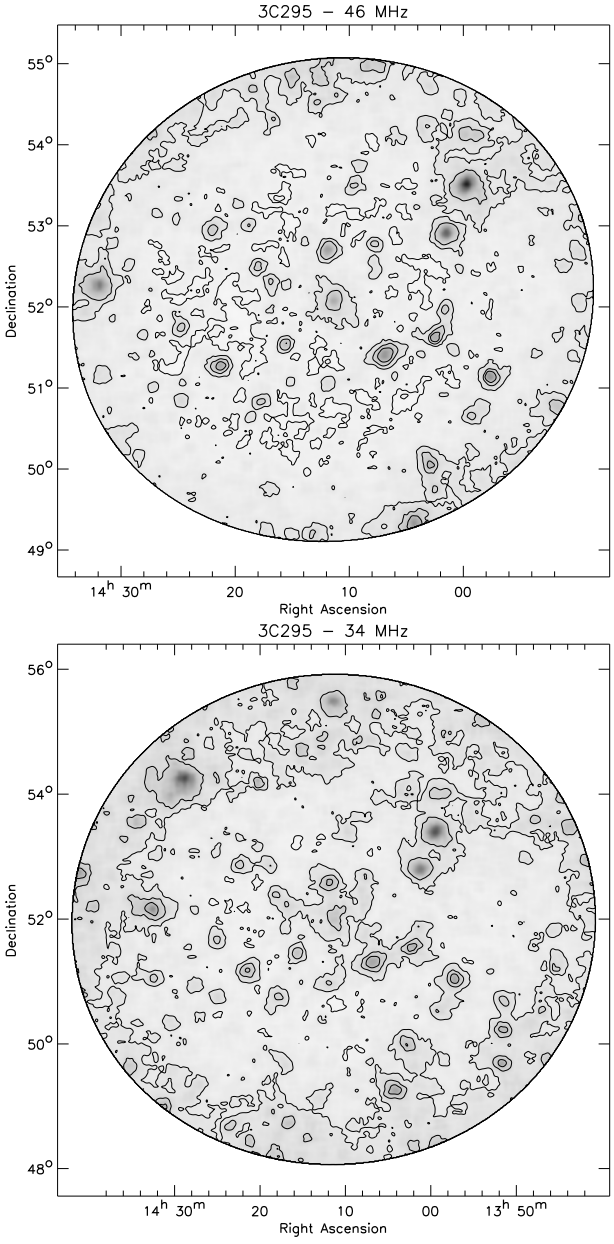


Figure 3.3: Figures showing the local rms noise in the images. A box size of 80×80 pixels was used in computing the local rms noise. The pixel sizes are listed in Table 3.2. The gray scales display the range from $0.5\sigma_{\rm rms}$ to $10\sigma_{\rm rms}$, with the $\sigma_{\rm rms}$ values taken from Table 3.2. Contour levels are drawn at $\left(\sqrt{2}\right)^n \times \sigma_{\rm rms}$, with n ranging from -1 to 3. The local noise variations are correlated with the position of strong sources.

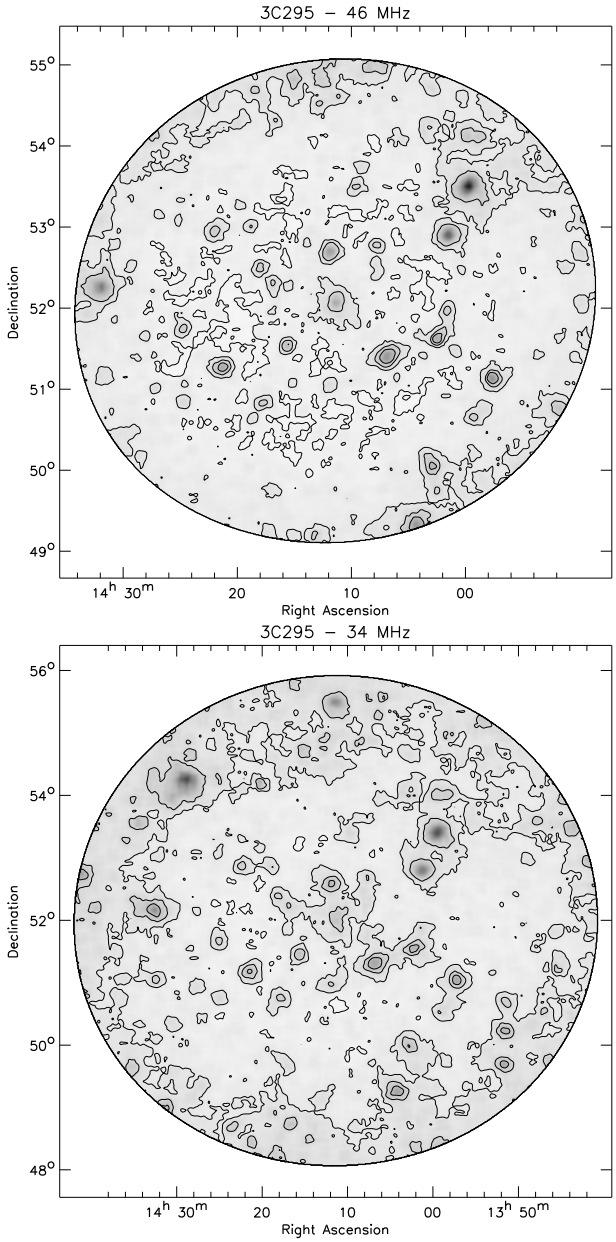


Figure 3.3: Continued.

do not record 'true' linear correlation products due to the fixed orientation of the dipole antennas on the ground.

The (only) reason for converting to circular correlations is that differential Faraday Rotation, which is important in the LBA frequency range, only affects the RR and LL phases, while in linear correlations, flux from XX and YY leaks into the cross-hand XY and YX correlations. Therefore by converting to circular correlations the calibration is simplified, since we only have to solve for the RR and LL phases to remove the effects of differential Faraday Rotation (e.g., Smirnov 2011). The conversion from linear to circular correlations depends on the accuracy of the beam models. It is also possible to solve for differential Faraday Rotation in a more direct way using the observed linear correlations but this requires solving for an extra free parameter.

After converting to circular correlations we obtained amplitude and phase solutions for the RR and LL correlations for each subband using the 3C 295 model (with BBS) . We used a solution interval of 5 s. This takes care of the frequency dependence of ionospheric phase variations, differential Faraday Rotation, clock errors, and the overall LBA bandpass (with a single complex gain correction for each time interval per subband). Good quality solutions were obtained over the entire time and frequency range, except for time periods affected by RFI. We then subtracted 3C 295 from the data using these gain solutions. This avoids many CLEAN cycles and CLEAN dynamic range limitations such as described in Cotton & Uson (2008). After the 3C 295 gain calibration we converted back the calibrated visibilities from circular to linear correlations because of limitations in the imaging software.

Boötes field

We transferred the amplitude solutions from the corresponding frequencies of the 3C 295 observation to the Boötes field dataset. The Boötes field does not contain any bright dominating sources. This means that there is not enough signal available per subband for a phase-only calibration on a timescale of 5 sec. To increase the signal to noise, all subbands were combined into a new measurement set consisting of 81 channels covering the entire 54-70 MHz range, with each channel corresponding to one individual subband. We then performed a phase-only calibration for groups of 27 channels each to obtain sufficient signal to noise to calibrate the distant remote stations against the GMRT 153 MHz model.

For the Boötes field, the calibration model is derived from a deep GMRT 153 MHz image (Williams et al. 2013) using the PyBDSM source detection software[1].

3.2.2 Imaging and cleaning

Imaging and CLEANing was carried out with AWIMAGER (Tasse et al. 2013), which incorporates the complex valued, time varying and frequency dependent individual station beams using A-Projection (Bhatnagar et al. 2008). For LOFAR, all 4×4 Mueller terms have to be taken into account in the A-Projection. For AWIMAGER a hybrid AW-projection algorithm was developed to apply the time, frequency, baseline, and direction dependent effects in full-polarization in an efficient way. Also, a new parallel gridding technique is used, which differs from the CASAPY[2] gridder.

For the imaging, we combined all available 54–70 MHz subbands for the Boötes and 3C 295 fields to improve the uv-coverage with multi-frequency synthesis (MFS). We did not correct for

[1] http://dl.dropboxusercontent.com/u/1948170/html/index.html
[2] http://casa.nrao.edu

Table 3.2: LOFAR LBA image characteristics

Field	Frequency [MHz]	Field of view[a] [deg^2]	Bandwidth [MHz]	rms noise [mJy beam^{-1}]	Synthesized beam [arcsec]	Pixel size [arcsec]
Boötes	62	19.4	16	4.8	31×19	4.0
3C295	62	17.0	16	5.3	29×18	4.0
3C295	46	30.5	4.9	8.2	40×24	6.0
3C295	34	52.3	4.1	12	56×30	8.0

[a] with a primary beam correction factor < 0.4

the spectral index of individual sources (Rau & Cornwell 2011) because such an algorithm is not yet implemented for AWIMAGER. For the 3C 295 field, we made two additional images from the subbands in the ranges 30–40 MHz and 40–54 MHz. We employed various robust weighting schemes (Briggs 1995) to find that a robust parameter of about 0.0 typically gave the lowest rms noise level. All final images have sizes of 8192^2 pixels and were made with a robust value of 0.0 and all baselines were included. The Point Spread Functions for the 54–70 MHz images are shown in Fig. 3.2. An overview of the image properties is given in Table 3.2.

We used CLEAN masks during the final imaging step to minimize CLEAN bias effects (e.g., Condon et al. 1998; White et al. 1997). The mask was derived from a previous imaging run without any mask. The CLEAN mask was generated with PyBDSM, detecting islands of emission with a $3\sigma_{\rm rms}$ island threshold, a pixel threshold of $5\sigma_{\rm rms}$, and a locally varying rms box with a size of 80×80 pixels to take into account artefacts around strong sources. The 80-pixels approximately correspond to the spatial scale over which the local rms noise changes in the presence of strong sources. Maps of the local rms noise are shown in Fig. 3.3.

3.3 Results

An overview of the resulting images, resolution, FoV, and noise levels obtained is given Table 3.2. The primary beam corrected images are displayed in Figs. 3.4 to 3.7. The artefacts visible around the brighter sources in the fields are due to imperfect calibration and errors in the station beam model. These artefacts also give rise to the increased noise around bright sources (Fig. 3.3). The 'spoke'-like patterns are likely caused by direction dependent ionospheric phase errors. The spokes are not visible at the position of 3C 295 because the ionospheric phase variations in this direction were properly taken into account (phase calibration was performed in the 3C 295 direction).

The 'smudge' visible in the 3C 295 field (labeled with a circle in Figs. 3.6 and 3.7) at 14:03, +54:21 is the galaxy NGC 5457 (M101). In the Boötes field, faint diffuse emission is found at 14:21.5, +35:12, labeled with a circle in Fig. 3.4. This source (1421+35) was previously also noted by Delain & Rudnick (2006) and Williams et al. (2013). A more detailed study of the source was performed by de Gasperin et al. (2014). They conclude that the extended radio emission is the remnant of a past AGN activity cycle of NGC 5590 at $z = 0.0107$.

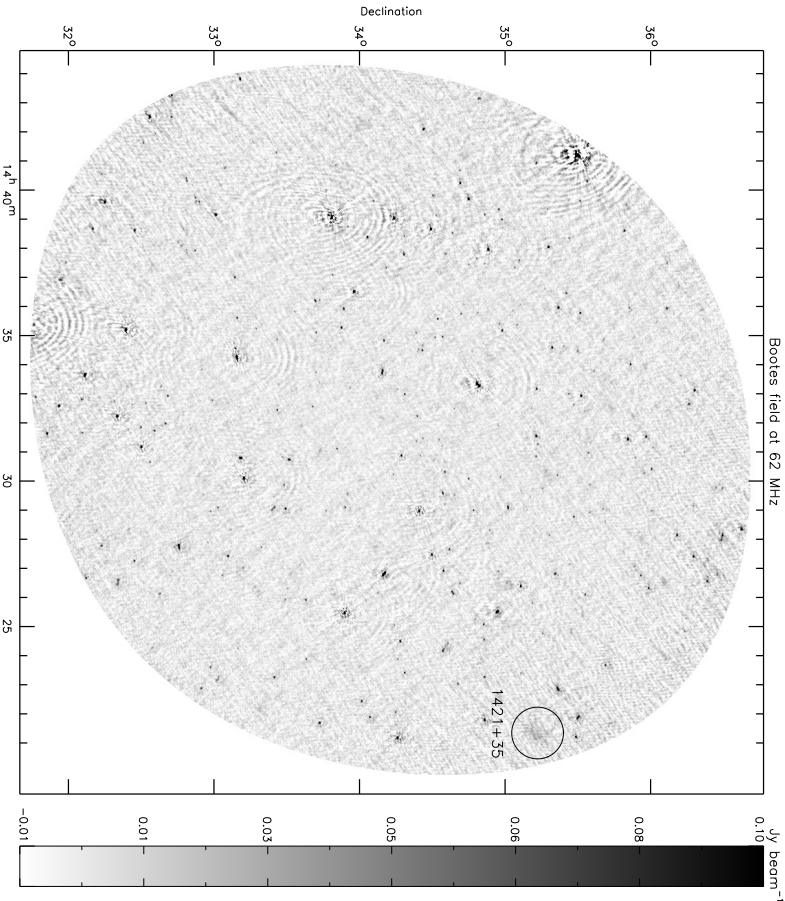


Figure 3.4: Primary beam corrected Boötes field 62 MHz image. The image is blanked beyond a primary beam attenuation factor of 0.4. The position of the diffuse source 1421+35 is indicated.

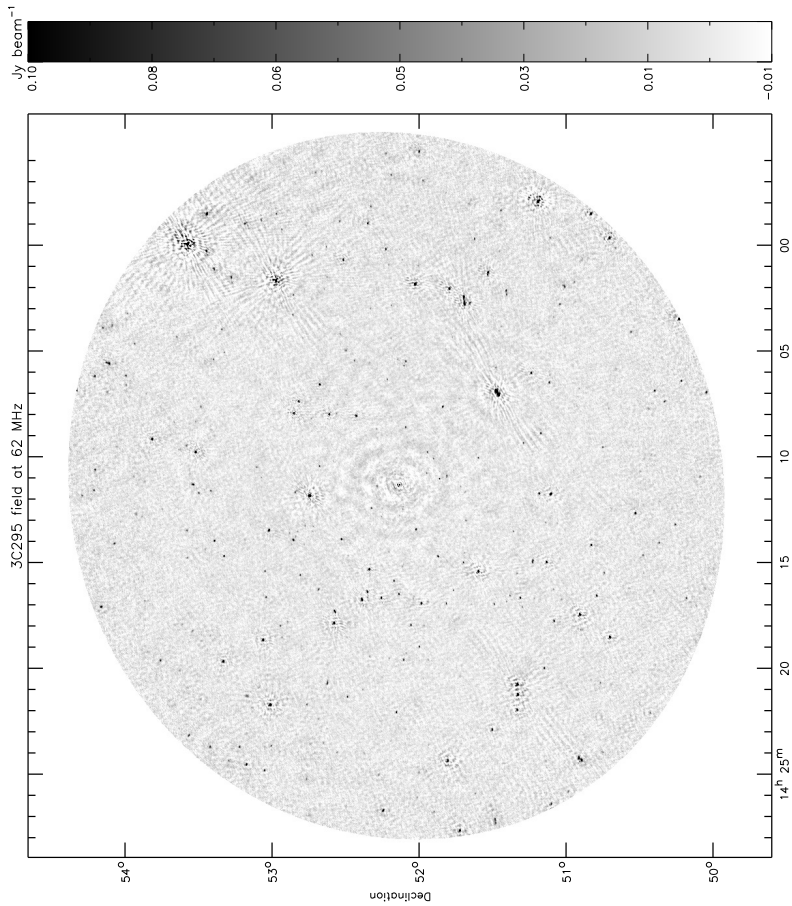


Figure 3.5: Primary beam corrected 3C 295 field 62 MHz image. The image is blanked beyond a primary beam attenuation factor of 0.4.

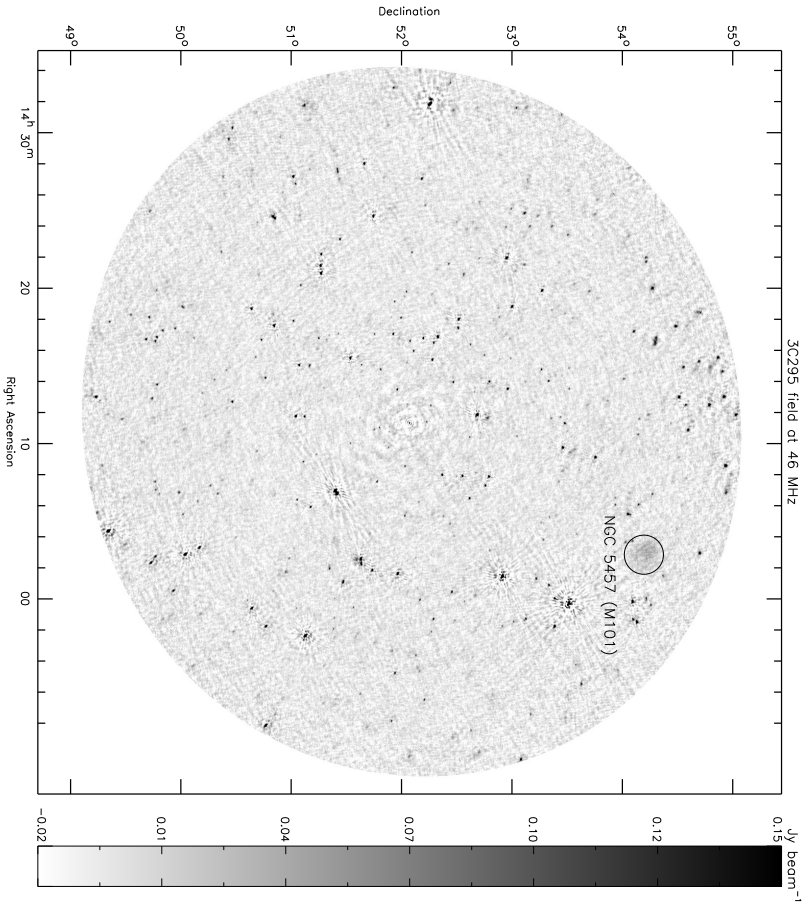


Figure 3.6: Primary beam corrected 3C 295 field 46 MHz image. The image is blanked beyond a primary beam attenuation factor of 0.4. The position of NGC 5457 is indicated.

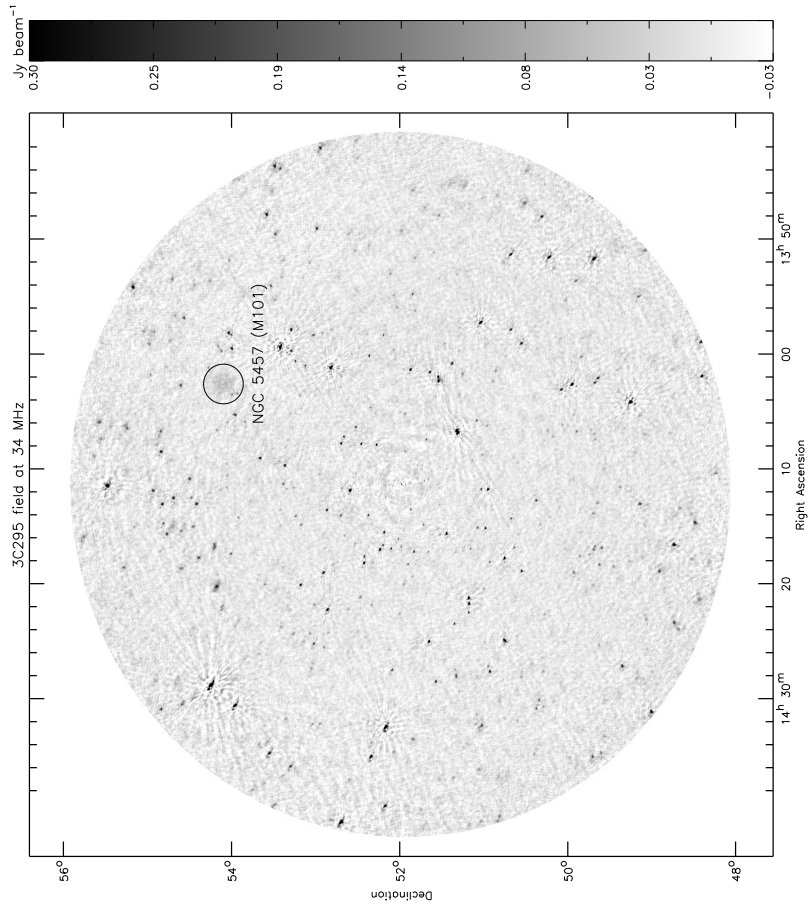


Figure 3.7: Primary beam corrected 3C 295 field 34 MHz image. The image is blanked beyond a primary beam attenuation factor of 0.4. The position of NGC 5457 is indicated.

3.3.1 Source detection

We used the PyBDSM software for source detection. PyBDSM works by identifying islands of contiguous pixels above a certain detection threshold and fitting each island with Gaussians. For detecting islands, we took a threshold of $3\sigma_{\rm rms}$ and a pixel threshold of $5\sigma_{\rm rms}$, meaning that at least one pixel in each island needs to be above $5\sigma_{\rm rms}$. We used a locally varying rms noise with a sliding box size of 80×80 pixels to take into account the rms noise increase around the bright sources. We manually inspected the output source catalogues to remove about a dozen false detections. These false detections were associated to side-lobes near bright sources. No sources beyond a primary beam attenuation factor of 0.4 were included.

Because the sources are distorted and smeared, and this distortion varies across FoV due to the ionosphere, the fitted major and minor axes for the Gaussian components cannot be simply used to determine whether a source is resolved or not. To first order, the derived integrated flux densities for the sources should not be affected by the smearing. We carried out a visual inspection for actual resolved sources, images of these sources are given in Appendix 3.A. In Fig. 3.8 we plot histograms of the fitted major and minor axes for the sources in the 3C 295 and Boötes fields. The decrease of the effective resolution towards lower frequencies can be seen by the broadening of the distribution of fitted major and minor axes. The final source list at 62 MHz contains 329 sources for both the Boötes and 3C 295 fields. At 46 and 34 MHz, the lists contain 367 and 392 sources for the 3C 295 field, respectively. Our LBA images reach a similar depth as the 325 MHz WENSS survey (scaling with a spectral index of -0.7). Because of the ionospheric distortions, we do not classify resolved or unresolved sources. The uncertainties for the measured flux densities and positions are discussed in Sects. 3.3.2 and 3.3.3. An example of the source catalogues is shown in Table 3.3. For each source we list the source name, the flux weighted coordinates and uncertainties, and the integrated flux densities and uncertainties.

3.3.2 Astrometric uncertainties

Ionospheric phase distortions and residual calibration errors can have an effect on the source positions. To assess the accuracy of the LBA source positions we compared them to the source positions from the 325 MHz WENSS survey (Rengelink et al. 1997). The positional accuracy of the WENSS survey is reported to be $5 - 10$ arcsec for the faintest sources and increases to 1.5 arcsec for the brighter sources.

For all our sources detected in the LOFAR images, we searched for the closest counterpart in the WENSS survey. The difference between the LOFAR positions and WENSS positions are displayed in Fig. 3.9. The positional offsets ($\Delta\alpha$, $\Delta\delta$) are a combination of imperfect calibration, noise dependent offsets from position determination using Gaussian fitting by PyBDSM, and offsets due to differences in source structure between 325 and 34–62 MHz, related to spectral index variations across the sources and/or differences in resolution between the WENSS and LOFAR images.

The median source position offsets between LOFAR and WENSS are smaller than 1/10th of the beam size for all frequencies, and therefore we do not correct our lists for systematic position offsets. To reduce the effect of the noise dependent term in the position offsets, we re-calculated the offsets taking only sources that are detected with a signal to noise ratio larger than 20 in the LOFAR images. Using only these bright sources, we find a scatter of

$$(\sigma_\alpha, \sigma_\delta = 1.8\,\text{arcsec}, 1.9\,\text{arcsec})_{\text{Bootes,62 MHz}},$$

$$(\sigma_\alpha, \sigma_\delta = 2.1\,\text{arcsec}, 3.1\,\text{arcsec})_{\text{3C 295,62 MHz}},$$

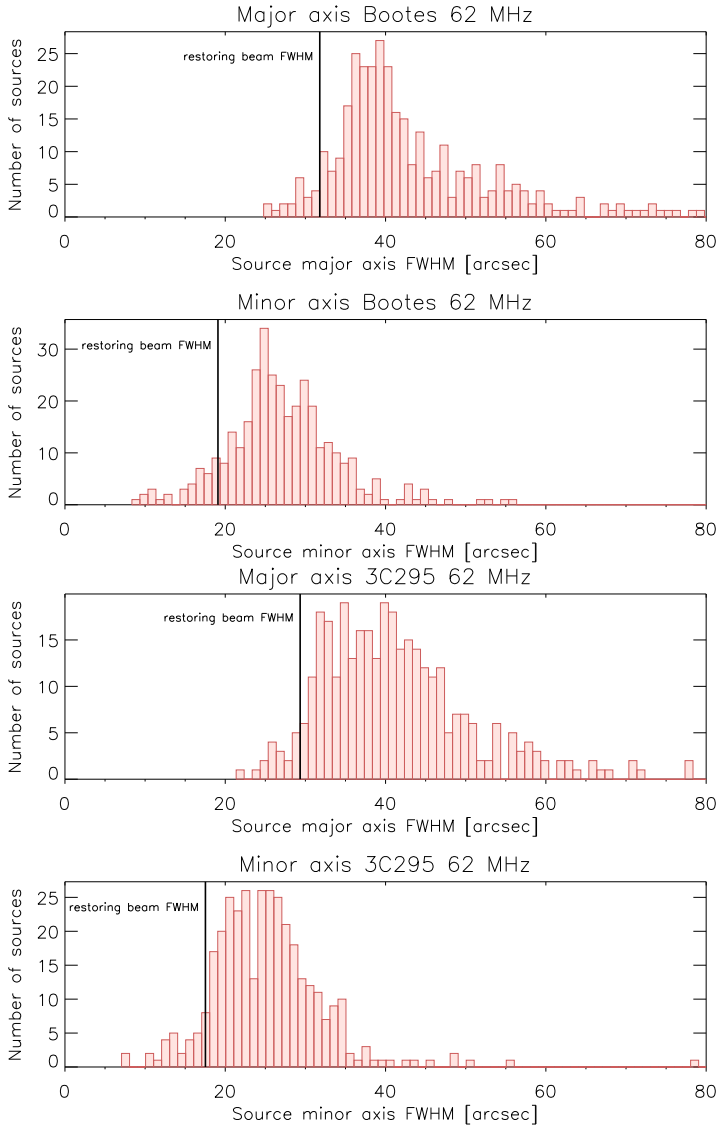


Figure 3.8: Distribution of fitted major and minor axes (full width half maximum) for the Boötes and 3C 295 fields. These values are not deconvolved by the beam. Solid black line indicates the fitted restoring beam based on the uv coordinates. Uncorrected ionospheric phase variations causes 'smearing' of sources and decreases the effective resolution. This effect increases towards lower frequencies.

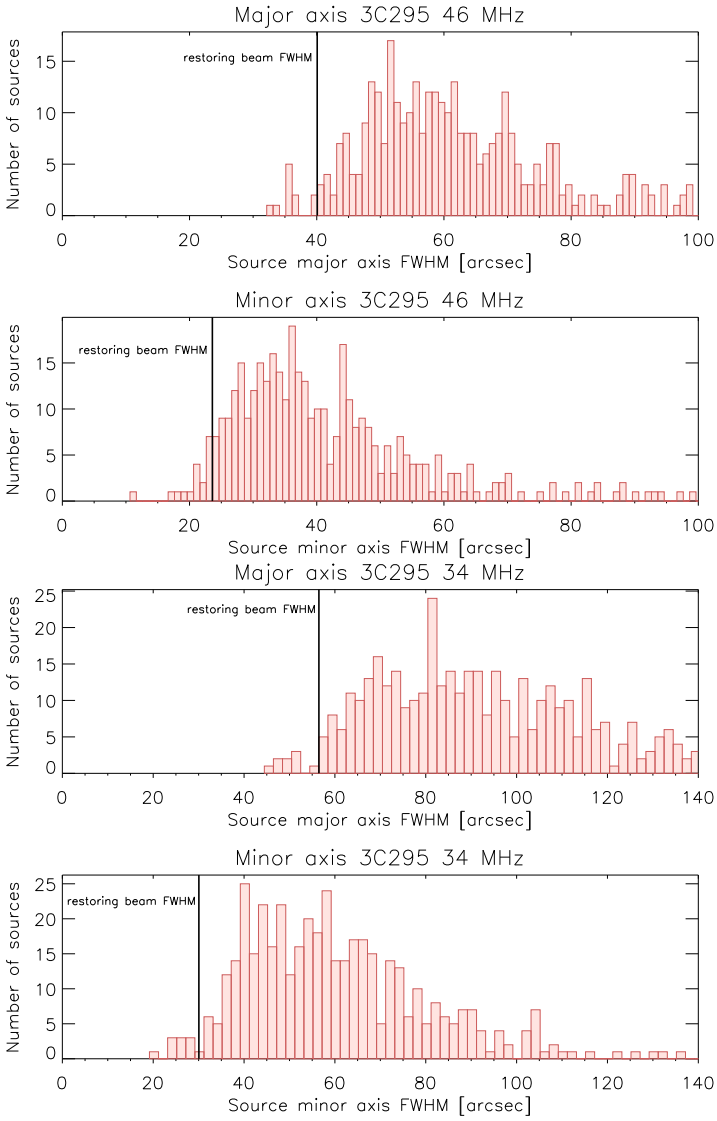


Figure 3.8: Continued.

Table 3.3: Sample of the LOFAR 62 MHz Boötes field source catalogue

Source ID	RA [deg]	$\sigma_{\rm RA}$ [arcsec]	DEC [deg]	$\sigma_{\rm DEC}$ [arcsec]	$S \pm \sigma_S$ [mJy]
J143859.5+345312	219.74800	2.2	34.88676	2.1	237 ± 40
J143856.4+343310	219.73524	3.2	34.55297	2.5	145 ± 29
J143849.0+335015	219.70420	1.8	33.83753	1.9	6469 ± 1008
J143849.3+341553	219.70580	1.8	34.26481	1.9	2816 ± 439
J143850.4+350020	219.71027	2.0	35.00571	2.0	298 ± 49
J143831.3+335652	219.63057	4.4	33.94792	3.2	174 ± 36
J143828.9+343107	219.62059	1.8	34.51874	1.9	2035 ± 317
J143819.1+321149	219.57987	2.1	32.19706	2.1	566 ± 91
J143831.6+355053	219.63205	2.1	35.84832	2.1	516 ± 81
J143817.1+322905	219.57145	1.8	32.48483	2.0	1251 ± 196
J143821.6+344000	219.59040	2.6	34.66683	2.2	194 ± 34
J143814.2+342010	219.55944	2.8	34.33632	2.2	148 ± 27
J143810.9+340500	219.54543	1.8	34.08339	1.9	797 ± 125
J143814.8+352807	219.56189	2.6	35.46880	2.3	186 ± 32
J143750.2+345451	219.45921	1.8	34.91425	2.1	2106 ± 328

$$(\sigma_\alpha, \sigma_\delta = 3.7\,\text{arcsec}, 5.6\,\text{arcsec})_{\text{3C 295,46 MHz}}, \text{ and}$$

$$(\sigma_\alpha, \sigma_\delta = 6.5\,\text{arcsec}, 10.2\,\text{arcsec})_{\text{3C 295,34 MHz}},$$

between LOFAR and WENSS. We added these values in quadrature to the position uncertainties determined from the Gaussian fitting. The strong increase in the scatter towards the lower frequencies suggests that this is the result of residual ionospheric phase errors. The Boötes field has the smallest spread in position offsets.

3.3.3 Flux density uncertainties

For our absolute flux calibration (bootstrapping) we took the scale from Scaife & Heald (2012) for 3C 295. Scaife & Heald report an uncertainty in the 3C 295 flux-scale of about 8 per cent at 34 MHz, 6 per cent at 46 MHz, and 4 per cent at 62 MHz.

We performed a check on the accuracy of the beam model and bootstrapping of the flux-scale. We did this by checking for flux density variations within the FoV, and by looking for an overall scaling factor (which applies to all sources within a field). For this, we compared the measured LBA flux densities to predicted flux densities from external surveys. These predicted fluxes are based on the NVSS (Condon et al. 1998), WENSS (Rengelink et al. 1997), GMRT 153 MHz (Williams et al. 2013, in the case of the Boötes field only), and VLSS Redux (VLSSr, Lane et al. 2014) surveys. We fitted second order polynomials to these flux measurements in $\log(S) - \log(\nu)$ space. We use these polynomial fits to predict the flux densities at the relevant LBA frequencies. To obtain reliable predictions, we only included LOFAR sources that were detected in all external surveys.

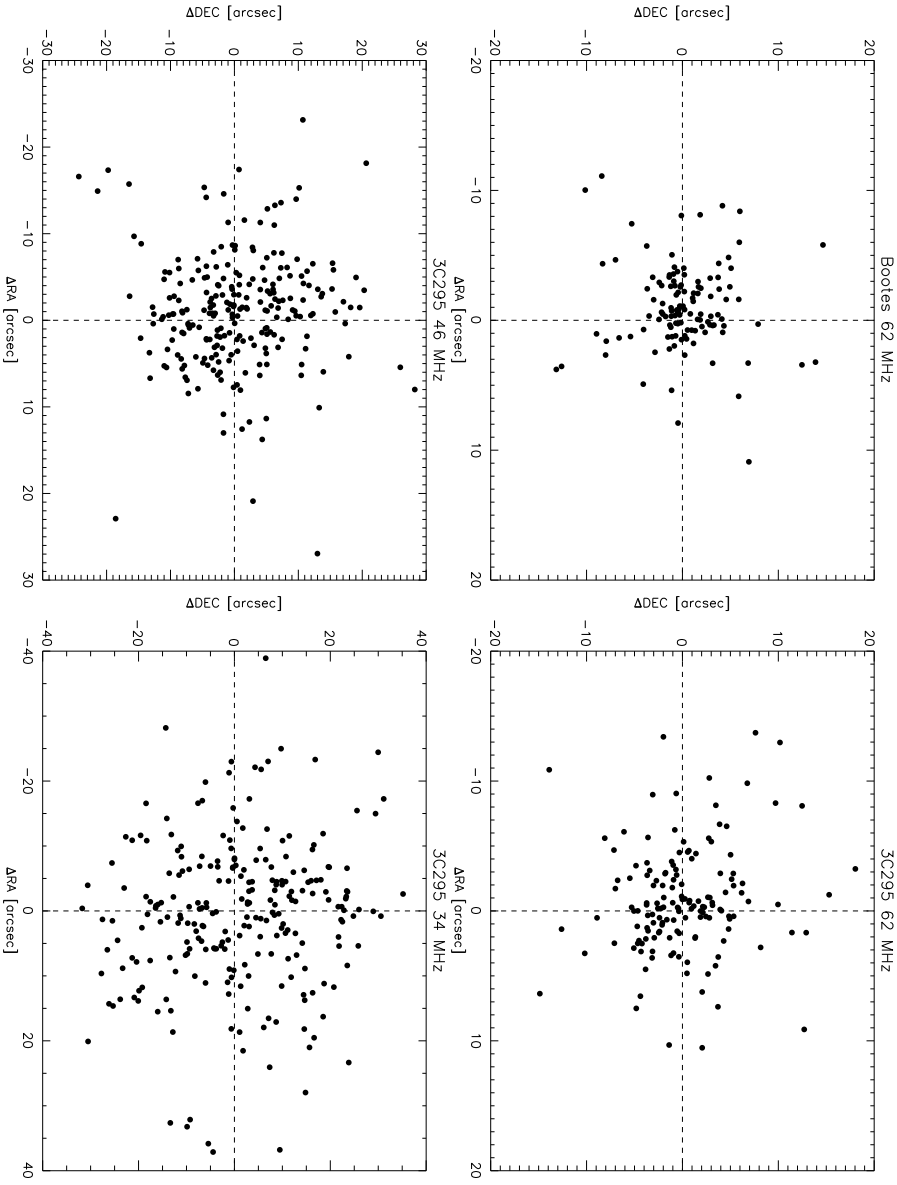


Figure 3.9: The position offsets between the LOFAR LBA and the 325 MHz WENSS sources.

For the Boötes field, we find a scatter of 15 per cent between the measured and predicted 62 MHz fluxes and a mean flux ratio of 0.8 (measured flux divided by predicted flux), see Fig. 3.10. If we use the polynomial fits from NVSS, WENSS, and GMRT 153 MHz to predict the VLSSr fluxes we find a scatter of 5 per cent. Therefore, some of the scatter can be attributed to the intrinsic uncertainties in the predicted LOFAR LBA fluxes due to measurement errors. For the 3C 295 field, we find a scatter of 18, 29, and 48 per cent, at 62, 46 and 34 MHz, respectively. No clear trends with radial distance from the field centre are found. The increase in the scatter for the 3C 295 field at 62 MHz, compared to the Boötes field, is not unexpected since we do not have high-quality GMRT 153 MHz flux density measurements available which help to predict the LBA fluxes. In addition, the predicted 46 and 34 MHz flux densities are considerably more uncertain as we extrapolate from higher frequency data. We therefore argue that the Boötes field 62 MHz fluxes are best suited to determine the flux-scale accuracy across the FoV.

The average measured to predicted flux ratios for the 3C 295 field are 1.0, 1.0, and 1.05, at 62, 46 and 34 MHz, respectively. The mean flux density ratios for the 3C 295 field are consistent with the uncertainty in the adopted flux-scale for 3C 295 itself, reported by Scaife & Heald (2012). The mean flux ratio of 0.8 for the Boötes field likely resulted from the amplitude transfer from 3C 295 to the Boötes field. This transfer relies on the accuracy of the global beam model. At the time of our observations there were issues with the remote station processing (RSP) boards which could have affected the beam shapes and sensitivities of some stations, resulting in errors when transferring the flux-scale from one pointing to another. The RSP boards were fixed about half a year after our observations.

From the above results, we conclude that the relative uncertainties in the flux-scale within a single FoV due to uncertainties in the beam model, are likely less than 15 per cent. We note that this 15 per cent refers to the averaged beam model of all stations over the entire period of the observations. This result is similar to the $\approx$ 10 per cent we found for LBA observations of Abell 2256 (van Weeren et al. 2012). The transfer of the flux-scale from one field to the other (i.e., from calibrator to target) seems to be more uncertain, in our case we find a mean ratio of 0.8 (Fig. 3.10). To bring the Boötes field flux densities to the same scale as the 3C 295 field, we multiplied them by a factor of 1.25.

The integrated flux density errors (σ_S, Eq. 3.3) are thus a combination of the uncertainties from 3C 295 flux-scale, the uncertainties from the Gaussian fitting ($\sigma_{\rm gauss}$), and a conservative 15 per cent uncertainty to account for the beam model used during the imaging process:

$$\sigma_S^2 = \begin{cases} (0.04S)^2 + \sigma_{\rm gauss}^2 + (0.15S)^2 & 62\,\mathrm{MHz} \\ (0.06S)^2 + \sigma_{\rm gauss}^2 + (0.15S)^2 & 46\,\mathrm{MHz} \\ (0.08S)^2 + \sigma_{\rm gauss}^2 + (0.15S)^2 & 34\,\mathrm{MHz} \end{cases} \tag{3.3}$$

In addition, averaging over a wide frequency range leads to an additional flux density error that depends on spectral index of the source. In this work we neglect this error as it is smaller than 1 per cent for a source with $\alpha = -1$.

3.3.4 Completeness and reliability

To quantify the completeness and reliability of the source lists, we performed a Monte-Carlo (MC) simulation in which we generated 25 random fields corresponding to each LOFAR image. Each field contains $\approx$1200 randomly positioned point sources with peak flux densities between 2.5 mJy and 6.3 Jy (the catalogue range) for the Boötes 62 MHz field, 2.3 mJy and 6.6 Jy for

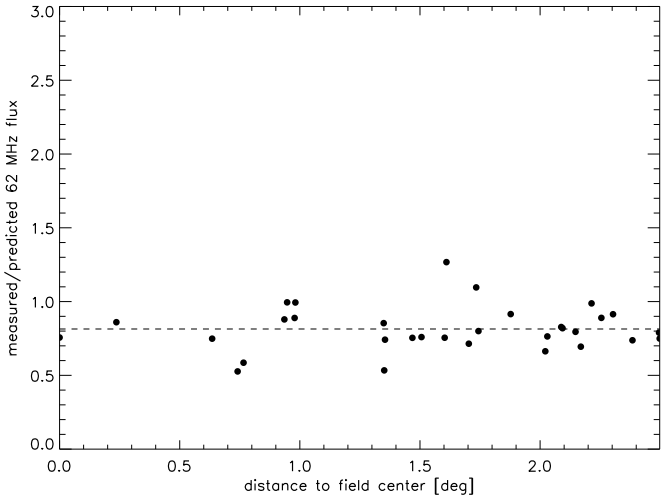


Figure 3.10: Measured flux densities over the predicted flux densities as function of radial distance to the Boötes field centre. Dashed line shows the robust mean of the plotted data points.

the 3C 295 62 MHz field, 3.9 mJy and 8.3 Jy for the 3C 295 46 MHz field, and 8.9 mJy and 8.0 Jy for the 3C 295 34 MHz field. The source flux densities are drawn randomly from the source count distribution, $dN/dS \propto S^{-1.6}$ (Williams et al. 2013). We neglect the deviation of the true source counts from a power law slope at high flux densities because there are very few sources at these flux densities. The effect of the beam is naturally taken into account by inserting sources in the noise-inhomogeneous maps. We also deal with non-Gaussian noise (calibration errors) in this way. Our MC simulation also accounts for the strong ionospheric and bandwidth smearing in the real LOFAR images by scaling the size of the point sources with radial distance from the centre of the field. The radial scaling factor is determined by the median value within radial distance bins of the ratio of the measured fitted major-axes to the beam major axis in each field. For comparison we also ran the MC simulation without any smearing. Simulated sources were inserted into the residual images resulting after source detection with PyBDSM. Source detection was performed for each randomly simulated field in the same manner as described in Sect. 3.3.1. Only $\approx 300 - 400$ sources in each field satisfy the detection criterion of peak flux density $> 5\sigma$.

We have estimated the catalogue completeness by plotting the fraction of detected sources in our MC simulation as a function of integrated flux density (*left* panel of Fig. 3.11), i.e., the fraction of input sources that have a catalogued flux density using the same detection parameters. The completeness at a given flux density is determined by integrating the detected fraction upwards from a given flux density limit and is plotted as a function of integrated flux density in the *right* panel of Fig. 3.11. Due to the variation in the rms noise across the image, the detection fraction has first been multiplied by the fraction of the total area in which the source can be detected. We thus estimate that the catalogue is 95 per cent complete above a peak flux density of 37 mJy (Boötes 62 MHz) and 88, 51, and 30 mJy (3C 295 34, 46 and 62 MHz respectively).

The reliability of the catalogue indicates how many sources above a given flux density are real. In the *left* panel of Figs. 3.12 and 3.13, the false detection rate FDR, i.e., the fraction of

catalogued sources that do not have an input source, is plotted as a function of the integrated flux density. Integrating up from a given limit and multiplying by the normalized source flux distribution, we can determine an estimate of the overall FDR or reliability, $R = 1 - FDR$, of the catalogue. The reliability is plotted as a function of integrated flux density limit in the *right* panel of Figs. 3.12 and Fig. 3.13. We thus estimate that the source list is 95 per cent reliable above a peak flux density of 42 mJy (Boötes 62 MHz) and 108, 53, and 32 mJy (3C 295 34, 46 and 62 MHz respectively). These estimates include source smearing.

3.4 Analysis

3.4.1 Source counts

We use the source lists to compute the Euclidean-normalized source counts at 62, 46 and 34 MHz. For this, we have to take into account the large variations of the rms noise across the images (e.g., Windhorst et al. 1985). We choose the flux density bin sizes such that we have approximately 30–60 sources per bin, except for the first and last bins. We corrected these source counts using the Monte-Carlo simulations described in Sect. 3.3.4 with the detected fraction of sources as a function of flux density. The propagated errors in the source counts are based on the Poissonian uncertainties and the uncertainties in the derived detection fraction, see Table 3.4. The resulting Euclidean-normalized source counts are shown in Figs. 3.14 and 3.15.

Only a few source count studies exist below 100 MHz. Cohen et al. (2003, 2004) and Tasse et al. (2006) published source counts at 74 MHz with the VLA. We compare our source counts with those from Cohen et al. (2004) and Tasse et al. (2006) because they go to fainter flux densities than those from Cohen et al. (2003). For that comparison, we rescale the Cohen et al. (2004) and Tasse et al. (2006) flux densities to the newly adopted VLSSr flux-scale (Lane et al. 2014). The VLSSr counts are included as well (Lane et al. 2014). We also compare with 153 MHz source counts from the GMRT for the Boötes field (Williams et al. 2013) because it overlaps to a large extent with our Boötes field data.

The combined source counts at 62 MHz from the Boötes and 3C 295 fields show very good agreement with the results at 74 MHz, which are scaled using $\alpha = -0.7$. The 62 MHz counts reach significantly fainter (about a factor of 6), flux density levels than the 74 MHz counts. The 62 MHz counts fall slightly below the GMRT 153 MHz counts, if we scale these with a spectral index of -0.7. The simulated 151 MHz SKAD S^3-SEX counts (Wilman et al. 2008) closely follow the GMRT 153 MHz counts.

The 34 MHz source counts fall significantly below the extrapolated source counts from 153 and 74 MHz if we scale with $\alpha = -0.7$. This is also the case for the simulated 151 MHz SKAD S^3-SEX counts. The 46 MHz differential source counts show a similar situation, although the difference is most pronounced below 0.5 Jy. Scaling with $\alpha = -0.5$ gives a better agreement with the 34 and 46 MHz source counts, an indication that the average spectral index of the sources flattens towards lower frequencies, a result that has been reported before (e.g., Lacy et al. 1992). However, part of the difference could also be caused by field to field variations (Heywood et al. 2013). To check this, we compared the separate source counts for the two fields at 62 MHz, instead of the combined counts that are shown in Fig. 3.14. We find that the 3C 295 field source counts are generally about 20–30 per cent lower than for the Boötes field (see Fig. 3.C.1) so this could explain some of the difference.

Spectral flattening is expected for some sources because of absorption effects and low-frequency spectral indices are flatter than high-frequency ones due to spectral ageing operating at higher

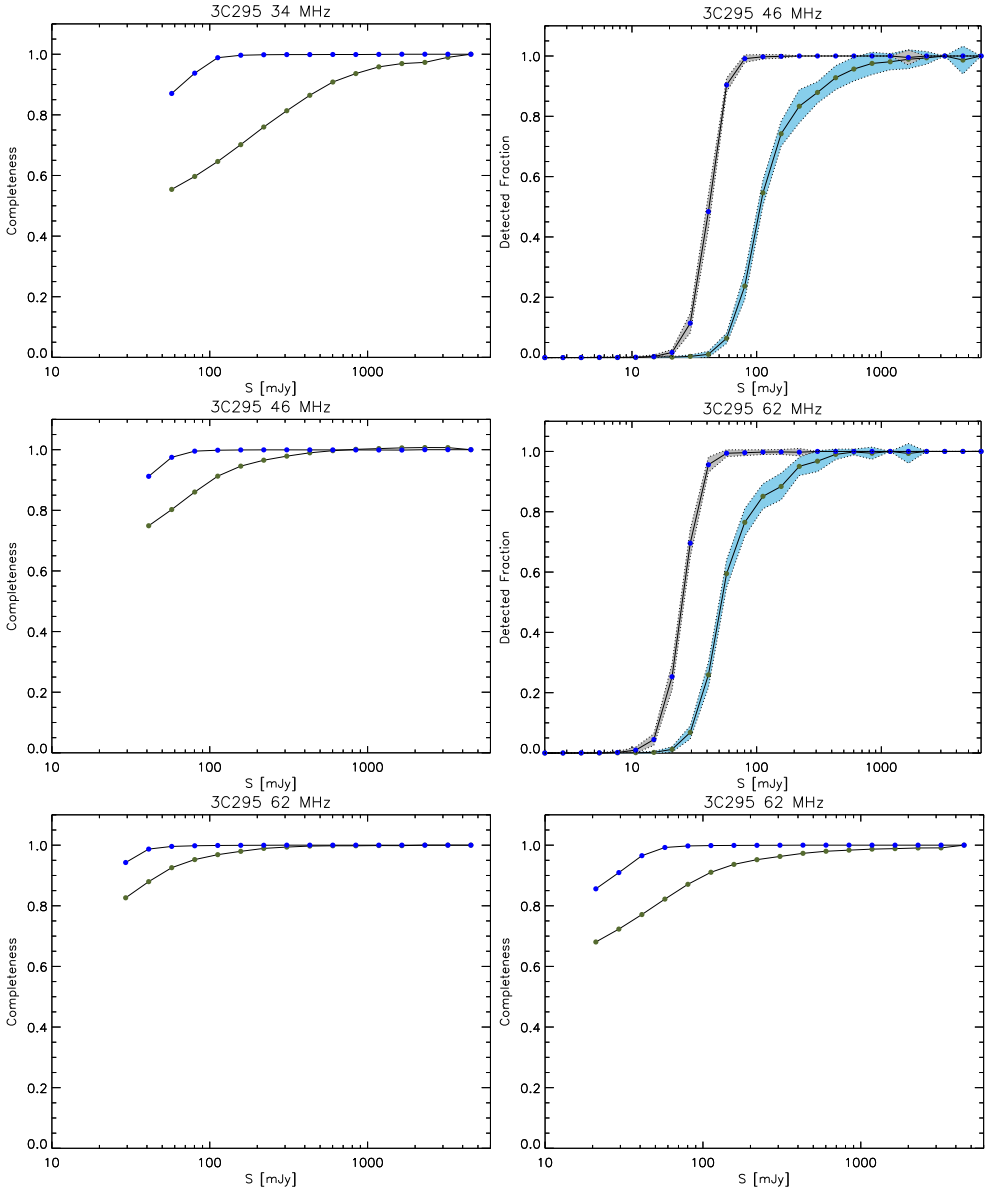


Figure 3.11: Detection fraction and completeness. From *top* to *bottom:* 3C 295 34, 46 and 62 MHz and Boötes 62 MHz. *Left:* Fraction of sources detected as a function of integrated flux density calculated from 25 Monte-Carlo simulations. The solid line shows the mean of all 25 randomly generated fields and the shaded areas show the 1σ uncertainty. The blue shaded areas and olive points include source smearing in the MC simulations (see the main text of Sect. 3.3.4). The grey shaded areas and blue points do not include source smearing. *Right:* Estimated completeness of the catalogue as a function of integrated flux density limit accounting for the varying sensitivity across the field of view. The olive points include source smearing, the blue points do not.

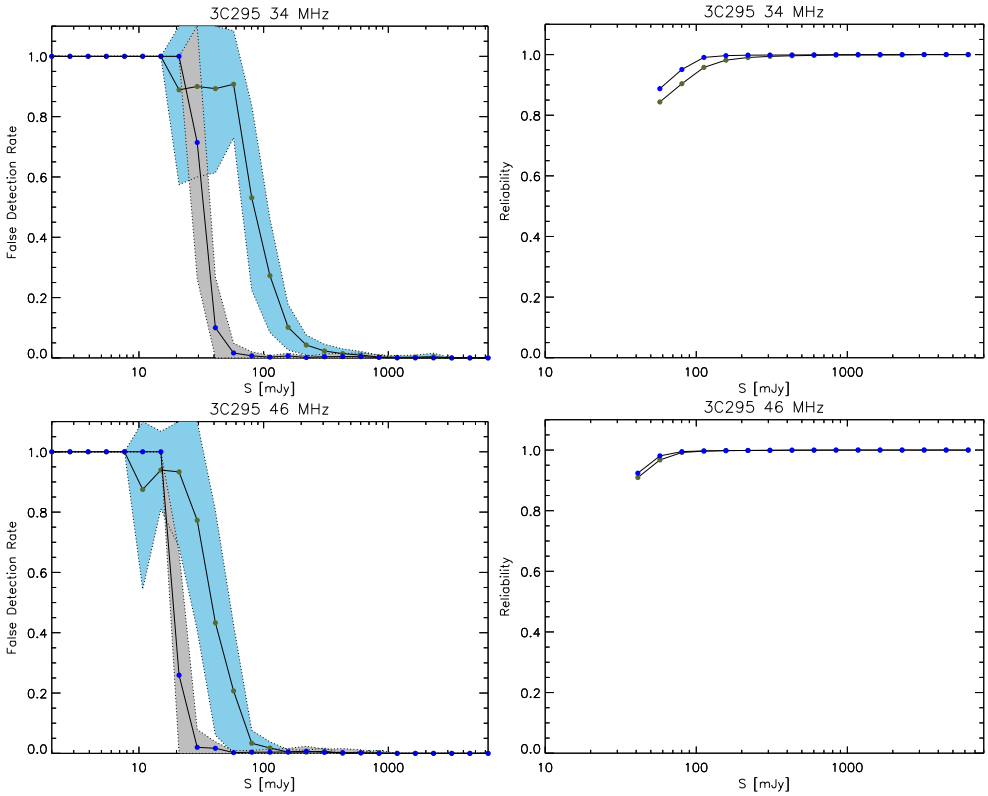


Figure 3.12: False detection rate and reliability. From *top* to *bottom:* 3C 295 34 and 46 MHz. *Left:* False detection rate as a function of peak flux density to local signal-to-noise ratio calculated from 25 Monte-Carlo simulations. The solid line shows the mean of all 25 randomly generated fields and the shaded areas show the 1σ uncertainty. The blue shaded areas and olive points include source smearing in the MC simulations (see main the text of Sect. 3.3.4). The grey shaded areas and blue points do not include source smearing. *Right:* Estimated reliability of the catalogue as a function of integrated flux density limit accounting for the varying sensitivity across the field of view. The olive points include source smearing, the blue points do not.

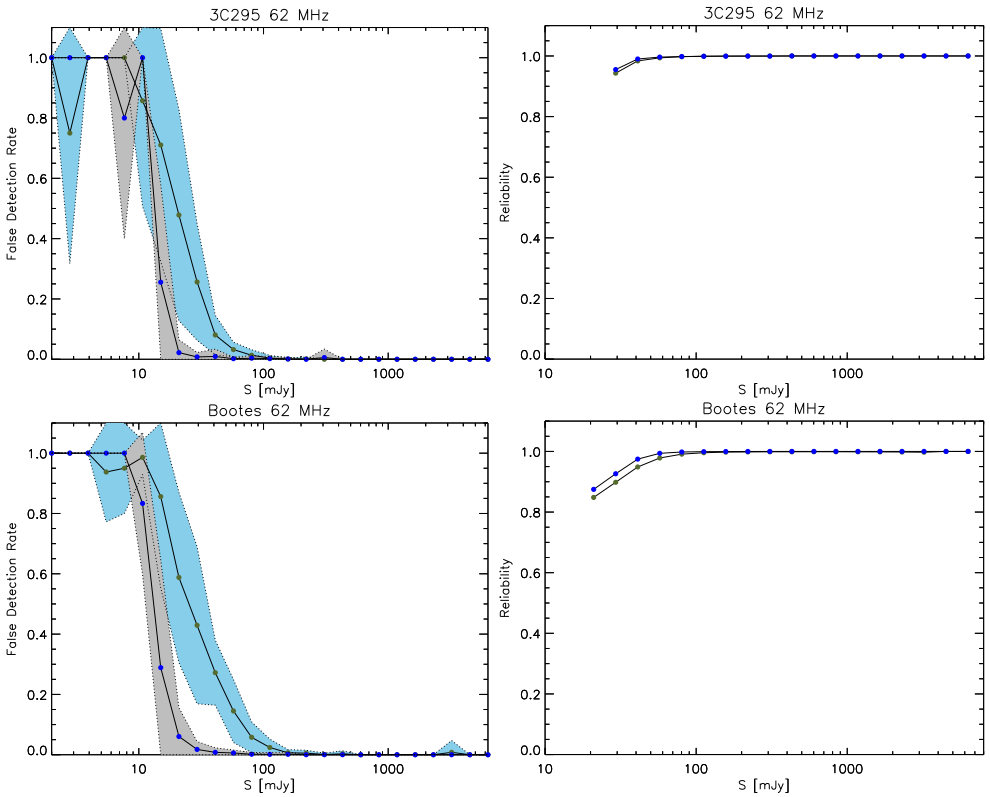


Figure 3.13: False detection rate and reliability. From *top* to *bottom:* 3C 295 62 MHz and Boötes 62 MHz. *Left:* False detection rate as a function of peak flux density to local signal-to-noise ratio calculated from 25 Monte-Carlo simulations. The solid line shows the mean of all 25 randomly generated fields and the shaded areas show the 1σ uncertainty. The blue shaded areas and olive points include source smearing in the MC simulations (see main the text of Sect. 3.3.4). The grey shaded areas and blue points do not include source smearing. *Right:* Estimated reliability of the catalogue as a function of integrated flux density limit accounting for the varying sensitivity across the field of view. The olive points include source smearing, the blue points do not.

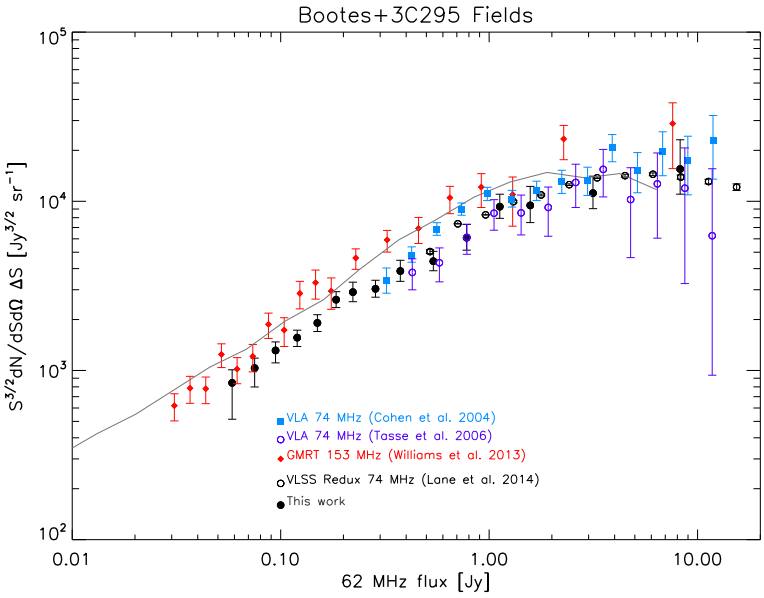


Figure 3.14: Euclidean-normalized differential source counts at 62 MHz combining the Boötes and 3C 295 fields. The LOFAR points are indicated by the black symbols. Red diamonds are Boötes field source counts at 153 MHz, scaled to 62 MHz using $\alpha = -0.7$. Black open circles, blue squares and purple open circles are 74 MHz differential source counts from Tasse et al. (2006); Cohen et al. (2004); Lane et al. (2014) and the solid grey line displays the counts from the 151 MHz SKADS S^3-SEX simulation (Wilman et al. 2008). These are all scaled to 62 MHz assuming $\alpha = -0.7$.

frequencies. We note though that our flux reference 3C 295 also incorporates a strong spectral turnover below ≈ 60 MHz and hence we have to be careful to conclude whether the flattening is intrinsic, or is caused by our uncertain calibrator flux-scale. Fortunately, the 8C 38 MHz counts allow for a more direct comparison at flux densities above ≈ 1 Jy (Rees 1990; Hales et al. 1995). We find good agreement between our 34 MHz sources counts and those from the 8C survey. In addition, the 8C counts match up with the extrapolated counts from the VLSSr (at 74 MHz) and the GMRT (at 153 MHz) using a spectral index scaling of $\alpha = -0.5$. The 8C source counts at 38 MHz are not consistent with the VLSSr and GMRT counts if we scale with a spectral index of $\alpha = -0.7$. This indeed shows that on average the spectral indices of sources flatten. It is important to note that the VLSSr and 8C counts are not affected by field to field variations given the large sky area they cover.

3.4.2 Spectral indices

In the above section we found evidence for spectral flattening of sources towards lower frequencies. In this subsection we investigate the spectral properties of the detected LBA sources.

For the Boötes field sources we search for counterparts in the NVSS and GMRT 153 MHz catalogs using a matching radius of 20 arcsec. If more than one counterpart to a 62 MHz source is found we add up the flux of all counterparts within the 20 arcsec radius. In Fig. 3.16 we plot α_{62}^{1400} against the 62 MHz flux density. From this we find an average spectral index of -0.79.

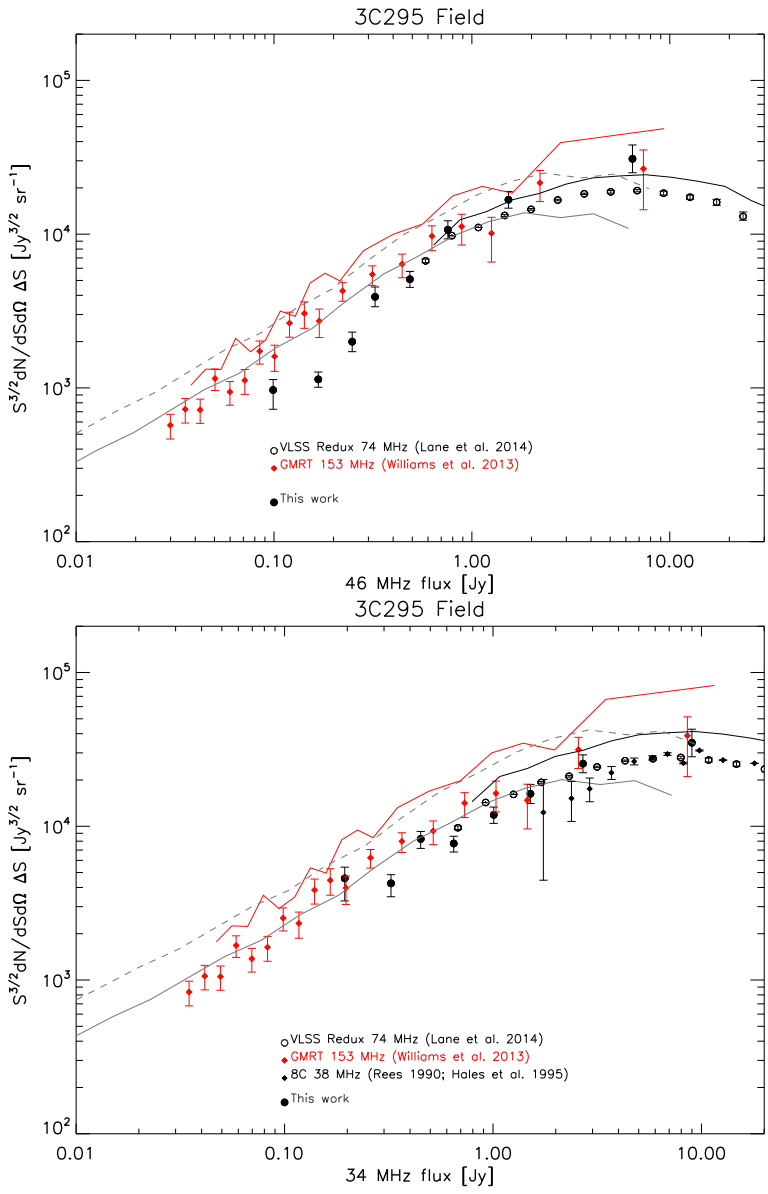


Figure 3.15: Euclidean-normalized differential source counts at 46 (*left*) and 34 MHz (*right*) for the 3C 295 field. The LOFAR points are indicated by the black circles. The red diamonds are Boötes field source counts at 153 MHz and the black open circles show the VLSSr counts at 74 MHz (Lane et al. 2014), both scaled with $\alpha = -0.5$. Red and black solid lines show the same source counts but scaled with $\alpha = -0.7$. The solid and dashed grey lines displays the counts from the 151 MHz SKADS S^3-SEX simulation (Wilman et al. 2008) scaled with $\alpha = -0.5$ and $\alpha = -0.7$, respectively. For the 34 MHz panel we have also plotted the 8C source counts at 38 MHz with black diamonds. The 8C source counts are complete to a flux level of about 5 Jy. Below a flux density of 5 Jy we have corrected the source counts using the information provided in Fig. 7 from Rees (1990).

Table 3.4: Source Counts

Flux bin Jy	Raw counts	Corrected counts	Normalized counts $Jy^{3/2}\ sr^{-1}$
62 MHz Boötes and 3C295			
0.051–0.066	32	181	844^{+164}_{-329}
0.066–0.084	47	143	$1{,}032^{+150}_{-234}$
0.084–0.105	51	119	$1{,}312^{+162}_{-204}$
0.105–0.135	62	111	$1{,}562^{+167}_{-175}$
0.135–0.165	52	78	$1{,}909^{+226}_{-210}$
0.165–0.204	65	83	$2{,}621^{+300}_{-267}$
0.204–0.240	45	53	$2{,}904^{+422}_{-354}$
0.240–0.330	65	75	$3{,}037^{+376}_{-327}$
0.330–0.420	44	49	$3{,}869^{+612}_{-505}$
0.420–0.660	55	59	$4{,}424^{+634}_{-538}$
0.660–0.900	31	32	$6{,}087^{+1{,}206}_{-945}$
0.900–1.35	36	37	$9{,}295^{+1{,}716}_{-1{,}367}$
1.35–1.80	16	16	$9{,}456^{+2{,}792}_{-1{,}975}$
1.80–4.50	20	20	$11{,}175^{+2{,}899}_{-2{,}132}$
4.5–12.0	7	7	$15{,}509^{+7{,}595}_{-4{,}491}$
46 MHz 3C 295			
0.072–0.126	27	155	969^{+165}_{-242}
0.126–0.208	46	76	$1{,}136^{+132}_{-127}$
0.208–0.288	39	48	$1{,}998^{+308}_{-278}$
0.288–0.360	38	44	$3{,}913^{+622}_{-542}$
0.360–0.612	65	72	$5{,}087^{+637}_{-577}$
0.612–0.900	55	54	$10{,}686^{+1{,}535}_{-1{,}367}$
0.900–2.16	66	68	$16{,}747^{+2{,}218}_{-1{,}994}$
2.16–10.8	23	23	$30{,}898^{+7{,}133}_{-5{,}812}$
34 MHz 3C 295			
0.136–0.252	40	505	$4{,}615^{+843}_{-1323}$
0.252–0.396	50	163	$4{,}257^{+591}_{-773}$
0.396–0.504	51	105	$8{,}270^{+984}_{-1090}$
0.504–0.792	63	105	$7{,}726^{+883}_{-927}$
0.792–1.22	61	80	$11{,}864^{+1{,}467}_{-1{,}422}$
1.22–1.80	46	53	$16{,}252^{+2{,}409}_{-2{,}178}$
1.80–3.60	55	61	$25{,}548^{+3{,}574}_{-3{,}262}$
3.60–14.4	23	25	$34{,}940^{+7{,}840}_{-6{,}624}$

This average drops to -0.74 for α_{62}^{153} and increases to -0.81 for α_{153}^{1400}. The average spectral index between 1400 and 153 MHz we find is within the range of previously reported values: -0.87, (Williams et al. 2013), -0.79 (Intema et al. 2011), -0.78 (Ishwara-Chandra et al. 2010), -0.82 (Sirothia et al. 2009), and -0.85 (Ishwara-Chandra & Marathe 2007).

We compute the same values for the 3C 295 field, but starting with the 34 MHz source catalog. We find an average spectral index of -0.81 between 1400 and 34 MHz for the sources. This decreases to -0.85 between 1400 and 62 MHz and increases to -0.64 between 62 and 34 MHz, indicating that the average spectral index flattens towards lower frequencies. The value of -0.64 is somewhat steeper than the -0.5 suggested by the source count scalings.

For the brighter, $S_{34} \gtrsim 1$ Jy, 34 MHz sources we also fitted the radio spectra with a second order polynomial ($\log_{10}(S) = a_0 + a_1 \log_{10}(\nu) + a_2 \left(\log_{10}(\nu)\right)^2$), including the flux densities from the VLSSr, WENSS and NVSS surveys. In total we compute spectra for 27 sources, basically all 34 MHz sources that have a counterpart in the VLSSr survey (the VLSSr survey has a rms noise level of $\approx 0.1\,\mathrm{Jy\,beam^{-1}}$). From the polynomial fits we derive the spectral curvature between 500 and 50 MHz, i.e., the difference in the slope (spectral index) between 50 and 500 MHz. The resulting histogram is displayed in Fig. 3.16 (right panel). The histogram shows an excess of sources with curved spectra. We find that 14 sources have curved spectra ($a_2 < -\sigma_{a_2}$, where σ_{a_2} is the uncertainty in a_2) , while 13 other sources have fits that are consistent with straight (power-law) spectra. None of these sources had an inverted spectrum, with $a_2 > \sigma_{a_2}$. The average spectral curvature of 0.3 is consistent with the increase of the average spectral index from $\alpha_{153}^{1400} = -0.85$ to $\alpha_{34}^{62} = -0.64$ which we found earlier. This average was based on 133 sources so it shows that the spectral flattening is not only confined to the 27 brighter ($S_{34} \gtrsim 1$ Jy) 34 MHz sources.

3.4.3 Ultra-steep spectrum sources

A large number of deep surveys at multiple wavelengths are available that cover the Boötes field, in particular at radio wavelengths. We therefore carried out a search for sources which have ultra-steep radio spectra to select candidate HzRGs. USS sources that are detected at low frequencies could be missed by the higher frequency WENSS and/or NVSS survey due to their steep spectra. We therefore selected all sources detected at 62 and 153 MHz (from Williams et al. 2013), but that are missed in either the WENSS or NVSS survey. In total we find 5 of these sources, see Table 3.5. In addition, we selected sources from the 62 MHz source list that satisfied the criteria $\alpha_{62}^{153} < -1.1$ and $\alpha_{153}^{1400} < -1.1$, since a large part of our field overlaps with the deep 1.4 GHz WSRT survey of the Boötes field from de Vries et al. (2002) which can be used to compute the spectral indices. Three additional sources were found in this way (Table 3.5).

Croft et al. (2008) also searched for HzRGs in the Boötes field. They selected candidate HzRGs with $S_{1400} > 1$ mJy in a matched 325 MHz/1.4 GHz sample. The five sources with the steepest radio spectra and without optical counterparts were followed up with deep K-band imaging. None of the sources listed in Table 3.5 are reported by Croft et al. (2008), as all but one of the sources from Croft et al. have $\alpha_{325}^{1400} > -1.0$. The source with the steepest spectral index from Croft et al. (J142631+341557) is not detected in our LOFAR 62 MHz image. The source is detected at 153 MHz with an integrated flux of 20 ± 5 mJy, giving $\alpha_{153}^{1400} = -1.3$.

For the USS sources we identify candidate counterparts in the NOAO Deep Wide-Field Survey (NDWFS) I-band images. For the optical identification we use the likelihood ratio technique (Sutherland & Saunders 1992; Tasse et al. 2008a). In this way we obtain a probability $P(i)$ that candidate i is the true optical counterpart to a given radio source. For the radio po-

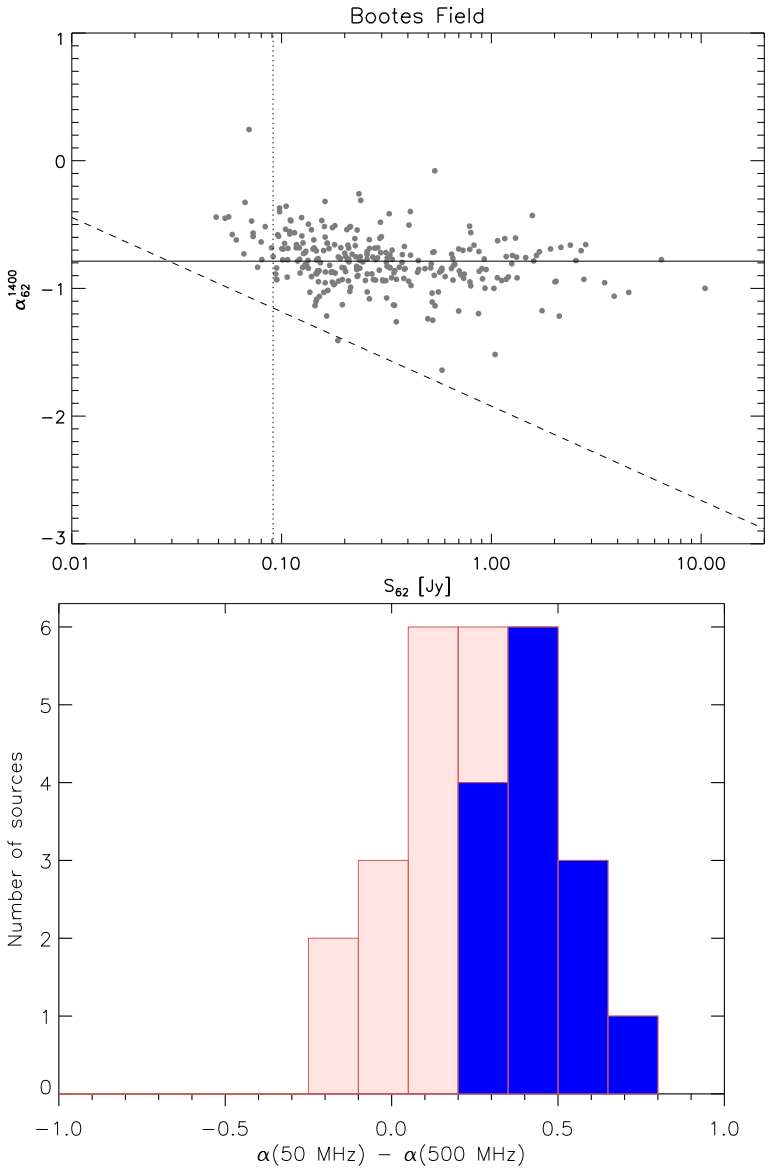


Figure 3.16: Top: Spectral index between 62 and 1400 MHz of sources in the Boötes field plotted against the integrated flux density. The solid line represents the average spectral index of the sources. The vertical dotted line is drawn at $10\sigma_{\mathrm{rms,avg}}$ and the dashed line indicates the completeness limit due to the NVSS sensitivity. Bottom: Histogram of spectral curvature between 500 and 50 MHz for bright 34 MHz sources. The spectral curvature was computed by fitting second order polynomials to the flux density measurements. The blue colors represent sources that cannot be properly fitted with power-law spectra and have $|a_2| > \sigma_{a_2}$, see Sect. 3.4.2.

Table 3.5: USS sources

Source	RA [J2000]	DEC[a] [J2000]	S_{62} [mJy]	S_{153} [mJy]	S_{1400}[b] [mJy]	α_{62}^{153}	α_{153}^{1400}
J143117.9+351549*[c]	14:31:18.1	+35:15:50	252 ± 41	53 ± 11	1.74 ± 0.08	-1.72 ± 0.29	-1.54 ± 0.10
J143127.4+343506*[d]	14:31:27.3	+34:35:07	140 ± 23	40 ± 8	3.00 ± 0.12	-1.39 ± 0.31	-1.17 ± 0.09
J143236.1+333251*	14:32:36.3	+33:32:54	65 ± 14	23 ± 5	2.00 ± 0.09	-1.15 ± 0.34	-1.10 ± 0.10
J143345.9+353856*	14:33:46.0	+35:38:55	153 ± 26	57 ± 12	2.86 ± 0.14[c]	-1.09 ± 0.30	-1.35 ± 0.10
J143501.0+342531*	14:35:01.0	+34:25:31	173 ± 28	55 ± 11	2.18 ± 0.09	-1.27 ± 0.28	-1.46 ± 0.09
J143426.1+342809[ce]	14:34:25.6	+34:28:19	341 ± 54	115 ± 24	10.1 ± 0.5	-1.20 ± 0.29	-1.10 ± 0.10
J143506.8+350058	14:35:06.9	+35:00:59	581 ± 91	141 ± 29	4.02 ± 0.16	-1.57 ± 0.29	-1.61 ± 0.09
J143520.5+345949	14:35:20.5	+34:59:50	185 ± 31	57 ± 12	1.55 ± 0.07	-1.30 ± 0.30	-1.63 ± 0.10

* source not detected in the NVSS and/or WENSS survey

[a] 1.4 GHz position from de Vries et al. (2002)

[b] 1.4 GHz flux density from de Vries et al. (2002)

[c] Source detected in the HerMES survey (Roseboom et al. 2010; Oliver et al. 2012; Smith et al. 2012)

[d] Position and flux density from the 1.4 GHz FIRST survey (White et al. 1997)

[e] Position from the 1.4 GHz FIRST survey and flux density from the NVSS survey

sition we take the GMRT 153 MHz position, or when available the 1.4 GHz FIRST position. We then obtain flux measurements for all candidate counterparts (with $P(i) > 5$ per cent) from the NOAO Deep Wide Field Survey (NDWFS, B_W, R, I, K; Jannuzi & Dey 1999), the Flamingos Extragalactic Survey (FLAMEX, J, K_s; Elston et al. 2006), the zBootes survey (z'; Cool 2007), the Spitzer Deep Wide Field Survey (SDWFS, [3.6], [4.5], [5.8], [8.0]; Ashby et al. 2009), GALEX GR5 (NUV, FUV; Morrissey et al. 2007) and the MIPS AGN and Galaxy Evolution Survey (MAGES [24]; Jannuzi et al. 2010) to obtain photometric redshifts ($z_{\rm phot}$). For the spectral energy distribution (SED) and $z_{\rm phot}$-fitting we require measurements in at least 5 bands. The fitting is performed using both the LRT code from Assef et al. (2008) and EAZY[1] (Brammer et al. 2008) for comparison. A much more extensive description of the radio counterpart identification and SED fitting will be given in Williams et al. (in prep). The results of the fitting are summarized in Table 3.6. Figures showing the SEDs for each source and I band, IRAC 4.5 micron, IRAC 8.0 micron and MIPS 24 micron postage stamps, with GMRT (and FIRST where there is a source) contours, are shown in Appendix 3.B.

We find that the photometric redshifts of the sources are mostly in the $0.7 \lesssim z_{\rm phot} \lesssim 2.5$ range. Given the correlation between optical brightness and redshift, counterparts without photo-z's are likely located at a higher redshift. For J143127.4+343506 and J143345.9+353856 the differences between the EAZY and LRT codes are substantial. We note that the LRT code is supposed to do a better job of fitting AGN and LRT also takes into account the upper limits. Larger USS samples are needed to detect more distant objects as they are more rare. However, steep-spectrum selection also misses a significant fraction of HzRGs (e.g., Jarvis et al. 2009) and not all USS sources are associated with HzRGs (e.g., Jarvis et al. 2001; Cruz et al. 2007; van Weeren et al. 2009). Therefore a combination of deep radio and optical/NIR survey data will be a more powerful way of identifying HzRGs by searching for optically/NIR faint counterparts to the radio sources (e.g., Brookes et al. 2006; Ker et al. 2012).

3.5 Conclusions

We have presented the results of LOFAR LBA observations of the Boötes and 3C 295 fields. In our 62 MHz Boötes field image, with a central noise level of 4.8 mJy beam^{-1}, we detect a total of 329 sources over a 19.4 deg^2 area. Our images of the 3C 295 field cover an area from 17 to 52.3 deg^2 from 62 to 34 MHz, respectively. We reach central noise levels of 5.3, 8.2 and 12 mJy beam^{-1} at 62, 46 and 34 MHz for the 3C 295 field. In total we detect 329, 367, 392 sources at 62, 46 and 34 MHz.

From our source lists, we derive the deepest differential source counts at 62, 46 and 34 MHz to date. At 62 MHz the source counts are in good agreement with 74 MHz counts from VLA observations and scaling with a spectral index of -0.7. At 34 MHz the measured source counts fall significantly below extrapolated source counts from 74 and 153 MHz, using a spectral index scaling of -0.7. Instead, we find that a spectral index scaling of -0.5 provides a better match to the observed 34 MHz source counts. Our 34 MHz source counts are also consistent with those obtained from the 38 MHz 8C survey. In addition, evidence for spectral flattening is found from the increase of the average radio spectral index from high to low frequencies. From polynomial fits to the individual flux densities of bright ($\gtrsim 1$ Jy) 34 MHz sources, we conclude that about half of these sources have curved spectra. The curved spectra of these sources could be caused by absorption effects, as well as by spectral ageing.

[1]EAZY does not use the 24 micron band for the fitting

Table 3.6: USS Sources SED fit results

Source	GMRT ID	P_{match}	$N_{\rm bands}$	$z_{\rm eazy}$			z_{lrt}	
		per cent		z_a	z_m	χ^2/n.d.f.	z	χ^2/n.d.f.
J143520.5+345949	428	**99.6**	11	0.746	$0.743^{+0.056}_{-0.056}$	1.793	0.70	9.37
J143506.8+350058	440	**86.7**	8	1.988	$2.016^{+0.285}_{-0.279}$	1.054	2.46	1.32
J143506.8+350058	440	13.0	2	-	-	-	-	-
J143501.0+342531	445	**99.4**	11	1.400	$1.380^{+0.171}_{-0.175}$	0.749	1.34	1.91
J143426.1+342809	485	**55.3**	4	-	-	-	-	-
J143426.1+342809	485	41.6	3	-	-	-	-	-
J143345.9+353856	517	**99.8**	6	1.871	$1.935^{+0.125}_{-0.137}$	1.534	2.45	1.93
J143236.1+333251	591	**99.1**	11	0.967	$1.033^{+0.096}_{-0.089}$	1.677	1.06	20.59
J143127.4+343506	667	**76.6**	8	1.815	$1.851^{+0.208}_{-0.182}$	1.549	0.32	0.28
J143127.4+343506	667	23.2	1	-	-	-	-	-
J143117.9+351549	679	**92.4**	7	1.548	$2.253^{+0.750}_{-0.695}$	0.107	1.56	0.09

The radio source name and GMRT radio source ID are given in Cols. 1 and 2; Col. 3 gives the probability that a given source is the true optical counterpart to the radio source. The highest probability match is marked in boldface; The number of bands available for SED fitting ($N_{\rm bands}$) is given in Col. 4.; Cols. 5 and 6 give the redshift obtained via EAZY, with z_a the redshift at the minimum χ^2, and z_m the redshift marginalized over the $p(z)$ distribution, with the 68 per cent confidence intervals; The reduced χ^2 of the fit is listed in Col. 7; The fitted redshift from the LRT code and corresponding reduced χ^2 are given in Cols. 8 and 9.

[a] No SED/$z_{\rm phot}$ fitting could be performed since there are less than 5 flux measurements were available.

We also selected sources with steep radio spectra ($\alpha < -1.1$) in the Boötes field to find candidate high-z radio galaxies. We identified optical counterparts to these sources and fitted the SEDs to obtain photometric redshifts. We conclude that most of these USS sources seem to be located in the $0.7 \lesssim z \lesssim 2.5$ range.

Acknowledgments

We thank the anonymous referee for useful comments. LOFAR, the Low Frequency Array designed and constructed by ASTRON, has facilities in several countries, that are owned by various parties (each with their own funding sources), and that are collectively operated by the International LOFAR Telescope (ILT) foundation under a joint scientific policy. This work made use of images and/or data products provided by the NOAO Deep Wide-Field Survey (Jannuzi & Dey 1999), which is supported by the National Optical Astronomy Observatory (NOAO). NOAO is operated by AURA, Inc., under a cooperative agreement with the National Science Foundation.

Support for this work was provided by NASA through Einstein Postdoctoral grant number PF2-130104 awarded by the Chandra X-ray Center, which is operated by the Smithsonian Astrophysical Observatory for NASA under contract NAS8-03060. Chiara Ferrari acknowledges financial support by the *'Agence Nationale de la Recherche'* through grant ANR-09-JCJC-0001-01.

Appendix

3.A Extended sources at 62 MHz

Figures 3.A.1 and 3.A.2 show the 62 MHz LOFAR images of extended sources in the Boötes and 3C 295 fields.

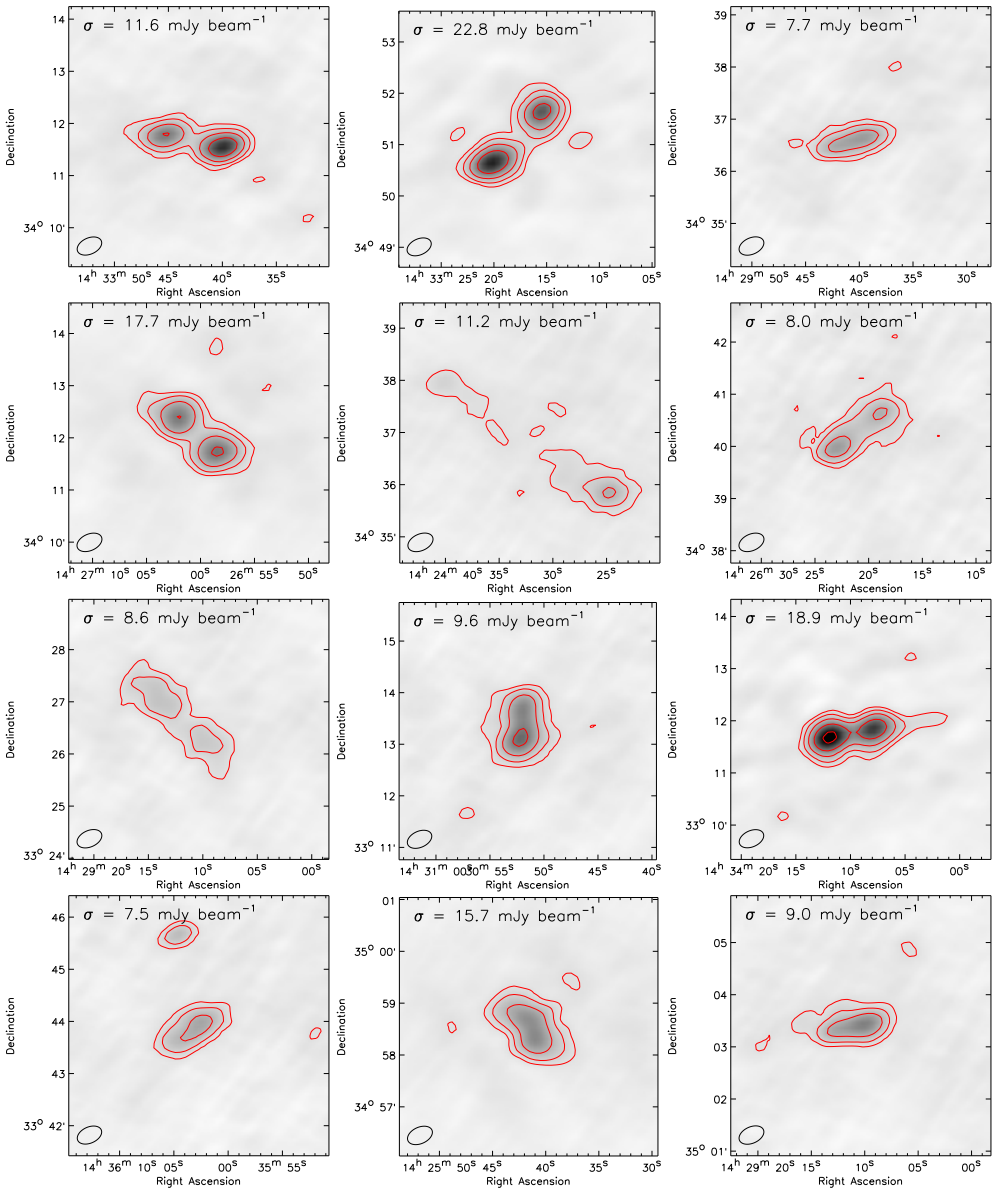


Figure 3.A.1: Images of resolved sources in the Boötes field at 62 MHz. Contour levels are drawn at $[1, 2, 4, 8, \ldots] \times 3\sigma_{\rm local}$, with $\sigma_{\rm local}$ reported in each image. The beam size is shown in the bottom left corner of the images.

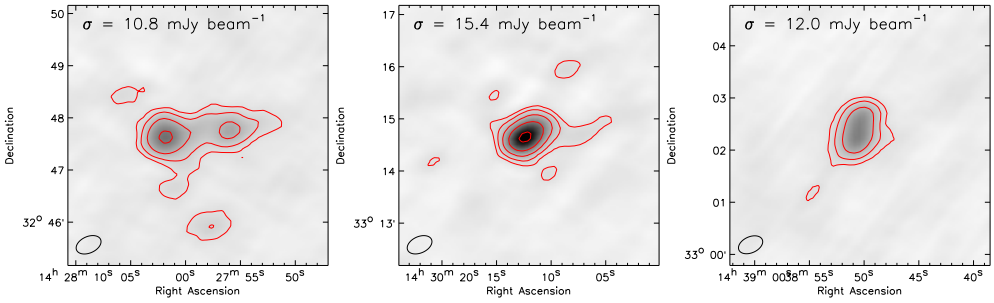


Figure 3.A.1: Continued.

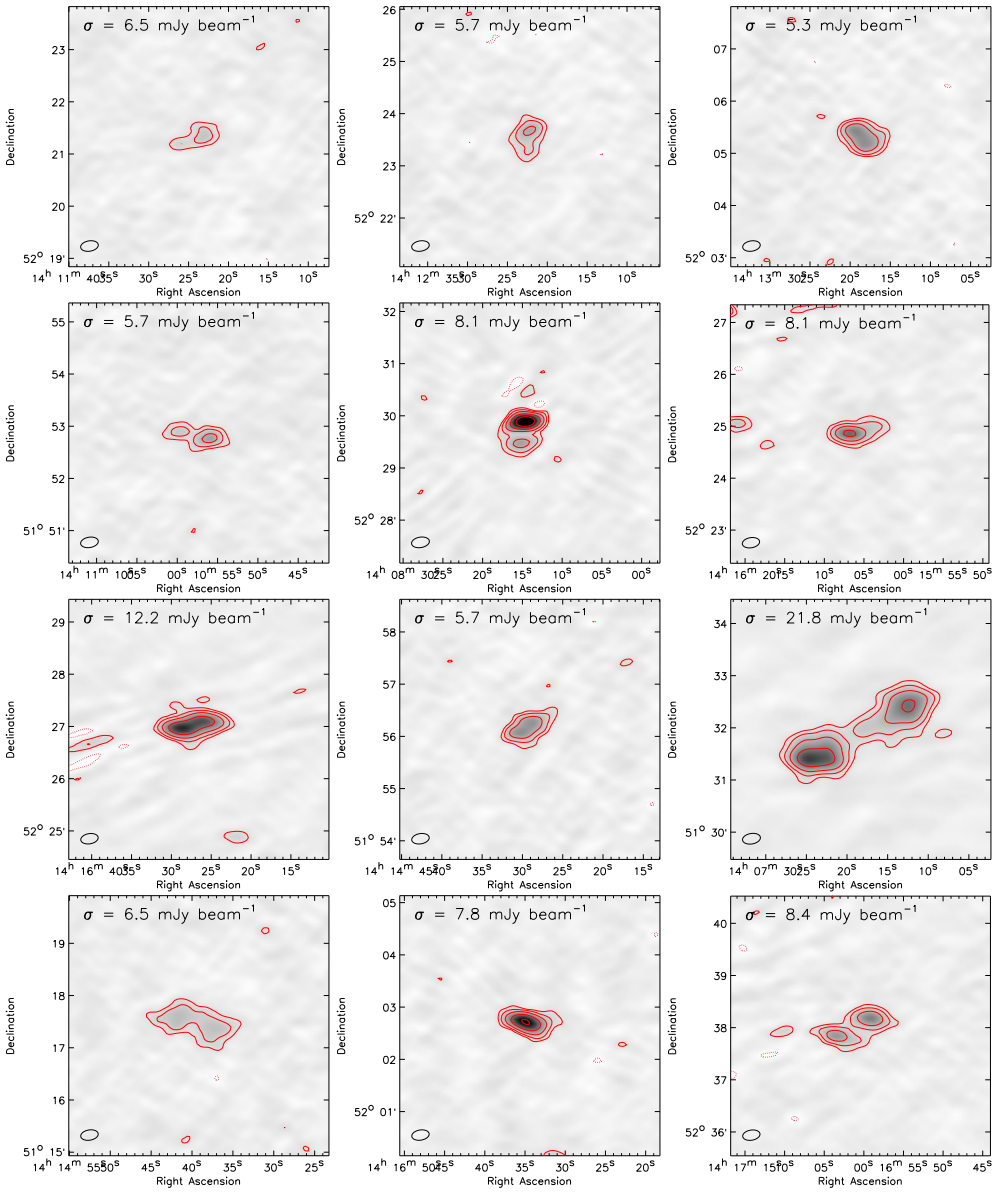


Figure 3.A.2: Images of resolved sources in the 3C 295 field at 62 MHz. Contour levels are drawn at $[1, 2, 4, 8, \ldots] \times 3\sigma_{\rm local}$, with $\sigma_{\rm local}$ reported in each image. The beam size is shown in the bottom left corner of the images.

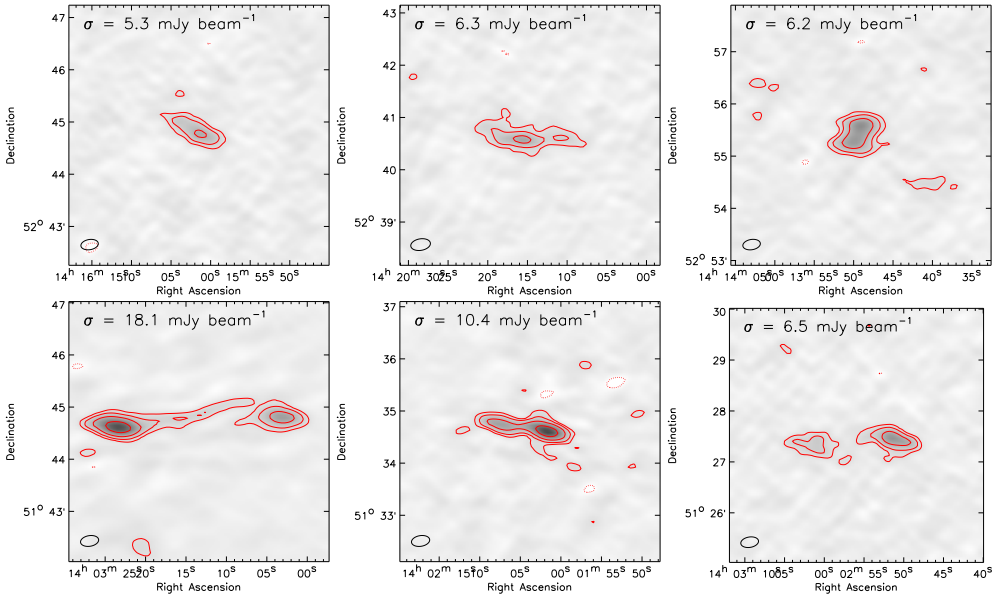


Figure 3.A.2: Continued.

3.B SED & photo-z fitting results

Figure 3.B.1 shows the SEDs for each counterpart to a USS source and I band, IRAC 4.5 micron, IRAC 8.0 micron and MIPS 24 micron postage stamps, with GMRT (and FIRST where there is a source) contours overlaid.

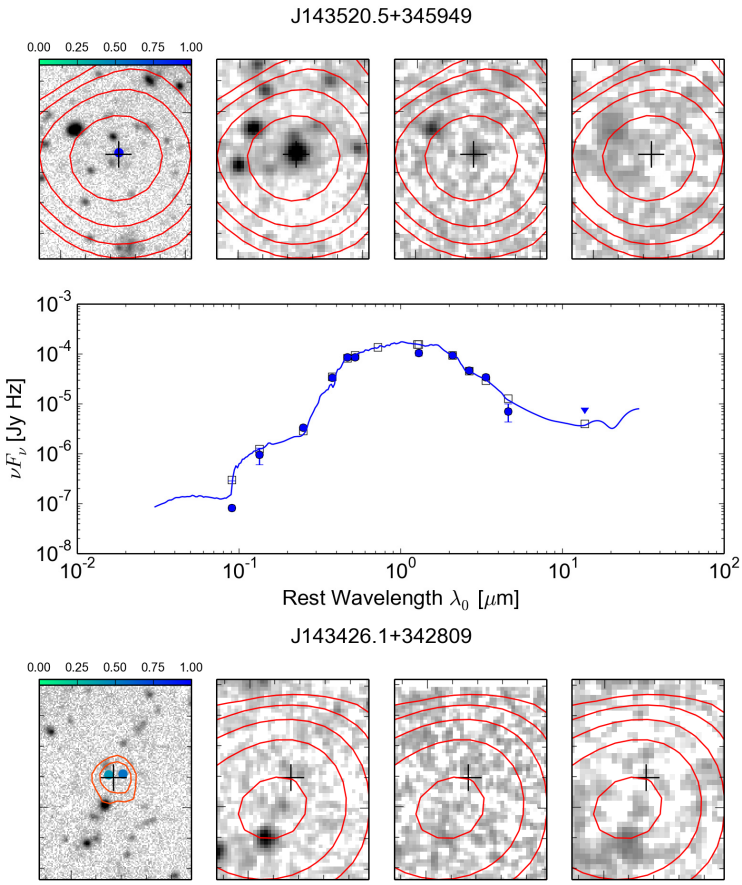


Figure 3.B.1: Top panels: postage stamps showing NDWFS I-band, IRAC 4.5 micron, IRAC 8.0 micron and MIPS 24 micron images. GMRT 153 MHz (red) and FIRST 1.4 GHz (orange, when available) contours are overlaid. Radio contour levels are drawn at $[1, 2, 4, \ldots] \times 3\sigma_{\rm rms}$. A black cross indicates the GMRT radio position and the color scale at the top of the I-band image shows the probability that the I-band source, marked with a colored point, is the true optical counterpart. Bottom panels: Spectral energy distribution and best fitted LRT model for the optical counterpart(s). The flux measurements were taken from Jannuzi & Dey (1999); Elston et al. (2006); Cool (2007); Ashby et al. (2009); Morrissey et al. (2007); Jannuzi et al. (2010).

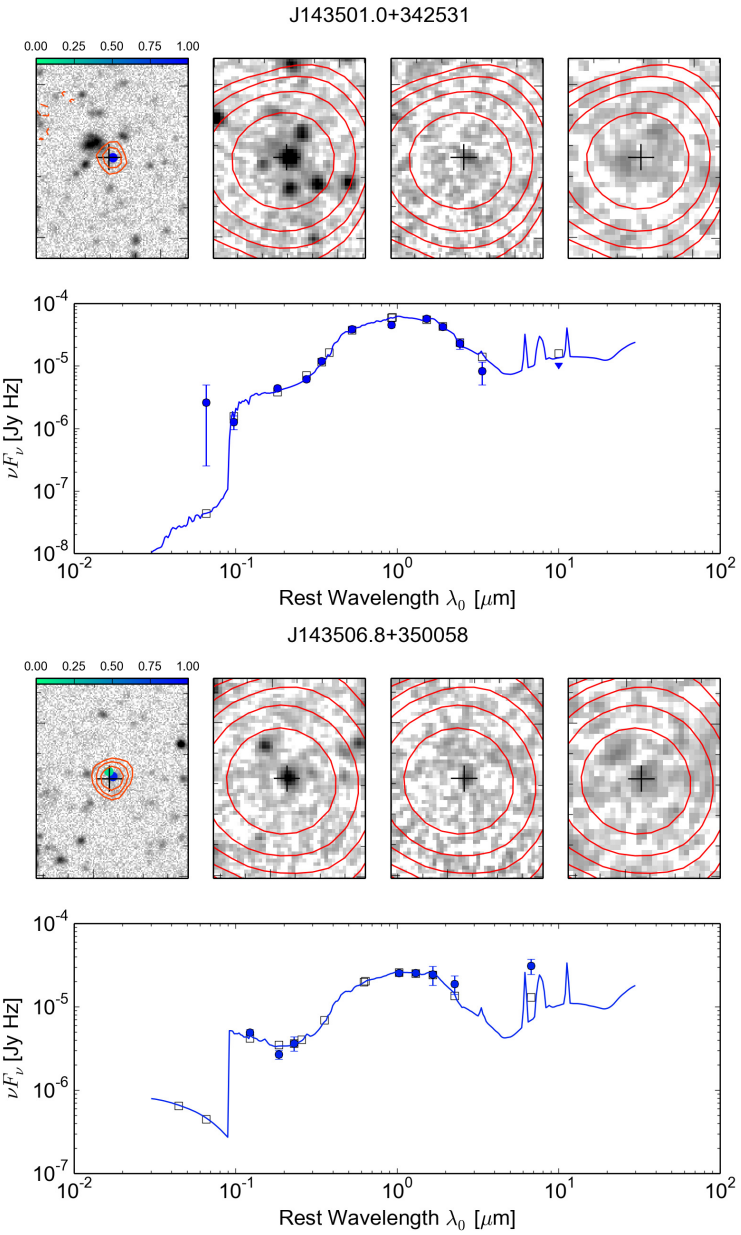


Figure 3.B.1: Continued.

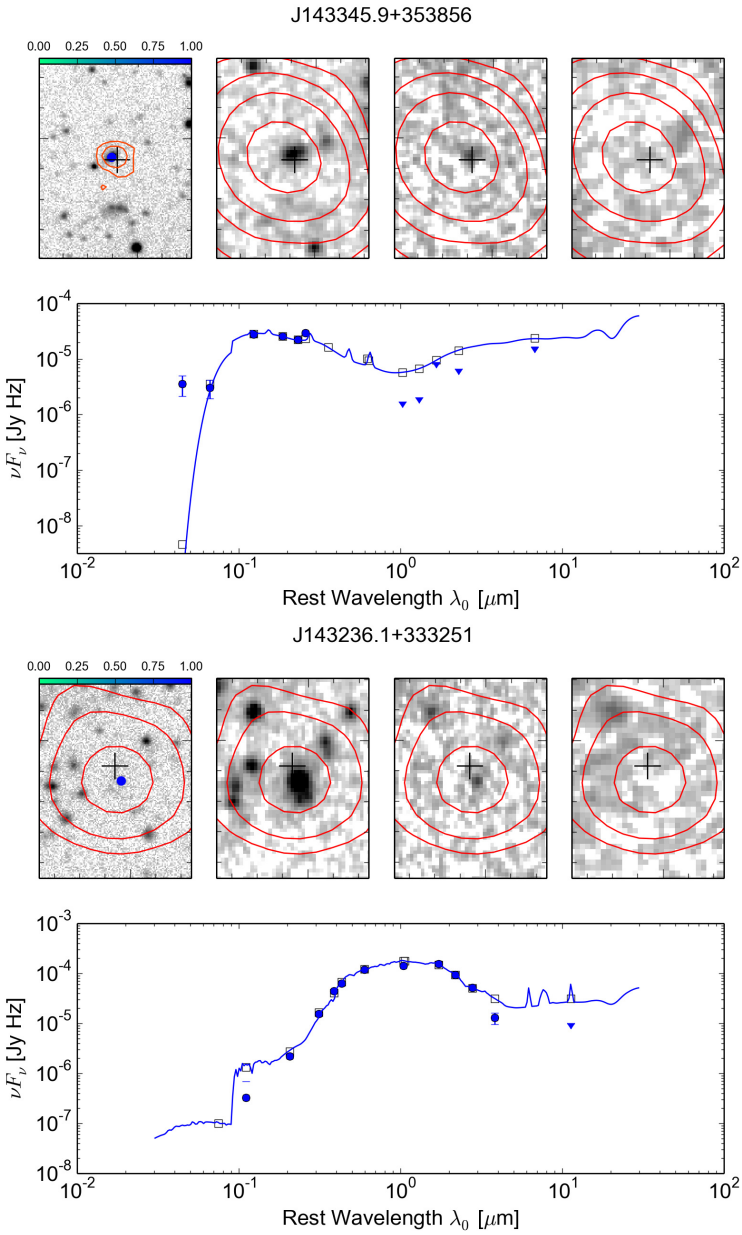


Figure 3.B.1: Continued.

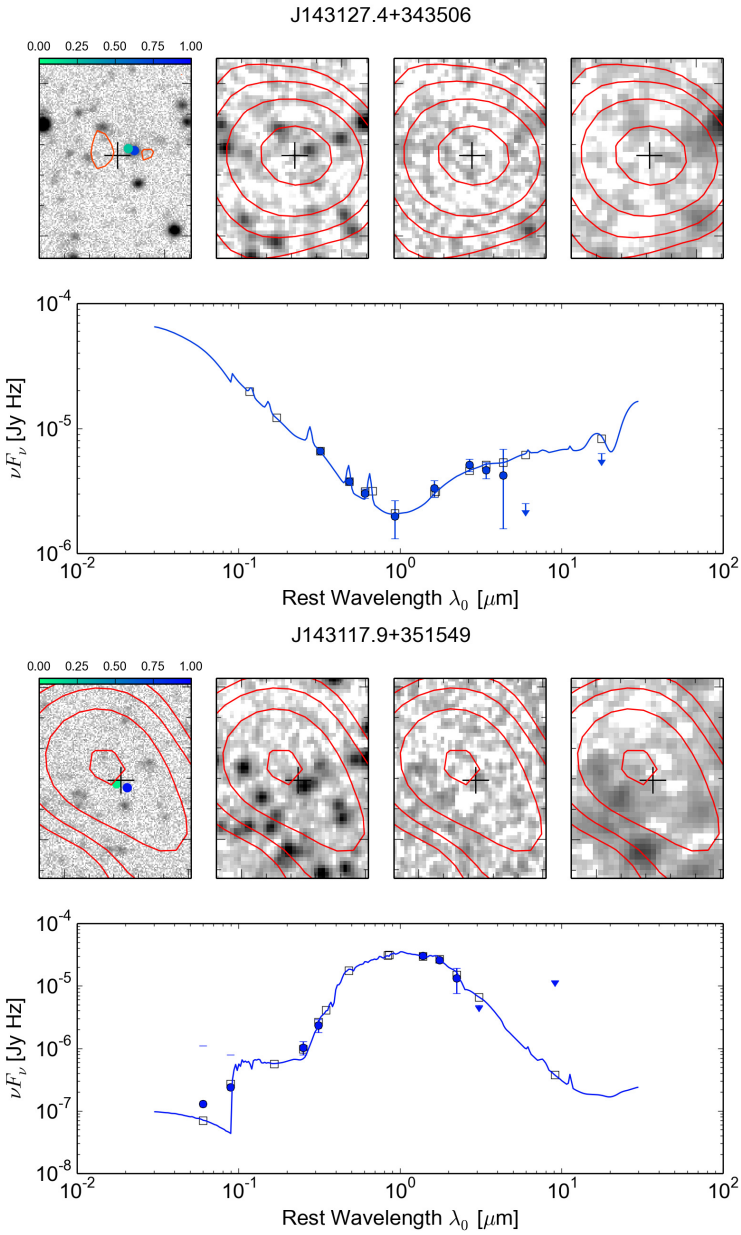


Figure 3.B.1: Continued.

3.C Source counts at 62 MHz for the Boötes field and 3C 295 fields

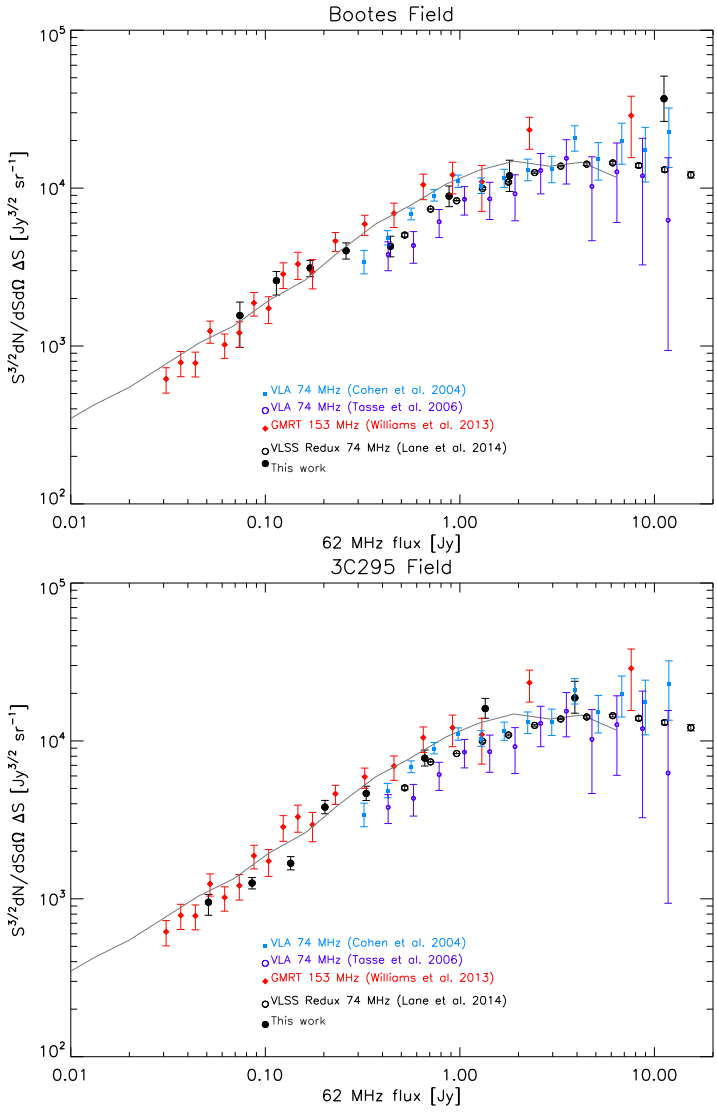


Figure 3.C.1: Euclidean-normalized differential source counts at 62 MHz for the Boötes and 3C 295 fields. The LOFAR points are indicated by the black symbols. Red diamonds are Boötes field source counts at 153 MHz, scaled to 62 MHz using $\alpha = -0.7$. Black open circles, blue squares and purple open circles are 74 MHz differential source counts from Tasse et al. (2006); Cohen et al. (2004); Lane et al. (2014) and the solid grey line displays the counts from the 151 MHz SKADS S^3-SEX simulation (Wilman et al. 2008). These are all scaled to 62 MHz assuming $\alpha = -0.7$.

CHAPTER 4

LOFAR 150 MHz observations of the Boötes field: Catalogue and Source Counts

We present the first wide area (19 deg^2), deep ($\approx 120-150$ μJy beam^{-1}), high resolution (5.6×7.4 arcsec) LOFAR High Band Antenna image of the Boötes field made at $130-169$ MHz. This image is at least an order of magnitude deeper and $3-5$ times higher in angular resolution than previously achieved for this field at low frequencies. The observations and data reduction, which includes full direction-dependent calibration, are described here. We present a radio source catalogue containing 5 652 sources detected over an area of 19 deg^2, with a peak flux density threshold of 5σ. As the first thorough test of the facet calibration strategy, introduced by van Weeren, we investigate the flux and positional accuracy of the catalogue. We present differential source counts that reach an order of magnitude deeper in flux density than previously achieved at these low frequencies, and show flattening at 147 MHz flux densities below 10 mJy associated with the rise of the low flux density star-forming galaxies and radio-quiet AGN.

Williams, W. L., van Weeren, R. J., Röttgering, H. J. A., et al.
MNRAS, submitted

4.1 Introduction

The LOw Frequency ARray (LOFAR) is a new generation radio telescope operating at 10–240 MHz (van Haarlem et al. 2013). Its large instantaneous field-of-view, combined with multi-beaming capabilities, high-spatial resolution, and large fractional bandwidth make LOFAR an ideal instrument for carrying out large surveys of the sky which will have long-lasting legacy value. As such, 'Surveys' is one of the six LOFAR Key Science Projects (KSP). The science goals of the Surveys KSP are broad, covering aspects from the formation and evolution of large-scale structure of the Universe; the physics of the origin, evolution and end-stages of radio sources; the magnetic field and interstellar medium in nearby galaxies and galaxy clusters; to Galactic sources. The deep LOFAR surveys will be crucial in the study of AGN evolution and the history of black-hole accretion. In particular, the Surveys KSP aims to answer questions related to the nature of the different accretion processes, the properties of the host galaxies, the role of AGN feedback in galaxy growth and evolution, the radio-source duty cycle and the relation of the AGN with their environment (e.g. Heckman & Best 2014, and references therein). The radio-source population has not been well-studied at low flux densities and low frequencies. To achieve the diverse goals of the LOFAR surveys, which will be carried out over the next five years, a tiered approach is being used: Tier-1 covers the largest area at the lowest sensitivity, and will include low-band (LBA; $15-65$ MHz) and high-band (HBA; $110-180$ MHz) observations across the whole 2π steradians of the northern sky with a targeted rms noise of ≈ 0.1 mJy beam^{-1} and a resolution of ≈ 5 arcsec. Deeper Tier-2 and Tier-3 observations will cover smaller areas, focussing on fields with the highest quality multi-wavelength datasets available (for details see Rottgering 2010).

Several low-frequency surveys have been performed in the past, such as the Cambridge surveys 3C, 4C, 6C and 7C at 159, 178, 151 and 151 MHz, respectively (Edge et al. 1959; Bennett 1962; Pilkington & Scott 1965; Gower et al. 1967; Hales et al. 1988, 2007), the UTR-2 sky survey between $10-25$ MHz (Braude et al. 2002), and the VLSS at 74 MHz (Cohen et al. 2007; Lane et al. 2014). The GMRT significantly improved low frequency imaging, particularly in terms of sensitivity and angular resolution, and several GMRT surveys have now been performed at 153 MHz (e.g. Ishwara-Chandra & Marathe 2007; Sirothia et al. 2009; Ishwara-Chandra et al. 2010; Intema et al. 2011), 325 MHz (e.g Mauch et al. 2013) and 610 MHz (e.g Garn et al. 2007, 2008a,b). Recently, the Murchison Widefield Array (MWA; Lonsdale et al. 2009; Tingay et al. 2013), operating at $72-231$ MHz, has yielded the GaLactic and Extragalactic All-sky MWA survey (GLEAM; Wayth et al. 2015). GLEAM covers the entire Southern sky ($\delta < 25^{\circ}$) with a noise level of a few mJy beam^{-1} and angular resolution of a few arcminutes. However, for extragalactic science in particular, LOFAR provides a significant advantage in both image resolution and sensitivity.

Advanced calibration and processing techniques are needed to obtain deep high-fidelity images at low radio frequencies. In particular, direction-dependent effects (DDEs) caused by the ionosphere and imperfect knowledge of the station beam shapes need to be corrected for. van Weeren (prep, submitted) have recently presented a new scheme for calibrating the direction-dependent effects and imaging LOFAR data that combines elements from existing direction-dependent calibration methods such as SPAM (Intema et al. 2009) and SAGECal (Yatawatta et al. 2013; Kazemi et al. 2011). The Boötes field observations presented here also serve as a testbed for this calibration strategy, which allows us to produce science quality images at the required Tier-1 survey depth.

Here we report on the first LOFAR Cycle 2 High Band Antenna (HBA) observations of the Boötes field. The Boötes field is one of the Tier-3 Survey fields and the aim is to eventually

survey this field to the extreme rms depth of 12 μJy beam^{-1} (1σ) at 147 MHz. The Boötes field has been extensively studied at higher radio frequencies and in other parts of the electromagnetic spectrum. Radio observations have been carried out at 153 MHz with the GMRT, both as a single deep 10 deg^2 pointing (Intema et al. 2011) and as a seven-pointing 30 deg^2 mosaic (Williams et al. 2013). Further observations include those at 325 MHz with the VLA (Croft et al. 2008; Coppejans et al. 2015), and deep, 28 μJy beam^{-1} rms, 1.4 GHz observations with WSRT (de Vries et al. 2002). The field has also been observed with the LOFAR Low Band Antennae at 62 MHz (van Weeren et al. 2014).

The Boötes field is one of the largest of the well-characterised extragalactic deep fields and was originally targeted as part of the NOAO Deep Wide Field Survey (NDWFS; Jannuzi et al. 1999) covering ≈ 9 deg^2 in the optical (B_W, R, I) and near infra-red (K) bands. There is a wealth of ancillary data available for this field, including X-ray (Murray et al. 2005; Kenter et al. 2005), UV (GALEX; Martin et al. 2003), and mid infrared (Eisenhardt et al. 2004). The AGN and Galaxy Evolution Survey (AGES) has provided redshifts for 23, 745 galaxies and AGN across 7.7 deg^2 of the Boötes field (Kochanek et al. 2012). This rich multiwavelength dataset, combined with the new low frequency radio data presented here, will be important for determining the evolution of black-hole accretion over cosmic time.

The outline of this paper is as follows. In Section 4.2 we describe the LOFAR observations covering the NOAO Boötes field. In Section 4.3 we describe the data reduction techniques employed to achieve the deepest possible images. Our data reduction relies on the 'Facet' calibration scheme (van Weeren prep, submitted) which corrects for direction-dependent ionospheric phase corruption as well as LOFAR beam amplitude corruption. In Section 4.4 we present the final image and describe the source-detection method and the compilation of the source catalogue. This section also includes an analysis of the quality of the catalogue. The spectral index distribution and differential source counts are presented in Section 4.5. Finally, Section 4.6 summarises and concludes this work. Throughout this paper, the spectral index, α, is defined as $S_\nu \propto \nu^\alpha$, where S is the source flux density and ν is the observing frequency. We assume a spectral index of -0.8 unless otherwise stated.

4.2 Observations

The Boötes field was observed on 2014 August 10 with the LOFAR High Band Antenna (HBA) stations. An overview of the observations is given in Table 4.1. By default, all four correlation products were recorded with the frequency band divided into 195.3125 kHz–wide subbands (SBs). Each SB was further divided into 64 channels. The integration time used was 1 s in order to facilitate the removal of radio frequency interference (RFI) at high time resolution. The maximum number of SBs for the system in 8 bit mode is 488 and the chosen strategy was to use 366 for the Boötes field giving a total bandwidth of 72 MHz between 112–181 MHz. The remaining 122 SBs were used to observe the nearby bright calibrator source, 3C 294, located 5.2° away, with a simultaneous station beam, with SBs randomly spread between 112–181 MHz. The main observations were preceded and succeeded by 10 min observations of the primary flux calibrators 3C 196 and 3C 295, respectively, with identical SB setup to the Boötes observation, i.e. 366 SBs (72 MHz bandwidth) between 112–181 MHz. For the observations 14 Dutch remote and 24 Dutch core stations were used. This setup results in baselines that range between 40 m and 120 km. The uv-coverage for the Boötes field observation is displayed in Fig. 4.1. The 'HBA_DUAL_INNER' configuration was employed. In this configuration, the core stations are

Table 4.1: LOFAR HBA observation parameters.

Observation IDs	L240762 (3C 196)
	L240764 (Boötes, 3C 294)
	L240766 (3C 295)
Pointing centres	08 : 13 : 36 48 : 13 : 03 (3C 196)
	14 : 32 : 00 +34 : 30 : 00 (Boötes)
	14 : 06 : 44 +34 : 11 : 25 (3C 294)
	14 : 11 : 20 52 : 12 : 10 (3C 295)
Integration time	1 s
Observation date	2014 August 10
Total on-source time	10 min (3C 196, 3C 295)
	8 hr (Boötes, 3C 294)
Correlations	XX, XY, YX, YY
Sampling mode	8-bit
Sampling clock frequency	200 MHz
Frequency range	112–181 MHz
Bandwidth	71.48 MHz (Boötes, 3C 196, 3C 295)
	23.83 MHz (3C 294)
Subbands (SBs)	366 contiguous (Boötes, 3C 196, 3C 295)
	122 randomly distributed[a] (3C 294)
Bandwidth per SB	195.3125 kHz
Channels per SB	64
Stations	62 total
	14 remote
	24 core (48 split)

[a]between 112–181 MHz

each split into two substations (48 total), and only the inner ≈ 30.8 m of the remote stations (which have a total diameter of 41 m) are used to obtain similar station beam sizes to the core stations (which have a diameter of 30.8 m). The resulting half-power beam width (HPBW) is $\approx 4.2^{\circ}$[1] at 150 MHz.

4.3 Data Reduction

In this section we describe the calibration method that was used to obtain the required deep high-fidelity high-resolution images. The data reduction and calibration consists of two stages: a non-directional and a directional part to correct DDEs caused by the ionosphere and imperfect station beam models. The non-directional part includes the following steps:

1. initial flagging and removal of RFI;

[1]Based on the calculated average primary beam for the Boötes observation (see Section 4.3.2)

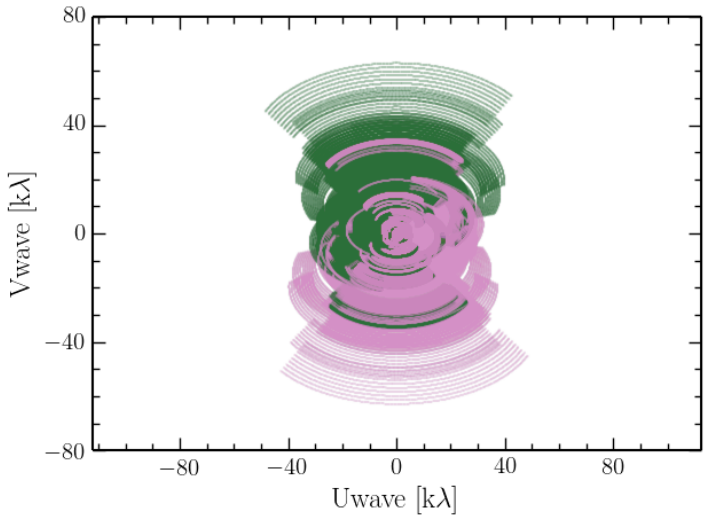


Figure 4.1: uv-coverage for the Boötes field at $130-169$ MHz. The maximum baseline is 120 km (or 60 kλ). Only one out of every ten uv-points in time and one out of every 40 points in frequency are plotted: the plot nevertheless shows how the large fractional bandwidth fills the uv-plane radially. The two colours show the symmetric uv points obtained from the conjugate visibilities.

2. solving for the calibrator complex gains, including 'clock-TEC (Total Electron Content) separation', and transfer of the amplitudes, median clock offsets and the XX–YY phase offset from calibrator to the target field;
3. removal of bright off-axis sources;
4. averaging; and
5. amplitude and phase (self-)calibration of the target field at medium (20–30 arcsec) resolution

This is then followed by a scheme to correct for DDEs in order to reach near thermal-noise-limited images using the full resolution offered by the longest 'Dutch-LOFAR' baselines of about 120 km. All calibration steps are performed with the BlackBoard Selfcal (BBS) software system (Pandey et al. 2009) and other data handling steps were undertaken with the LOFAR Default Pre-Processing Pipeline (DPPP). These steps are explained in more detail below. The direction-dependent calibration scheme is described in full by van Weeren (prep, submitted).

We used the full frequency coverage of the 10 min 3C 196 observation as the primary calibrator observation to derive the time-independent instrumental calibration including amplitudes, median clock offsets and the XX–YY phase offset. We did not use the simultaneous, but sparse, frequency coverage on the calibrator 3C 294. For the Boötes field we selected 200 out of the total 366 observed SBs (55 per cent) covering the frequency range 130–169 MHz for further processing. The main limitation to the number of subbands processed was computational time; the main data reduction was carried out on a node with 20 virtual cores on ASTRON's CEP3

cluster[1] and most of the parallelisation in the reduction is performed over 10-SB blocks, so that the full 'facet' reduction could be achieved in a reasonable time.

4.3.1 Direction-independent calibration

Flagging and RFI removal

The initial preprocessing of the data was carried out using the Radio Observatory pipeline and consisted of RFI excision (using AOFlagger; Offringa et al. 2010, 2012), flagging the noisy first channel channel and last three channels of each SB, and averaging in time and frequency to 2 s and 8 channels per SB. The data were stored at this resolution in the LOFAR Long Term Archive (LTA) at this point. One core station (CS007) and one half of another core station (CS501HBA1) were flagged entirely due to malfunction (failure to record data or low gains). CS013 was also flagged entirely due its different design (the dipoles are rotated by $45°$).

Calibration transfer from Primary Calibrator 3C 196

Using BBS we obtained parallel hand (XX and YY) gain solutions for 3C 196, on timescales of 2 s for each frequency channel independently. In this step we also solved simultaneously for 'Rotation Angle' per station per channel to remove the effects of differential Faraday Rotation from the parallel hand amplitudes. The solutions were computed with the LOFAR station beam applied to separate the beam effects from the gain solutions. We used a second-order spectral model for 3C 196 consisting of 4 point sources separated by $3 - 6$ arcsec each with a spectral index and curvature term (V. N. Pandey (ASTRON), priv. comm.). This is close to, but not exactly the same as the Scaife & Heald (2012) flux scale. We used these calibration solutions to determine the direction-independent and time-invariant instrumental calibrations, including amplitude calibration, correction of clock delays between the remote and core stations and an offset between the XX and YY phases.

The remote LOFAR stations have their own clocks which are not perfectly synchronized with the single clock that is used for all the core stations – the offsets between these clocks can be of the order of 100 ns, which is large enough to cause strong phase delays within a single SB for the remote-remote and core-remote baselines. In addition to these clock offsets, which appear to be similar from observation to observation, the clocks can drift by ≈ 15 ns over a few hours. The primary calibrator phase solutions were used to calculate the clock offsets to be applied to the target observation (we do not correct for the 15 ns clock drifts). We used the 'Clock-TEC separation' method described in detail by van Weeren (prep, submitted) that uses the frequency-dependent phase information across the full frequency range to separate the direction-independent clock errors from the direction-dependent ionospheric effects. The clock phase errors, or delays, vary linearly with frequency (phase $\propto \delta t \times \nu$, where δt is the clock difference), while the ionospheric phases vary inversely with frequency (phase $\propto$ dTEC $\times \nu^{-1}$, where dTEC is the differential Total Electron Content). Fitting was performed on a solution interval timescale of 5 s and smoothed with a running median filter with a local window size of 15 s. The results are shown in Fig. 4.2, from which it can be seen that the clock offsets for the remote stations in our observation were between -90 ns and 80 ns with respect to the core. The ionospheric conditions during the 10 min calibrator observation were good, showing relatively smooth variations in the differential TEC of $\approx 0.2 \times 10^{16}$ m^{-2}.

[1]Each node has 2 ten-core Intel Xeon e5 2660v2 (25M Cache, 2.20 GHz) processors with 128 GB RAM

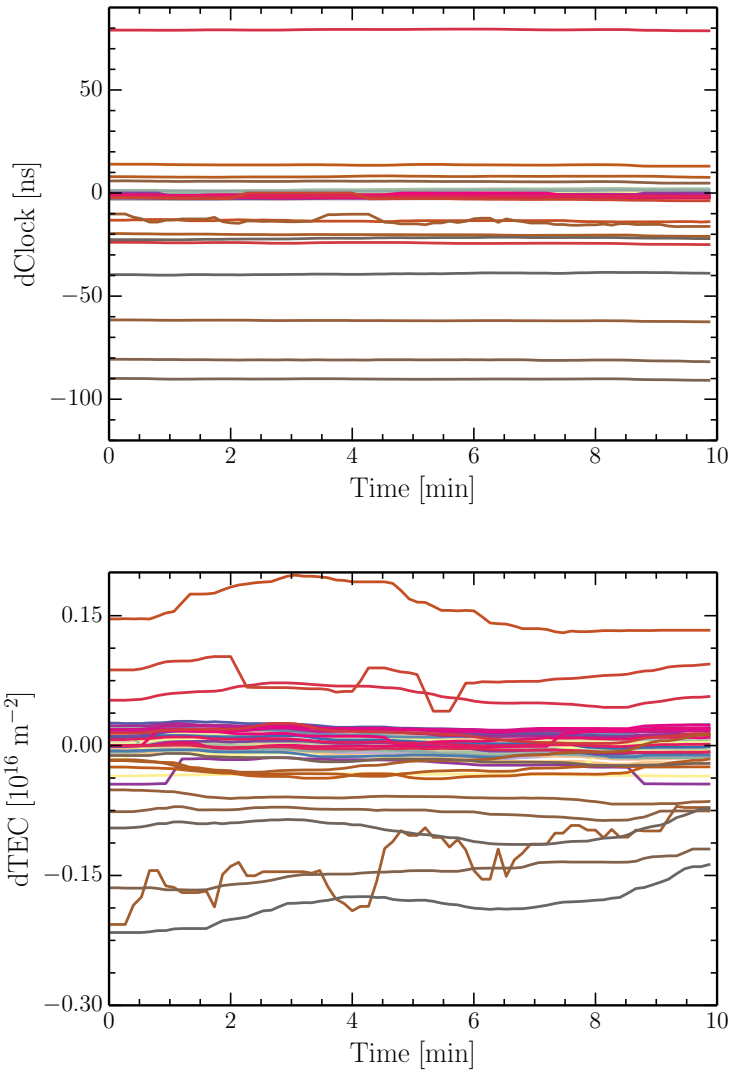


Figure 4.2: Fitted clock and TEC differences from the 3C 196 phase solutions. The fitting was performed on the solution interval timescale of 2 s and smoothed with a running median filter with a local window size of 10 s. Top: Fitted station clock offsets as a function of time with respect to the reference (core) station CS001HBA0. The core stations all have clock values close to zero, while the remote stations have large clock offsets with respect to the core stations, between -90 ns and 80 ns. Bottom: Differential TEC values for the same stations. These show typical dTEC values (≈ 0.2 TEC units). The core stations all have similar dTEC values around zero as they essentially probe the same patch of ionosphere. RS310 has the largest variation in dTEC and also has discrete jumps in its dClock values as a result of its noisier amplitudes.

For a few stations we found small but constant offsets between the XX and YY phases. We determined these offsets by taking the median phase difference between the XX and YY phases during the 3C 196 observation for each station.

The amplitudes were inspected for outliers and smoothed in the frequency axis with a running median filter with window size of 3 SBs (≈ 0.6 MHz), and a single median value in the time axis of the 10 min observation.

These calculated median clock offsets, XX–YY phase offsets and amplitude values were transferred from the 10 min observation of 3C 196 to the target-field data. The resulting target-field visibilities have amplitudes in Janskys and are free of global clock offsets (note that we do not correct for the 15 ns clock drifts during the target observation) and XX–YY phase offsets.

Removal of bright off-axis sources

A few radio sources are sufficiently bright to contribute flux through the sidelobes of the station beams, the amplitudes of which are strongly modulated in frequency, time and baseline as they move in and out of the station-beam sidelobes. To remove these effects we simply predicted the visibilities of the brightest of these 'A-team' sources (Cyg A, Cas A, Vir A, and Tau A) with the station beam applied in BBS, and flagged all times, frequencies and baselines where the contributed flux density from these sources exceeded 5 Jy. The amount of data flagged in this step was typically 2–5 per cent per SB.

Averaging

The data were then averaged in time to a more manageable 8 s and two channels per SB (98 kHz channelwidth). The main limit on the time resolution is set by the requirement to avoid decorrelation due to rapid ionospheric phase variations. Even at this time and frequency resolution we expect some smearing at large radial distances from the field centre due to time and bandwidth smearing, of the order of 7 and 10 per cent respectively at the half-power point of the primary beam (2.1° from the pointing centre) and 13 and 15 per cent respectively at 2.5° at 150 MHz. The individual corrected SBs were combined in groups of ten, providing datasets of ≈ 2 MHz bandwidth and 20 channels, each of which was ≈ 30 GB in size.

Self-calibration of target

We used a single 10-SB block at 148–150 MHz on which to perform direction-independent self-calibration. We started with a model derived from the 30 deg^2 GMRT image of the Boötes field at 153 MHz (Williams et al. 2013). Then a Gaussian component model was derived using PyBDSM (Mohan & Rafferty 2015), which identifies islands of contiguous emission above a given island threshold (PyBDSM parameter `thresh_isl`) around pixels exceeding a given pixel threshold (`thresh_pix`). The thresholds are given in factors above the varying background rms determined within a sliding box of a given size (`rms_box`), which takes into account the increased rms near bright sources due to calibration artefacts. The source detection parameters are described in more detail by Williams et al. (2013). The resolution of this initial sky model is 25×25 arcsec – the native resolution of the GMRT image – and it includes all sources in the GMRT image greater than 20 mJy ($\approx 6\sigma$). The brightest 10 sources in the GMRT model were replaced by Gaussian components taken from the ≈ 5 arcsec resolution FIRST catalogue (Becker et al. 1995), with their total GMRT 150 MHz flux density and flux density ratios taken from FIRST.

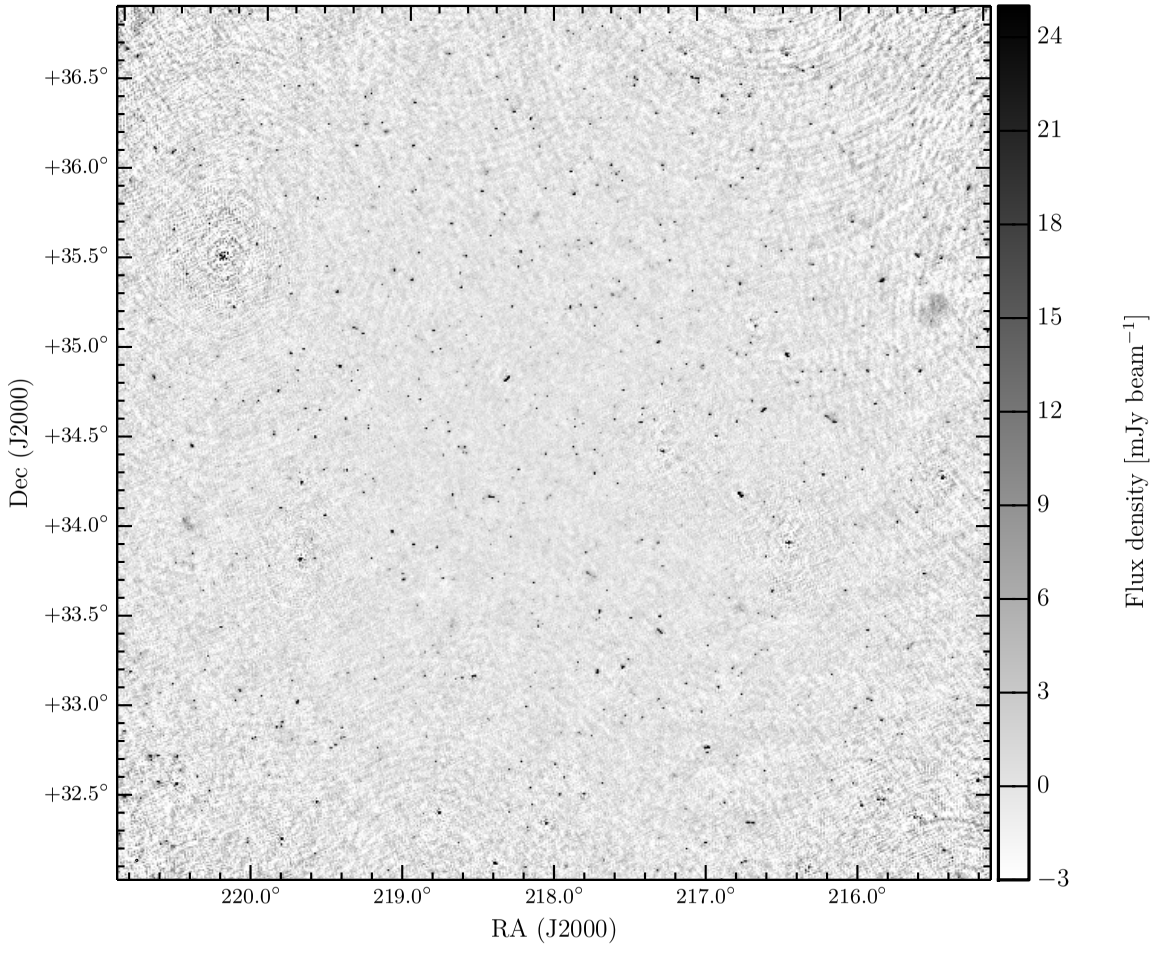


Figure 4.3: Final self-calibrated image for the 10-SB block at 148–150 MHz. The resolution is 23×20 arcsec. The greyscale shows the flux density from -3σ to 25σ where $\sigma = 1$ mJy beam^{-1} is the approximate rms noise in the central part of the image. Calibration artefacts are clearly visible around the brightest sources as only direction-independent self-calibration has been performed.

The self-calibration was performed with two iterations with phase-only solutions followed by two iterations with amplitude and phase solutions. The solution interval in the first phase-only iteration was 8 s and we obtained a single solution in frequency, neglecting phase changes within the 2 MHz bandwidth. The signal-to-noise ratio within the 10-SB block was high enough to obtain good-quality, i.e. coherent, solutions in each timestep. The station beam model was applied in the 'solve' step in BBS and the solutions were applied. The data were corrected for the station beam in the phase centre. Imaging was carried out using AWImager (Tasse et al. 2013), which deals with the non-coplanar nature of the array and performs a proper beam correction across the field-of-view in imaging. From the resulting 'corrected' images we created a new sky model, again using PyBDSM (with `rms_box` = (boxsize, stepsize) = $(150, 40)$ pixels, `thresh_pix` = 5σ and `thresh_isl` = 3σ), and included all Gaussians in the model. We then performed an additional iteration of phase-only self-calibration followed by two iterations of phase and amplitude self-calibration before making a final self-calibrated image for the 10-SB block at 149 MHz. A part of this image is shown in Fig. 4.3. The noise level achieved is ≈ 1 mJybeam. While deeper images at a similar resolution can be made with more bandwidth, this is sufficient for the purpose of initial calibration prior to the direction-dependent calibration. All the imaging at this stage was carried out with a field-of-view of 6.4° at a resolution of $\approx$ 20 arcsec by imposing an outer uv-limit of 40 kλ and Briggs (1995) robust weighting (`robust` = 0). This weighting results in a slightly lower resolution, with less emphasis on the calibration artefacts. The imaging at each step performed in two stages: first without a mask and then with a mask. The clean masks for each image were generated automatically from the first image (without a mask) by using PyBDSM (with `rms_box` = $(85, 30)$ pixels) to create a 3σ island threshold map.

All the 10-SB blocks were then corrected for the station beam in the phase centre before further processing. We then used the final image of the self-calibration cycle at $148 - 150$ MHz to make a Gaussian input sky model with PyBDSM to (self)-calibrate the remaining 10-SB blocks. All the components in this model were assumed to have a spectral index of -0.8. For all the bands we performed a single phase and amplitude calibration against this model and made images of each band with the Common Astronomy Software Applications (Casa; McMullin et al. 2007) version 4.2.1 using W-projection (Cornwell et al. 2008, 2005) to handle the non-coplanar effects; Casa does not allow for the full beam correction across the field-of-view but it does allow a much larger field to be imaged than with AWImager. Because the beam correction was not performed in imaging, the resulting images are *apparent* sky images. The imaging was carried out in two iterations. The first image was made at 'medium resolution' using a uv-cut of 7 kλ and Briggs weighting (`robust` = 0) to limit the resolution to $\approx$ 20 arcsec, with 7.5 arcsec pixels; the field-of-view imaged was $\approx 10^\circ$. Next, in each 10-SB dataset we subtracted the clean components with their self-calibration gain solutions and re-imaged the subtracted data using a 'low resolution' of $\approx$ 2 arcmin with a uv-cut of 2 kλ and Briggs weighting (`robust` = 0), 25 arcsec pixels, and a field-of-view of $\approx 30^\circ$. This field-of-view extends to the second sidelobe of the station beams, allowing us to image and subtract these sources. The low-resolution image also picks up extended low-surface-brightness emission in the field not cleaned in the medium-resolution image. Both medium- and low-resolution images were created with clean masks automatically generated from images made without clean masks and PyBDSM with `rms_box` = $(50, 12)$ and `rms_box` = $(60, 12)$ respectively. The clean components in the low-resolution image were then subtracted in the same way as the medium-resolution components and a combined list of clean components for the medium- and low-resolution images was created.

The resulting products are 20 sets of 2-MHz residual datasets between 130 and 169 MHz – i.e. with all sources out to the second sidelobes subtracted using the gain solutions, but with the

residual data itself not corrected for the gain solutions. In addition, there are 20 corresponding CLEAN-component *apparent* sky models of the sources that were subtracted. These products serve as the input for the direction-dependent calibration scheme, which is described in the following section.

4.3.2 Directional calibration – 'Facet' scheme

Significant artefacts remain in the self-calibrated images, even at 20 arcsec resolution, and the rms noise of a few mJy beam^{-1} is a factor of $3-5$ higher than what is expected with these imaging parameters. Both of these issues result from the direction-dependent effects of the station beams and ionosphere. To correct for these we follow the direction-dependent calibration, or 'facet', scheme, of van Weeren (prep, submitted), in which calibration is performed iteratively in discrete directions and imaging is carried out within mutually exclusive facets around each calibration direction. The key concern is keeping the number of degrees of freedom in the calibration small with respect to the number of measured visibilities, in order to facilitate solving for DDEs in tens of directions. The 'facet' scheme has the following underlying assumptions:

1. the only calibration errors are a result of ionosphere and beam errors;
2. the station beams vary slowly with time and frequency;
3. differential Faraday rotation is negligible, so that XX and YY phases are affected identically by the ionosphere;
4. the phase frequency dependence is phase $\propto v^{-1}$ as a result of ionosphere only; and
5. DDEs vary slowly across the field-of-view.

For a more detailed description and discussion of the underlying problems and assumptions see van Weeren (prep, submitted) and references therein. The following sub-sections describe our implementation of the 'facet' scheme on the Boötes field data. At this point we selected 20 contiguous 10-SB datasets covering the frequency range of 130–169 MHz, i.e. 55 per cent of the total observed bandwidth. This selection was made primarily as a trade-off between the expected achievable depth and computational constraints.

Facetting the sky

Initially we identified 28 calibration directions or groups consisting of single bright sources or closely (few arcminute) separated sources with a combined total flux density $\gtrsim 0.3$ Jy. The bright source positions or centres of the groups define the facet directions that were used to tile the sky using Voronoi tessellation, ensuring that each point on the sky lies within the facet of the nearest calibrator source. The assumption here is that the calibration solutions for the calibrator group applies to the full facet. The typical facet size is a few tens of arcminutes in diameter. Around and beyond the HPBW of the station beam, the assumption that DDEs, in particular the beam, vary slowly across the field-of-view breaks down. We found that two of the facets initially defined were too large and showed worsening calibration artefacts away from the calibrator source. These two facets were subdivided into smaller facets each having new calibrator groups. The final set of facets is shown in Fig. 4.4. The following steps were then performed for each direction sequentially, starting with the brightest calibrator sources.

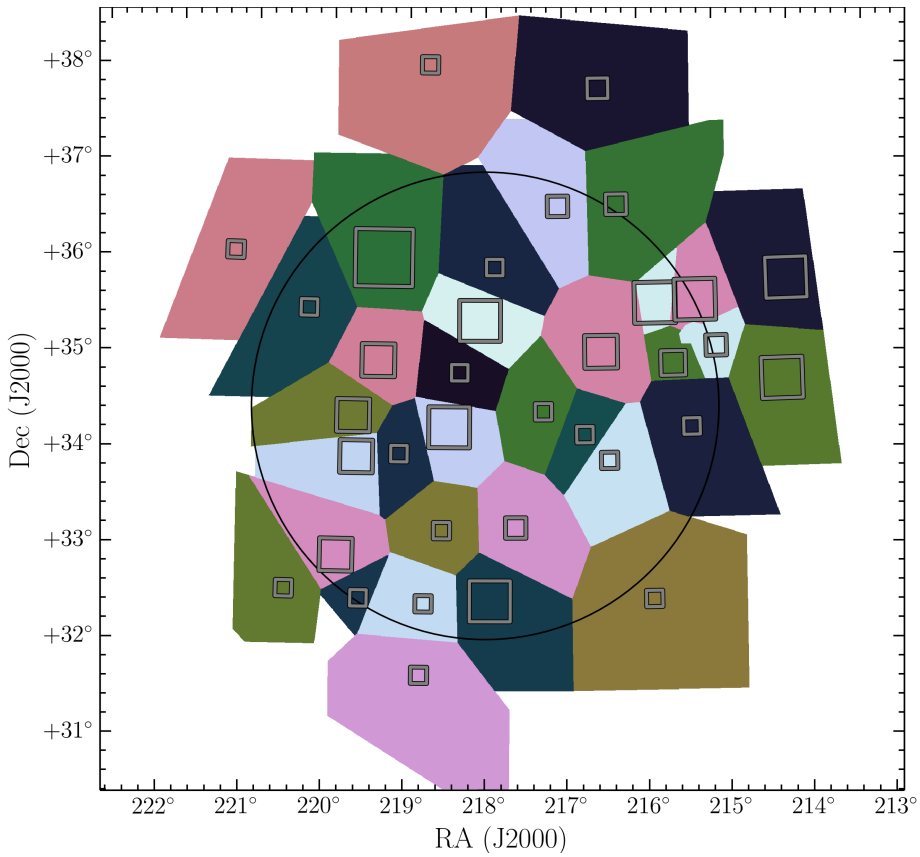


Figure 4.4: Facet coverage of the Boötes field. The grey boxes show the positions of the calibrator directions and the size of these boxes show the area used for self-calibration, i.e. larger boxes include more sources. The coloured polygons show the Voronoi tessellation of the image plane based on these calibrator positions. The maximum size of the facets is limited to 50 arcmin radius from the calibrator direction (2048 pixels at 1.5 arcsec pixel^{-1}) resulting in some incomplete coverage particularly outside the FWHM. The black circle has a radius of $2.44°$, at the approximate 40 per cent power point of the average primary beam.

Directional self-calibration

The CLEAN components of all the sources within the calibrator group were added back in each 10-SB dataset (with the direction-independent calibration solutions with which they had been initially subtracted). These datasets were then phase-rotated to the direction of the calibration group and averaged in frequency (but not in time) to 1 channel per 2-MHz dataset. The frequency averaging greatly speeds up calibration without any bandwidth-smearing effects in the small (few arcminute) calibrator group images.

A self-calibration cycle with four iterations was then performed. The imaging at each iteration was carried out using CASA with the full $130 - 169$ MHz bandwidth and multi-frequency synthesis (MFS) CLEAN with a second-order frequency term (i.e. including spectral index and curvature, `nterms` $= 2$) (Conway et al. 1990), with the automated masking described in Section 4.3.1. This resulted in a CLEAN-component model with both flux and spectral index. Multi-scale CLEAN (MS-MFS; Rau & Cornwell 2011; Cornwell 2008) was used only in the case of a few complex extended sources. We used a Briggs robust parameter of -0.25, a pixel size of 1.5 arcsec, and imposed a uv-minimum of $80\,\lambda$ to achieve a resolution of approximately 5.6×7.4 arcsec. Using a more negative robust weighting allows for higher resolution images after the direction-dependant effects have been accounted for.

In the first two self-calibration cycles we solved for a single Stokes I phase-offset and TEC term per station in groups of 5 10-SB datasets, i.e. within 10 MHz bands. This gave 8 parameters (4 phase and 4 TEC) per station per solution interval. The solutions were computed on timescales of 8 s where possible, but this was increased to 16 s for fainter calibration groups and even to 24 s for the faintest calibration groups where the signal-to-noise was lower.

After having solved for, and applied, the short timescale phase-offset and TEC solutions, we then ran a third and fourth iteration of self-calibration in which we solved for XX and YY gains independently per 10-SB dataset on timescales between 5 and 20 min, depending on the flux density of the calibrator group. This yielded an additional 4 parameters per 10-SB block. This calibration primarily takes out the slowly-varying complex station beams. As expected the phase component of these solutions is small because the fast phase component has been taken out. In the final self-calibration cycle, the amplitudes were normalised to unity across the full frequency range to prevent changes to the flux-scale. The normalisation corrections were typically smaller than a few percent. Example solutions are shown in Fig. 4.5 for a single direction and in Fig. 4.6 for all directions as a snapshot in time. Both the amplitudes and phases show consistent values between directions. When viewed as a movie in time, trends can be seen 'moving across' the field-of-view, in particular in the fast phases, which is consistent with ionospheric phase disturbances propagating through the field-of-view. The significant improvement made in the self-calibration cycles is demonstrated by the calibrator images shown in Fig. 4.7. It is clear that both the phase *and* amplitude calibration are currently required: the phase distortions resulting from ionospheric effects will always have to be corrected for, but future improvements in the LOFAR beam models may eliminate the need for the amplitude calibration.

Facet imaging and subtraction

After obtaining the direction-dependent calibration solutions for the given direction, the remaining sources within the facet were added back (with the direction-independent solutions with which they had been subtracted). Assuming the solutions for the calibrator group apply to the full facet, we applied those solutions to the facet data at the original 2 channels per SB

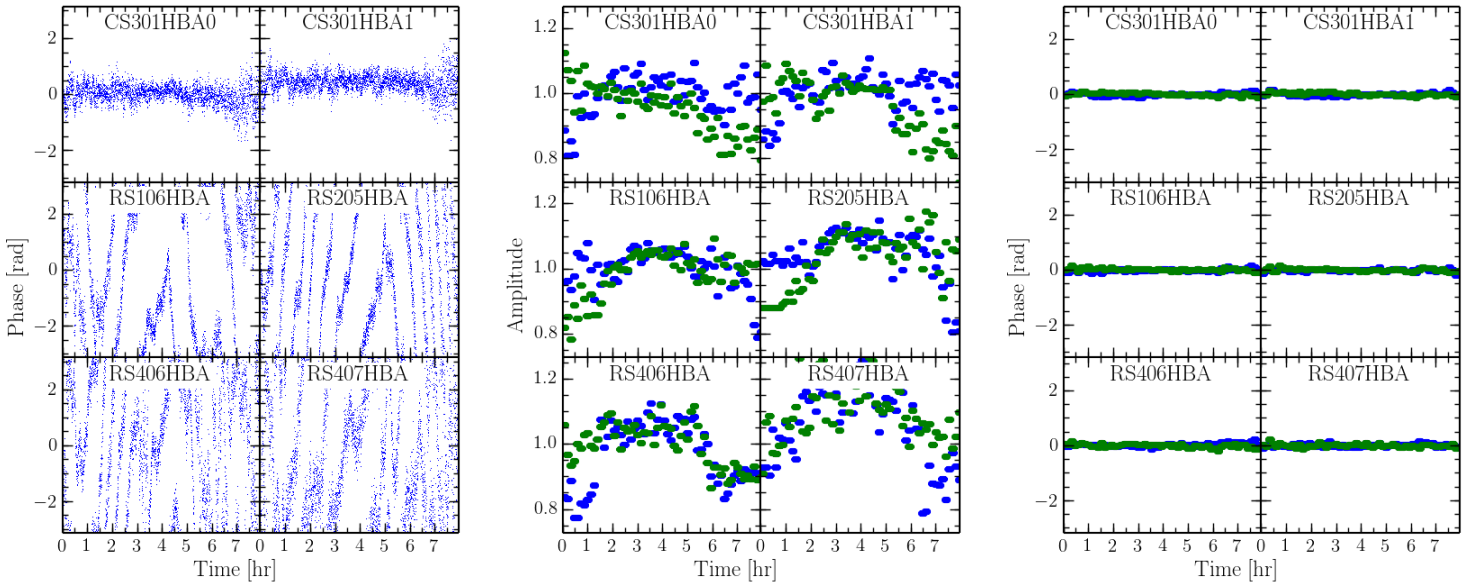


Figure 4.5: Example good DDE solutions for a few selected stations obtained for a single direction s3 (the images corresponding to this direction are shown in Fig. 4.7). Left: The effective Stokes I phase corrections, evaluated at an arbitrary frequency of 150 MHz. The solutions are obtained on a timescale of 8 s using 10 MHz of bandwidth. Centre and Right: the additional XX and YY amplitude (centre) and phase (right) solutions for the $160 - 162$ MHz SB block obtained on a timescale of 10 min after application of the short-timescale phase offsets and TEC solutions. In all cases phases are plotted with respect to core station CS001HBA0.

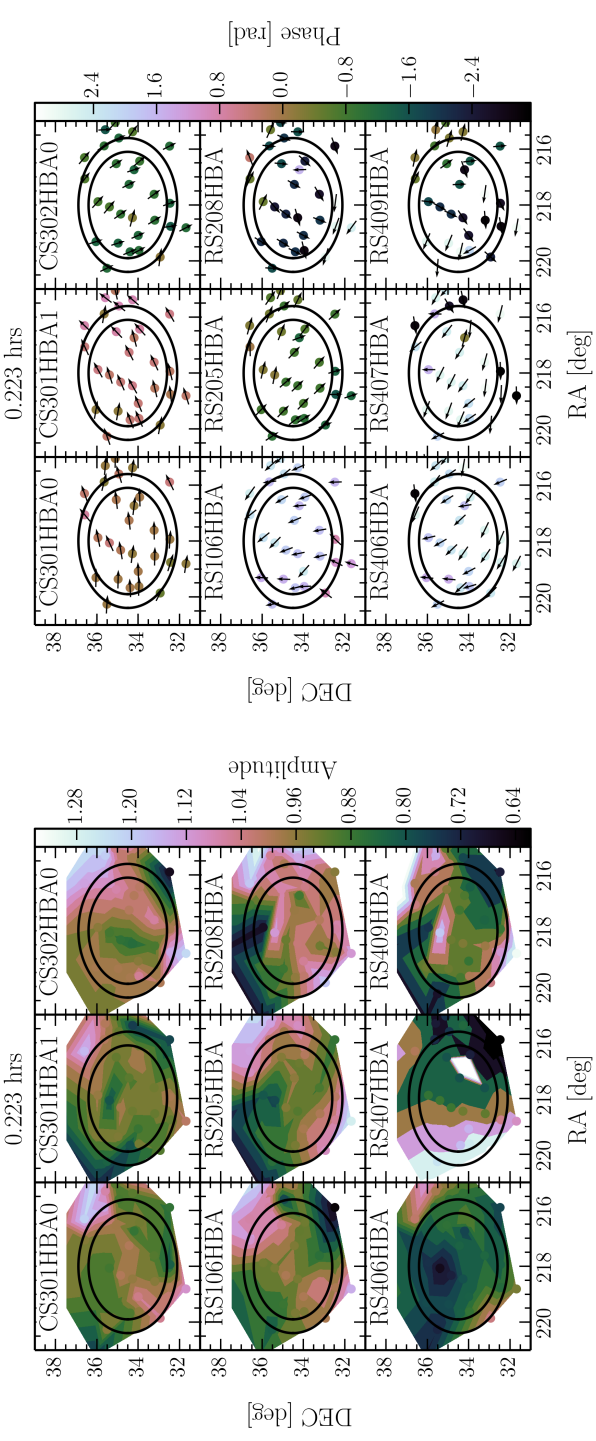


Figure 4.6: Example good DDE solutions for a few selected stations obtained for all directions for a given timestep. Top: XX amplitude solutions for the $160 - 162$ MHz SB block obtained within a particular 10 min time interval. Bottom: The effective Stokes I phase corrections evaluated at an arbitrary frequency of 150 MHz and plotted as an angle. In both plots, the two outer and inner circles show, respectively, the 30 and 50 per cent power points of the average station beam. The solutions are obtained on a timescale of 8 s using 10 MHz of bandwidth. Phases are again plotted with respect to core station CS001HBA0.

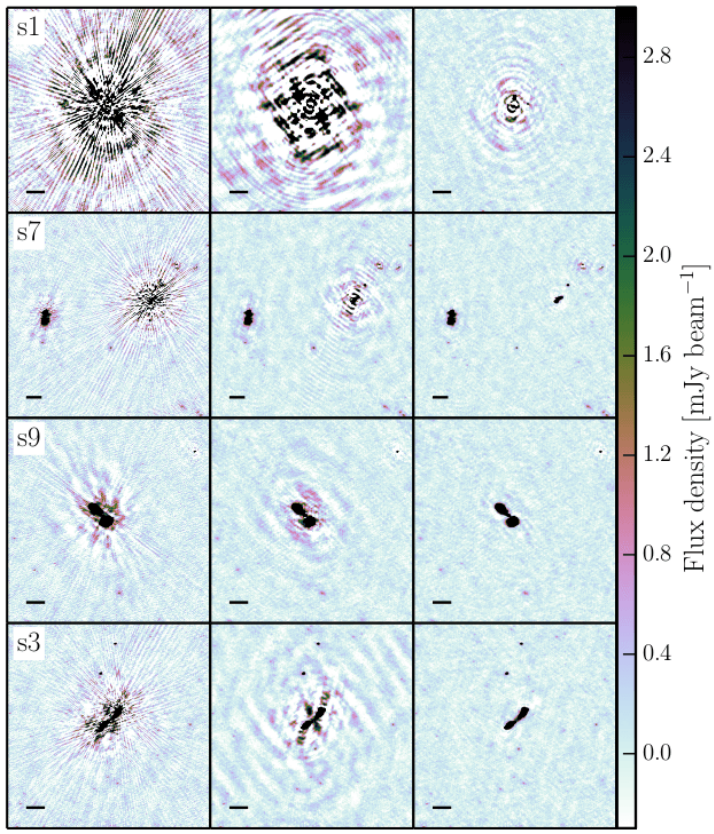


Figure 4.7: Images showing the improvements during the DDE calibration for a few example directions. All images are made using the full dataset ($120-181$ MHz, `nterms` $= 2$, `robust` $= -0.25$) and have a resolution of 5.6×7.4 arcsec. Note that at this resolution many of the bright DDE calibrator sources are resolved. The leftmost column shows the initial images made with only the direction-independent self-calibration solutions. The centre column displays the improvements after two iterations of TEC and phase-offset-only DDE calibration step. The right column shows the improvement after the final DDE self-calibration iteration after two further iterations of DDE TEC+phase offset calibration and DDE XX and YY gain (amplitude and phase). For all four directions shown, the TEC+phase offsets were solved for on 8 s time intervals. The XX and YY gains were solved for on 10 min timescales. The scalebar in each image is 1 arcmin.

resolution, which allows the $1/\nu$ dependence of the TEC term to be applied on a channel-to-channel basis. At this point the corrected facet data were averaged 5 times in frequency and 3 times in time (to 0.5 MHz per channel and 24 s) to avoid bandwidth and time smearing within the facet image. Each facet was then imaged with MS-MFS CLEAN with `nterms` $= 2$ over the full $130 - 169$ MHz bandwidth, with a Briggs robust parameter of -0.25, 1.5 arcsec pixels and a uv-minimum of 80 λ. Note that since all facets have different phase centres, their uv coverage differs slightly and so the restoring beams are slightly different. As in Section 4.3.1 we do not use AWIMAGER mainly due to its limitations in imaging beyond the HPBW of the station beam.

Each facet image provided an updated sky model that was then subtracted from the full-resolution data with the corresponding direction-dependent solutions, thereby improving the residual data to which the subsequent facets were added. This process (from Section 4.3.2) was repeated until all facets had been calibrated and imaged. The order in which the facets were handled is determined by the severity of the calibration artefacts in the direction-independent images, which roughly corresponds to the brightness of the calibration groups, so that the directions with the worst artefacts were corrected first and did not influence later directions. After all the facets were calibrated in this way, we re-imaged all the facets. This step removes the artefacts present in the given facet resulting from bright sources in neighbouring facets which had only been calibrated after the given facet. It reduces the rms by a few per cent. This was achieved by adding back the facet sky model to the residual data, applying the relevant directional-dependent solutions, and imaging with the same parameters (using the full $130-169$ MHz bandwidth with `nterms` $= 2$, `robust` $= -0.25$, a pixel-size of 1.5 arcsec, and a uv-minimum of 80 λ). At this point we applied a common restoring beam of 5.6×7.4 arcsec to all the facets; this resolution was chosen as the smallest beam containing all the fitted restoring beam from the individual facets.

The resulting products are (i) high-resolution images of the facets, combined in a single image ('mosaic') covering the full field-of-view, (ii) short-timescale corrections for the phases variation of the ionosphere, and (iii) long-timescale phase and amplitude corrections for the station beams in the directions of each facet.

'Primary beam' correction

CASA was used to image the individual facets so the images are in 'apparent' flux units, with the station beam taken out only in the phase centre. In order to measure real sky fluxes we performed a primary-beam correction to take into account the LOFAR station beam response across the field-of-view. We used AWIMAGER to produce an average primary beam map from all the 20 10-SB datasets, using the same Briggs weighting (`robust` $= -0.25$), but with much larger pixels (5.5 arcsec), and imaging out to where the average station beam power drops to 20 per cent (approximately 6.2° in diameter). We corrected the combined 'mosaic' image by dividing by the regridded AWIMAGER average primary beam map[1]. We imposed a 'primary beam' cut where the average primary beam power drops below 40 per cent, at an approximate radius of 2.44°, which results in an image covering a total area of $\approx 19\,\mathrm{deg}^2$.

4.4 Final Image and Catalogue

The combined 'mosaic' image at 5.6×7.4 arcsec resolution is shown in Fig. 4.8. The central rms noise level is relatively smooth and $\lesssim 125\,\mu\mathrm{Jy\,beam}^{-1}$, and 50 per cent of the map is at

[1]The actual average primary beam map used is the square root of the AWIMAGER output.

a noise level below $180\,\mu\mathrm{Jy\,beam^{-1}}$ (see also Fig.4.11). A small portion of the image covering the inner $0.25\,\mathrm{deg^2}$ is shown in Fig. 4.9 to illustrate the resolution and quality of the map. There remain some phase artefacts around the brightest sources (see for example the source in the lower right of the image in Fig. 4.9), which have not been entirely removed during the facet calibration; however, these are localised around the bright sources. Fig. 4.10 shows a comparison between the 153 MHz GMRT image, the LOFAR $148 - 150$ MHz direction-independent self-calibration image (see Section 4.3.1) and the final $130 - 169$ MHz direction-dependent calibrated image for three arbitrary positions. This serves to illustrate the significant improvement in both noise and resolution achieved with the new LOFAR observations over the existing GMRT data, which has an rms noise level of $\approx 3\,\mathrm{mJy\,beam^{-1}}$ and resolution of 25 arcsec.

4.4.1 Source Detection and Characterisation

We compiled a source catalogue using PyBDSM (Mohan & Rafferty 2015) to detect and characterise sources. We ran PyBDSM separately on each facet image, using the pre-beam-corrected image as the detection image and the primary beam-corrected image as the extraction image. The rms map was determined with a sliding box `rms_box` $= (160, 50)$ pixels (i.e. a box size of 160 pixels every 50 pixels), with a smaller box `rms_box` $= (60, 15)$ pixels in the regions around bright sources (defined as having peaks exceeding 150σ). Using a smaller box near bright sources accounts for the increase in local rms as a result of calibration aretefacts. For source extraction we used `thresh_pix` $= 5\sigma$ and `thresh_isl` $= 3\sigma$ (i.e. the limit at which flux is included in the source for fitting). Fig. 4.11 illustrates the variation in rms noise thus determined across the combined 'mosaic' image.

PyBDSM fits each island with one or more Gaussians, which are subsequently grouped into sources. We used the `group_tol` parameter with a value of 10.0 to allow larger sources to be formed. This parameter controls how Gaussians within the same island are grouped into sources; the value we chose is a compromise between selecting all Gaussians in a single island as a single source, thus merging too many distinct nearby sources, and selecting them as separate sources, thus separating the radio lobes belonging to the same radio source. Sources are classified as 'S' for single sources and 'M' for multiple-Gaussian sources. PyBDSM reports the fitted Gaussian parameters as well as the deconvolved sizes, computed assuming the image restoring beam. Uncertainties on the fitted parameters are computed following Condon (1997). The total number of sources detected by PyBDSM in all the facets is 5 652 comprised of 10 771 Gaussian components of which 3 010 were single-component sources. We allowed PyBDSM to include sources that were poorly fitted by Gaussians; these sources are included in the catalogue with the integrated flux density being the total flux density within the source island and flagged as having poor Gaussian fits. Additionally, based on visual inspection, 49 sources were flagged as artefacts near bright sources, or false detections, or detections on the edge of the image. We also identified and flagged sources lying on the facet boundaries as these lie in two facets and may have corrupted fluxes because their CLEAN components were added back in separate facet images.

4.4.2 Astrometric and Flux Density Uncertainties

In this section we evaluate the uncertainties in the measured LOFAR flux densities and positions. For both the flux densities and positions we make corrections to the catalogue we present in Section 4.4.5, to account for systematic effects.

Given the uncertainties in the low-frequency flux density scale (e.g. Scaife & Heald 2012)

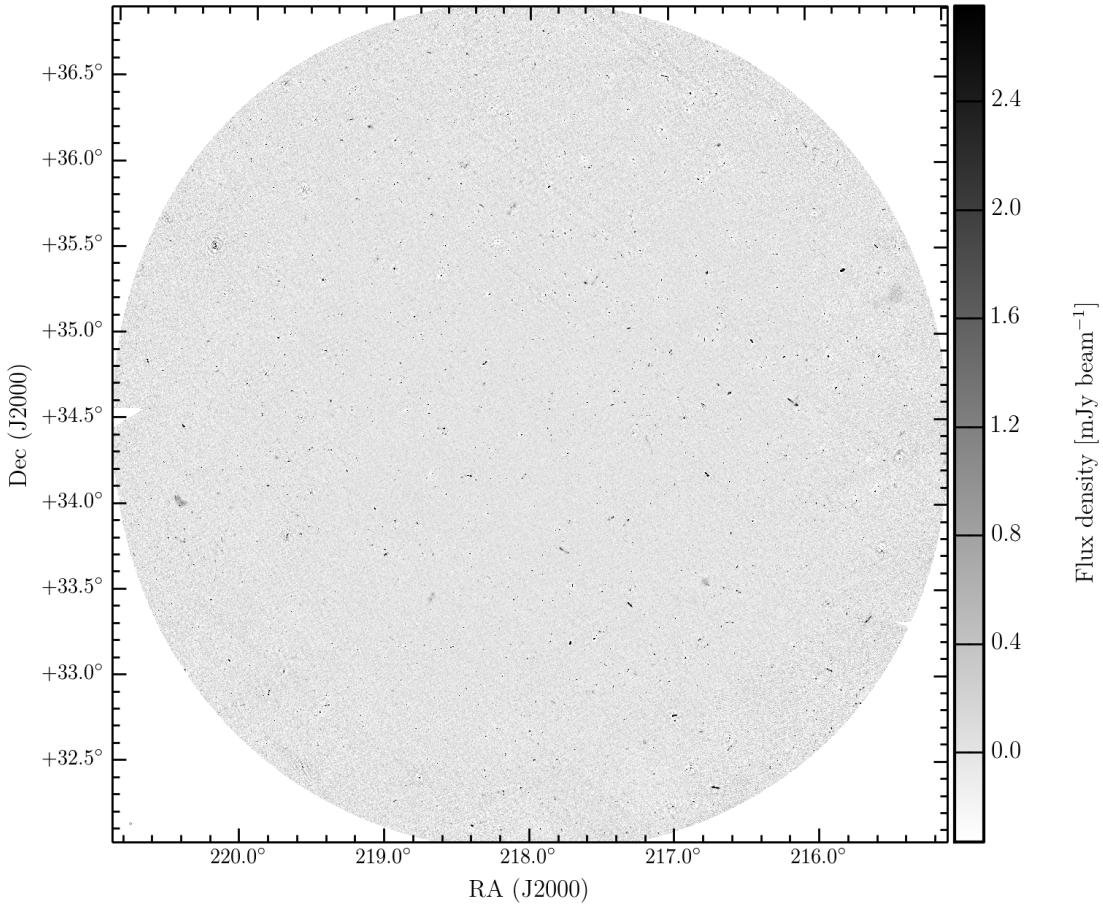


Figure 4.8: Greyscale map showing the entire mosaic. The image covers $\approx 19\,\mathrm{deg}^2$. The greyscale shows the flux density from $-3\sigma_{\mathrm{cen}}$ to $25\sigma_{\mathrm{cen}}$ where $\sigma_{\mathrm{cen}} = 110\,\mu\mathrm{Jy\,beam}^{-1}$ is the approximate rms in the mosaic centre.

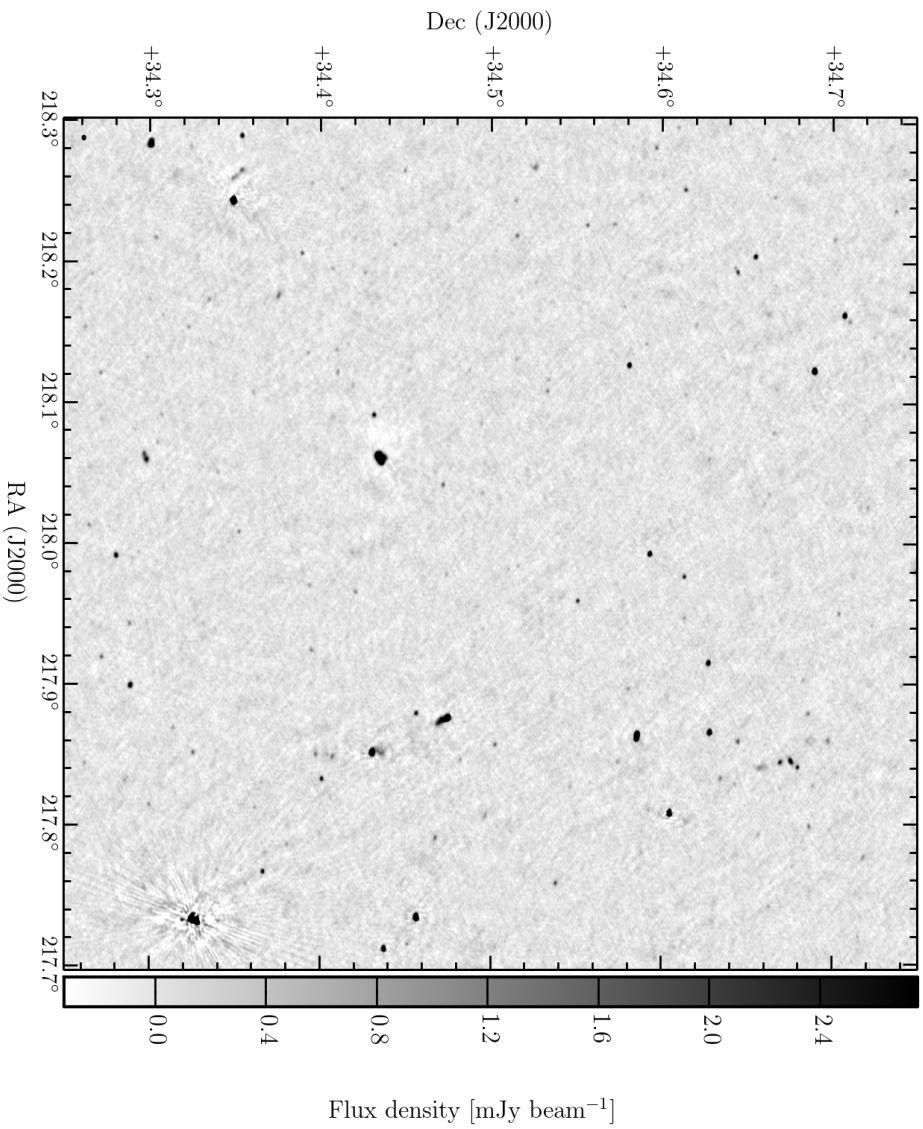


Figure 4.9: Zoom-in of the central part of the mosaic. The image covers $0.25\,\mathrm{deg}^2$. The greyscale shows the flux density from $-3\sigma_{\mathrm{cen}}$ to $25\sigma_{\mathrm{cen}}$ where $\sigma_{\mathrm{cen}} = 110\,\mu\mathrm{Jy\,beam}^{-1}$ is the approximate rms in the mosaic centre.

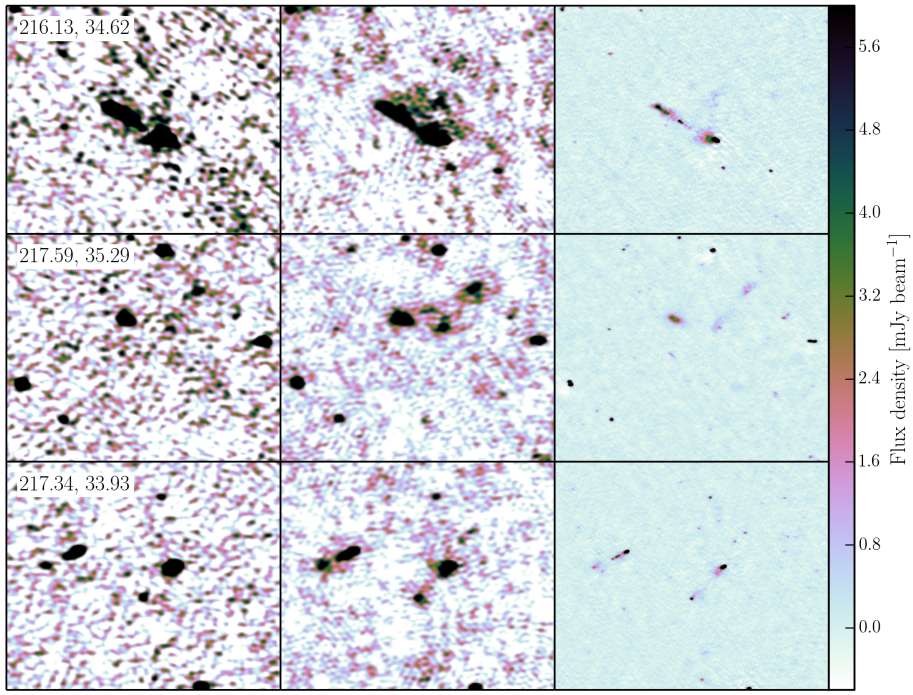


Figure 4.10: Images showing a comparison between a few random sources in the GMRT image (*left* column), the LOFAR $148 - 150$ MHz direction-independent self-calibration image (*centre* column, see Section 4.3.1) and the final $130 - 169$ MHz direction-dependent calibrated image (*right* column). The noise in the three images is respectively ≈ 3, ≈ 1 and ≈ 0.15 mJy beam^{-1} and the resolution is 25, 20 and 5.6×7.4 arcsec respectively. Each image is 15 arcmin on a side. The image centre J2000 coordinates (right ascension and declination) are shown in degrees in the top left of each row and they are all plotted on the same colourscale.

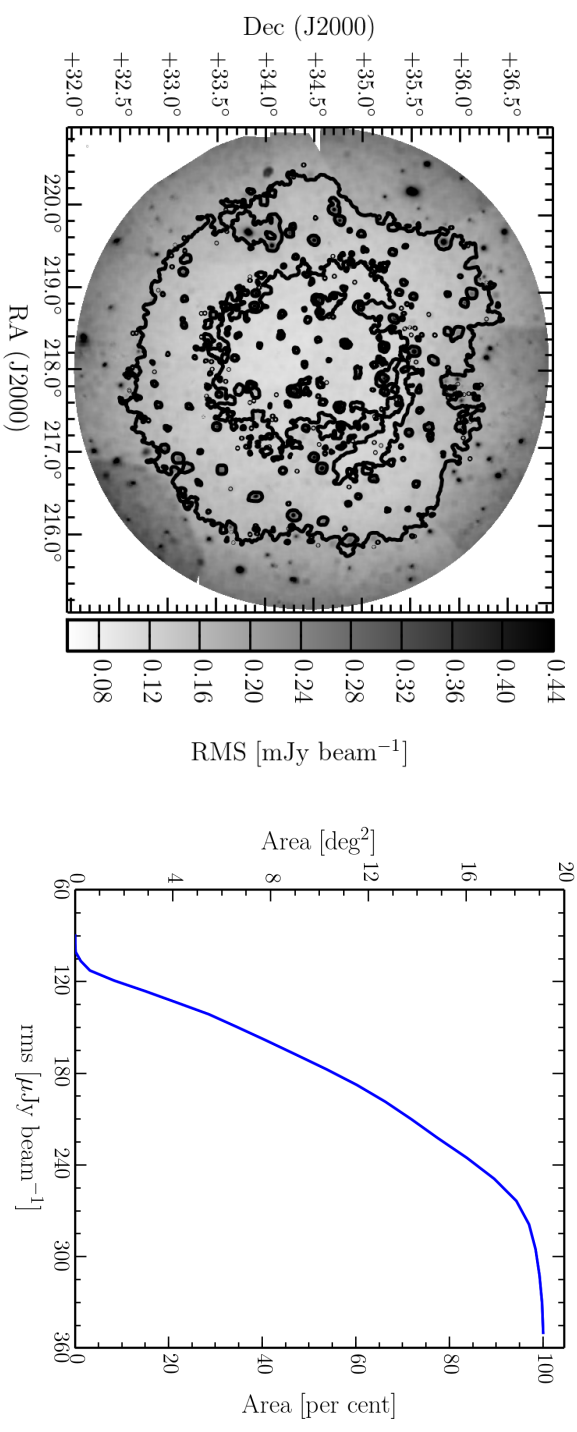


Figure 4.11: Left: Greyscale map showing the local rms noise measured in the mosaic image. The greyscale shows the rms noise from $0.5\sigma_{\rm cen}$ to $4\sigma_{\rm cen}$, where $\sigma_{\rm cen} = 110\,\mu$Jy beam^{-1} is the approximate rms in the mosaic centre. The contours are plotted at $125\,\mu$Jy beam^{-1} and $175\,\mu$Jy beam^{-1}. Peaks in the local noise coincide with the locations of bright sources. Right: Cumulative area of the map with a measured rms noise level below the given value.

and the LOFAR station beam models, we may expect some systematic errors in the measured LOFAR flux densities. In order to determine any systematic offsets we have compared the LOFAR flux densities to those of the GMRT image of the Boötes field at 153 MHz (Williams et al. 2013), selecting only sources detected at high signal-to-noise ($S_{\rm peak}/\sigma > 10$) in both maps. For this sub-sample of 448 sources we determined the ratio of integrated flux densities between LOFAR and the GMRT $f_S = S_{\rm LOFAR}/S_{\rm GMRT}$. We measured a median ratio of $\langle f_S \rangle = 1.04$ with a standard deviation of $\sigma_{f_S} = 0.22$. The flux density ratio showed no significant variation with distance from the phase centre. However we noticed a small variation with position on the sky, plotted in Fig. 4.12. The variation is such that the LOFAR flux densities are slightly higher towards the North-North-West (upper right of the map) and lower towards the South-South-East (lower left of the map). We note that the trend is consistent across different facets so is a result of some global effect and not a result of discrete calibration in facets. Moreover, the trend is similar, but noisier, if we consider LOFAR sources extracted from the self-calibrated-only image from the single 10-SB block at 148–150 MHz. This further suggests that the flux offset is not introduced by the direction dependent calibration procedure. The flux density ratio is plotted as a function of the position angle between the source and the phase centre in Fig. 4.13, to which we fitted a sinusoid of the form $f_S = 1.05 + 0.10\sin(116^\circ + \phi)$. The median ratio was $\langle f_S \rangle = 1.00$ with a standard deviation of $\sigma_{f_S} = 0.20$ after applying this sinusoid function to correct the LOFAR flux densities. This correction assumes that the GMRT flux densities are 'correct'. To evaluate this we performed a similar comparison with sources in the deep 1.4 GHz WSRT catalogue of the Boötes Field (de Vries et al. 2002). Scaling the higher frequency flux densities to 150 MHz with a spectral index of -0.8 we recovered a similar, albeit noisier, trend for the sample of high signal-to-noise LOFAR sources matched to the WSRT sources. This suggests that it is likely not to be GMRT pointing errors causing systematic trends in the GMRT flux densities. We speculate that the observed trend in the flux density errors may be the result of an incorrect primary-beam correction, which itself may be caused by errors in the LOFAR station beam model used in AWImager, or a map projection error. Finally, we assume an overall flux density error of 15 per cent, to account for systematic effects (see also Intema et al. 2011; Williams et al. 2013).

It is possible that errors in the phase calibration can introduce uncertainties in the source positions. We used the 1.4 GHz FIRST catalogue (Becker et al. 1995) to assess the LOFAR positional accuracy. The uncertainty on the FIRST positions is given by $\sigma = s\,(1/SNR + 0.05)$, where s is the source size in arcsec. FIRST counterparts were identified within 2 arcsec of our LOFAR sources with high signal-to-noise ratios, i.e. $S_{\rm peak}/\sigma_{\rm local} > 10$. This yielded 968 matches, of which 313 were fitted with a single Gaussian in the LOFAR image, making them more likely to be point sources. For the high signal-to-noise point source sample, we measured a small mean offset in right ascension of $\Delta\alpha = \alpha_{\rm LOFAR} - \alpha_{\rm FIRST} = -0.062 \pm 0.001$ arcsec, with rms $\sigma_\alpha = 0.43$ arcsec and a somewhat larger mean offset in declination of $\Delta\delta = \delta_{\rm LOFAR} - \delta_{\rm FIRST} = -0.321 \pm 0.002$ arcsec with rms $\sigma_\alpha = 0.55$ arcsec . The offset is negligible and we note that it is within the size of the LOFAR image pixels (1.5 arcsec). However, closer inspection of the offsets showed that the offset in declination varied systematically across the full 5° field-of-view, and to a lesser extent for the offsets in right ascension. A correction for this offset has been made by fitting a plane, $\Delta = a\alpha + b\delta + c$, where Δ is in arcsec, to the offset values and applying the fitted offsets to all sources in the catalogue. While this could be expressed as a rotation and therefore a sinusoidal correction could be made, as we have done for the flux densities, we find that the positional offests are asymmetric with respect to the pointing centre. The fitted planes were $\Delta\alpha = -0.12(\alpha - 218^\circ) + 0.03(\delta - 34.5^\circ) - 0.03$ and $\Delta\delta = 0.13(\alpha - 218^\circ) + 0.30(\delta + 34.5^\circ) - 0.36$. These offsets

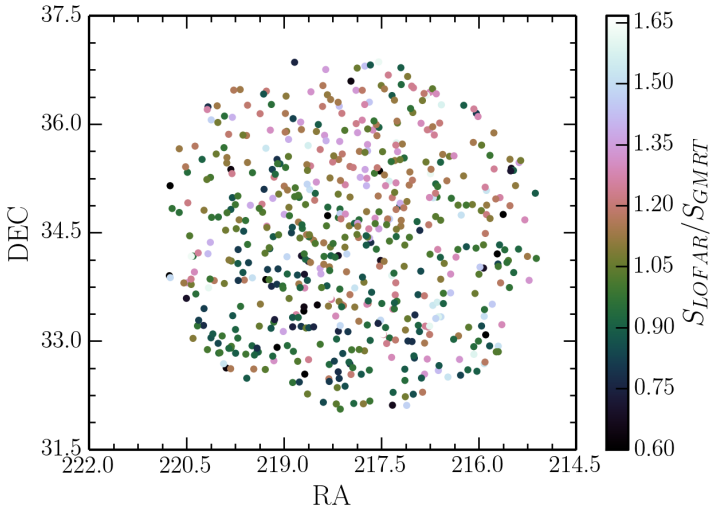


Figure 4.12: Map of the measured ratios of integrated flux densities for high signal-to-noise LOFAR sources with respect to the GMRT. The colourscale shows the the flux density ratio.

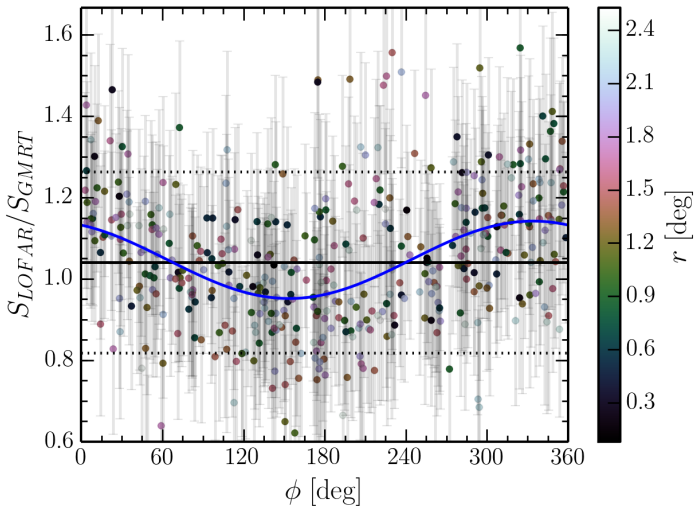


Figure 4.13: Measured ratios of integrated flux densities for high signal-to-noise LOFAR sources with respect to the GMRT as a function of source position angle with respect to the phase centre (plotted as points). The colourscale shows the distance of each source to the pointing centre. The blue curve shows a fitted sinusoid which we used for correcting the positions of the LOFAR catalogued sources. The solid and dashed horizontal lines show the measured median and standard deviation of the flux density ratio.

and functional corrections are shown in Fig. 4.14. After applying this correction we measured $\Delta\alpha = \alpha_{\rm LOFAR} - \alpha_{\rm FIRST} = -0.017 \pm 0.001$ arcsec with rms deviation $\sigma_{\Delta\alpha} = 0.39$ arcsec, and $\Delta\delta = \delta_{\rm LOFAR} - \delta_{\rm FIRST} = -0.007 \pm 0.001$ arcsec, with $\sigma_{\Delta\delta} = 0.38$ arcsec. We note that since the initial phase calibration of the LOFAR data was performed against the GMRT model sky, these positional offsets may originate from the GMRT model. We did evaluate the GMRT positions in a similar way and found no significant variations, but this may be due to the much larger positional uncertainty and the 25 arcsec synthesised beam of the GMRT map. We also consider LOFAR sources extracted from the self-calibrated-only image from the single 10-SB block at 148–150 MHz compared to FIRST and find a similar trend. This suggests that the position offsets are not introduced by the direction dependent calibration procedure. We hypothesise that a map projection or mosaic construction error could be the cause of these offsets, but note that it is a small correction.

The scatter in the offsets between the LOFAR and FIRST positions is a combination of noise-independent calibration errors, ϵ, in both the LOFAR and FIRST data as well as a noise-dependent error, σ, from position determination via Gaussian-fitting:

$$\sigma^2 = \epsilon^2_{\rm LOFAR} + \epsilon^2_{\rm FIRST} + \sigma^2_{\rm LOFAR} + \sigma^2_{\rm FIRST}$$

To separate the noise-dependent and -independent uncertainties we select from the above sample only the FIRST sources with position errors of less than 0.6 arcsec and measure an rms scatter of $(\sigma_\alpha, \sigma_\delta)_{\rm LOFAR} = (0.37\,{\rm arcsec}, 0.35\,{\rm arcsec})$ between the corrected LOFAR and FIRST source positions for this very high signal-to-noise sub-sample of 89 sources. From Becker et al. (1995), the FIRST calibration errors are $(\epsilon_\alpha, \epsilon_\delta)_{\rm FIRST} = (0.05\,{\rm arcsec}, 0.05\,{\rm arcsec})$. The noise-dependent fit errors for both the LOFAR and FIRST can be assumed to be small so we determine the LOFAR calibration errors to be $(\epsilon_\alpha, \epsilon_\delta)_{\rm LOFAR} = (0.37\,{\rm arcsec}, 0.35\,{\rm arcsec})$. This scatter may contain a small contribution resulting from any spectral variation between 150 and 1400 MHz on scales smaller than the resolution of the surveys (≈ 5 arcsec).

4.4.3 Reliability

The reliability of a source catalog indicates the probability that all sources above a given flux density are real. It is defined as the fraction of all detected sources in the survey area above a certain total flux density limit that are real sources and are not accidental detections of background features or noise. To estimate the reliability, we extracted sources from the inverted residual mosaic image, assuming that negative image background features are statistically the same as positive ones. We grouped the detected negative 'sources' by total flux density into 20 logarithmic flux density bins and compare these to the binned results of the regular (positive) source extraction as described in Section 4.4.1. For convenience, we define the real number of sources to be the number of positive sources minus the number of negative sources.

The left panel of Fig. 4.15 shows the false detection rate, FDR, determined from the number ratio of negative sources over positive sources per flux density bin. The right panel shows the reliability curve, $R = 1 - FDR$, determined from the number ratio of real sources over positive sources above the total flux density limits that define the lower edges of the flux density bins. For a 1 mJy total flux density threshold, the reliability is 90 per cent.

4.4.4 Resolved Sources

In the absence of noise, resolved sources can easily be identified based on the ratio of the integrated flux density to the peak flux density, $S_{\rm int}/S_{\rm peak} > 1$. However, since the uncertainties

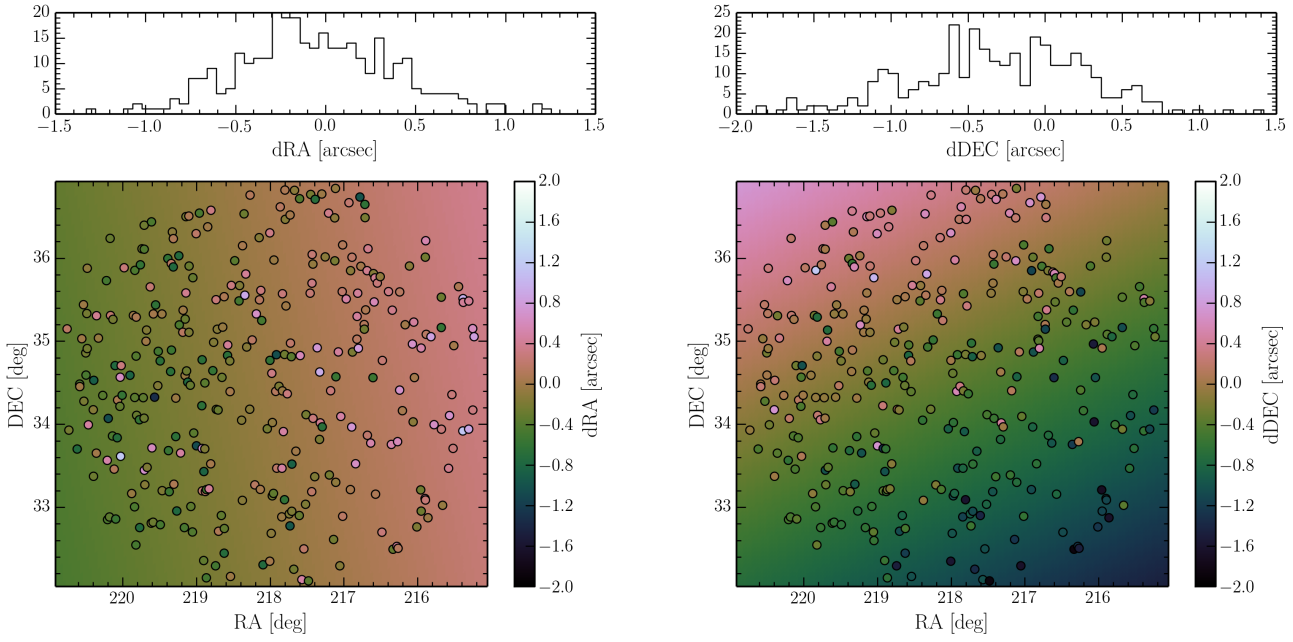


Figure 4.14: Measured offsets in right ascension (left) and declination (right) for high signal-to-noise sources of LOFAR with respect to FIRST (plotted as points). The colourscale shows the value of the given offset. The top panels show the distribution of the offsets. The offsets, particularly in declination, show a variation across the field-of-view. The background colourscale shows a fitted plane used for correcting the LOFAR catalogued sources.

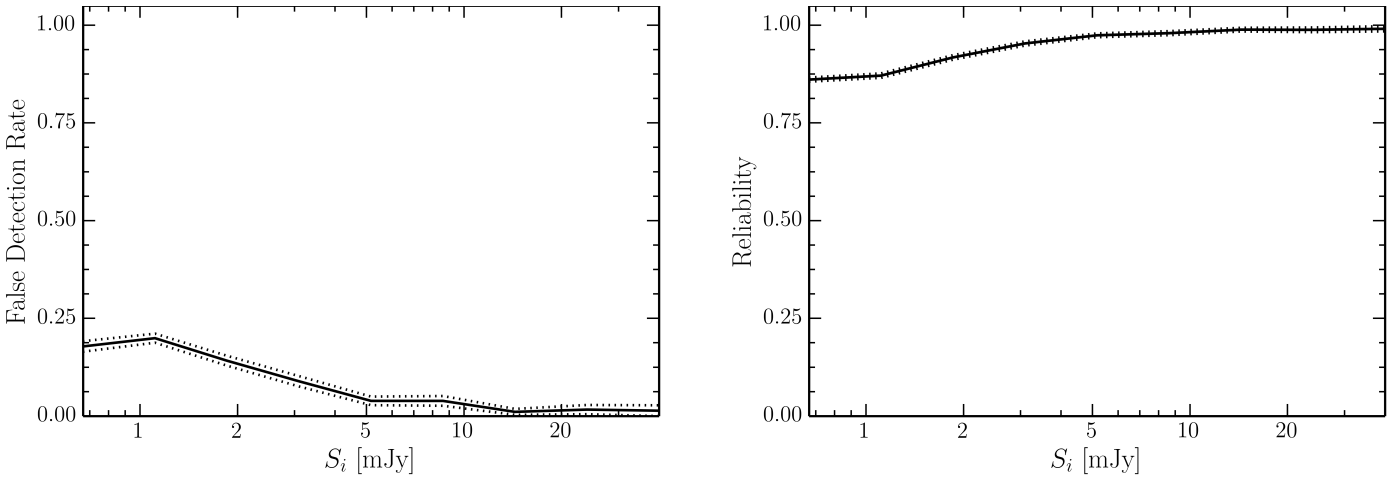


Figure 4.15: *Left* False detection rate as a function of peak flux density to local signal-to-noise ratio calculated from source detection on an inverted residual map. *Right* Estimated reliability of the catalogue as a function of integrated flux density limit accounting for the varying sensitivity across the field-of-view.

on $S_{\rm int}$ and $S_{\rm peak}$ are correlated, the $S_{\rm int}/S_{\rm peak}$ distribution is skewed, particularly at low signal-to-noise. The flux density ratio as a function of signal-to-noise is shown in Fig. 4.16. We note that the scatter that we observe is large and skewed towards values > 1. This is in some part due to the effects of bandwidth- and time-smearing, which both reduce the peak flux densities of sources as a function of distance from the phase centre. Given the fact that the data were phase-shifted to the facet centres and averaged further, there may be additional smearing within the facet images. However, both the images and the time and frequency averaging are small enough that this should not be significant. Given the averaged channel, time and imaging resolution, we estimate (using the equations given by Bridle & Schwab 1989) the combined effect of bandwidth and time smearing due to the averaging in the full dataset to be of the order of 74 per cent (i.e. measured peak flux densities at 74 per cent of the expected value) at the edge of our field at 2.4°. Our empirical estimate for the correction factor for each source due to the combined effect is included in the source catalogue. While the traditional way of estimating this is to perform a Monte Carlo simulation in which fake sources are added to the uv-data and before calibration, this involves significant computational time and so has not been done here.

The effect of noise on the total-to-peak flux density ratios as a function of signal-to-noise can be determined by running complete simulations in which artificial sources are injected into the real data and imaged and detected in the same way as the observed data. However this requires re-running the full calibration and imaging routine, which we have not yet done due to computational constraints. Alternatively, it is common practice to determine a lower envelope, or flux-varying limit, above which a given fraction of sources lie and reflect it to obtain an upper envelope above which sources can be classified as resolved. In this case there is more scatter with $S_{\rm int} > S_{\rm peak}$, likely due to a further smearing effect which we have not accounted for. This may be a result of uncorrected residual phase errors away from the calibrator directions. We note though that the integrated flux densities are still correct – see Section 4.4.2. Thus, in preference to fitting a lower envelope, we have identified by eye a conservative upper envelope, defined by $S_{\rm int}/S_{\rm peak} > 1.25 + 250/SNR^{2.7}$, where $SNR = S_{\rm peak}/\sigma$, and classified 1 158 sources above this envelope as resolved.

We have identified 187 large extended sources by visual inspection of the images. These sources span sizes (largest angular size, LAS) of ≈ 20 arcsec to ≈ 250 arcsec. The largest (LAS$>$ 45 arcsec) of these sources are presented in Fig. 4.A.1 in the Appendix. In the cases of the largest sources these can appear as separate sources within our catalogue because the emission from the lobes of these giant radio galaxies is not contiguous.

Many diffuse extended sources are also clearly visible in the facet images. These sources can be missed as their peak flux densities fall below the detection threshold. We identifed four very clear large diffuse sources – see Fig. 4.A.2 in the Appendix. A full study of diffuse emission is deferred to a subsequent paper, as this will require re-imaging of the facets with optimized parameters.

4.4.5 Source Catalogue

The final catalogue consists of 5 652 sources with flux densities between 0.4 mJy and 5 Jy and is available as part of the online version of this article. The astrometry in the catalogue has been corrected for the systematic offset described in Section 4.4.2. Both the integrated and peak flux densities in the catalogue have been corrected for the systematic offset (Section 4.4.2). Resolved sources are identified as described in Section 4.4.4. A sample of the catalogue is shown in Table 4.2 where the columns are:
Column (1) – IAU Source name,

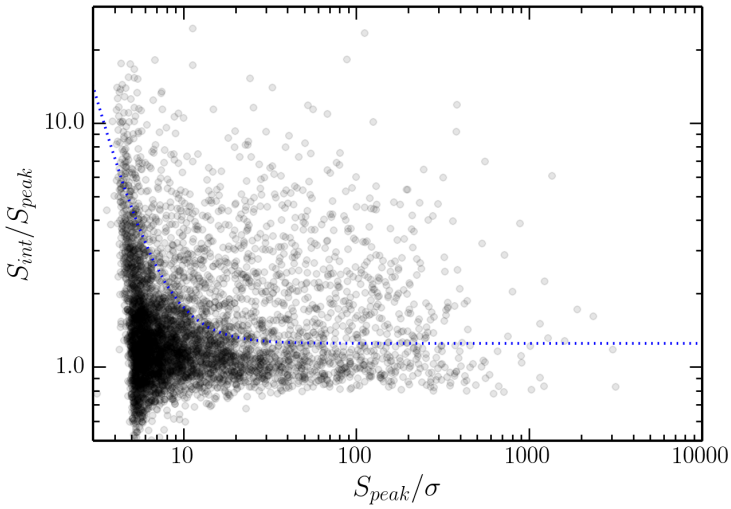


Figure 4.16: The measured ratio of integrated to peak flux density as a function of signal-to-noise ratio. The dotted blue line shows the conservative upper envelope identified by eye above which sources are likely to be fully resolved.

Columns (2) and (3) – flux-weighted right ascension (RA) and uncertainty,
Columns (4) and (5) – flux-weighted declination (DEC) and uncertainty,
Column (6) – integrated source flux density and uncertainty,
Column (7) – peak flux density and uncertainty,
Column (8) – approximate correction factor to the peak flux density to account for bandwidth- and time-smearing,
Column (9) – the local rms noise used for the source detection,
Column (10) – number of Gaussian components,
Column (11) – Flag indicating the resolved parameterisation of the source. 'U' refers to unresolved sources and 'R' to resolved sources.

4.5 Results

In this section, we report two results based on the LOFAR catalogue: the spectral indices between 150 and 1400 MHz, and the 150 MHz faint source counts. Further analysis of these data will be presented in future publications.

4.5.1 Spectral Index Distributions

We use the deep WSRT 1.4 GHz data covering the Boötes Field (de Vries et al. 2002) to calculate spectral indices between 150 MHz and 1.4 GHz, α_{150}^{1400}, the distribution of which is shown in Fig. 4.17. The WSRT map has a resolution of 13×27 arcsec, so some sources appear as separate sources in the LOFAR map but are identified as single sources in the WSRT image. To exclude erroneous spectral indices derived for such sources, we limit this selection to sources that are not

Table 4.2: Sample of the LOFAR 153 MHz source catalogue.

Source ID	RA	σ_{RA}	DEC	σ_{DEC}	$S_{\rm int}$	$S_{\rm peak}$	F_{smear}	rms	Gaussians	Resolved
	[deg]	[arcsec]	[deg]	[arcsec]	[mJy]	[mJy beam^{-1}]		[mJy beam^{-1}]		
(1)	(2)	(3)	(4)	(5)	(6)	(7)	(8)	(9)	(10)	(11)
J143506.04+363241.0	218.78	0.49	36.54	0.56	4.25 ± 0.75	1.74 ± 0.26	1.30	0.19	4	U
J143302.77+341853.1	218.26	2.20	34.31	1.08	4.25 ± 0.44	0.56 ± 0.11	1.00	0.12	1	R
J143635.58+334506.5	219.15	0.71	33.75	0.53	4.24 ± 0.49	1.04 ± 0.17	1.09	0.13	2	R
J143126.36+344109.8	217.86	1.51	34.69	1.36	4.24 ± 0.44	0.49 ± 0.11	1.00	0.12	1	R
J142244.06+354749.5	215.68	0.45	35.80	0.45	4.24 ± 0.78	2.75 ± 0.35	1.36	0.22	3	U
J143504.13+354743.8	218.77	0.45	35.80	0.47	4.24 ± 0.55	2.17 ± 0.26	1.13	0.14	3	R
J142730.62+334120.5	216.88	0.47	33.69	0.42	4.24 ± 0.47	2.80 ± 0.31	1.09	0.13	1	U
J143037.25+324208.2	217.66	1.20	32.70	1.73	4.24 ± 0.46	0.82 ± 0.18	1.21	0.17	1	U
J142737.16+344313.8	216.90	0.42	34.72	0.44	4.24 ± 0.51	3.13 ± 0.34	1.05	0.12	2	U
J143415.72+352456.8	218.57	0.53	35.42	0.49	4.24 ± 0.48	1.93 ± 0.25	1.06	0.15	1	R

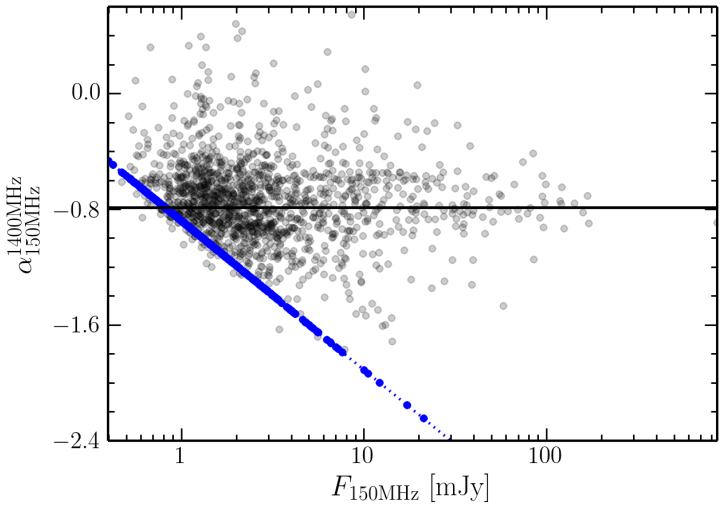


Figure 4.17: Spectral index, α_{153}^{1400}, distribution of sources matched between 1.4 GHz and 153 MHz (points). The difference in resolution is 13×27 arcsec (WSRT) and 5.6×7.4 arcsec (LOFAR). The blue points show upper limits to the spectral index for LOFAR sources which do not have a higher frequency counterpart. The horizontal line shows the median spectral index of -0.79 determined using LOFAR sources with flux densities greater than 2 mJy.

identified as extended in either the LOFAR or WSRT catalogues and that do not have multiple matches within a 30 arcsec search radius.

Using LOFAR sources with flux densities greater than 2 mJy, we find a median spectral index between 1400 and 153 MHz of -0.79 ± 0.01 and scatter of $\sigma = 0.30$ which is consistent with previously reported values: -0.87 ± 0.01, (Williams et al. 2013), -0.79 (Intema et al. 2011), -0.78 (Ishwara-Chandra et al. 2010), -0.82 (Sirothia et al. 2009), and -0.85 (Ishwara-Chandra & Marathe 2007). A detailed spectral-index analysis using the other available radio data is deferred to later works.

4.5.2 Source Counts

We used the LOFAR catalogue to compute the 150 MHz source counts down to $\approx$ 1 mJy. This is at least an order of magnitude deeper than previously studied at these low frequencies (e.g. McGilchrist et al. 1990; Intema et al. 2011; Williams et al. 2013). The source counts are computed using the integrated flux densities, but sources are detected based on their *measured* peak flux density over the local noise level. Thus, the completeness of the source counts depends both on the variation of the noise in the image and on the relation between integrated and peak flux densities. The latter is dependant both on systematic effects (e.g. smearing) and the intrinsic relation between integrated and peak flux densities of radio sources due to their intrinsic sizes. In the following paragraphs we discuss these effects and how we correct for them in deriving the source counts.

Visibility Area

Due to the large variation in rms across the single pointing image (see Fig. 4.11), sources of different flux densities are not uniformly detected across the image, i.e. faint sources can only be detected in a smaller area in the inner part of the image. Moreover, smearing causes a reduction in peak flux density while conserving the integrated flux density, and the amount of smearing depends on the distance to the phase-centre. We have noted already the effect of bandwidth- and time-smearing (see Section 4.4.4) and use the equations given by Bridle & Schwab (1989) to calculate an approximate correction to the peak flux density of each source based on its position in the map. The maximal correction is at most $S^{\rm meas}_{\rm peak} \approx 0.74 S^{\rm corr}_{\rm peak}$, so sources with *corrected* peak flux densities $> 6.7\sigma$ will have effective measured peak flux densities above the 5σ detection threshold. We therefore select only sources based on this threshold for deriving the source counts. To correct for the varying rms, we weight each source by the reciprocal of the area in which it can be detected, its visibility area, (e.g. Windhorst et al. 1985), based on its smearing-corrected peak flux density value. This also accounts for the varying detection area within a given flux-density bin.

Systematic Effects

Another effect that could potentially influence both the peak and integrated flux densities is CLEAN bias, which could bias both downwards at the lowest flux levels, thus leading to low source counts. However, we expect this to be negligible because the use of masks in the imaging and good uv-coverage should minimise the CLEAN bias. In general, noise can scatter sources into adjacent bins, again most noticeably at low flux densities. A positive bias is introduced by the enhancement of weak sources by random noise peaks (Eddington bias; Eddington 1913). Both of these effects could be quantified by simulations, but our source counts are not corrected for them, due to the computational expense of running the full required simulation.

Resolution Bias

A resolved source of a given integrated flux density will be missed by the peak-flux-density selection more easily than a point source of the same integrated flux density. This incompleteness is called the resolution bias and to make a correction for it requires some knowledge of the true angular size distribution of radio sources. We have estimated a correction for the resolution bias following Prandoni et al. (2001). First we calculate the approximate maximum size $\theta_{\rm max}$ a source could have for a given integrated flux density before it drops below the peak-flux detection threshold. Fig. 4.18 shows the angular size of the LOFAR sources. We use the relation

$$\frac{S_{\rm int}}{S_{\rm peak}} = \frac{\theta_{\rm min}\theta_{\rm max}}{b_{\rm min}b_{\rm max}},$$

where $b_{\rm min}$ and $b_{\rm max}$ are the synthesized beam axes and $\theta_{\rm min}$ and $\theta_{\rm max}$ are the source sizes, to estimate the maximum size a source of a given integrated flux density can have before dropping below the peak-flux detection threshold. Given this $\theta_{\rm max}$ we estimate the fraction of sources with angular sizes larger than this limit using the assumed true angular size distribution proposed by Windhorst et al. (1990): $h(> \theta_{\rm lim}) = \exp[-\ln 2(\theta_{\rm lim}/\theta_{\rm med})^{0.62}]$ with $\theta_{\rm med} = 2S^{0.30}_{1.4\,\rm GHz}$ arcsec (with S in mJy; we have scaled the $1.4\,$GHz flux densities to $150\,$MHz with a spectral index of -0.8). We have also calculated the correction using $\theta_{\rm med} = 2$ arcsec for sources with $S_{1.4\,\rm GHz} <$

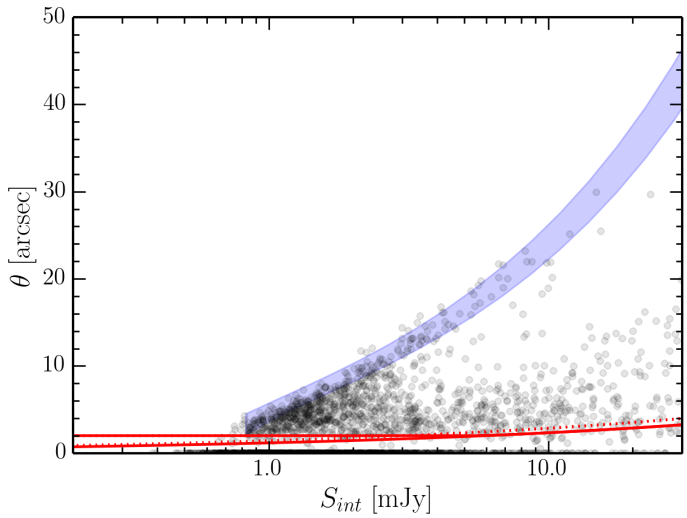


Figure 4.18: Angular size, θ (geometric mean), for the LOFAR sources as a function of integrated flux density. The blue shaded region shows the range of maximum size ($\theta_{\rm max}$) a source of a given integrated flux density can have before dropping below the peak-flux detection threshold (the range reflects the range of rms noise in the LOFAR map). The red lines show the two functions used for the median angular size ($\theta_{\rm med}$) as a function of integrated flux density.

1 mJy (see Windhorst et al. 1993; Richards 2000). The resolution bias correction $c = 1/[1 - h(> \theta_{\rm max})]$ is plotted in Fig. 4.19 for the two different assumed distributions. In correcting the source counts we use an average of the two functions. We use the uncertainty in the forms of $\theta_{\rm med}$ and in $\theta_{\rm lim}$ to estimate the uncertainty in the resolution bias correction. We further include a overall 10 per cent uncertainty following Windhorst et al. (1990). While we have used the extrapolated Windhorst et al. (1990) size distribution from 1.4 GHz to correct the source counts persented here, we note that the observed size distribution (see Appendix 4.B) suggests that the low frequency emission is more extended. Thus the real resolution bias correction factor is likely to be somewhat larger, particularly in the lowest flux density bins, and may explain the turndown in source counts (see Fig. 4.20). A full study of the true low frequency angular size distrubution of radio sources is beyond the scope of this paper.

Complex Sources

The source counts need to be corrected for multi-component sources, i.e. cases where the radio-lobes are detected as two separate sources. The flux densities of physically related components should be summed together, instead of counted as separate sources. We use the method described in White et al. (2012) and Magliocchetti et al. (1998) to identify the double and compact source populations. This is done by considering the separation of the nearest neighbour of each component and the summed flux of the component and its neighbour. Pairs of sources are regarded as single sources if the ratio of their flux densities is between 0.25 and 4, and their separation is

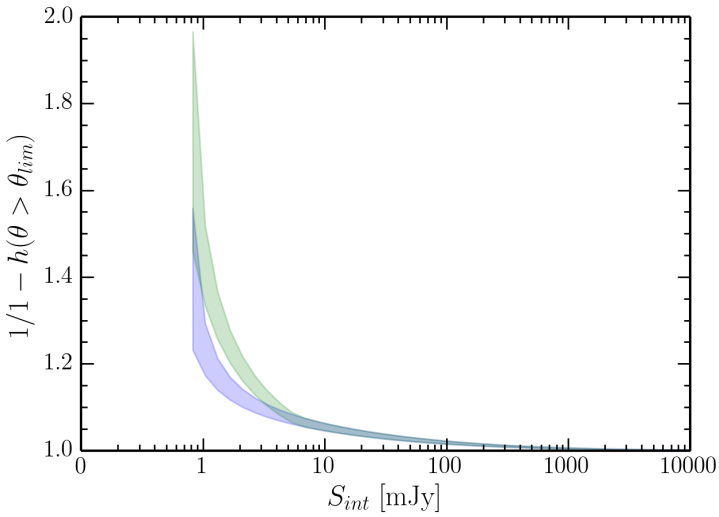


Figure 4.19: Resolution bias correction $1/[1 - h(> \theta_{\rm lim})]$ for the fraction of sources with angular size larger than $\theta_{\rm max}$ at a given integrated flux density. For the faintest sources two curves are shown: the blue curve shows $\theta_{\rm med}$ as a function of $S_{\rm int}$ and the green curve shows the result assuming $\theta_{\rm med} = 2$ arcsec at these flux densities (the range of each reflects the range of rms noise in the LOFAR map).

less than a critical value dependent on their total flux density, given by

$$\theta_{\rm crit} = 100 \left[\frac{S}{10}\right]^{0.5},$$

where S is in mJy and θ is in arcsec. Approximately 460 sources in the sample used for calculating the source counts, or 8.5 per cent, are considered to be a part of double or multiple sources for the source count calculation.

The Low-Frequency mJy Source Counts

The Euclidean-normalized differential source counts are shown in Fig. 4.20. Uncertainties on the final normalised source counts are propagated from the errors on the correction factors and the Poisson errors (Gehrels 1986) on the raw counts per bin. Table 4.3 lists (1) the flux density bins, (2) the central flux density of the bin, (3) the raw counts, (4) the effective detection areas for sources at the lower and upper limits of the flux density bin where they are different, (5) the effective area corresponding to the bin centre, (6) the mean weight of the sources in the bin, (7) the resolution bias correction factor, and (8) the corrected normalised source counts.

Model source counts have been derived by Wilman et al. (2008) for the 151 MHz and 610 MHz source populations predicted from the extrapolated radio luminosity functions of different radio sources in a ΛCDM framework. We show the source counts for both AGN and star-forming (SF) galaxies on Fig. 4.20. The Wilman et al. (2008) model catalogue has been corrected with their recommended default post-processing, which effectively reduces the source count slightly at low flux densities. At low flux densities it is likely that the Wilman et al. (2008)

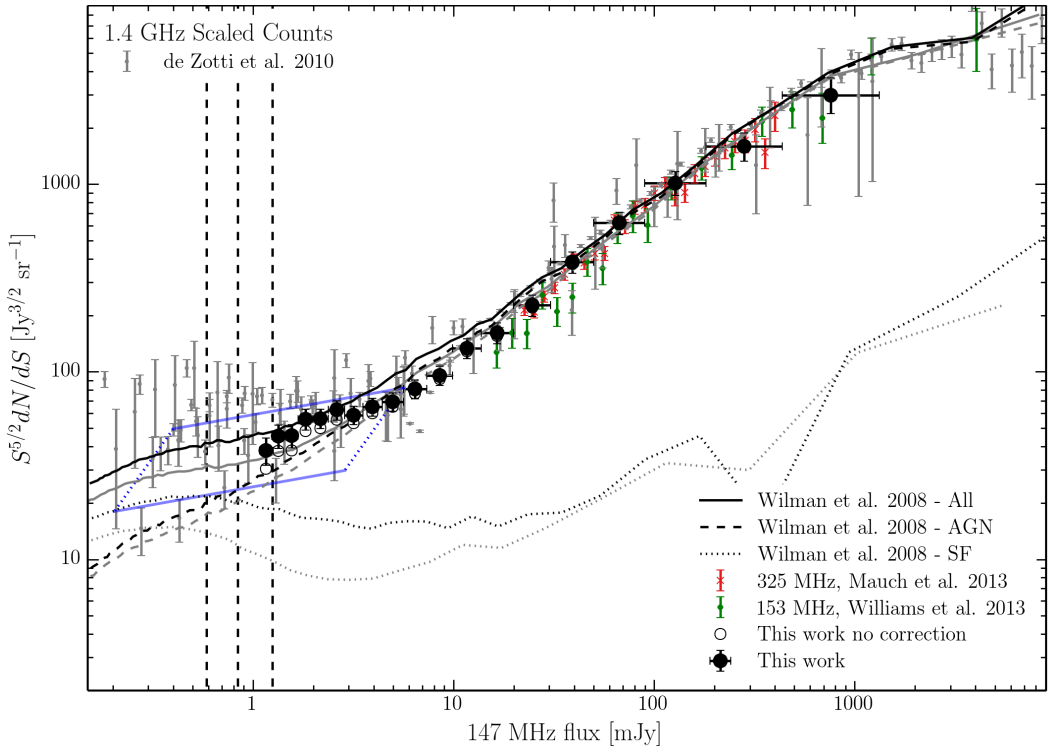


Figure 4.20: Euclidean-normalized differential source counts for the LOFAR 153 MHz catalogue (filled black circles) between 1 mJy and 5 Jy. Open black circles show the sources counts without the resolution bias correction. For comparison we plot the SKADS model counts (Wilman et al. 2008) separated into AGN and SF for 151 MHz (in grey) and scaled from 610 MHz (in black). We show also the measured 153 MHz source counts (Williams et al. 2013) (in green) and scaled from 325 MHz (Mauch et al. 2013) (in red). Additionally, we have included several source counts determinations from 1.4 GHz from the compilation of de Zotti et al. (2010) scaled down to 150 MHz assuming a spectral index of -0.8 (grey points). The blue lines at the low flux density end show how the higher frequency counts would scale if a flatter spectral index of -0.5 was used, i.e. the tail of the source counts would lie further down and to the left in the plot. The vertical dashed lines show the minimum integrated flux density at which a point source could be detected in 10, 50 and 90 per cent of the map.

Table 4.3: Euclidean-normalized differential source counts for the LOFAR 150 MHz catalogue.

S Range [mJy] (1)	S_c [mJy] (2)	Raw Counts (3)	Area [deg^2] (4)	$A(S_c)$ [deg^2] (4)	$\langle W \rangle$ (5)	Correction (6)	Normalised counts [Jy$^{3/2}$ sr^{-1}] (7)
$1.13 - 1.31$	1.22	284^{+18}_{-17}	$14.43 - 17.25$	15.85	1.84	1.3 ± 0.3	32^{+1}_{-1}
$1.31 - 1.52$	1.41	314^{+19}_{-18}	$17.25 - 18.80$	18.33	1.49	1.2 ± 0.2	34^{+1}_{-1}
$1.52 - 1.78$	1.65	365^{+20}_{-19}	$18.80 - 19.17$	19.06	1.54	1.2 ± 0.2	47^{+1}_{-1}
$1.78 - 2.11$	1.94	374^{+20}_{-19}	$19.17 - 19.24$	19.22	1.29	1.2 ± 0.2	47^{+2}_{-2}
$2.11 - 2.53$	2.31	385^{+21}_{-20}	$19.24 - 19.27$	19.26	1.19	1.1 ± 0.1	53^{+2}_{-2}
$2.53 - 3.08$	2.80	369^{+20}_{-19}	$19.27 - 19.29$	19.28	1.11	1.1 ± 0.1	57^{+3}_{-2}
$3.08 - 3.81$	3.43	298^{+18}_{-17}	$19.29 - 19.30$	19.29	1.07	1.1 ± 0.1	54^{+3}_{-3}
$3.81 - 4.79$	4.27	299^{+18}_{-17}	...	19.30	1.08	1.1 ± 0.1	71^{+4}_{-4}
$4.79 - 6.16$	5.44	230^{+16}_{-15}	...	19.30	1.02	1.1 ± 0.1	65^{+4}_{-4}
$6.16 - 8.13$	7.08	220^{+16}_{-15}	...	19.30	1.04	1.0 ± 0.1	87^{+6}_{-5}
$8.13 - 11.05$	9.48	218^{+16}_{-15}	...	19.30	1.03	1.0 ± 0.1	116^{+8}_{-8}
$11.05 - 15.59$	13.13	177^{+14}_{-13}	...	19.30	1.01	1.0 ± 0.1	133^{+11}_{-10}
$15.59 - 23.04$	18.95	169^{+14}_{-13}	...	19.30	1.00	1.0 ± 0.1	192^{+16}_{-15}
$23.04 - 36.09$	28.83	165^{+14}_{-13}	...	19.30	1.00	1.0 ± 0.1	305^{+26}_{-24}
$36.09 - 60.94$	46.89	143^{+13}_{-12}	...	19.30	1.00	1.0 ± 0.1	470^{+42}_{-39}
$60.94 - 113.67$	83.23	122^{+12}_{-11}	...	19.30	1.00	1.0 ± 0.1	786^{+78}_{-71}
$113.67 - 242.77$	166.12	83^{+10}_{-9}	...	19.30	1.00	1.0 ± 0.1	1233^{+150}_{-135}
$242.77 - 626.60$	390.03	49^{+8}_{-7}	...	19.30	1.00	1.0 ± 0.1	2062^{+339}_{-294}
$626.60 - 2124.44$	1153.76	20^{+6}_{-4}	...	19.30	1.00	1.0 ± 0.1	3247^{+902}_{-719}

counts slightly overestimate the true counts due to double counting of hybrid AGN-SF galaxies. These models are based on low-frequency data at higher flux density limits and higher frequency data so some deviations are not unexpected; however, our observed counts do follow their model quite well. Mauch et al. (2013) suggest that the spectral curvature term used in the Wilman et al. (2008) models mean that their 151 MHz counts under-predict reality. For this reason we include the model counts at both frequencies.

Source counts below 1 mJy at 1.4 GHz have been the subject of much debate. For comparison, in Fig. 4.20, we have included the several source count determinations from 1.4 GHz scaled down to 150 MHz from the compilation of de Zotti et al. (2010) (including counts from Bridle et al. 1972; White et al. 1997; Ciliegi et al. 1999; Gruppioni et al. 1999; Richards 2000; Hopkins et al. 2003; Fomalont et al. 2006; Bondi et al. 2008; Kellermann et al. 2008; Owen & Morrison 2008; Seymour et al. 2008). This is a representative comparison and not an exhaustive list of available source counts. In particular, there are even deeper models of higher frequency counts using statistical methods (e.g. Vernstrom et al. 2014; Zwart et al. 2015). The source counts are scaled assuming a spectral index of -0.8. The blue lines at the low flux density end show how the higher frequency counts would scale if a flatter spectral index of -0.5 was used, i.e. the blue line drawn through the tail of the source counts would lie at lower 147 MHz fluxes (left in the plot) and at lower normalised count values (down in the plot) mostly due to the $S^{5/2}$ term in the normalised counts. We note that the flattening of the source counts at $5 - 7$ mJy, associated with the growing population of SF galaxies and faint radio-quiet AGN at lower flux densities (see e.g. Jarvis & Rawlings 2004; Simpson et al. 2006; Padovani et al. 2015), is clear and is the same as that seen at the higher frequencies. The further drop in the lowest flux density bins may be the result of some unaccounted for incompleteness in our sample or different resolution bias correction (see Section 4.5.2 and Appendix 4.B).

4.6 Conclusion

We have presented LOFAR High Band Antenna observations of the Boötes field made as part of the LOFAR Surveys Key Science Project. These are the first wide area (covering 19 deg^2), deep (reaching $\approx 120 - 150\,\mu$Jy beam^{-1}), high resolution (5.6×7.4 arcsec) images of one of the extragalactic deep fields made at $130 - 169$ MHz. These observations are at least an order of magnitude deeper and $3 - 5$ times higher in resolution than previously obtained at these frequencies. We have used a new calibration and imaging method to correct for the corrupting effects of the ionosphere and LOFAR digital beams.

The radio source catalogue presented here contains 5 652 sources detected with peak flux densities exceeding 5σ. We have quantified the positional and flux density accuracy of the LOFAR sources and used the source catalogue to derive spectral indices between 150 and 1400 MHz, finding a median spectral index of -0.79 ± 0.01. Finally, we have presented the deepest differential source counts at these low frequencies. These source counts follow quite well the model predictions of Wilman et al. (2008) and show the flattening at a few mJy as a result of the increasing contribution of SF galaxies.

Acknowledgements

LOFAR, the Low Frequency Array designed and constructed by ASTRON, has facilities in several countries, that are owned by various parties (each with their own funding sources), and

that are collectively operated by the International LOFAR Telescope (ILT) foundation under a joint scientific policy. The Open University is incorporated by Royal Charter (RC 000391), an exempt charity in England & Wales and a charity registered in Scotland (SC 038302). The Open University is authorized and regulated by the Financial Conduct Authority.

Appendix

4.A Postage stamp images

The largest (LAS>45 arcsec) of the visually identified extended sources are shown in Fig. 4.A.1, and the four very clear large diffuse sources are shown in Fig. 4.A.2.

4.B Source size distribution

We have investigated the extent to which the extrapolation of the Windhorst et al. (1990) size distribution might be valid at low frequencies. This is relevant to the resolution bias correction to the source counts, described in Section 4.5.2. We have done this by comparing the true angular size distribution of the 147 MHz LOFAR sources to the Windhorst et al. (1990) distribution, given by

$$h(>\theta_{\rm lim}) = \exp[-\ln 2(\theta_{\rm lim}/\theta_{\rm med})^{0.62}],$$

with the median size, in arcsec, as a function of flux density of

$$\theta_{\rm med} = 2S_{1.4\,{\rm GHz}}^{0.30},$$

where S is in mJy and we have scaled the 1.4 GHz flux densities to 150 MHz with a spectral index of -0.8. The observed and extrapolated size distributions are shown in Fig. 4.B.1 for four flux density bins. The low frequency emission appears to be more extended, which would suggest that the actual resolution bias correction should be somewhat larger. Future LOFAR Survey results, in particular, at high resolution using very long baseline interfereometry with the LOFAR international stations, will allow for more detailed studies of the true angular size distribution of radio sources.

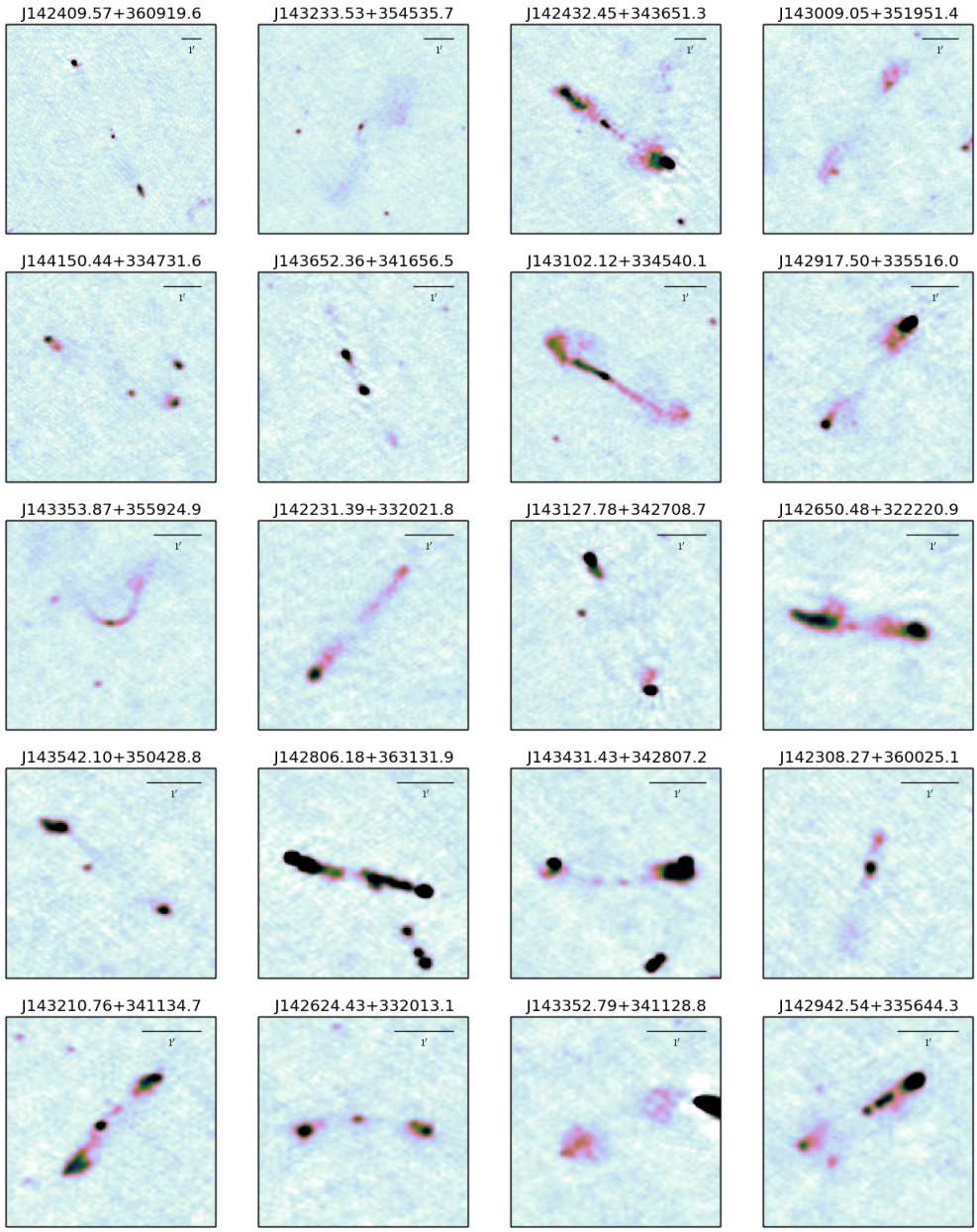


Figure 4.A.1: Postage stamps of extended sources identified visually, showing all the sources with approximate LAS>45arcsec. These include some Giant Radio Galaxies. The greyscale shows the flux density from $-3\sigma_{\rm local}$ to $30\sigma_{\rm local}$ where $\sigma_{\rm local}$ is the local rms noise. The scalebar in each image is 1arcmin.

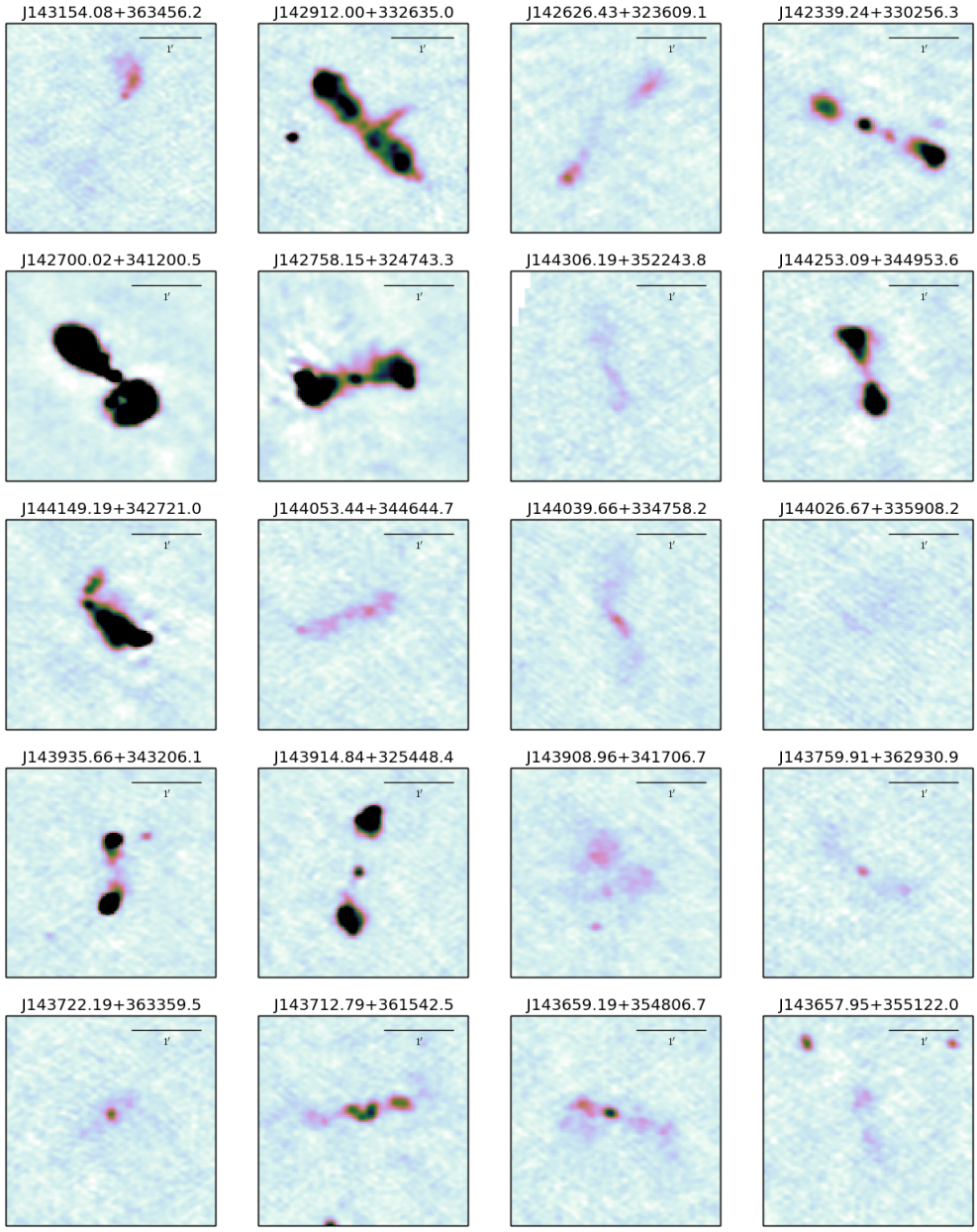


Figure 4.A.1: Continued.

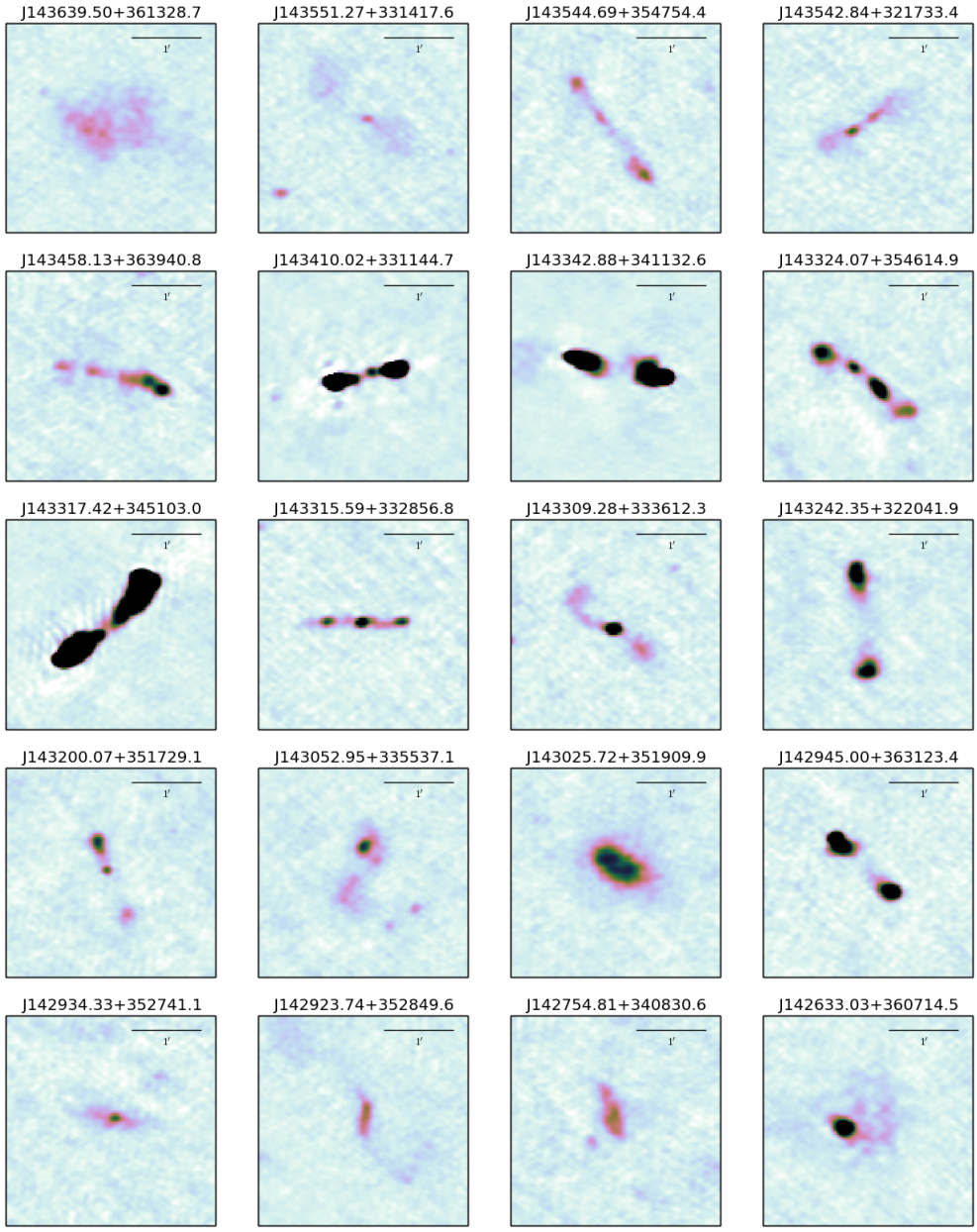


Figure 4.A.1: Continued.

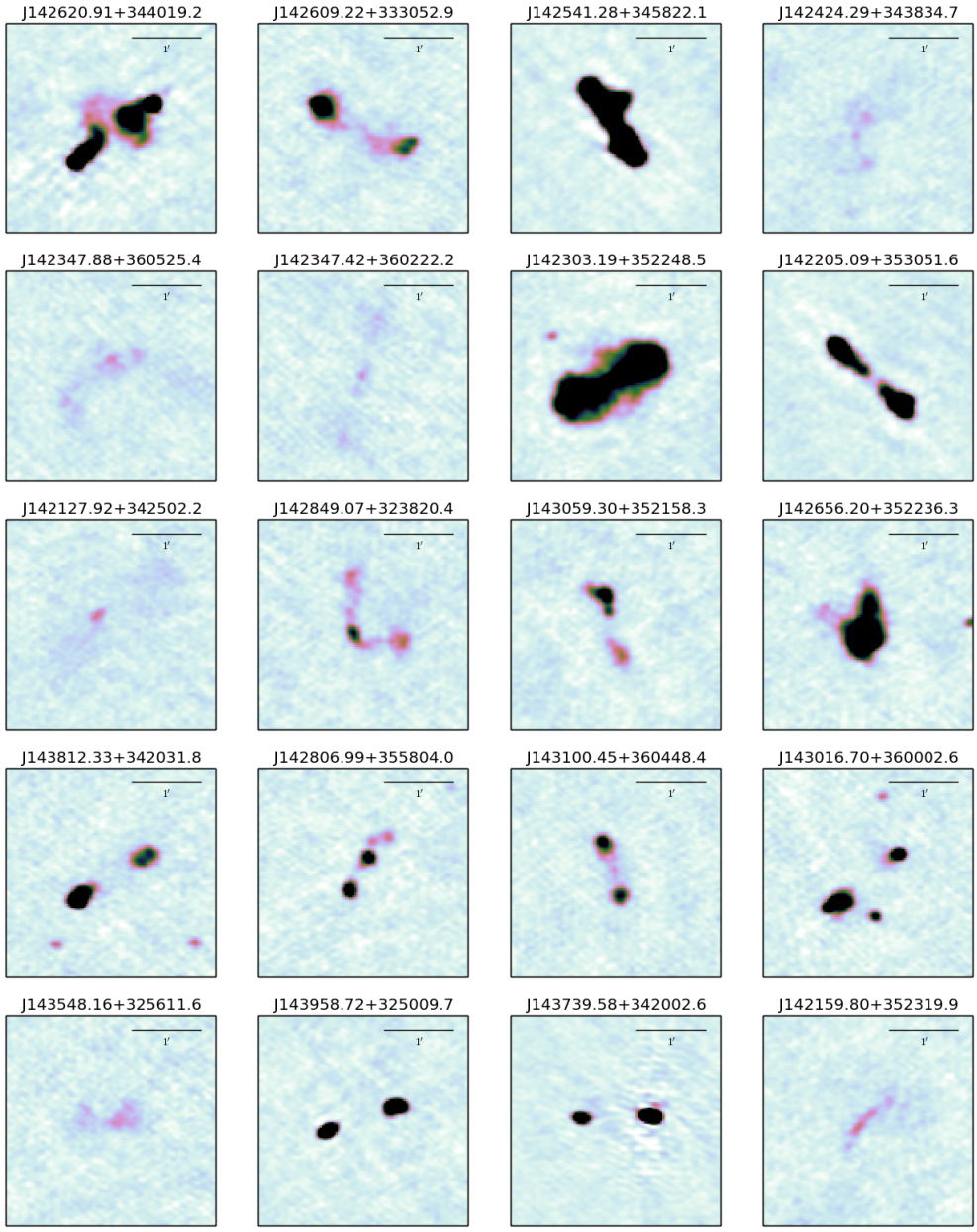


Figure 4.A.1: Continued.

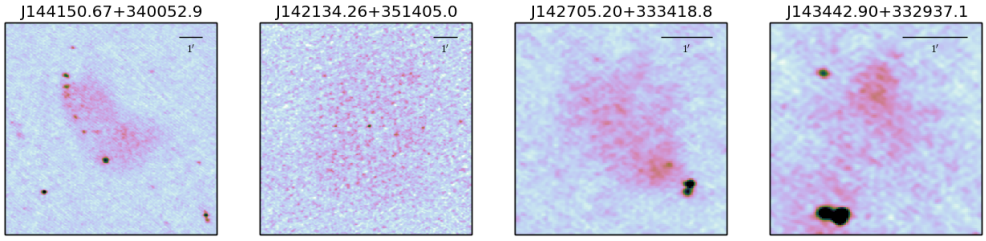


Figure 4.A.2: Postage stamps of large diffuse sources identified by eye. The greyscale shows the flux density from $-3\sigma_{\rm local}$ to $15\sigma_{\rm local}$ where $\sigma_{\rm local}$ is the local rms noise. The scalebar in each image is 1 arcmin.

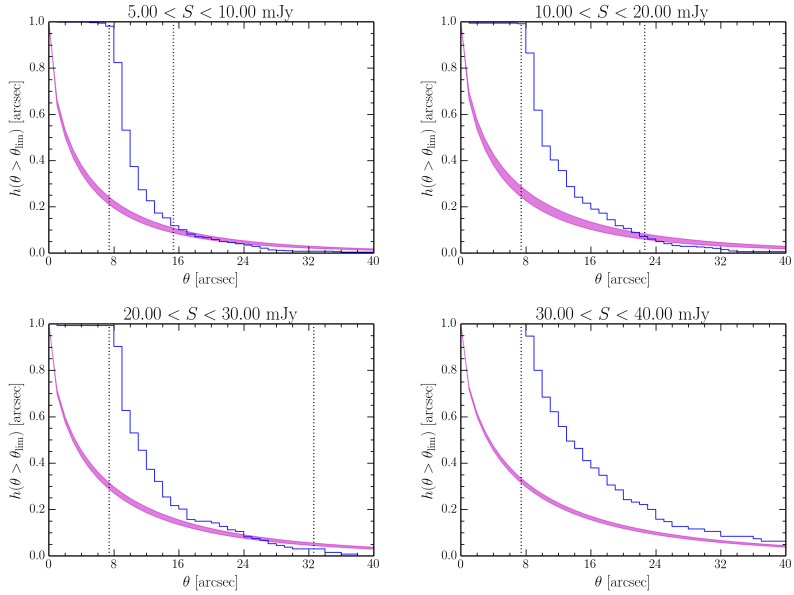


Figure 4.B.1: The observed source size distribution (in blue) in four flux density intervals. The magenta curves show the Windhorst et al. (1990) size distribution for the upper and lower bounds of the flux density bin. In each the vertical dotted lines are $b_{\rm maj}$ (on the left) and the approximate maximum size a source can have before it drops below the peak-flux detection threshold (on the right). The catalogue will be incomplete for sources larger than the right line.

CHAPTER 5

Radio-AGN Feedback: When the Little Ones were Monsters

We present a study of the evolution of the fraction of radio-loud active galactic nuclei (AGN) as a function of their host stellar mass. We make use of two samples of radio galaxies: one in the local universe, $0.01 < z \leqslant 0.3$, using a combined SDSS-NVSS sample and one at higher redshifts, $0.5 < z \leqslant 2$, constructed from the VLA-COSMOS_DEEP Radio Survey at 1.4 GHz and a K_s-selected catalogue of the COSMOS/UltraVISTA field. We observe an increase of more than an order of magnitude in the fraction of lower mass galaxies ($M_* < 10^{10.75}$ $M_\odot$) which host Radio-Loud AGN with radio powers $P_{1.4\,\mathrm{GHz}} > 10^{24}\,\mathrm{W\,Hz^{-1}}$at $z \approx 1 - 2$ while the radio-loud fraction for higher mass galaxies ($M_* > 10^{11.25}\,M_\odot$) remains the same. We argue that this increase is driven largely by the increase in cold or radiative mode accretion with increasing cold gas supply at earlier epochs. The increasing population of low mass Radio-Loud AGN can thus explain the upturn in the Radio Luminosity Function (RLF) at high redshift which is important for understanding the impact of AGN feedback in galaxy evolution.

Williams, W. L. and Röttgering, H. J. A.
MNRAS, 450, 1538 (2015)

5.1 Introduction

During recent years it has become increasingly apparent that the radio jets of radio-loud Active Galactic Nuclei (RL AGN or radio-AGN) play a crucial role in the process of galaxy formation and evolution via 'AGN feedback' (see e.g. Best et al. 2006, 2007; Bower et al. 2006; Croton et al. 2006; Fabian et al. 2006). This feedback can occur because the enormous energy output of the AGN can be injected into the surrounding medium, possibly also the fuel source of the AGN, via ionizing radiation and/or relativistic jets, thereby providing enough energy to affect star formation in the host galaxy. Radio galaxies have been shown to comprise two different populations: high and low excitation (Best et al. 2005a; Tasse et al. 2008b; Hickox et al. 2009), each of which may have a separate and different effect of feedback, the exact nature and evolution of which is still debated. The first population of RL AGN is associated with the classic optical 'quasars'. These sources radiate across the electromagentic spectrum and are consistent with the unified models of quasars where emission is obscured at some wavelengths when the source is viewed edge-on (e.g. Barthel 1989; Antonucci 1993; Urry & Padovani 1995). In this 'high-excitation', 'cold mode' or 'radiative mode', accretion is postulated to occur via an accretion disc in a radiatively efficient manner (e.g. Shakura & Sunyaev 1973). These high excitation radio galaxies (HERGs) are typically hosted by lower mass, bluer galaxies in less dense environments (e.g. Tasse et al. 2008b; Janssen et al. 2012). The second mode of radio activity was first noted by their lack of strong high-excitation narrow-line optical excitation expected from the 'quasar' mode (Hine & Longair 1979; Laing et al. 1994; Jackson & Rawlings 1997). Moreover they show no evidence of mid-infrared emission from dusty tori (Whysong & Antonucci 2004; Ogle et al. 2006) and no evidence of accretion-related X-ray emission (Hardcastle et al. 2006; Evans et al. 2006). Hardcastle et al. (2007) first suggested that this mode, known as the 'low-excitation', 'radio mode', 'hot mode' or 'jet mode' occurs when hot gas is accreted directly onto the supermassive black hole in a radiatively inefficient manner via advection dominated accretion flows (ADAFs, e.g. Narayan & Yi 1995). Best et al. (2005a) showed that these low excitation radio galaxies (LERGs) are hosted by fundamentally different galaxies: higher mass, redder and occurring in more dense environments. This mode in particular provides a direct feedback connection between the AGN and its hot gas fuel supply in the manner of work done by the expanding radio lobes on the hot intra-cluster gas. For a more detailed review of the HERG versus LERG dichotomy see Heckman & Best (2014) and references therein.

In order to understand the relative significance of the different types of radio-AGN feedback we need to understand the cosmic evolution of radio sources in detail. It has been known for several decades that the comoving number density of powerful radio sources is two to three orders of magnitude greater at a redshift of two to three compared to the local Universe (e.g. Schmidt 1968; Sandage 1972; Osmer 1982; Peacock 1985; Schmidt et al. 1988; Dunlop & Peacock 1990; Rigby et al. 2011). Similarly, the space density of optically selected quasars (QSOs) peaks at redshift $2 < z < 3$ (e.g. Boyle et al. 1988; Hewett et al. 1993; Warren et al. 1994). It is also well known that, within the local universe ($z \lesssim 0.3$), the fraction of galaxies which host a radio source, i.e. the radio-loud fraction, is a very steep function of host galaxy stellar mass ($f_{\rm radio-loud} \propto M_*^{2.5}$, Best et al. 2005b), increasing to > 30 per cent at stellar masses above $5 \times 10^{11}\,{\rm M}_\odot$ for radio luminosities $> 10^{23}\,{\rm W\,Hz^{-1}}$. This pervasiveness of radio-loudness among high mass galaxies in the local Universe, combined with the dramatic increase in density of radio-loud sources at earlier times suggests that there must be an increase in the prevalence of radio activity among galaxies of lower mass. To test this, we investigate the fraction of radio-loud sources out to redshift ≈ 2 as a function of their host stellar mass.

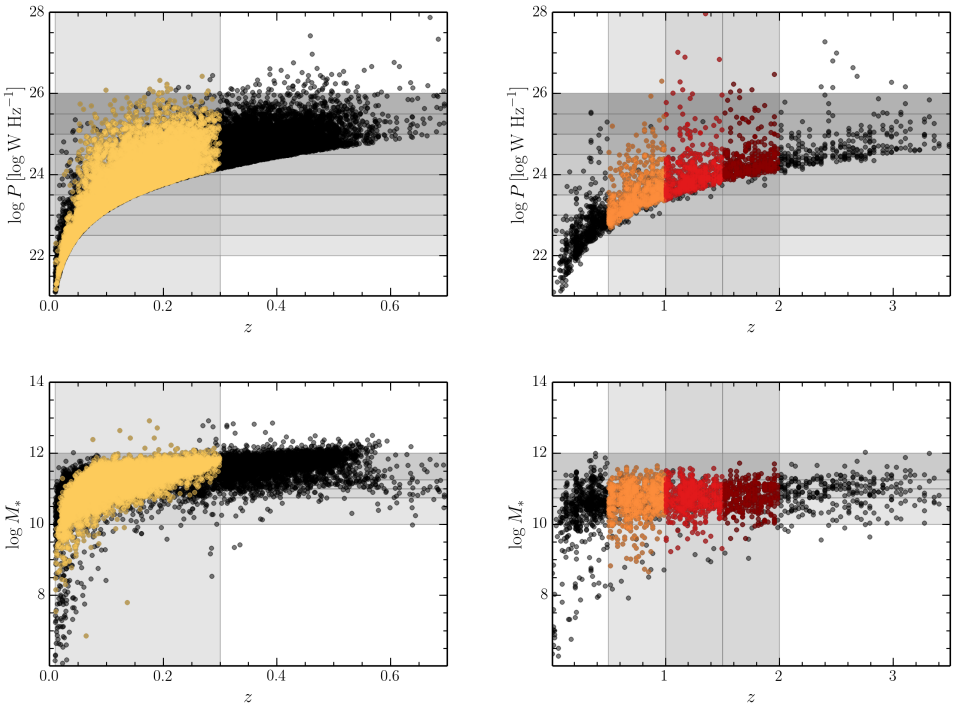


Figure 5.1: *Left* Full SDSS-NVSS Sample and the selected 'local' $0.01 < z \leqslant 0.3$ sample : radio power vs z and stellar mass, M_*, vs z. *Right* Full VLA-COSMOS Sample and the three selected 'high redshift' $0.5 < z \leqslant 1$ and $1 < z \leqslant 2$ samples : radio power vs z and stellar mass, M_*, vs z. The grey shaded regions show the regions in mass-space, redshift-space and radio power-space which demarcate the redshift samples, mass bins and power bins for the Luminosity Functions. The selected clean mass-complete radio samples are shown in yellow, orange and red symbols (these colours denote these redshift bins thought this paper).

This paper is structured as follows. In Section 5.2 we describe the construction of the Radio-Loud AGN samples and the catalogues from which they are selected. In Section 5.3 the luminosity functions for these samples are constructed and binned by host galaxy stellar mass. The radio-loud fraction as a function of host stellar mass is also determined. We discuss the results and their implications in Section 5.5 and conclude in Section 5.6. Throughout this paper, we use the following cosmological parameters: $H_0 = 70\,\mathrm{km\,s^{-1}\,Mpc^{-1}}$, $\Omega_m = 0.3$ and $\Omega_\Lambda = 0.7$. The spectral index, α, is defined as $S_\nu \propto \nu^{-\alpha}$ and unless otherwise specified, we adopt a default value of 0.8.

5.2 Radio-Loud AGN Samples

To investigate the evolution of the Radio Luminosity Function (RLF) for different stellar-masses over a similar luminosity range several samples with good ancillary and derived data are needed, to provide both the required statistics at low redshift and the sensitivity at high redshift. In this work we combine one already existing matched radio-optical dataset in the local universe using the SDSS-NVSS sample, described in Section 5.2.1, and one at redshifts $0.5 < z < 2$, which we

have constructed using the VLA-COSMOS DEEP Radio Survey at 1.4 GHz and a K_s-selected catalogue of the COSMOS/UltraVISTA field, which is described in Section 5.2.2.

5.2.1 Local SDSS Sample

For the local radio source sample we use the catalogue compiled by Best & Heckman (2012), which was constructed by cross-matching optical galaxies from the seventh data release (DR7; Abazajian et al. 2009) of the Sloan Digital Sky Survey (SDSS) spectroscopic sample with radio sources in the NRAO Very Large Array (VLA) Sky Survey (NVSS; Condon et al. 1998) and the Faint Images of the Radio Sky at Twenty centimetres (FIRST; Becker et al. 1995). The parent optical sample consists of all galaxies in the value-added spectroscopic catalogues (VASC) created by the Max Plank Institute for Astrophysics and Johns Hopkins University (MPA-JHU) group (see Brinchmann et al. 2004, available at `http://www.mpa-garching.mpg.de/SDSS/`). The cross-matching was done for all radio sources with flux densities > 5 mJy, which corresponds to radio luminosities of $P_{1.4\,\mathrm{GHz}} \gtrsim 10^{23}\,\mathrm{W\,Hz^{-1}}$at redshift $z = 0.1$ and $P_{1.4\,\mathrm{GHz}} \gtrsim 10^{24}\,\mathrm{W\,Hz^{-1}}$at redshift $z = 0.3$. The combined radio-optical area covered is 2.17 str (Best & Heckman 2012). Of the 927 522 galaxies in the VASC, Best & Heckman (2012) selected a magnitude-limited sample of 18 286 radio sources, which they showed to be 95 per cent complete and 99 per cent reliable (Best et al. 2005a). The sample was restricted to the 'main galaxy sample' (Strauss et al. 2002), comprising galaxies within the magnitude range $14.5 \leqslant r < 17.7$ mag and the redshift range $0.01 < z \leqslant 0.3$. This local radio-optical sample consists of 9168 radio sources. We note that, being based on the SDSS main galaxy sample, this local matched radio-optical sample excludes both radio-loud quasars and broad-line radio galaxies. However, Best et al. (2014) show that this is only problematic at radio powers above $P_{1.4\,\mathrm{GHz}} \gtrsim 10^{26}\,\mathrm{W\,Hz^{-1}}$. Since our LFs do not probe those high powers we make no correction for this bias. Moreover, we know that the dominant population of radio sources in this sample are not quasars.

Properties of the host galaxies are taken from the VASCs which, for each source, provide several basic measured parameters from the imaging data such as magnitudes, colours and sizes (York et al. 2000), as well as derived properties including, most importantly for this work, the stellar mass M_* (Kauffmann et al. 2003). For their matched radio sample, Best & Heckman (2012) also separated the sources into star-forming galaxies and RL AGN (7302 sources), which are further sub-divided into high-excitation (HERG) and low-excitation (LERG) sources, based on their optical photometric and spectroscopic parameters.

The left panels in Fig. 5.1 show the radio power and host stellar mass as a function of redshift for the radio sources in the SDSS-NVSS sample. All the radio sources are plotted in black, and sources in the restricted sub-sample within the redshift bin which defines our local sample are plotted in yellow.

5.2.2 Distant VLA-COSMOS Sample

The VLA-COSMOS Large Project covered the 2 deg^2 of the COSMOS Field at 1.4 GHz with observations by the VLA in the A configuration. This survey, extensively described in Schinnerer et al. (2004, 2007), provides continuum radio observations with a resolution (half-power beam width) of 1.5×1.4 arcsec and a mean 1σ sensitivity of about 10.5 μJy in the innermost 1 deg^2 region and of about 15 μJy in the outer parts. From the VLA-COSMOS catalogue we selected sources above 50 μJy, which corresponds to sources $> 5\sigma$ over 50 per cent of the survey area.

The optical data for this sample comes from the K_s-selected catalogue of the COSMOS/UltraVISTA field (Muzzin et al. 2013a) which contains PSF-matched photometry in 30 photometric bands covering the wavelength range 0.15μm $\rightarrow$ 24μm. The entire region overlaps with the radio survey so the combined area is that of the COSMOS/UltraVISTA data, $1.62\,\mathrm{deg}^2$. Following the recommended criteria of Muzzin et al. (2013a), we selected a 'clean' sample from the K_s catalogue of sources with flags: 'star' $\neq$ 1, 'K_flag' $\leqslant$ 4, 'contamination' $\neq$ 1, and 'nan_contam'$\leqslant$ 3 (these flags relate to stars and saturated sources and the quality of the photometry for nearby sources). Finally we selected sources brighter than the 90 per cent completeness limit of $K_s \leqslant 23.4$ mag. The redshifts provided are determined from SED fitting to the broadband photometry using the EAZY code (Brammer et al. 2008) and for source $z < 1.5$ they quote an rms error of $(\delta z/(1+z)) = 0.013$ and a catastrophic outlier fraction of 1.56 per cent. While the quoted outlier fraction is very low, we do expect that many of the outliers will be quasars (i.e. HERGs). It is well known that photometric redshifts determined for quasars are less reliable than those obtained for galaxies (e.g. Richards et al. 2001; Babbedge et al. 2004; Mobasher et al. 2004; Polletta et al. 2007).

Within this sample we defined three 'high-redshift' sub-samples in the redshift ranges $0.5 < z \leqslant 1.0$, $1.0 < z \leqslant 1.5$ and $1.5 < z \leqslant 2.0$, chosen such that each contains $\approx 300-700$ galaxies. The right panels of Fig. 5.1 show the radio power and host stellar mass as a function of redshift for the radio sources in the VLA-COSMOS sample. Sources in the restricted ranges which define our high redshift samples are plotted in orange and red, and all the remaining sources are shown in black.

Note that at radio powers $P_{1.4\,\mathrm{GHz}} \gtrsim 10^{23}\,\mathrm{W\,Hz^{-1}}$, the samples should consist almost entirely of RL AGN – we expect very little contamination from star-forming galaxies. We confirmed this using the spectroscopy-based AGN/SF separation in the local sample (Best et al. 2005b). Moreover, the star formation rate for this radio power is in excess of $25\,\mathrm{M_\odot\,yr^{-1}}$ (Condon 1992) so we expect AGN to continue to dominate even at higher redshifts.

5.3 The Stellar-Mass dependent Luminosity Function

5.3.1 The Luminosity Function

A standard technique for quantifying the rate of evolution of a population of galaxies is to compare their luminosity functions (LFs) at two different epochs. In this section, we therefore determine the evolution of the Radio-Loud AGN population among host galaxies of different masses by comparing the luminosity functions of the SDSS-NVSS and VLA-COSMOS samples. Determining the radio LFs for the full samples first serves to confirm our sample selection and methods.

These radio luminosity functions were calculated in the standard way, using $\rho = \Sigma_i 1/V_i$ method (Schmidt 1968; Condon 1989), where V_i is the volume in which a given source could be detected. This volume is determined by both the minimum and maximum distance at which a given source would be included in the sample as a result of the selection criteria: $V_i = V_{\mathrm{max}} - V_{\mathrm{min}}$, where V_{max} and V_{min} are the volumes enclosed within the observed sky area out to the maximum and minimum distances respectively. The minimum accessible volume is a result of the optical cut-off on the bright end (> 14.5 mag for SDSS-NVSS, while the VLA-COSMOS sample has no bright flux limit). The maximum accessible volume is determined by the flux limits of both the optical (< 17.77 mag for SDSS-NVSS and < 23.4 mag for VLA-COSMOS) and radio data (> 5 mJy for SDSS-NVSS and $> 50\,\mu$Jy for the VLA-COSMOS sample). In practice, the

Table 5.1: Number of sources in each stellar mass–redshift bin.

Mass bin	Redshift bin			
$\log(M_*/\mathrm{M}_\odot)$	$0.01-0.3$	$0.5-1.0$	$1.0-1.5$	$1.5-2.0$
$10.00-10.75$	1021	296	231	147
$10.75-11.00$	843	153	126	90
$11.00-11.25$	1639	127	111	74
$11.25-12.00$	5306	51	35	26
Total	9006	672	518	343

maximum redshift is dominated by the radio flux limits. The normalization of the luminosity function requires knowledge of the precise intersection area of all input surveys. The sky area for the SDSS-NVSS sample is taken to be 2.17 sr (Best et al. 2005b). For the VLA-COSMOS sample, the sky area is taken to be $1.62\,\mathrm{deg}^2$ for all sources above $100\,\mu$Jy. For the faintest sources in the VLA-COSMOS sample, the area in which the sources could be detected is smaller due to the non-uniform rms noise level in the VLA-COSMOS mosaic. We therefore weight each source by the inverse of the area in which it can be detected, which also accounts for the varying detection area within a given luminosity bin. Uncertainties are calculated as the statistical Poissonian errors with a contribution of cosmic variance where appropriate; in some luminosity/mass bins, these errors are so small that the error will be dominated by systematic effects. The area covered by VLA-COSMOS sample of $1.62\,\mathrm{deg}^2$ is small enough that the effects of cosmic variance are not negligible for very massive galaxies. The total area covered by COSMOS/UltraVISTA is approximately 1.5 square degrees in one single field, making the effects of cosmic variance not negligible for very massive galaxies. The contribution of cosmic variance to the total error budget was estimated through the recipe of (Moster et al. 2011). The average uncertainties due to this effect for the least massive galaxies vary from 6 to 7 per cent and for the most massive galaxies vary from 10 to 12 per cent across the three highest redshift bins. These values were added in quadrature to the Poissonian error of the LFs.

We have compared our derived RLFs for radio-loud sources of all stellar masses with those in the literature. For the full samples, our local RLF agrees with that of Best et al. (2005a) and our RLF for the high redshift VLA-COSMOS sample agrees with that of Smolčić et al. (2009). The agreement is not unexpected as we are using the same data, but it serves to validate out sample selections and method.

We next split the samples into four bins of different host galaxy stellar masses: $10.0 < \log(M_*/\mathrm{M}_\odot) \leqslant 10.75$, $10.75 < \log(M_*/\mathrm{M}_\odot) \leqslant 11.0$, $11.0 < \log(M_*/\mathrm{M}_\odot) \leqslant 11.25$, and $11.25 < \log(M_*/\mathrm{M}_\odot) \leqslant 12.0$. These bins are chosen to sample the stellar masses well with similar numbers of sources in each bin (see Fig. 5.1). The RLFs derived in each of these stellar mass bins in the four redshift bins are plotted in Fig. 5.2. Note that in the low redshift sample we exclude the points below $P_{1.4\,\mathrm{GHz}} \lesssim 10^{23}\,\mathrm{W\,Hz}^{-1}$for the highest stellar mass bin as these sources are only detectable out to $z \lesssim 0.1$ and this sample is incomplete for high mass sources at these redshifts. Table 5.1 shows the number of sources in each stellar mass-redshift bin. From these LFs we see that in the local universe and for $P_{1.4\,\mathrm{GHz}} \gtrsim 10^{23}\,\mathrm{W\,Hz}^{-1}$, the number density of the highest host stellar mass bin is the greatest, while in the higher redshift bins the number density within all the stellar mass bins is becoming increasingly similar.

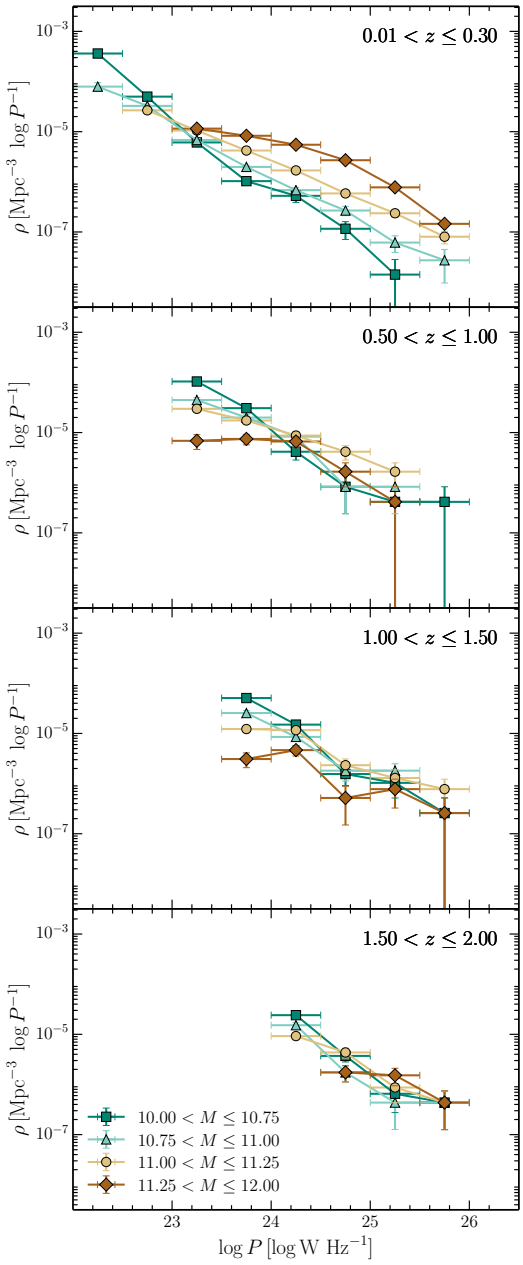


Figure 5.2: The comoving space density of radio-loud sources. This is the RLF in redshift bins $0.01 < z \leqslant 0.3$ (*top*), $0.5 < z \leqslant 1.0$ (*top-middle*), $1.0 < z \leqslant 1.5$ (*bottom-middle*) and $1.5 < z \leqslant 2.0$ (*bottom*) for the four host stellar mass bins (plotted in colour).

Table 5.2: Relative space density of radio-loud sources with respect to the local density as a function of redshift for all sources with radio powers greater than the cut-off $P_{1.4\,\mathrm{GHz}} > 10^{24}\,\mathrm{W\,Hz^{-1}}$.

Mass bin	Redshift bin		
$\log(M_*/\mathrm{M}_\odot)$	$0.5-1.0$	$1.0-1.5$	$1.5-2.0$
$10.00-10.75$	8.9 ± 3.1	27.6 ± 6.9	45 ± 11
$10.75-11.00$	9.5 ± 2.2	12.1 ± 2.1	17.3 ± 2.6
$11.00-11.25$	5.7 ± 1.0	6.45 ± 0.86	5.89 ± 0.77
$11.25-12.00$	0.95 ± 0.21	0.68 ± 0.14	

5.3.2 Space Density Evolution

Now, to quantify the disproportional increase in radio activity among galaxies of different mass at higher redshifts, we investigate the relative comoving space density of radio-loud sources with respect to the local comoving space density. We do this by dividing the stellar mass dependent RLFs in redshift bins $0.5 < z \leqslant 1.0$, $1.0 < z \leqslant 1.5$ and $1.5 < z \leqslant 2.0$ by the local RLF ($0.01 < z \leqslant 0.3$). These relative RLFs are plotted in Fig. 5.3, from which it is clear that there is a difference between the relative comoving space density of low mass galaxies hosting radio sources and that of high mass hosts. We derive the relative comoving space density of radio-loud sources with respect to the local comoving space density for all sources with radio powers greater than a cut-off luminosity of $P_{1.4\,\mathrm{GHz}} > 10^{24}\,\mathrm{W\,Hz^{-1}}$. This is plotted as a function of redshift in Fig. 5.4 and the values listed in Table 5.2.

At $z \approx 1.5-2$ the space density of the least massive galaxies hosting Radio-Loud AGN above $P_{1.4\,\mathrm{GHz}} > 10^{24}\,\mathrm{W\,Hz^{-1}}$is 45 ± 11 times greater than the local space density. Even the sources with stellar masses in the range $10.75 < \log(M_*/\mathrm{M}_\odot) \leqslant 11.0$ are 17.3 ± 2.6 times more prevalent. We note that there is a slight decrement in the space density of the most massive galaxies hosting Radio-Loud AGN at both radio power cuts going out to $z < 1.5$. If we consider the slightly less powerful sources, $P_{1.4\,\mathrm{GHz}} > 10^{23.5}\,\mathrm{W\,Hz^{-1}}$, and only go out to redshift $z < 1.5$ (not plotted here), the effect is only really seen in the lowest mass bin where the increase in space density increases more rapidly with redshift: the space density of the least massive galaxies hosting Radio-Loud AGN is 40.8 ± 6.2 times greater than locally compared to the 27.6 ± 6.9-fold increase for $P_{1.4\,\mathrm{GHz}} > 10^{24}\,\mathrm{W\,Hz^{-1}}$sources in the $1.0 < z \leqslant 1.5$ bin.

5.4 The Radio-Loud Fraction

Another way of looking at the increase in prevalence of AGN in lower mass hosts is to consider the fraction of sources which are radio-loud as a function of the host stellar mass in our four redshift bins. The mass-dependence of the radio-loud fraction can be an indicator of the accretion mode of the radio-AGN largely because of the different dependence of the fuelling source (hot vs. cold gas) on stellar mass (Best et al. 2006). The radio-loud fraction can be easily calculated by dividing the stellar mass function (SMF) for radio-loud sources, ρ_{Rad} (for sources above a given radio power limit), by the SMF for all galaxies, ρ_{Opt}:

$$f_{\mathrm{radio-loud}} = \rho_{\mathrm{Rad}}/\rho_{\mathrm{Opt}}.$$

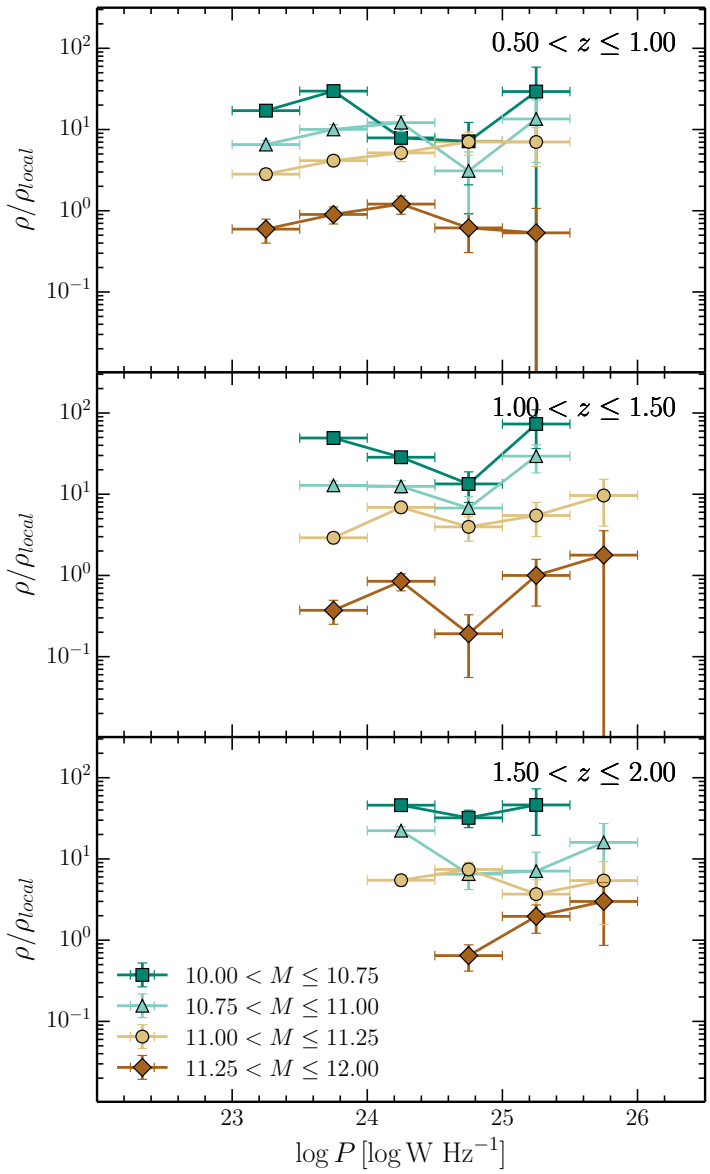


Figure 5.3: The relative comoving space density of radio-loud sources with respect to the local comoving space density. This is the RLF in redshift bins $0.5 < z \leqslant 1.0$ (*top*), $1.0 < z \leqslant 1.5$ (*middle*) and $1.5 < z \leqslant 2.0$ (*bottom*) by the local, $0.01 < z \leqslant 0.3$, RLF for the four host stellar mass bins (plotted in colour).

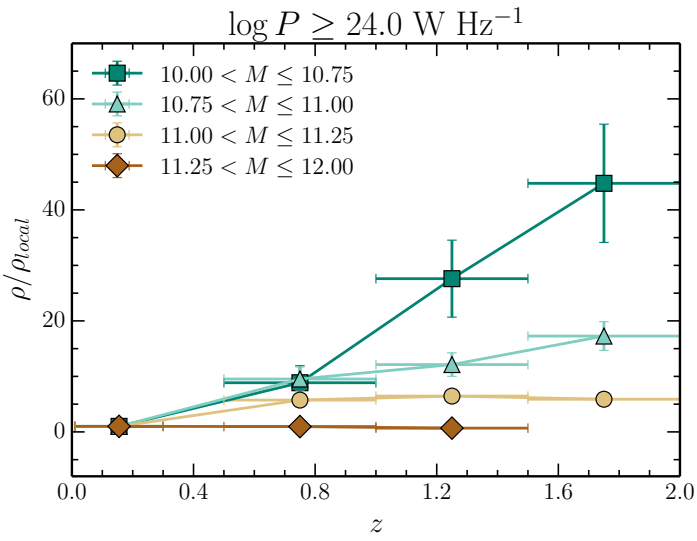


Figure 5.4: Relative space density of radio-loud sources with respect to the local density as a function of redshift for all sources with radio powers greater than the cut-off $P_{1.4\,\mathrm{GHz}} > 10^{24}\,\mathrm{W\,Hz^{-1}}$.

5.4.1 The Stellar Mass Function

In order to calculate the radio-loud fraction we first derived the SMFs for all galaxies and for the radio source hosts by using the $1/V_{max}$ estimator (Schmidt 1968) as previously described for the LFs, which corrects for the fact that the samples are magnitude limited. In order to construct the SMFs, the redshift-dependent limiting M_* above which the magnitude-limited sample is complete needs to be known. For the COSMOS/UltraVISTA sample we use the empirical 95 per cent completeness limit calculated by Muzzin et al. (2013a).

The SMFs for radio-loud galaxies and all galaxies are plotted in Fig. 5.5 for a radio-power cut-off of $P_{1.4\,\mathrm{GHz}} > 10^{24}\,\mathrm{W\,Hz^{-1}}$. We choose this limit because the highest redshift bin is only able to probe radio powers greater than this (see also Fig. 5.1). The SMFs we derive for our optical galaxy samples (for both the SDSS and COSMOS samples) are consistent with those of Muzzin et al. (2013b) who use a more sophisticated maximum-likelihood analysis to derive the SMFs in several redshift bins. As expected (Best et al. 2005b), ρ_{Rad} differs significantly from ρ_{Opt} – the hosts of radio sources are biased towards more massive systems. Interestingly, while the comoving number density of all galaxies decreases with redshift, that of the radio source hosts with $\log(M_*/\mathrm{M}_\odot) \lesssim 11.0$ increases. This is consistent with the results of Tasse et al. (2008b) and shows that the radio-loud galaxy population evolves differently from the population of galaxies as a whole.

5.4.2 The Radio-Loud Fraction

Having computed the relevant SMFs we can calculate the radio-loud fraction as described above. Figure 5.6 shows the radio-loud fraction for a radio-power cut-off of $P_{1.4\,\mathrm{GHz}} > 10^{24}\,\mathrm{W\,Hz^{-1}}$. The radio-loud fraction clearly increases with redshift. Moreover, the slope of the mass depen-

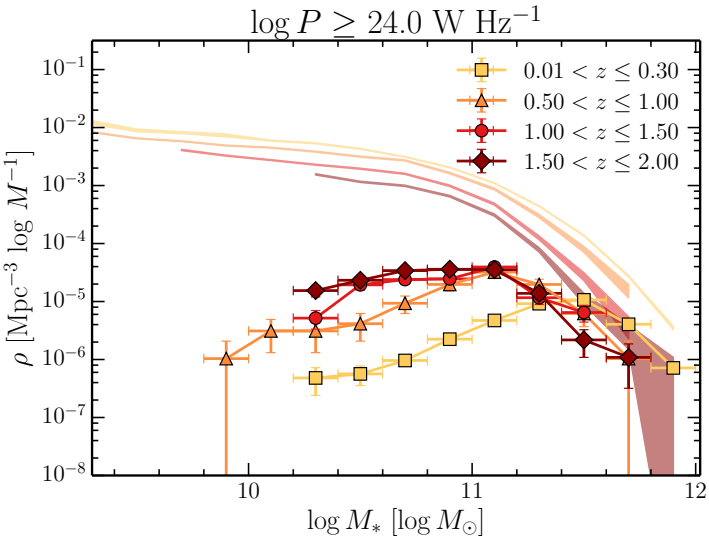


Figure 5.5: SMFs for all galaxies, $\rho_{\rm Opt}$, (shaded lines) and radio-loud galaxies, $\rho_{\rm Rad}$, (lines with points) for a radio-power cut-off $P_{1.4\,\rm GHz} > 10^{24}\,\rm W\,Hz^{-1}$in the four redshift bins.

dence becomes shallower, showing that the fraction of lower mass galaxies hosting radio sources increases more with redshift than the fraction for high mass galaxies. The slopes are shallower at higher redshifts, for $P_{1.4\,\rm GHz} > 10^{24}\,\rm W\,Hz^{-1}$going from $f_{RL} \propto M_*^{2.7\pm0.2}$ in the local sample, flattening to $f_{RL} \propto M_*^{1.7\pm0.1}$, $f_{RL} \propto M_*^{1.5\pm0.1}$ and $f_{RL} \propto M_*^{1.0\pm0.1}$ in the higher redshift bins. This is highlighted in the plot of the radio-loud fraction relative to the local redshift bin (fig. 5.7), where the relative radio-loud fraction is up to two orders of magnitude greater at the low mass end. We note that the flattening is quicker with redshift when the lower power $P_{1.4\,\rm GHz} > 10^{23.5}\,\rm W\,Hz^{-1}$sources are considered (in the first three redshift bins only, not plotted here): $f_{RL} \propto M_*^{2.7\pm0.1}$, $f_{RL} \propto M_*^{1.3\pm0.1}$ and $f_{RL} \propto M_*^{1.1\pm0.1}$.

5.5 Interpretation

In this section we aim to interpret and explain our results within the context of the HERG-LERG population dichotomy and their differential cosmic evolution and mass dependence.

In the local Universe, the density of high mass Radio-Loud AGN is an order of magnitude higher than that of low mass Radio-Loud AGN at all radio powers (cf. top panel Fig. 5.2). In the more distant Universe, up to $z < 2$ we see a sharp increase in the number density of Radio-Loud AGN hosted by lower mass galaxies, while the number density of high mass Radio-Loud AGN remains constant.

This large increase in the prevalence of radio activity among galaxies of lower mass at higher redshifts (cf. Fig. 5.4) shows that it is the lower mass galaxies which are the cause of the upturn in the observed RLFs (e.g. Dunlop & Peacock 1990; Rigby et al. 2011). Moreover we suggest that this upturn is likely due to an increasing population of cold mode accretors at earlier epochs. From Best et al. (2005a) we know that locally, despite the wide distributions in host stellar mass

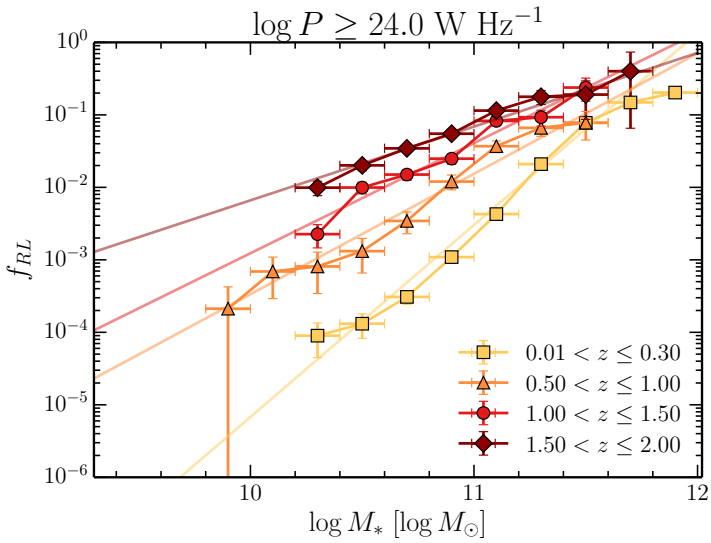


Figure 5.6: The fraction of galaxies hosting a radio source (radio-loud fraction) for a radio-power cut-off of $P_{1.4\,\mathrm{GHz}} > 10^{24}\,\mathrm{W\,Hz^{-1}}$in the four redshift bins. The coloured lines show a linear fit over the stellar mass range $10 < \log(M_*/\mathrm{M}_\odot) < 11.5$. The slopes of these fits are 2.7 ± 0.2, 1.7 ± 0.2, 1.5 ± 0.1 and 1.0 ± 0.1 from the lowest to highest redshift bins.

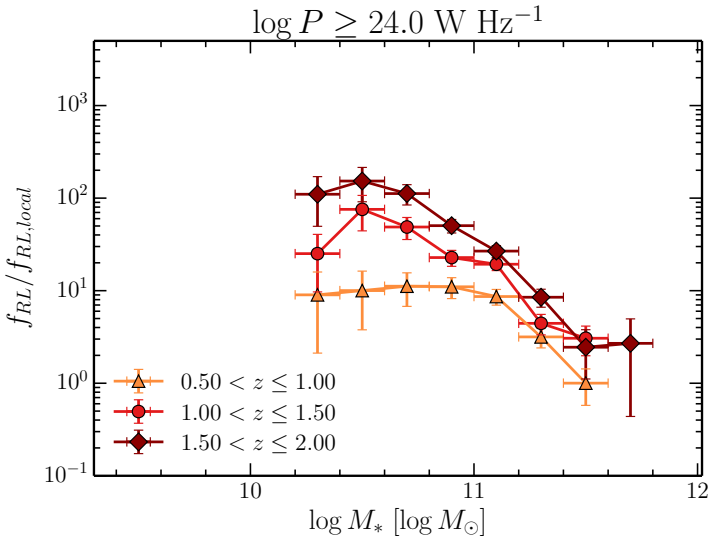


Figure 5.7: The fraction of galaxies hosting a radio source (radio-loud fraction) relative to the local fraction for a radio-power cut-off of $P_{1.4\,\mathrm{GHz}} > 10^{24}\,\mathrm{W\,Hz^{-1}}$in the three higher redshift bins.

of both HERGs and LERGs, LERGs have a strong preference to be hosted by galaxies with higher masses, while HERGs are hosted by galaxies with a lower median stellar mass but with a broader distribution. Assuming this still holds at higher redshifts, it implies that this strongly evolving population of lower mass Radio-Loud AGN are HERGs. We also expect the highest mass, most powerful sources to peak in space density at higher redshifts ($z \approx 2-3$ Rigby et al. 2011) in line with the cosmic downsizing picture where the most massive black holes have formed by $z \approx 4$. Indeed, results from many of the earlier radio surveys show that the most powerful ($P_{1.4\,\mathrm{GHz}} \gtrsim 10^{26}\,\mathrm{W\,Hz^{-1}}$) radio galaxies at $z \gtrsim 1$ (e.g. Eales et al. 1997; Jarvis et al. 2001; Seymour et al. 2007; Fernandes et al. 2015) are predominantly HERGs hosted by the most massive galaxies.

Indications from studies out to $z \lesssim 1$ show that the HERGs are indeed evolving more strongly with redshift than the LERG population (Best et al. 2014) such that within the redshift ranges of this study the radio-AGN population should be dominated by HERGs, opposite to that within the local universe. The mass dependence that we observe in this study supports this idea. Moreover, the evolution in the optical quasar luminosity function (i.e. that corresponding to radio-quiet cold mode accretion; Hasinger et al. 2005; Hopkins et al. 2007; Croom et al. 2009) is comparable to the kind of increase we observe for the low mass galaxies.

Furthermore, the slope of the radio-loud fraction (cf. Fig. 5.6) we observe at the higher redshifts, $f_{RL} \propto M_*^{\approx 1.3}$, is more consistent with the slope of the radio-loud fraction found in the local universe for HERGs only (Janssen et al. 2012). On the other hand, in the local sample, our derived slope of $f_{RL} \propto M_*^{\approx 2.5}$ matches that which Janssen et al. (2012) found for only LERGs and matches the theoretical value for the accretion of hot gas from a halo (Best et al. 2006). In this case we know that the dominant population of all local radio sources is that of the LERGs. This lends support to the idea that there is an increase in the prevalence of HERG activity or cold mode accretion and that this mode is becoming the dominant population out to redshifts of $0.5 < z \leqslant 2$.

Lastly, as Heckman & Best (2014) state, the crucial requirement for cold mode accretion is the abundant central supply of cold dense gas. And as reflected in the increase in cosmic star formation rate density which has increased tenfold out to $z \approx 2$ and threefold out to $z \approx 0.5$ (e.g. Sobral et al. 2013; Madau & Dickinson 2014, and references therein), there is significantly more cold gas fuelling star formation at these epochs.

A closer inspection of Fig. 5.3 reveals some interesting features, most particularly in highest mass bin, $11.25 < \log(M_*/\mathrm{M}_\odot) < 12$, in the highest redshift interval, $1 < z \leqslant 1.5$. We suggest that while the radio-AGN sample as a whole at these redshifts is becoming dominated by cold mode accretors, the highest mass, intermediate power ($10^{24} < P_{1.4\,\mathrm{GHz}} < 10^{25}\,\mathrm{W\,Hz^{-1}}$) sources could still be hot mode/LERG sources because of their high mass. We observe a slight decrease in the number density of these specific sources consistent with the modelling results of Rigby et al. where the $\approx 10^{24}\,\mathrm{W\,Hz^{-1}}$population peaks at $z \approx 1$ and is likely dominated by LERGs. This could be significant in the context of the models of LERG evolution presented by Best et al. (2014). If these are indeed LERGs the decrease in number density does not match the order of magnitude decrease predicted by the preferred model of Best et al. (2014) extrapolated out to $z \approx 1.5$ from fits to data out to $z \approx 0.7$. This model includes a time delay of ≈ 1.5 Gyr between the formation of massive quiescent galaxies and when they are able to produce hot mode AGN, and at redshifts above ≈ 1 the available population of host galaxies is declining so rapidly that such a delay in the onset of hot mode AGN activity would imply a drastic fall in the number densities of these sources above $z \approx 1$.

5.6 Summary and Conclusions

In this paper we have used the SDSS value-added spectroscopic sample of radio-loud galaxies (Best & Heckman 2012) and the VLA-COSMOS radio sample (Schinnerer et al. 2004, 2007) matched to a K_s-selected catalogue of the COSMOS/UltraVISTA field (Muzzin et al. 2013a) to compile two samples of Radio-Loud AGN going out to $z = 2$. The samples are of sufficiently high radio power that they are dominated by RL AGN. Using these samples we have constructed radio luminosity functions for four host stellar mass bins between $\log(M_*/\mathrm{M}_\odot) = 10.0$ and $\log(M_*/\mathrm{M}_\odot) = 12.0$, in four redshift bins between $z = 0.01$ and $z = 2$. We have also investigated the radio-loud fraction as a function of stellar mass in these redshift bins. Together, we found the following:

1. Radio activity among galaxies of different mass increases differently towards higher redshifts. By considering the relative comoving space density of radio-loud sources with respect to the local comoving space density, we showed that at $1.5 < z < 2$ the space density of galaxies with stellar masses in the range $10.00 < \log(M_*/\mathrm{M}_\odot) \leqslant 10.75$ and $10.75 < \log(M_*/\mathrm{M}_\odot) \leqslant 11.0$ hosting Radio-Loud AGN with $P_{1.4\,\mathrm{GHz}} > 10^{24}\,\mathrm{W\,Hz^{-1}}$is respectively 45 ± 11 and 17.3 ± 2.6 times greater relative to the local space density while that of higher mass galaxies hosting Radio-Loud AGN remains the same.
2. The fraction of galaxies which host Radio-Loud AGN with $P_{1.4\,\mathrm{GHz}} > 10^{24}\,\mathrm{W\,Hz^{-1}}$ as a function of stellar mass shows a clear increase with redshift and a flattening with mass with the mass dependence evolving from $f_{RL} \propto M_*^{2.7}$ in the local sample to $f_{RL} \propto M_*^{1.0}$ at $1.5 < z < 2$.

We have argued that this increase in the prevalence of radio activity among galaxies of lower mass at higher redshifts is largely due to a rising contribution of AGN accreting in the radiative mode (HERGs). With this data we cannot yet conclusively show the evolution of the different accretion modes as a function of their host stellar mass because we lack the information on the excitation state of these sources at higher redshifts. However, future work combining this and other radio-optical samples will allow more detailed studies of optical hosts of the high-redshift ($1 \lesssim z \lesssim 2$) population of radio-AGN.

Acknowledgements

The authors thank Philip Best, George Miley and Emma Rigby for useful discussions which contributed to the interpretation in this paper. The authors thank the anonymous referee for useful comments which have improved this manuscript.

This study uses a K_s-selected catalogue of the COSMOS/UltraVISTA field from Muzzin et al. (2013a). The catalogue contains PSF-matched photometry in 30 photometric bands covering the wavelength range $0.15\mu\mathrm{m} \rightarrow 24\mu\mathrm{m}$ and includes the available $GALEX$ (Martin et al. 2005), CFHT/Subaru (Capak et al. 2007), UltraVISTA (McCracken et al. 2012), S-COSMOS (Sanders et al. 2007), and zCOSMOS (Lilly et al. 2009) datasets. This work uses the catalogue compiled by Best & Heckman (2012), which combines data from the VASC (Brinchmann et al. 2004) of the SDSS DR7 (Abazajian et al. 2009) with NVSS (Condon et al. 1998) and FIRST (Becker et al. 1995).

CHAPTER 6

Radio AGN in the Boötes field

This paper presents a study of the redshift evolution of radio-loud active galactic nuclei (AGN) as a function of the properties of their galaxy hosts in the Boötes field. To achieve this we produce a catalogue of galaxies for which we derive photometric redshifts, stellar masses and rest-frame colours. The galaxies are matched to low frequency radio sources from 150 MHz LOFAR observations. From the matched radio-optical catalogues, we select a subsample of 974 high power $P_{150\,\mathrm{MHz}} > 10^{25}\,\mathrm{W\,Hz^{-1}}$ radio sources between $0.5 \leqslant z < 2$. We present further spectral energy distribution (SED) fitting to determine the mid-infrared AGN contribution for the radio-sources and use this information to classify them as High versus Low Excitation Radio Galaxies (HERGs and LERGs). We study the radio-loud fraction for HERGs and LERGs as a function of stellar mass and host galaxy colour. The fraction of HERGs increases with redshift. The fraction of sources in blue galaxies increases with redshift, while that in red galaxies decreases.

Williams, W. L., Röttgering, H. J. A., Rigby, E. E., and Calistro Rivera, G.
in preparation

6.1 Introduction

The growth and evolution of black holes plays a significant role in the framework of galaxy evolution. It is important then to understand the fueling mechanisms of Active Galactic Nuclei (AGN) and their 'feedback' processes by which the central black holes can control or terminate star formation in their host galaxies (see e.g. Best et al. 2006, 2007; Bower et al. 2006; Croton et al. 2006; Fabian et al. 2006; Cattaneo et al. 2009). From studies of radio-loud AGN, which are identified by their synchrotron emission from their jets, it has become clear that there are two classes of sources distinguished by their Eddington-scaled accretion rates (Best & Heckman 2012; Son et al. 2012; Russell et al. 2013; Mingo et al. 2014; Gürkan et al. 2014; Fernandes et al. 2015) The first population of RL AGN is associated with radiatively efficient accretion via an accretion disc (e.g. Shakura & Sunyaev 1973). These sources fit the paradigm of classic optical 'quasars' (Silk & Rees 1998), radiating across the electromagentic spectrum (e.g. Barthel 1989; Antonucci 1993; Urry & Padovani 1995). This 'cold mode' or 'radiative mode' is characterised by strong optical emission lines and so are refered to as 'high-excitation' sources. It has been found that high excitation radio galaxies (HERGs) are typically hosted by lower mass, bluer galaxies in less dense environments (e.g. Tasse et al. 2008b; Janssen et al. 2012). This mode may be important in curtailing star formation at high redshift and setting up the tight black hole vs bulge mass relation observed in the nearby Universe (Magorrian et al. 1998). The second class of radio galaxies was first noted by their lack of emission lines (Hine & Longair 1979; Laing et al. 1994; Jackson & Rawlings 1997) and are thought to occur when hot gas accretes directly onto the supermassive black hole in a radiatively inefficient manner (Hardcastle et al. 2007) through advection dominated accretion flows (ADAFs, e.g. Narayan & Yi 1995). They also lack any evidence of mid-infrared emission from dusty tori (Whysong & Antonucci 2004; Ogle et al. 2006) and accretion-related X-ray emission (Hardcastle et al. 2006; Evans et al. 2006). These low excitation radio galaxies (LERGs) are hosted by fundamentally different galaxies: higher mass, redder and occurring in more dense environments (Best et al. 2005a). This 'radio mode', 'hot mode' or 'jet mode' in particular provides a direct feedback connection between the AGN and its hot gas fuel supply in the manner of work done by the expanding radio lobes on the hot intra-cluster gas. It may be responsible for maintaining elliptical galaxies at lower redshifts as 'old, red and dead' (e.g. Best et al. 2006) and for preventing strong cooling flows in galaxy clusters (e.g. Fabian et al. 2006). For a comprehensive review on the current understanding of the HERG/LERG dichotomy see Heckman & Best (2014) and McNamara & Nulsen (2012) and references therein.

In order to understand the relative significance of the different types of radio-AGN feedback we need to understand the cosmic evolution of radio sources in detail. It is also well known that, within the local universe ($z \lesssim 0.3$), the fraction of galaxies which host a radio source, i.e. the radio-loud fraction, is a very steep function of host galaxy stellar mass ($f_{\mathrm{radio-loud}} \propto M_*^{2.5}$, Best et al. 2005b; Janssen et al. 2012), increasing to > 30 per cent at stellar masses above $5 \times 10^{11}\,\mathrm{M}_\odot$ for radio luminosities $> 10^{23}\,\mathrm{W\,Hz^{-1}}$. At these redshifts the radio-loud AGN population is dominated by LERGs (Best et al. 2006) so when the radio-loud fraction for HERGs is considered separately, the mass-dependence is much shallower, $f_{\mathrm{radio-loud}} \propto M_*^{1.5}$ (Janssen et al. 2012). Furthermore, the fraction of radio-loud AGN for the two classes have different realtionships with radio luminosity, galaxy color and star formation rate. Red (passive) galaxies are a factor of a few times more likely to host LERGs than blue (star-forming) galaxies of the same stellar mass. Blue galaxies show a higher probability of hosting HERGs at all radio luminosities. Moreover, for blue galaxies, the likelihood of hosting any radio AGN is a strong positive function

of the SFR. The presence of cold, star-forming gas in a galaxy clearly enhances the probability of its central BH becoming a radio-loud AGN. This means that LERG activity, especially at high radio luminosities, is not solely related to hot halo gas accretion (Heckman & Best 2014). In studying the radio-loud fraction at $z \approx 1-2$, Williams & Röttgering (2015) found more than an order of magnitude difference in the fraction of lower mass galaxies ($M_* < 10^{10.75}$ $M_\odot$) which host radio-loud AGN with radio powers $P_{150\,\mathrm{MHz}} > 10^{24}\,\mathrm{W\,Hz^{-1}}$. The key open question is how the radio loud fraction, and radio source duty cyce, depend on host galaxy masses and colours for HERGs and LERGs at higher redshifts.

The main distinguishing point between HERGs and LERGs is their optical spectra. Best et al. (2014) provide the largest sample of intermediate redshift ($z < 1$) that is spectroscopically classified into jet- and radiative mode AGN. In order to pursue studies with large samples at higher redshift a method is needed that does not require spectroscopy. Mid-infrared (MIR) quasar-selection techniques (Stern et al. 2005; Donley et al. 2012; Stern et al. 2012) are insufficient as they do not select all high excitation sources. Neither does selecting on X-ray emission alone (e.g. Hickox et al. 2009). Using high power sources out to $z \approx 4$, all of which have optical spectroscopy, Gürkan et al. (2014) have recently suggested that there is a clear division between LERGs and HERGs in the mid-IR-radio plane and a simple cut in 22 μm luminosity can separate the populations. In this paper we attempt to classify a sample of radio-loud AGN as HERGs and LERGs based on fits to their broad-band spectral energy distributions (SEDs), and use this to study the radio-loud fraction for the two populations between $0.5 \leqslant z < 2$.

This paper is structured as follows: The LOFAR 150 MHz radio data is described in Section 6.2 and the multiwavelength datasets and catalogues we use are described in Section 6.3. In Section 6.4 we use SED fitting to determine photometric redshifts and galaxy parameters for the sample of optical galaxies. Section 6.5 describes our method for identifying optical counterparts to the LOFAR radio sources. Section 6.6 describes the selection of a well-defined sub-sample of radio-loud AGN and further SED fitting to classify sources from this radio-loud AGN sample as HERGs and LERGs. Throughout this paper we use Vega magnitudes and a concordance cosmology with $\Omega_M = 0.3$, $\Omega_\Lambda = 0.7$, and $H_0 = 70\,\mathrm{km\,s^{-1}\,Mpc^{-1}}$.The spectral index, α, is defined as $S_\nu \propto \nu^\alpha$, where S is the source flux density and ν is the observing frequency. We assume a spectral index of -0.8 unless otherwise stated.

6.2 Radio Data

We use the radio data described by Williams et al. (2015, submitted). The 8 hr observation was taken with the LOw Frequency ARray (LOFAR; van Haarlem et al. 2013) using the High Band Antennae (HBA) and covering the frequency range 130–169 MHz, with a central frequency of ≈ 150 MHz. Particular care was taken in the calibration and imaging to correct for direction-dependent effects (DDEs) caused by the ionosphere and imperfect knowledge of the LOFAR station beam shapes. This DDE calibration and imaging was achieved with the 'Facet' calibration scheme presented by van Weeren (prep, submitted). The resulting image covers 19 deg^2, with an rms noise of $\approx 120-150\,\mu\mathrm{Jy\,beam^{-1}}$. Assuming a spectral index of -0.8, the sensitivity of this map is comparable to the $28\,\mu\mathrm{Jy\,beam^{-1}}$ rms of the WSRT, 1.4 GHz, image made by de Vries et al. (2002). However, the LOFAR resolution of 5.6×7.4 arcsec, compared to 13×27 arcsec at 1.4 GHz, combined with its positional accuracy of < 1 arcsec makes it significantly better for the optical identification of the radio sources. The LOFAR 150 MHz radio source catalogue contains 5 652 sources detected with a peak flux density threshold of 5σ, where σ is the local rms

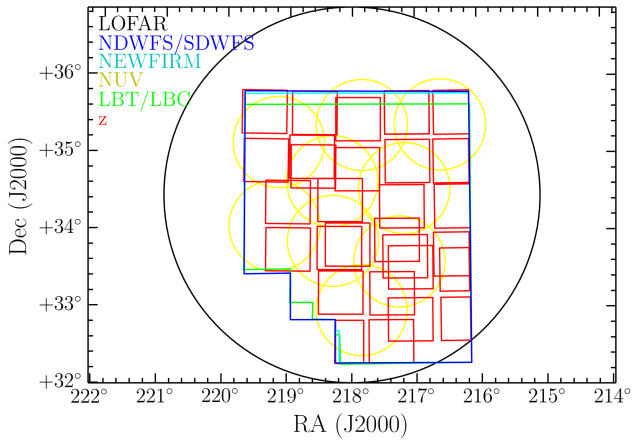


Figure 6.1: Coverage diagram for the Boötes field. The black circle shows the LOFAR 150 MHz coverage. The blue polygon shows the main I-selected psf-matched catalogue region, which is covered completely by both the NDWFS ($B_W RIK$) and SDWFS (3.6, 4.5, 5.8, and 8.0 μm). It covers a total of 9.1 deg^2, when regions contaminated by bright stars are excluded. The red squares show the zBoötes coverage, which has some gaps. The yellow circles show the GALEX NUV coverage. There is a small area not covered by the NEWFIRM survey (J, H, and K_s, shown in cyan) and the LBT/LBC survey ($U_{\rm spec}$, and Y, shown in light green).

noise. The radio coverage is shown as a circle in Fig. 6.1.

6.3 Multiwavelength Data

The Boötes field is one of the widest of the famous deep extragalactic fields and was originally targeted as one of two fields within the National Optical Astronomy Observatory (NOAO) Deep Wide Field Survey (NDWFS; Jannuzi et al. 1999). Since then it has been surveyed across the electromagnetic spectrum. We describe here the surveys and datasets that are used in this work.

6.3.1 Combined Photometry Catalogue

The primary catalogue that we make use of is the combined I-band-selected psf-matched photometry catalogue presented by Brown et al. (2007, 2008). This catalogue includes 15 bands spanning 0.14–24 μm and combines several different surveys. We describe here briefly the data sets that are included in this catalogue.

The NDWFS included observations in the optical (B_W, R, and I) and the NIR (K) bands. The areal coverage in these four bands is ≈ 9.3 deg^2. The photometry catalogue is based on the third NDWFS data release[1]. The B_W, R, I, and K-band images reach depths of 26.7, 25.5, 24.9, and 18.6 mag (5σ within a 2 arcsec diameter aperture) and with an absolute positional uncertainty of the sources of < 0.1 arcsec. The *Spitzer* Deep, Wide-field Survey (SDWFS; Ashby et al. 2009) is a four-epoch MIR survey covering 10 deg^2 using the InfraRed Array Camera (IRAC) instrument on the *Spitzer* Space Telescope, which provides images at 3.6, 4.5, 5.8, and 8.0 μm. The

[1]Available from the NOAO Science Archive at `http://www.archive.noao.edu/ndwfs/`.

average 5σ, 4 arcsec-diameter, aperture-corrected limits are 19.77, 18.83, 16.50, and 15.82 mag at 3.6, 4.5, 5.8, and 8.0 μm respectively. The Multiband Imaging Photometer (MIPS) AGN and Galaxy Evolution Survey (MAGES; Jannuzi et al. 2010) provided 24 μm images from *Spitzer*. Further and deeper NIR imaging comes from the NOAO Extremely Wide-Field Infrared Imager (NEWFIRM; Autry et al. 2003) survey[1], which provides J, H and K_s imaging down to a 5σ depth of approximately $J = 22$, $H = 20.8$, $K_s = 19.5$ mag within a 3 arcsec diameter aperture. z-band photometric imaging covering 7.62 deg^2 comes from the zBoötes survey (Cool 2007), which was performed with the 90Prime wide-field imager (Williams et al. 2004) at prime focus on the Bok 2.3 m Telescope located on Kitt Peak. There are some gaps in the coverage of the Boötes field (see Fig. 6.1) resulting from the 10 arcmin gaps in the instrument CCDs. The zBoötes survey is complete (at the 50 per cent level) to 22.7 mag over 50 per cent of the field. Bian et al. (2013) have performed a survey using the Large Binocular Camera (LBC) mounted on the 2×8.4 m Large Binocular Telescope (LBT) in binocular mode, which provides imaging in the $U_{\rm spec}$ ($\lambda_0 = 3590$Å, FWHM $= 540$Å), and Y-bands ($\lambda_0 = 9840$Å, FWHM $= 420$Å) covering 9 deg^2. They give a 5σ depth in the $U_{\rm spec}$-band of 25.5 mag. Finally, there is UV coverage of the Boötes field from GALEX/GR6 (Martin et al. 2003; Bianchi et al. 2014) which includes NUV (1800–2750Å) and FUV (1400–1700Å) imaging. The FUV coverage, however, is limited (< 25 per cent) so we exclude it in later analysis.

Brown et al. (2007) have constructed a combined psf-matched catalogue by regridding and smoothing the individual released survey images to a common scale so that the stellar point-spread function (PSF) is a Moffat profile with a full width at half-maximum (FWHM) of 1.35 arcsec and $\beta = 2.5$ for the B_w-, R-, I-, Y-, H, K-, and K_s-bands and with a FWHM of 1.6 arcsec for the u-, z- and J-bands. PSF fluxes are extracted from these images for all the sources in the I-band using SExtractor (Bertin & Arnouts 1996). For the remaining bands, aperture fluxes were extracted. Regions surrounding very extended galaxies and saturated stars were excluded. The final sample area is 9.1 deg^2. The geometry of the Boötes field is shown in Fig. 6.1.

6.3.2 Additional Multiwavelength Surveys

The Boötes field has been surveyd in the X-ray band: XBoötes is a 5 ks survey which was performed with ACIS-I on the *Chandra* X-Ray Observatory (Murray et al. 2005). This is a large (9.3 square degree) contiguous region imaged in the X-ray that has complementary deep optical and NIR observations. The source catalogue (Kenter et al. 2005) contains 3, 293 sources down to a 4 count flux limit, corresponding to 4.7×10^{-15} erg s^{-1} cm^{-2} in the soft band (0.5–2.0 keV), 1.5×10^{-15} erg s^{-1} cm^{-2} in the hard band (2.0–7.0 keV), and 7.8×10^{-15} erg s^{-1} cm^{-2} full X-ray band (0.5–7.0 keV). Brand et al. (2006) provide a catalogue of 3, 213 sources matched to the NDWFS DR3 catalogues using a Bayesian identification scheme.

Boötes is part of the *Herschel*[2] Multi-tiered Extragalactic Survey (HerMES; Oliver et al. 2012), which includes photometry using the Spectral and Photometric Imaging Receiver (SPIRE; Griffin et al. 2010) instrument at 250μm, 350μm, and 500μm. Within HerMES, Boötes has level 5 coverage of 3.25 deg^2 to 5σ noise levels of 13.8, 11.3, and 16.4 mJy and level 6 coverage of 10.57 deg^2 to 5σ noise levels of 25.8, 21.2, and 30.8 mJy. In this paper, we use the third data release (DR3) cross-identification catalogues based on *Spitzer* MIPS 24 μm source positions (Roseboom et al. 2010).

[1] `http://archive.noao.edu/nsa/NEWFIRM_NDWFS.html`

[2] Herschel is an ESA space observatory with science instruments provided by European-led Principal Investigator consortia and with important participation from NASA.

6.3.3 The AGN and Galaxy Evolution Survey

The AGN and Galaxy Evolution Survey (AGES; Kochanek et al. 2012) has provided redshifts for 23 745 galaxies and AGN across 7.7 deg^2 of the Boötes field. The survey used the Hectospec instrument (Fabricant et al. 2005) on the MMT to obtain 3700–9200 Å spectroscopy at a spectral resolution of 6 Å ($R \approx 1000$), and achieved a spectroscopic completeness of approximately 90 per cent (Kochanek et al. 2012; Cool et al. 2012). The median redshift of the galaxies in the survey is $\langle z \rangle = 0.3$, spanning the range $0 \lesssim z \lesssim 0.8$. However, the spectroscopic redshift completeness for the matched LOFAR sources at $z > 1$ is less than 50 per cent. For this reason we derive photometric redshifts, described in the following section. AGES also provides photometric redshifts, calculated using the LRT code by Assef et al. (2010) that fits a combination of an early-type, late-type, star forming, and (obscured) AGNs to the observed broadband SEDs. The photometry they used is a subset of that used in this work.

6.4 SED fitting

For the sample of $889,007$ optical sources in the Brown et al. (2007) psf-matched photometry catalogue with $m_I \leqslant 24$ mag, we perform spectral energy distribution (SED) fitting to determine photometric redshifts and galaxy parameters, including stellar mass, star formation rates and colours.

6.4.1 Photometric Redshifts

Photometric redshifts ($z_{\rm phot}$) are calculated for all galaxies using the EAZY software (Brammer et al. 2008). EAZY determines the $z_{\rm phot}$ for galaxies by fitting their SEDs to linear combinations of templates. We use an empirical set of templates derived from the atlas of 129 spectral energy distributions for nearby galaxies presented by Brown et al. (2014), with wavelength coverage spanning from the ultraviolet to the mid-infrared. This atlas spans a broad range of galaxy types, including ellipticals, spirals, merging galaxies, blue compact dwarfs, and luminous infrared galaxies. We select the subset of the Brown et al. (2014) templates given in their Appendix A. We found that this template set gave improved fits when including the MIR data points. A detailed description of EAZY's fitting process can be found in Brammer et al. (2008). Photometric redshifts were determined with EAZY primarily using the default set of parameters, using the Brown et al. (2014) templates, the K_s total magnitude prior, and allowed photometric redshift solutions in the range $0 < z < 6$.

The output EAZY photometric redshift catalogue contains the following columns:
Column 1 – id: Object identifier number
Column 2 – z_spec: Spectroscopic redshift, $z_{\rm spec}$, from AGES (-1 indicates no redshift available)
Column 3 – chi2: χ^2 of the best-fitting template
Column 4 – z_peak: Photometric redshift, $z_{\rm peak}$, from the peak of the $P(z)$ distribution
Columns 5 and 6 – l68, u68: Upper and lower 68 per cent confidence intervals on $z_{\rm peak}$
Columns 7 and 8 – l95, u95: Upper and lower 95 per cent confidence intervals on $z_{\rm peak}$
Columns 9 and 10 – l99, u99: Upper and lower 99 per cent confidence intervals on $z_{\rm peak}$
Column 11 – p_z: Peak probability, $P_{\rm peak}$
Column 12 – nfilt: Number of filters, $N_{\rm filt}$, used to determine $z_{\rm peak}$
The parameter $z_{\rm peak}$ corresponds to the peak probability of the $P(z)$ function, and is considered to be the most likely $z_{\rm phot}$. The 68 per cent and 95 per cent confidence intervals are calculated

Table 6.1: Sample photometric redshift catalogue.

id	$z_{\rm spec}$	χ^2	$z_{\rm peak}$	l68	u68	l95	u95	l99	u99	$P_{\rm peak}$	$N_{\rm filt}$
419194	-	3.4	1.569	1.099	2.092	0.699	2.545	0.207	2.853	0.998	12
420412	0.201	2.8	0.397	0.338	0.454	0.288	0.506	0.243	0.553	1.000	12
421383	-	6.0	0.427	0.285	0.578	0.172	0.673	0.084	0.768	1.000	13
421917	0.129	6.8	0.155	0.105	0.205	0.068	0.259	0.039	0.324	1.000	14
422118	0.778	29.2	0.779	0.687	0.870	0.596	0.933	0.515	0.996	0.999	14
424293	0.265	5.1	0.335	0.259	0.412	0.209	0.472	0.168	0.534	1.000	12
424369	-1.887	9.2	0.865	0.811	0.920	0.765	0.971	0.719	1.022	0.999	14
424393	-	9.6	1.506	1.363	1.659	1.272	1.805	1.188	1.988	0.999	13
424564	-	5.3	1.926	1.656	2.208	1.452	2.539	1.286	2.956	0.998	13
425016	0.267	1.2	0.352	0.287	0.416	0.239	0.471	0.198	0.516	1.000	12
425169	-	38.6	1.745	1.625	1.854	1.551	2.000	1.485	2.166	0.999	14
425332	0.126	26.6	0.470	0.306	0.609	0.224	0.680	0.168	0.751	0.999	14
426478	-	36.4	1.370	1.254	1.479	1.136	1.596	1.029	1.697	0.999	13
427404	0.212	15.2	0.374	0.298	0.443	0.223	0.547	0.170	0.646	1.000	14
427488	0.134	28.7	0.122	0.089	0.154	0.059	0.179	0.030	0.210	1.000	14

by integrating the $P(z)$ function. A sample of the photometric redshift catalogue is shown in Table 6.1.

Comparison with AGES Redshifts

In Fig. 6.2 we show a comparison between the EAZY $z_{\rm phot}$ and $z_{\rm spec}$ for the sources with good AGES spectroscopic redshifts (with a signal-to-noise > 5). In general, the photometric redshifts compare well to the spectroscopic redshifts, although we note that this comparison is primarily from galaxies at $z_{\rm spec} < 1.0$. Galaxies that are $> 3\sigma$ outliers from the one-to-one relation based on their redshift errors from EAZY are catastrophic outliers, the fraction of which is 1.8 per cent. As a measure of the accuracy of the photometric redshifts, we consider two quantities, computed after excluding the catastrophic outliers. The first goodness measure is the standard dispersion, $\sigma_z/(1+z)$, defined by

$$\left(\frac{\sigma_z}{1+z}\right)^2 = \frac{1}{N}\sum_{i=1}^{N}\left(\frac{z^i_{\rm phot} - z^i_{\rm spec}}{1+z^i_{\rm spec}}\right)^2. \quad (6.1)$$

The second is the normalized median absolute deviation, or NMAD, of the residuals, defined as NMAD$(\Delta z) = 1.48 \times$ Median(Δz), where $\Delta z = (z_{\rm phot} - z_{\rm spec})/(1+z_{\rm spec})$. We measure $\sigma_z/(1+z) = 0.09$ and NMAD $= 0.057$. It is well known that photometric redshifts are poorly determined for AGN (Brodwin et al. 2006; Rowan-Robinson et al. 2008; Assef et al. 2010, e.g.), and should preferably be fit using different methods (e.g. Salvato et al. 2009, 2011). We compare the $z_{\rm phot}$ and $z_{\rm spec}$ for normal galaxies and AGN separately in Fig. 6.3. For this we use the sources flagged as AGN by Assef et al. (2010), which is based on their having a significant contribution by an AGN SED template. Excluding the galaxies selected as AGN in AGES, we find that the photometric redshifts are more accuarate for normal galaxies, with $\sigma_z/(1+z) = 0.079$

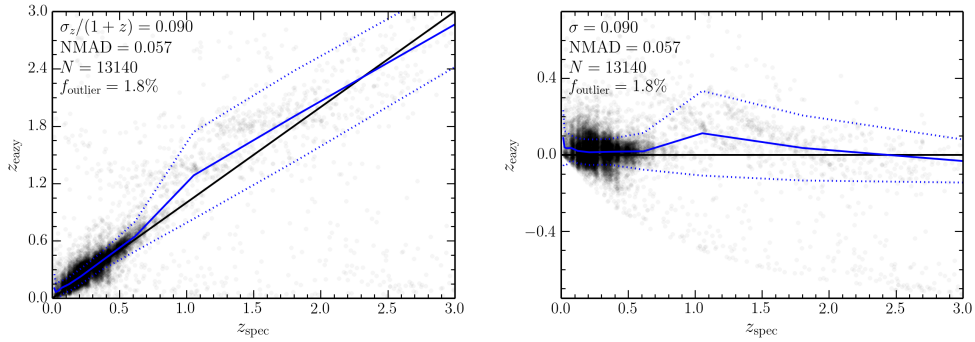


Figure 6.2: *Top panel* Photometric redshifts from the Boötes I-selected catalogue vs. spectroscopic redshifts from the AGES catalogue. Only galaxies with high-quality spectroscopic redshifts and uncontaminated photometry are shown. *Bottom panel* Difference between spectroscopic redshift and photometric redshift as a function of spectroscopic redshift. The solid and dotted blue curves show respectively the median and rms dispersion of $\delta z = (z_{\rm phot} - z_{\rm spec})/(1 + z_{\rm spec})$, within 11 logarithmic-spaced bins across the spectroscopic redshift range.

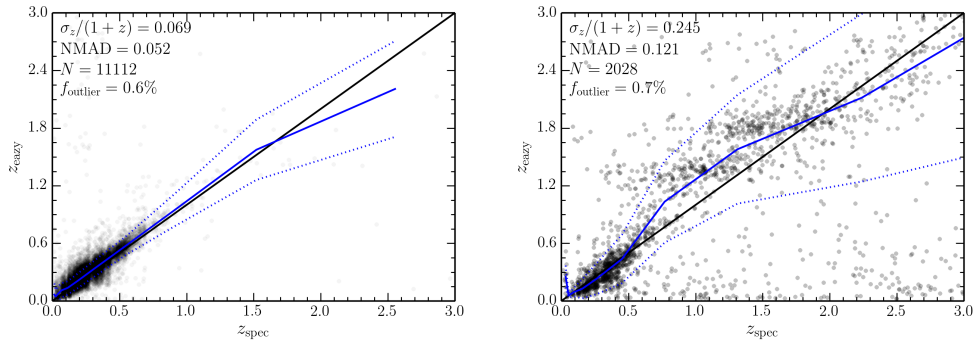


Figure 6.3: Photometric redshifts from the Boötes I-selected catalogue vs. spectroscopic redshifts from the AGES catalogue. *Left panel* Only galaxies not indicated as AGN in the AGES catalogue are plotted. *Right panel* Sources indicated to be AGN by the AGES SED fitting. The solid and dotted blue curves show respectively the median and rms dispersion of $\delta z = (z_{\rm phot} - z_{\rm spec})/(1 + z_{\rm spec})$, within 11 logarithmic-spaced bins across the spectroscopic redshift range.

and NMAD $= 0.039$. Considering only the AGES AGN, we find $\sigma_z/(1 + z) = 0.24$ and NMAD $= 0.12$.

Assef et al. (2010) determine their redshifts to be more accurate, with $\sigma_z/(1 + z) = 0.04$ for normal galaxies $\sigma_z/(1+z) = 0.18$ for point-like AGN. Although the photometric redshifts calculated here are not as good as those available from AGES, the sample is larger and complete, and the additional SED-fitting provides additional galaxy parameters (described in the next section). For comparison, the most accurate photometric redshift available typically have $\sigma_z/(1 + z) \lesssim 0.01$ (e.g. Ilbert et al. 2009; Muzzin et al. 2013a), but using 30 bands of broad, intermediate and narrow width, and typically do not fit the longer wavelength MIR bands.

Table 6.2: Sample FAST catalogue.

id	$z_{\rm peak}$	$\log(\tau)$	$\log(t)$	A_V	$\log(\mathrm{M}_*/M)$	$\log(sfr)$	$\log(ssfr)$	χ^2
419194	1.56	10	9.4	0.8	10.08	0.84	-9.24	0.523
420412	0.21	8.5	9.0	2.0	10.62	0.97	-9.65	1.670
421383	0.41	7	7.8	1.2	8.82	-0.79	-9.61	0.754
421917	0.11	7.5	7.0	2.6	9.05	2.00	-7.04	3.370
422118	0.76	9	9.2	1.2	10.57	1.19	-9.38	4.340
424293	0.26	10	9.0	2.0	10.46	1.62	-8.84	2.700
424369	0.86	8.5	9.2	1.0	11.02	0.57	-10.44	1.230
424393	1.51	9.5	9.0	1.8	11.18	2.29	-8.89	1.500
424564	1.91	10	8.6	2.2	10.9	2.44	-8.46	0.327
425016	0.26	7	8.4	1.8	10.3	-7.13	-17.43	2.540
425169	1.76	7	7.4	1.0	10.07	2.09	-7.98	3.850
425332	0.11	7.5	7.4	3.0	8.77	1.25	-7.52	4.490
426478	1.36	9.5	9.0	1.8	10.97	2.09	-8.89	5.250
427404	0.21	10	8.8	2.2	10	1.35	-8.65	4.280
427488	0.11	7	7.0	3.0	8.72	1.51	-7.20	4.640

6.4.2 Stellar Masses, Star Formation Rates and Rest-frame Colours

Stellar population parameters are determined by fitting galaxy SEDs using the FAST code (Kriek et al. 2009), based on the Bruzual & Charlot (2003) models. We assume solar metallicity, a Chabrier (2003) initial mass function (IMF), and a Calzetti et al. (2000) dust extinction law. The template SEDs are constructed in the standard way (see e.g. Muzzin et al. 2013a), assuming exponentially declining star formation histories (SFHs) of the form SFR $\propto \exp(-t/\tau)$, where t is the time since the onset of star formation and τ is the e-folding star formation timescale in units of Gyr. All galaxies are fit assuming their redshift is the best-fit EAZY $z_{\rm phot}$. In all, four parameters are determined per galaxy: τ , t, A_V, and a normalization. The stellar mass (M_*) is then determined from mass-to-light ratio of the best-fit SED multiplied by the best-fit normalization of the SED. The layout of the catalogue of stellar population parameters is:
Column 1 – id: Object identifier number
Column 2 – z: Photometric redshift, $z_{\rm peak}$ from EAZY
Column 3 – ltau: Best-fit value of $\log(\tau)$
Column 4 – lage: Best-fit value of $\log(t)$
Column 5 – Av: Best-fit value of A_V
Column 6 – lmass: Best-fit value of $\log(\mathrm{M}_*/M)$
Column 7 – lsfr: Best-fit value of $\log(sfr)$ from the SED
Column 8 – lssfr: Best-fit value of $\log(ssfr)$ from the SED
Column 9 – chi2: χ^2 of best-fitting model
A sample of the FAST catalogue is shown in Table 6.2. We compare the stellar masses derived by FAST with a stellar mass calculated from the rest-frame colour, $g-i$, and absolute magnitude, M_i, (Taylor et al. 2011). This is shown in Fig. 6.4. There is good agreement between the two values across three orders of magnitude in mass.

Rest-frame colours are derived using InterRest (Taylor et al. 2009) with the EAZY photo-

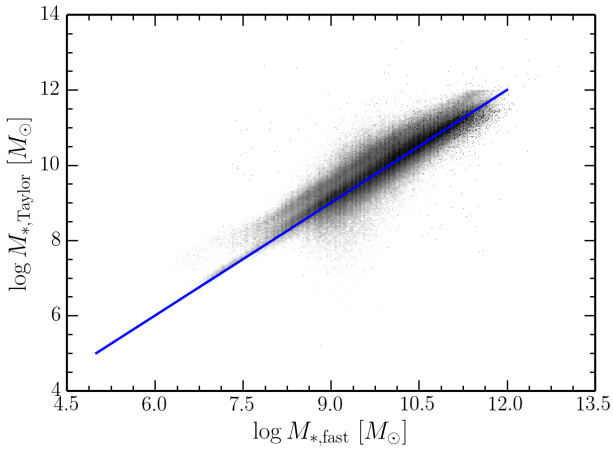


Figure 6.4: Comparison between stellar mass determined from FAST and rest-frame colour, $g - i$, and absolute magnitude, M_i. The greyscale shows log density.

metric redshifts. We determine colours for the ${}^{0.1}u$ and ${}^{0.1}r$ bands, defined as the AB magnitudes in the SDSS u and r bands at $z = 0.1$. These colours allow straightforward comparison to SDSS results (e.g. Blanton et al. 2003c,b; Kauffmann et al. 2003; Blanton et al. 2003a).

6.5 Optical identification of Radio Sources

In this section we describe the identification of optical counterparts, from the I-band-selected optical catalgoue described in Section 6.3, matched to the LOFAR radio sources, described in Section 6.2. We use the likelihood ratio (LR) method (Richter 1975) to quantify the probability of an I-band optical source being the true host of a given radio source. The LR method has been further developed by Prestage & Peacock (1983); Benn (1983); Wolstencroft et al. (1986) and Sutherland & Saunders (1992). Here we use the methodology outlined by Tasse et al. (2008a). Prior to the LR estimate, we inspect the images of each of the radio sources overlaid upon the corresponding I-band images, and classify their radio morphologies into different classes.

6.5.1 Visual Classification

In order to identify the host galaxies of radio sources, the true location of the host galaxy with respect to radio source should be known. Following Best et al. (2003) and Tasse et al. (2008a) we determine a strong subjective a priori of this location for each source by visually inspecting all the radio-optical images and dividing them into the following classes based on the radio morphology:
Class 1: For these sources the radio emission is assumed to be coincident with the optical emission (detected or not). This occurs in sources such as starburst galaxies, compact core dominated radio sources or radio sources where the radio core can be clearly identified. In these cases, the errors on the radio and optical positions can be used in a statistical way to identify the optical counterpart of each radio source. We note that because of some bandwidth- and time-smearing

in the LOFAR image (see Williams et al. 2015, submitted), we consider some radio sources which appear resolved to be unresolved point sources.
Class 2: In the case that no radio core is identified (such as for classical double lobe FRII (Fanaroff & Riley 1974) radio sources, only a weak a priori can be considered for the optical host position. The position of the host and associated errors are estimated based on the location of the multiple Gaussian fitting components, described in more detail in Best et al. (2003)
Class 3: When the environment has a large effect on the radio morphology, the flux weighted radio centroid and associated errors can be very far from the real optical host. We use the combination of radio morphology and optical properties (such as an elongated lobe pointing to a bright optical object), to infer the position of the optical counterpart. These sources are matched visually on a case-to-case basis and the statistical method described below cannot be used.
Class 4: These are clearly resolved and diffuse radio sources whose morphology is not suggestive of jets. This includes 'radio halos' and 'relics', typically found in clusters. These sources have been excluded from further analysis.
Class 5: When the radio source overlaps a bright saturated source, we have classified the source as Class 5. These sources likely have contaminated photometry and have been excluded in further analysis.

6.5.2 Likelihood Ratio

For the Class 1 and Class 2 sources we employ a statistical method to determine the optical counterparts to the radio source. The probability that an optical I-band source is the true optical counterpart of a given radio source is determined from the likelihood ratio (LR; Sutherland & Saunders 1992; Tasse et al. 2008a), defined as:

$$LR(r,m) = \frac{\theta(<m)\exp\left(-\frac{r^2}{2}\right)}{2\pi\sigma_\alpha\sigma_\delta\rho(<m)}, \tag{6.2}$$

where m is the I-band magnitude of the optical candidate, $\theta(<m)$ is the a priori probability that a radio source has an observed optical counterpart with magnitude $<m$, and $\rho(<m)$ is the surface number density of objects with magnitude $<m$. The parameter r is the uncertainty-normalised angular distance between the radio core and the optical host candidate, defined as $r^2 = (\Delta\alpha/\sigma_\alpha)^2 + (\Delta\delta/\sigma_\delta)^2$, where Δ is the positional difference, σ is the uncertainty, and α and δ are the right ascension and declination respectively. For each α and δ, the uncertainty is the quadratic sum of the uncertainty on the radio position, $\sigma_{\rm radio}$, and on the optical position, $\sigma_{\rm opt}$. We adopt an optical astrometry accuracy of $\sigma_{\rm opt} \approx 0.5$, independent of the magnitude m_I. The accuracy of the radio position, $\sigma_{\rm radio}$, is different for every source and depends on the local noise level in the radio data and the Gaussian fitting parameters (Williams et al. 2015, submitted). The probability $P_{id}(i)$ of the i-th candidate being a true identification is:

$$P_{id}(i) = \frac{LR_i(r,m)}{\sum_j LR_j(r,m) + [1-\theta(m_{\rm lim})]}, \tag{6.3}$$

where $\theta(m_{\rm lim})$ is the fraction of radio sources having detected optical counterparts at the limiting magnitude of the survey, i refers to the candidate under consideration and j runs over the set of all possible candidates. We estimate the association probability assuming that θ and ρ depend only on the object magnitude m, which is taken as the I-band magnitude of the optical candidate.

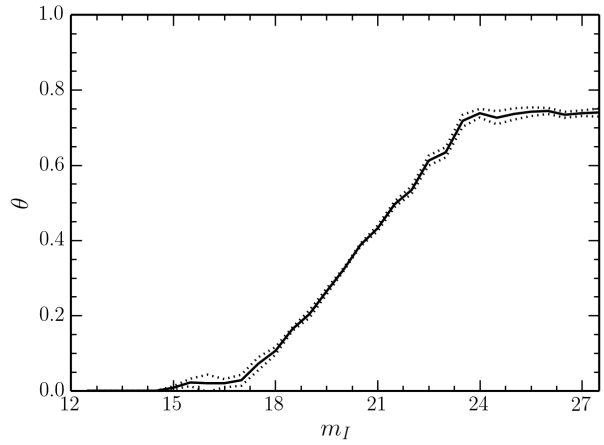


Figure 6.5: Fitted $\theta(< m)$, the a priori probability that a radio source has an observed optical counterpart with magnitude $< m$, as a function of the limiting magnitude. This is determined by simulating random radio and optical catalogues with a known fraction of radio sources and comparing to the observed distribution.

For each radio source we calculate the density function $\rho(m)$ within 2 arcmin of the radio source centroid, in order to account for the variation of the surface density with position, or clustering of optical sources. To estimate the function $\theta(< m)$, we follow the methodology of Tasse et al. (2008a). This involves simulating random radio and optical catalogues with a known fraction of radio-optical matches and comparing the simulated radio-optical separation distribution to the real distribution. We consider discrete I-band magnitude cuts in the interval $13 < i < 24$ with an increment $\Delta m_I = 0.2$. For each of these cuts a radio catalogue having uniformly distributed positions is generated, along with a set of optical catalogues. Each optical catalogues in the set is generated by assigning a given fraction, $\theta(< m)$, of radio sources an optical counterpart. The optical hosts of radio sources then have their positions scattered by the radio and optical positional uncertainties. The distribution of the angular distance between radio sources and their closest object in the optical catalogue is then computed and compared to the real distribution through a Kolmogorov-Smirnov test. The retained fraction, $\theta(< m)$, is the one corresponding to the maximum Kolmogorov-Smirnov probability. For each I-band magnitude cut, the test is repeated 10 times, to estimate an error on $\theta(< m)$. Fig. 6.5 shows the variation of $\theta(< m)$ with the limiting magnitude.

6.5.3 Match Results

Of the 5 652 sources in the LOFAR 150 MHz catalogue, 3 317 lie within the boundary of the optical catalogue and may therefore have potential optical-counterparts. Of these 3 317 sources, we found 2 555 sources with optical counterparts with $m_I < 24$ mag for 2 326 unique radio sources (70 per cent). The majority of these sources were classified as Class 1 (3, 033, 92 per cent), 113 sources (3.4 per cent) were classified as Class 2, 33 sources (1 per cent) were classified as Class 3, and 24 sources (1 per cent) were classified as Class 4. The remaining sources are Class 5 sources, with bad optical photometry. Some examples of the Class 1 and 2 sources with LR-

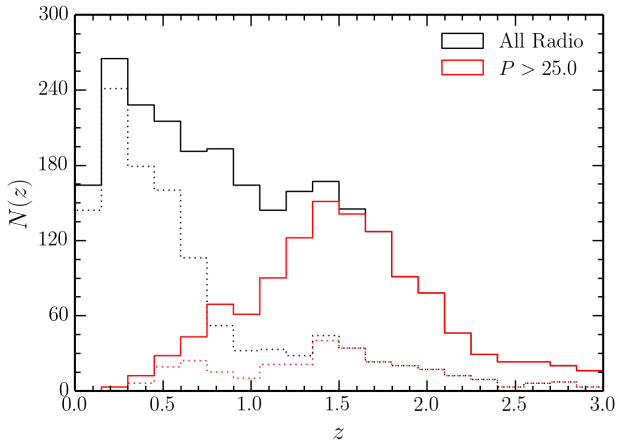


Figure 6.6: Redshift distribution. The high power sample defined in Section 6.6.2 is plotted in red and the full radio-optical sample is plotted in grey. The spectroscopic redshift distribution for each is plotted with dotted lines.

matched optical sources are shown in Fig. 6.A.1 and Fig. 6.A.2 respectively in Appendix 6.A.

Fig. 6.6 shows the redshift distribution of all the matched radio-optical sources. A small number (30) of sources have photometric redshifts in the range $3 < z < 6$. The dotted lines in this image show the distribution of sources with spectroscopic redshifts from AGES – the low completeness of which motivates the need for a complete sample with photometric redshifts. Throughout the rest of this paper we adopt the $z_{\rm spec}$ from AGES where possible, else we use the EAZY $z_{\rm phot}$. The radio-power versus redshift for these sources is shown in Fig. 6.7.

6.5.4 Contamination

In order to estimate the level of contamination by random matches, we generated 15 radio catalogues by randomising the positions of the sources in the real radio catalogue. We then cross-matched these 15 random radio catalogues with the optical sources in the same manner as described in the previous section. The distribution of optical identifications in optical magnitude m_I and stellar mass are plotted in Fig. 6.8. The contamination is high for sources with low stellar masses. The total contamination is ≈ 15 per cent for sources with stellar masses $M_* < 10^{12}\,{\rm M}_\odot$. However, for sources with stellar masses $M_* < 10^9\,{\rm M}_\odot$ the contamination exceeds 90 per cent. We therefore, do not consider stellar masses below this value in later analysis.

6.6 Properties of Radio Sources

6.6.1 Local Reference Sample

As a local comparison sample we use the catalogue compiled by Best & Heckman (2012). This matched radio-optical catalogue was constructed by from the seventh data release (DR7; Abazajian et al. 2009) of the Sloan Digital Sky Survey (SDSS) spectroscopic sample and the NRAO Very Large Array (VLA) Sky Survey (NVSS; Condon et al. 1998) and the Faint Images of the

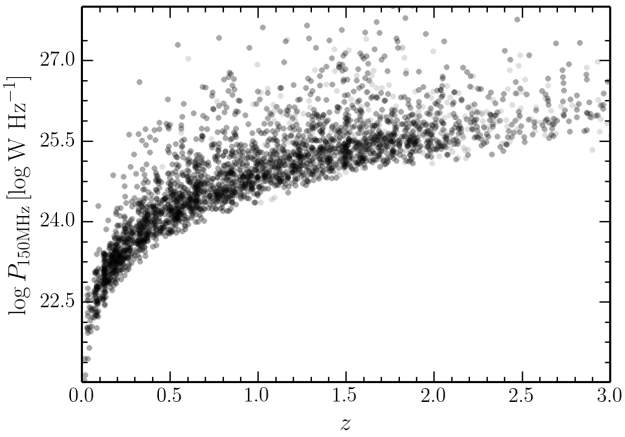


Figure 6.7: Distribution in the radio power vs. redshift plane of the matched radio-optical sources.

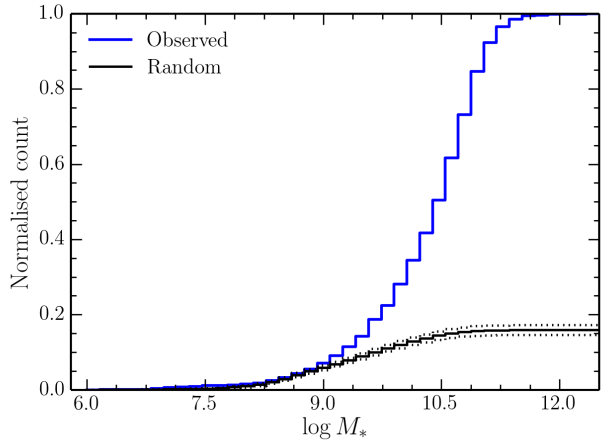


Figure 6.8: Stellar mass distributions for the observed sample (blue) and the 15 random radio catalogues (black). The total contamination is ≈ 15 per cent.

Radio Sky at Twenty centimetres (FIRST; Becker et al. 1995). The optical data includes parameters from the value-added spectroscopic catalogues (VASC) created by the Max Plank Institute for Astrophysics and Johns Hopkins University (MPA-JHU) group[1] (Brinchmann et al. 2004). This includes information from the imaging data such as magnitudes and sizes (York et al. 2000), as well as derived properties including the stellar mass (Kauffmann et al. 2003). The spectroscopy also provides D_n4000 (Balogh et al. 1999), a measure of the galaxy colour. Best & Heckman (2012) separated the sources into star-forming galaxies and RL AGN (7302 sources), which are further sub-divided into HERGs, LERGs and star forming (SF) galaxies, based on their optical photometric and spectroscopic parameters. Noting the different observed radio frequency, we select sources with $P_{150\,\mathrm{MHz}} > 10^{24}\,\mathrm{W\,Hz^{-1}}$, corresponding to $P_{1.4\,\mathrm{GHz}} > 10^{25}\,\mathrm{W\,Hz^{-1}}$, assuming a spectral index of $\alpha = -0.8$. This local radio-optical sample consists of 3736 radio sources between $0.01 < z \leqslant 0.3$.

6.6.2 Subsample Selection

The aim of this paper is to study the population of radio-loud AGN at intermediate redshifts. The radio power is plotted as a function of redshift in Fig. 6.7, for all the matched LOFAR-optical sources. At low redshifts, $z \lesssim 0.3$, the radio-optical sample is dominated by low luminosity radio sources and contains very few high power sources, while at higher redshifts we can only probe high power sources. For this reason we can not use this sample to directly compare high luminosity sources at both low and high redshift. The shallow wide LOFAR surveys will provide the areal coverage needed for such a comparison low redshift sample.

The rms in the radio map varies across the field of view (see Williams et al. 2015, submitted) between 100–250 μJy beam^{-1}, meaning that at a given redshift the lowest power sources can only be detected over a smaller area. We make a relatively low cut on radio flux of $S_{151\ \mathrm{MHz}} \geqslant 0.5$ mJy, and account for incompleteness resulting from the varying detection area later. From the $P - z$ plane it is clear that at $z = 2$ we can observe sources only with radio powers above $P_{150\,\mathrm{MHz}} \geqslant 10^{25}\,\mathrm{W\,Hz^{-1}}$. In this paper we therefore study only the high power sources at intermediate redshifts $0.5 \leqslant z < 2$. The final sample consists of 974 sources, which we divide the sample in to three redshift intervals:

1. $0.5 \leqslant z < 1.0$ (173 sources),
2. $1.0 \leqslant z < 1.5$ (336 sources),
3. $1.5 \leqslant z < 2.0$ (273 sources).

Note that at radio powers $P_{150\,\mathrm{MHz}} \gtrsim 10^{25}\,\mathrm{W\,Hz^{-1}}$ (corresponding to $P_{1.4\,\mathrm{GHz}} \gtrsim 10^{24}\,\mathrm{W\,Hz^{-1}}$, for a spectral index of -0.8), the samples should consist almost entirely of radio-loud AGN – we expect very little contamination from star-forming galaxies. The star formation rate for this radio power is in excess of $25\,\mathrm{M_\odot\,yr^{-1}}$ (Condon 1992).

6.6.3 IR SED fitting

While Gürkan et al. (2014) have suggested that a single cut in 22 μm flux can be used to separate LERGs and HERGs, our investigation using the complete lower luminosity sample from Best & Heckman (2012) indicates that this may be a result of selection effects (Rigby et al. 2015, in prep.). We therefore attempt to separate these sources based on further SED fitting to determine

[1] available at `http://www.mpa-garching.mpg.de/SDSS/`.

the AGN and galaxy contribution to their IR emission. For this fitting we have included the FIR fluxes of these sources at 250 μm, 350 μm, and 500 μm by matching to the HerMES catalogue for the Boötes Field (Oliver et al. 2012). The *Herschel* fluxes were found by matching the nearest neighbour to the optical positions within the *Herschel* beam sizes at each wavelengths. About 70 per cent of the sources have a detection in HerMES at either 250 μm or 350 μm. The FIR fluxes provide an important constraint to separate the starformation and AGN components. In order to decompose the SEDs of the sources we fit all the available multiwavelength photometry, including FIR, using the MCMC-based algorithm AGNfitter (Calistro Rivera et al. 2015, in prep). We have done this for the sub-sample of 974 sources.

An advantage of using AGNfitter is that it infers the probability density functions (PDFs) of the fitting parameters. This allows correlations and degeneracies among parameters to be recognised and allows for a robust calculation of the uncertainties for the inferred parameter values. The total active galaxy model in AGNfitter consists of the superposition of the host galaxy emission and the nuclear AGN emission. The host galaxy is modelled as a combination of a stellar emission and the reprocessed emission of cold/warm dust in starburst (SB) regions. At nuclear scales, the AGN emission is modelled as a combination of an accretion disk component (Big Blue Bump) and a hot dust torus component (or other obscuring structure).

The parameters of interest for our purposes are the disentangled host galaxy and AGN luminosities that contribute to the IR emission. While the AGN contribution, which affects specifically the MIR regime, arises mainly from the torus luminosity L_{TO}, the contribution from galaxy emission takes into account both the stellar emission L_{GA} and the reprocessed emission by cold/warm dust L_{SB}, since both have contributions in the MIR. For the matter of comparison, these luminosities are integrated over the respective templates in a single wavelength range $1\,\mu\text{m} < \lambda < 8\,\mu\text{m}$.

A small fraction of sources (183, $\approx$ 7 per cent) have very poor fits, i.e. have AGNfitter likelihood values < -100. These are excluded in further analysis. Some examples of the AGNfitter SEDs with components in the three redshift intervals are shown in appendix 6.B in Fig. 6.B.1 and Fig. 6.B.2 for sources with good quality fits (quantified by likelihood values close to -1) and in Fig. 6.B.3 for sources with poor fits (quantified by likelihood values $\lesssim -20$).

As a test of the robustness of the AGNfitter results, we compare the stellar masses and SFRs returned by AGNfitter to those we have derived using FAST (see Section 6.4.2). This comparison is shown in Fig. 6.9. While the two codes are used to fit the same data (with the exception that the FIR data is included for the AGNfitter fits), the fitting methods and templates used are independent.

HERG/LERG separation

We aim to differentiate between HERGs ('cold mode' or 'radiative mode' sources), and LERGs ('hot mode' or 'jet mode' sources) based on their broadband SED information. In the remainder of the paper we use the nomenclature of HERGs and LERGs for succinctness. From the AGNfitter output we calculated the value,

$$f_{TO} = \frac{L_{TO}}{L_{TO} + L_{GA}}, \tag{6.4}$$

which is a measure of the fraction of IR-emission that is coming from the torus with respect to that from the galaxy, independent of the starburst component. The error of f_{TO} is calculated by propogating the errors on L_{TO} and L_{GA} given by AGNfitter. The distribution of f_{TO} values

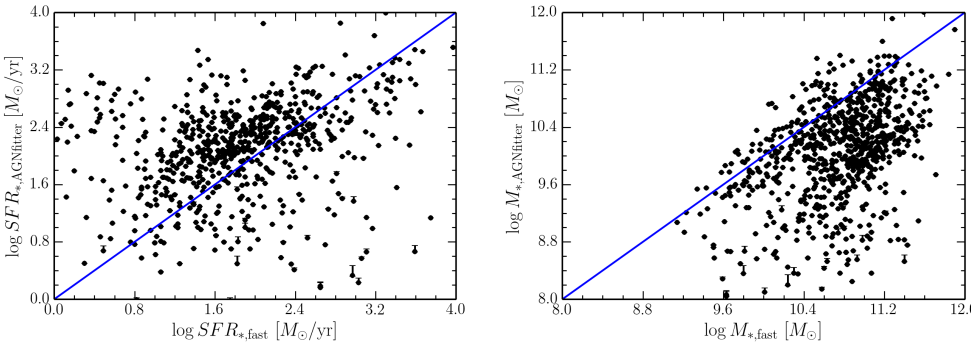


Figure 6.9: Comparision between SFR (*left*) and stellar mass (*right*) determined by FAST and AGNFITTER.

is plotted in Fig. 6.10, where we show the distribution for all radio sources, and for within each of the three redshift intervals. We expect that HERGs have significant contribution to the IR emission from the torus (or obscuring structure), and that LERGs have little or no such contribution. There is a maximum in the overall distribution for sources with $0.9 < f_{TO} < 1$, and a minimum at $0 < f_{TO} < 0.1$, and we note that there is a difference in the distribution at $0.5 < z \leqslant 1.0$ compared to the two higher redshift intervals. The two highest redshift intervals both show the significant maximum at $f_{TO} \approx 1$ and minimum at $f_{TO} \approx 0$, which suggests that there are more 'strongly AGN-dominated' sources and fewer 'AGN-free' sources in these intervals than at $0.5 < z \leqslant 1.0$. Given the uncertainties in the SED fitting procedure, it is unclear where to place a boundary which would separate sources that contain IR AGN emission, i.e. HERGs, from those that contain completely no IR AGN, which would be LERGs. Theoretically, LERGs would have $f_{TO} \approx 0$, however, they may appear with non-zero values due to errors in the photometry and fitting. We therefore choose a conservative boundary value of $f_{TO} = 0.25$ and classify sources with $f_{TO} < 0.25$ as LERGs and $f_{TO} > 0.25$ as HERGs. This uncertainty highlights the need to perform similar SED fitting for a sample with spectroscopic classification of HERGs and LERGs, in particular for this specific set of photometry. For this reason follow-up spectroscopy of these optically-identified LOFAR radio sources will be valuable.

The example AGNFITTER SEDs shown in Figs. 6.B.1, 6.B.2 and 6.B.3 include both HERGs and LERGs classified in this way in each redshift interval. The number of HERGs and LERGs in each redshift interval are given in Table 6.3, including those taken from the local reference sample, from which it can be seen that the fraction of HERGs increases between $0.5 \leqslant z < 1.0$ and $1.0 \leqslant z < 1.5$. The percentage of HERGs and LERGs within each redshift interval is given with respect to the total number of radio sources in that interval.

6.6.4 Star Formation contribution

Similarly, we define the quantity

$$f_{SB} = \frac{L_{SB}}{L_{SB} + L_{GA}}, \tag{6.5}$$

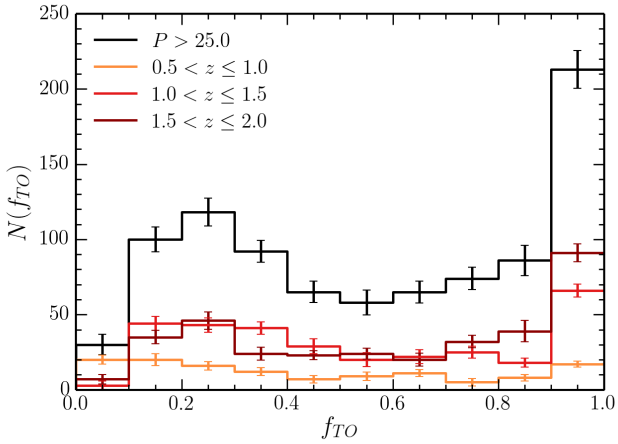


Figure 6.10: Distribution of the fraction of IR torus emission, f_{TO}, defined by equation 6.4 for the full sample (black), and the three redshift intervals: $0.5 \leqslant z < 1.0$ (orange), $1.0 \leqslant z < 1.5$ (red), and $1.5 \leqslant z < 2.0$ (dark red).

Table 6.3: Number of sources classified as HERGs and LERGs in the reference sample and the three redshift intervals.

z	N	LERGs (%)	HERGs (%)
0.01–0.3	3736	3066 (96%)	121 (4%)
0.5–1.0	173	52 (30%)	121 (69%)
1.0–1.5	384	72 (18%)	312 (81%)
1.5–2.0	390	67 (17%)	321 (82%)

Table 6.4: Two-sided Kolmogorov-Smirnov statistics in comparing the HERG and LERG distributions in colour and mass within each redshift interval.

z	$^{0.1}(u-r)$		$\log M_*/\mathrm{M}_\odot$	
	K-S statistic	p-value	K-S statistic	p-value
0.5–1.0	0.56	$1.1 \cdot 10^{-10}$	0.52	$2.1 \cdot 10^{-9}$
1.0–1.5	0.24	$1.4 \cdot 10^{-3}$	0.29	$1.0 \cdot 10^{-4}$
1.5–2.0	0.38	$1.8 \cdot 10^{-7}$	0.39	$4.4 \cdot 10^{-8}$

as a measure of the fraction of IR-emission that is coming from star formation with respect to that from the galaxy, independent of the AGN torus emission. The error of f_{SB} is calculated by propogating the errors on L_{SB} and L_{GA} given by AGNfitter. In Fig. 6.B.1 we show examples of sources with high f_{SB} values for HERGs and LERGs in the three redshift intervals, and in 6.B.2 we show examples of sources with low f_{SB} values. The distribution of f_{SB} values is plotted separately for HERGs and LERGs in Fig. 6.11, where we show the distribution for all radio sources, and for within each of the three redshift intervals. LERGs have a peak at $f_{SB} \approx 0$ in all redshift intervals, with a secondary peak at $f_{SB} \approx 1$ in the two higher redshift intervals. This is suggestive of a population of LERGs in star forming galaxies. HERGs, on the other hand, have a peak at $f_{SB} \approx 1$ with a secondary peak at $f_{SB} \approx 0$. The peak at $f_{SB} \approx 1$ is largely due to the two highest redshift intervals. It is interesting to note that some HERGs are found in galaxies with very little star formation.

6.6.5 Colour-mass distribution

Having classified the sources as HERGs and LERGs based on their AGN contribution in the MIR, we now study the distribution of the radio-loud AGN with respect to their optical host colours and masses. For the local reference sample we plot the colour, given by the spectroscopic D_n4000 value, against the stellar mass Fig. 6.12. In Figs. 6.13, 6.14, and 6.15 we show, for each redshift interval, a plot of the $^{0.1}(u-r)$ colour versus stellar mass for optical sources and radio sources. The f_{TO} values for the radio sources are shown in colour and the distributions of stellar mass and colour are shown for the optical sources, the radio sources and the HERGs and LERGs. In comparing the local and higher redshift samples, we note that the parameters used are different, for both the colour and mass, and the HERG/LERG separation. However, they provide a qualitative comparison, for the distribution of the radio and optical source populations in colour-mass space. In all redshift intervals it is clear that the distributions of optical and radio sources are different, as expected. In all cases the radio source distribution is skewed towards more massive galaxies and redder galaxies compared to the full galaxy population. The distributions of HERGs and LERGs are also different, in that the HERGs occur over a wider range of stellar masses $10^9 < M_*/\mathrm{M}_\odot < 10^{11.5}$ and over a wider range of colours. LERGs are much more likely to be in massive red galaxies. We use a two-sided Kolmogorov-Smirnov test, and in all cases can reject the null hypothesis that the distributions are the same. The Kolmogorov-Smirnov statistics and p-values are given in Table 6.4. We note that in these plots the radio source population is slightly incomplete due to the varying rms in the LOFAR map (see Section 6.6.2).

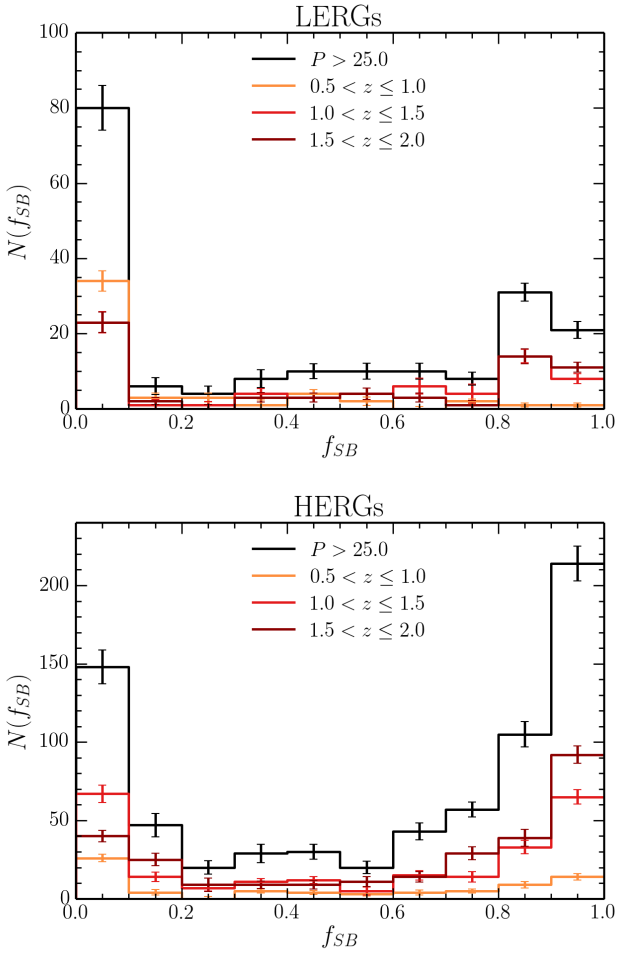


Figure 6.11: Distribution of the fraction of SB emission, f_{SB}, defined by equation 6.5, separately for LERGs (*top*) and HERGs (*bottom*), for the full sample (black), and the three redshift intervals: $0.5 \leqslant z < 1.0$ (orange), $1.0 \leqslant z < 1.5$ (red), and $1.5 \leqslant z < 2.0$ (dark red).

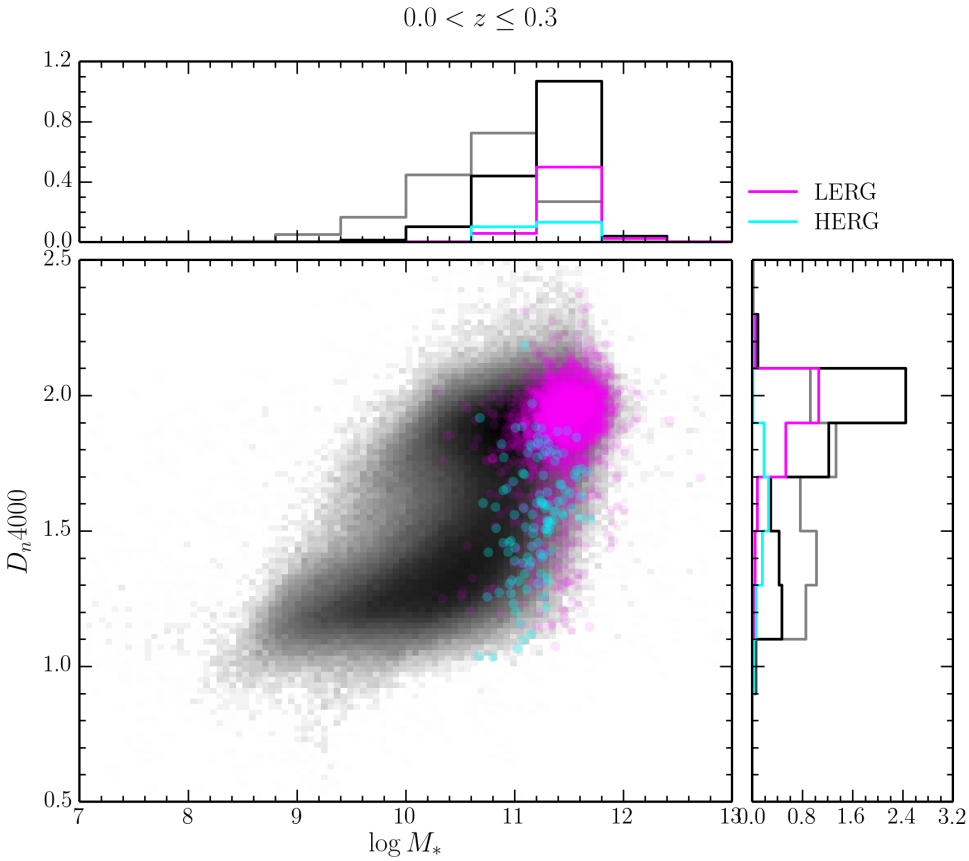


Figure 6.12: Colour, D_n4000, versus stellar mass in the redshift interval $0.01 \leqslant z < 0.3$ (*main* panel). The density of optical sources is plotted in black, in log units, and the radio sources are plotted in cyan (HERGs) and magenta (LERGs). The subpanels show the stellar mass (*top*) and colour distributions (*right*). The normalised distribution of optical sources is shown in grey, and that of all the radio sources in black. The HERGs and LERGs are shown in cyan and magenta respectively, normalised to the total number of radio sources. The HERG distributions is multiplied by a factor of 10 for visibility.

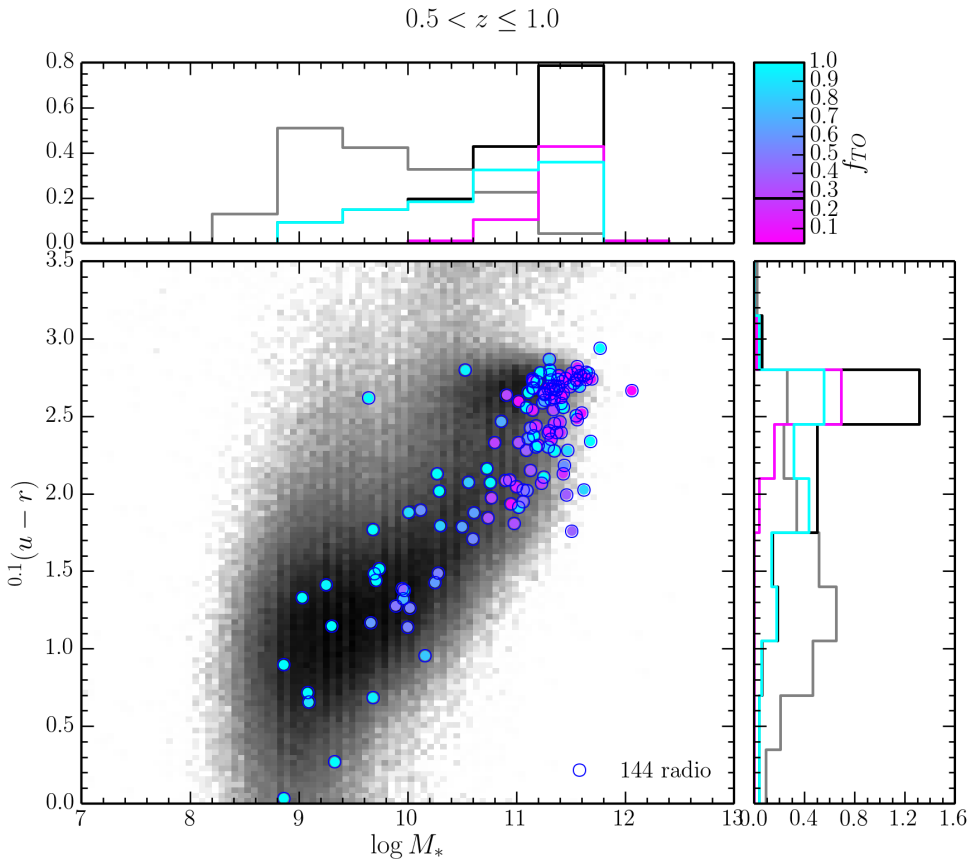


Figure 6.13: Colour, $^{0.1}(u-r)$, versus stellar mass in the redshift interval $0.5 \leqslant z < 1.0$ (*main* panel). The density of optical sources in the Boötes field is plotted in black, in log units, and the radio sources are plotted with blue circles, with the fill-colour indicating their f_{TO} values. Open circles show failed AGNFitter fits. The subpanels show the stellar mass (*top*) and colour distributions (*right*). The normalised distribution of optical sources is shown in grey, and that of all the radio sources in black. The HERGs and LERGs (separated at $f_{TO} = 0.25$) are shown in cyan and magenta respectively, normalised to the total number of radio sources.

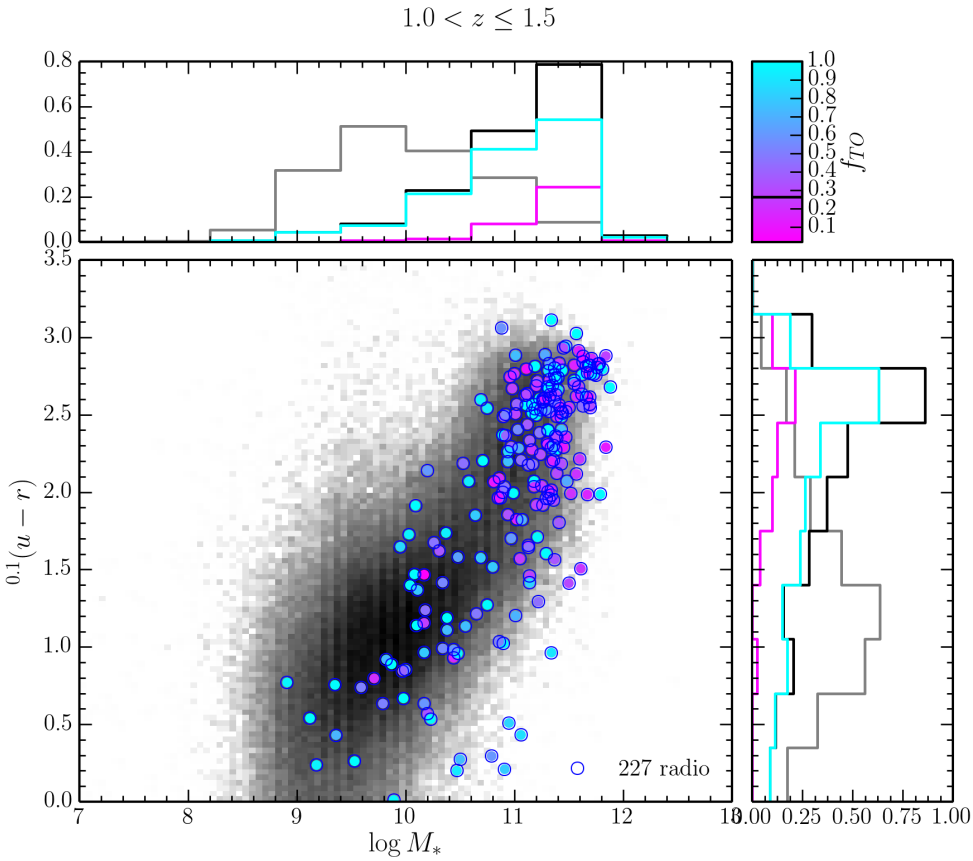


Figure 6.14: As for Fig. 6.13, but for the redshift interval $1.0 \leqslant z < 1.5$

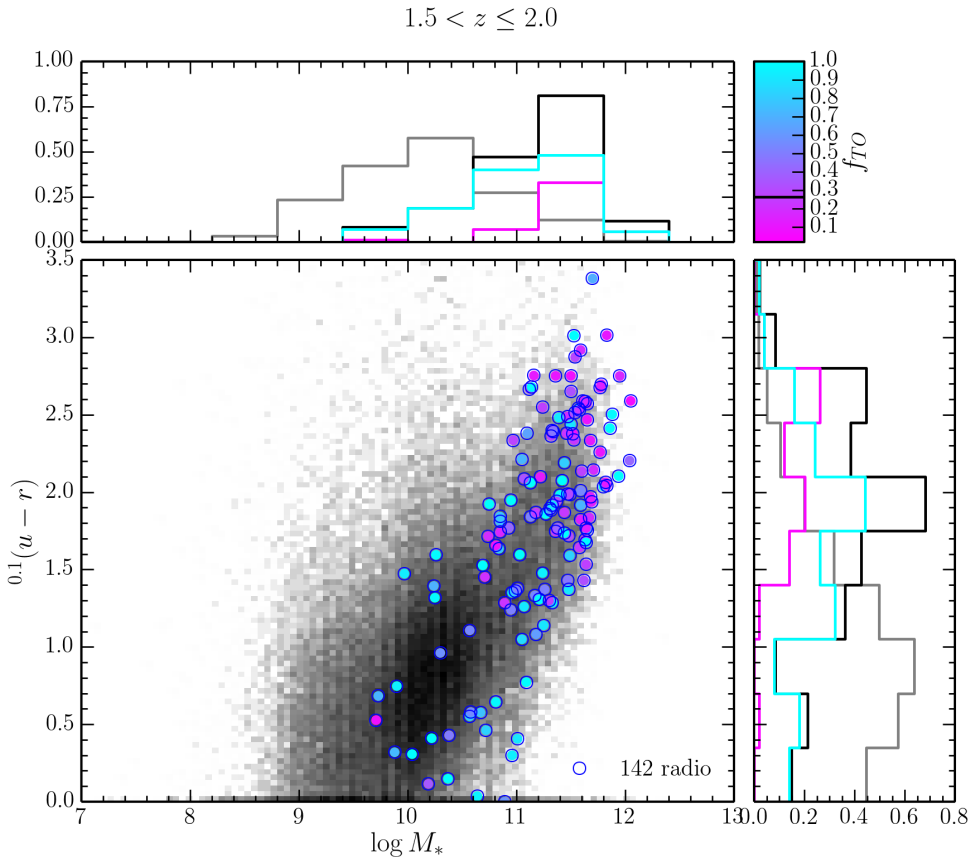


Figure 6.15: As for Fig. 6.13, but for the redshift interval $1.5 \leqslant z < 2.0$.

Table 6.5: Slope of the radio-loud fraction as a function of mass for HERGs and LERGs in the three redshift intervals.

z	All	LERGs	HERGs
0.5–1.0	1.25 ± 0.15	2.08 ± 0.28	0.93 ± 0.11
1.0–1.5	1.12 ± 0.10	1.70 ± 0.13	0.99 ± 0.09
1.5–2.0	1.05 ± 0.04	1.86 ± 0.21	0.93 ± 0.06

6.6.6 Radio-loud fraction

The mass-dependence of the radio-loud fraction can be an indicator of the accretion mode of the radio-AGN largely because of the different dependence of the fuelling source (hot vs. cold gas) on stellar mass (Best et al. 2006). As this is not a volume-limited sample, we use the radio-loud fraction defined by:

$$f_{\rm RL}^{y,x} = \left(\sum_{\rm i \in R^{y,x}} \frac{1}{V_{\rm max}^{i}} \right) \left(\sum_{\rm j \in A^{y,x}} \frac{1}{V_{\rm max}^{j}} \right)^{-1} , \tag{6.6}$$

where the sets A and R are, respectively, all galaxies and all radio sources in a given bin, defined by the parameters of colour, x, and excitation state, y. $V_{\rm max}$ is the maximum accessible volume over which each source can be observed, using the Schmidt (1968) and Condon (1989) formalism. This is determined by the flux limits of both the optical (< 24 mag) and radio data ($S_{151\ \rm MHz} \geqslant 0.5$ mJy). The maximum volume also takes into account the visibility area from the radio data, i.e. the area in which the radio source could be detected based on the varying rms map.

The radio-loud fraction for all radio sources, and separately for HERGs and LERGs is shown in Fig. 6.16. It can be seen that the radio-loud fraction for all sources at all masses increases with redshift. The dependence on stellar mass is flatter for HERGs than it is for LERGs at all redshifts. Table 6.5 gives the value of the slope fit to $\log f_{RL}$–$\log M_*/{\rm M}_\odot$ over the range $10^9 < M_*/{\rm M}_\odot < 10^{11.5}$. These results are consistent with those from many of the earlier radio surveys, which suggest that the most powerful radio galaxies ($P_{1.4\,\rm GHz} \gtrsim 10^{26}$ W Hz^{-1}) at $z \gtrsim 1$ are predominantly HERGs hosted by the most massive galaxies (e.g. Eales et al. 1997; Jarvis et al. 2001; Seymour et al. 2007; Fernandes et al. 2015).

In colour-magnitude space (not shown here), we use the empirically determined cuts to separate red and blue galaxies (Hickox et al. 2009) using the quantity:

$$A = {}^{0.1}(u - r) + 0.08\,(M_{0.1r} + 20)\,. \tag{6.7}$$

We use their median values of A for the red sequence of $A_{\rm red} = 2.64$ in our first redshift interval and $A_{\rm red} = 2.52$ in our second and third redshift intervals. The boundary between red and blue galaxies is set 0.3 mag blueward of the median values of A for the red sequence. The numbers of blue and red LERGs (BLERGs and RLERGs respectively) and HERGs (BHERGs and RLERGs respectively) within each redshift interval are listed in Table 6.6. This table also gives the fraction of each subgroup with respect to the number of radio-loud sources in each redshift interval. For the local reference sample, we use the D_n4000 parameter to determine colour: sources with $D_n4000 < 1.575$ are blue and sources with $D_n4000 \geqslant 1.575$ are red.

We then calculate the radio-loud fraction separately for each subgroup. This is shown in Fig. 6.17. The fraction of BHERGs increases at all masses with redshift, while the fraction of

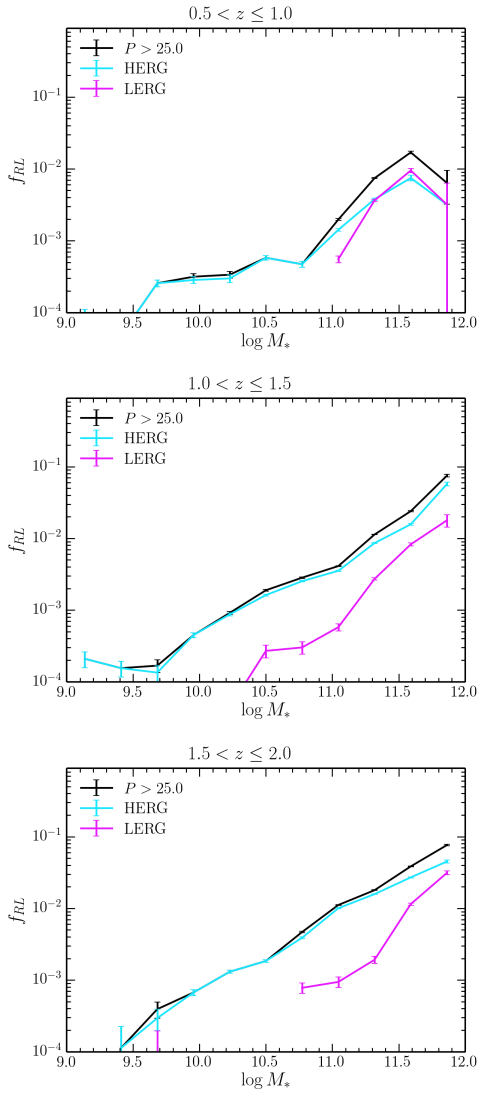


Figure 6.16: The fraction of galaxies hosting a radio source (radio-loud fraction) as a function of stellar mass for a radio-power cut-off of $P_{150\,\mathrm{MHz}} > 10^{25}\,\mathrm{W\,Hz^{-1}}$ in the three redshift bins. The errors are determined from Poisson statistics. All radio sources are plotted in black, HERGs in cyan and LERGs in magenta.

Table 6.6: Number of sources classified as blue and red HERGs and LERGs in the reference sample and the three redshift intervals.

z	N	BLERGs (%)	RLERGs (%)	BHERGs (%)	RHERGs (%)
0.01–0.3	3736	148 (3.9%)	2918 (78%)	61 (1.6%)	60 (1.6%)
0.5–1.0	173	17 (9%)	32 (18%)	89 (51%)	28 (16%)
1.0–1.5	384	52 (13%)	20 (5%)	248 (64%)	57 (14%)
1.5–2.0	390	55 (14%)	12 (3%)	301 (77%)	10 (2%)

RHERGs decreases. Janssen et al. (2012) have studied the radio-loud fraction for red, green and blue HERGs and LERGs in the local Universe ($0.03 \leqslant z \leqslant 0.3$). Since their colour-cut was made on the spectroscopic D_n4000 value, we can only qualitatively compare our results to those in their Fig. 4 for red and blue galaxies for their power cut of $P_{1.4\,\mathrm{GHz}} \geqslant 10^{24.5}\,\mathrm{W\,Hz^{-1}}$ (roughly equivalent to $P_{150\,\mathrm{MHz}} \geqslant 10^{25.5}\,\mathrm{W\,Hz^{-1}}$).

6.7 Conclusion

We have constructed a catalogue of photometric redshifts, stellar masses, and rest-frame colours via SED fitting of the multi-band photometry catalogue (Brown et al. 2007) available for the Boötes field. We have identified optical counterparts from this catalogue of sources to radio sources from the 150 MHz LOFAR observations of the Boötes field (Williams et al. 2015, submitted). For a well-defined sub-sample of 974 radio sources with optical matches between $0.5 \leqslant z < 2$ and radio-powers above $P_{150\,\mathrm{MHz}} > 10^{25}\,\mathrm{W\,Hz^{-1}}$, we have done additional SED fitting, including the FIR emission, to determine the relative contribution of AGN and galaxy emission in the MIR ($1\mu\mathrm{m} < \lambda < 8\mu\mathrm{m}$). From these results we have defined populations of HERGs and LERGs and studied the radio-loud fraction as a function of galaxy mass and colour. In summary, we have found the following:

1. The fraction of HERGs increases between $z = 0.5$ and $z = 2$;
2. While most LERGs are found in 'red and dead' (non-star forming) galaxies, at $z > 1$ there is a population of LERGs in star forming galaxies; and HERGs are found in both star forming and dead galaxies;
3. LERGs are predominantly found in more massive galaxies than HERGs;
4. LERGs are predominantly found in redder galaxies, but at higher redshifts are bluer;
5. The radio-loud fraction for blue HERGs increases with redshift while that for red HERGs decreases with redshift for all masses

6.7.1 Future work

There remain a few open questions and issues relating to this work. These include the following:

1. The incorporatation of the errors from AGNfitter in the determination of f_{TO} will enable us to investigate how they affect the resulting radio-loud fractions.

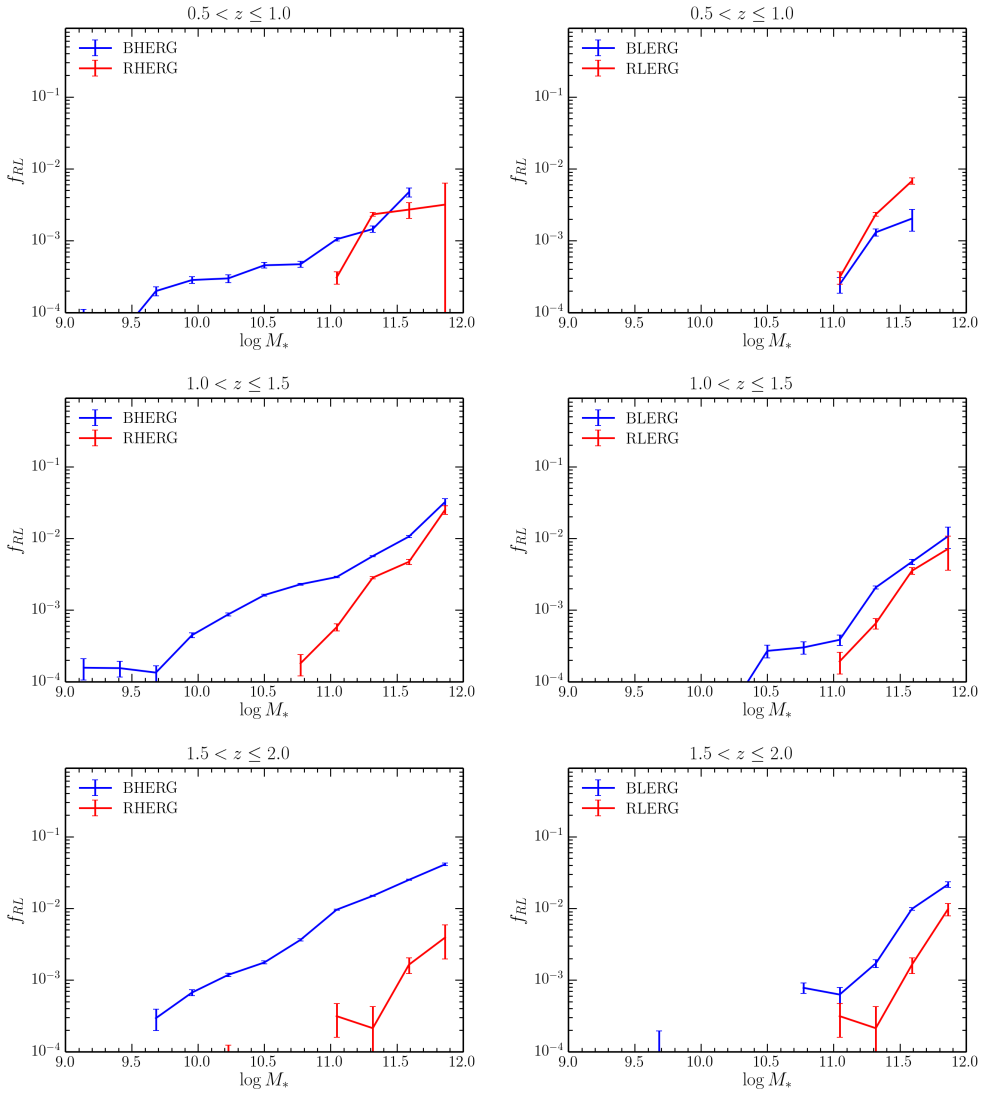


Figure 6.17: The fraction of red and blue galaxies hosting a radio source as a function of stellar mass for a radio-power cut-off of $P_{150\,\mathrm{MHz}} > 10^{25}\,\mathrm{W\,Hz^{-1}}$ in the three redshift bins (*top* to *bottom*) for HERGs (*left*) and LERGs (*right*). The errors are determined from Poisson statistics.

2. It is important to understand how the AGN populations determined using the f_{TO} values from SED fitting, described in Section 6.6.3, relate to the spectroscopically-classified populations. This could be done by comparing the AGNFitter output for spectroscopically classified sources. Initially this should involve using AGNFitter to investigate how f_{TO} varies for existing specotrocopically-classified HERGs and LERGs. In the future, follow-up spectroscopy of this sample will shed light on the quality of the f_{TO} results for this dataset.
3. We have no comparison sample at low redshift with which to directly track the evolution from $z \approx 0$. This will be possible with the wide area surveys currently underway with LOFAR, combined with the SDSS-NVSS sample (Best & Heckman 2012)

Acknowledgements

WW, HJR gratefully acknowledge support from the European Research Council under the European Union's Seventh Framework Programme (FP/2007-2013) /ERC Advanced Grant NEW-CLUSTERS-321271. This research has made use of data from HerMES project[1]. HerMES is a Herschel Key Programme utilising Guaranteed Time from the SPIRE instrument team, ESAC scientists and a mission scientist. The HerMES data was accessed through the Herschel Database in Marseille (HeDaM[2]) operated by CeSAM and hosted by the Laboratoire d'Astrophysique de Marseille.

Appendix

6.A Radio-Optical Matches

Some examples of the Class 1 and 2 sources with LR-matched optical sources are shown in Fig. 6.A.1 and Fig. 6.A.2 respectively.

6.B Example SED fits

Some examples of the AGNFitter SEDs with components in the three redshift intervals are shown in Fig. 6.B.1 and Fig. 6.B.2 for sources with good quality fits (quantified by likelihood values close to -1) and in Fig. 6.B.3 for sources with poor fits (quantified by likelihood values $\lesssim -20$). These include both HERGs and LERGs in each redshift interval.

[1] http://hermes.sussex.ac.uk/
[2] http://hedam.lam.fr

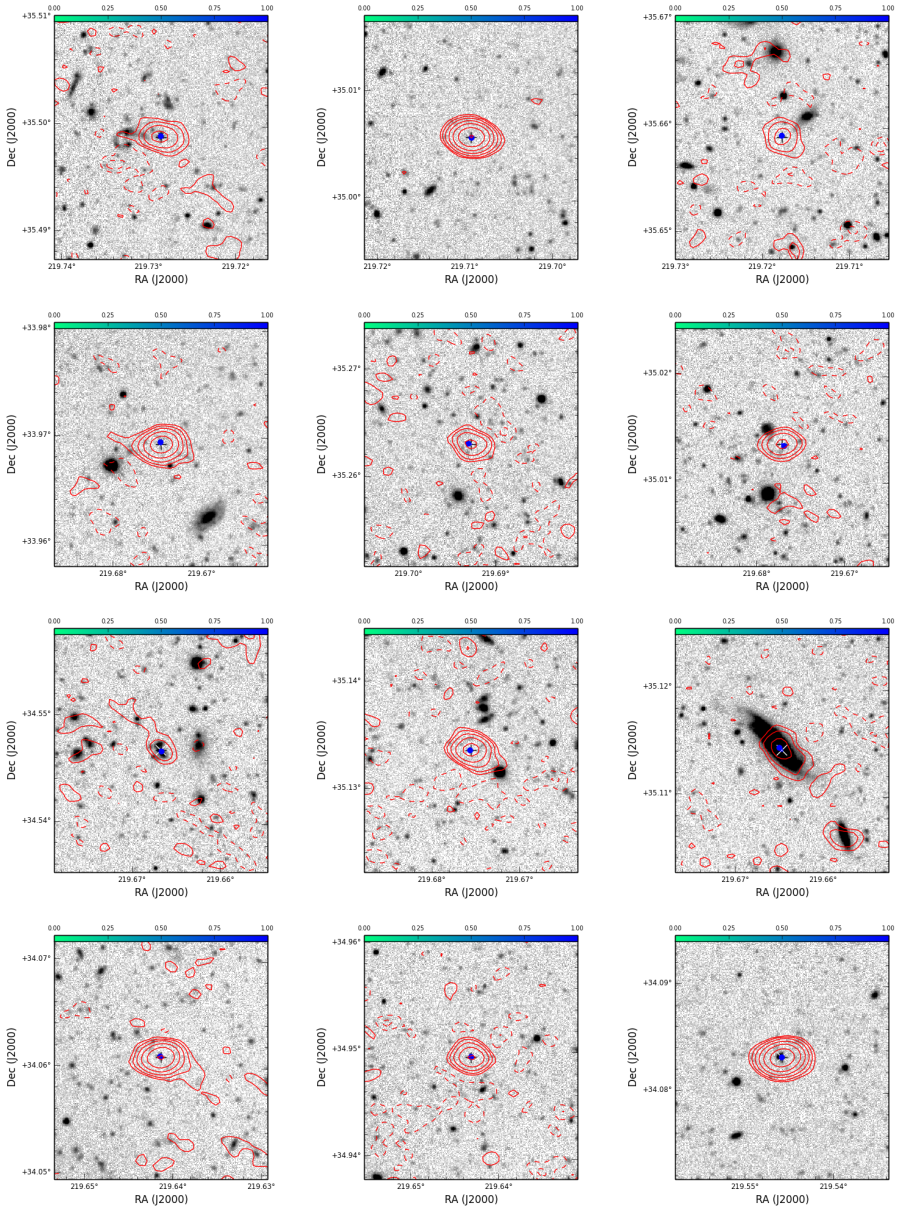


Figure 6.A.1: Examples of the radio-optical cross matches in Class 1. The greyscale image show the I-band NDWFS image. The red contours show the LOFAR $150\,\mathrm{MHz}$ image at levels of $3\sigma_{\mathrm{local}} \times [1, 1.4, 2, 2.8, \ldots]$ where σ_{local} is the local rms in the LOFAR map at the source position. The blue colorscale shows the LR probability of the matched optical source. Each image is $1.25\,\mathrm{arcmin}$ in diameter.

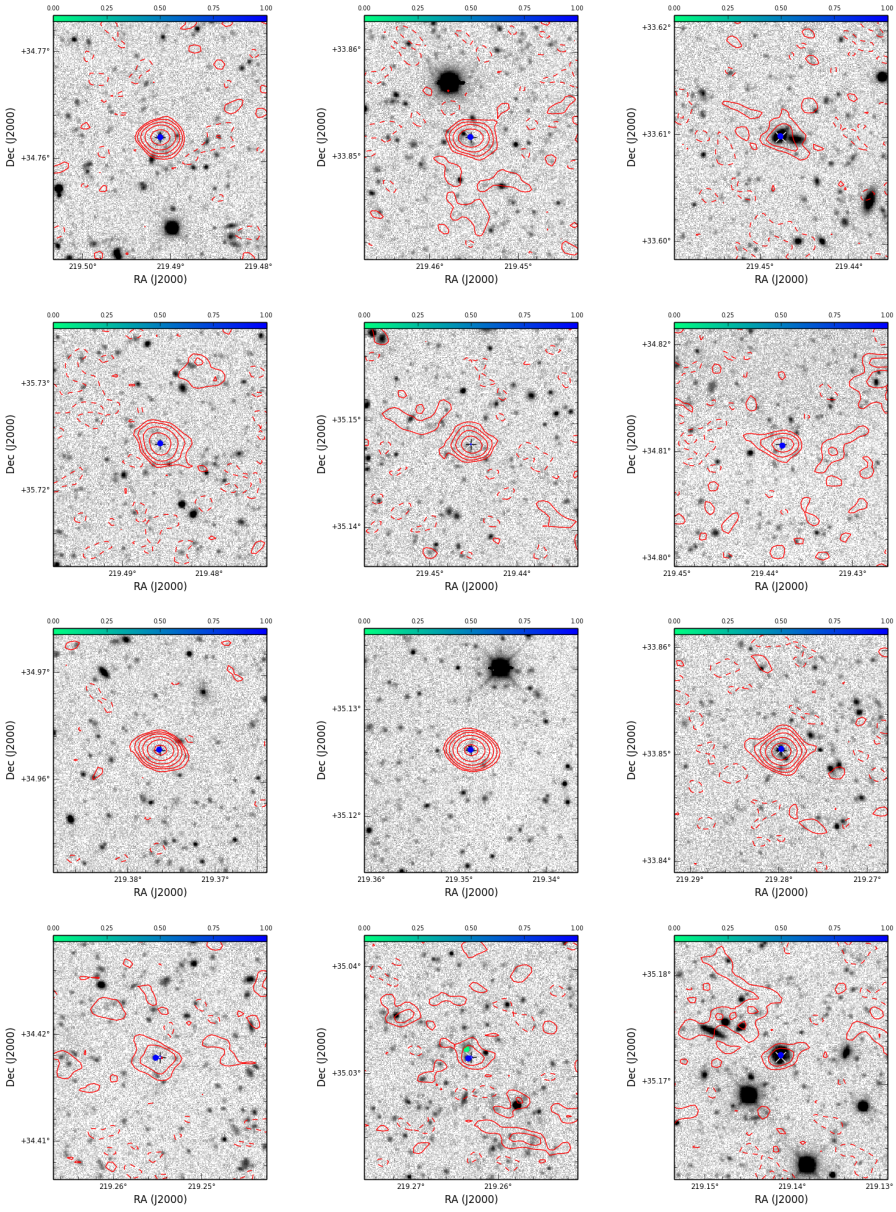


Figure 6.A.1: Cont.

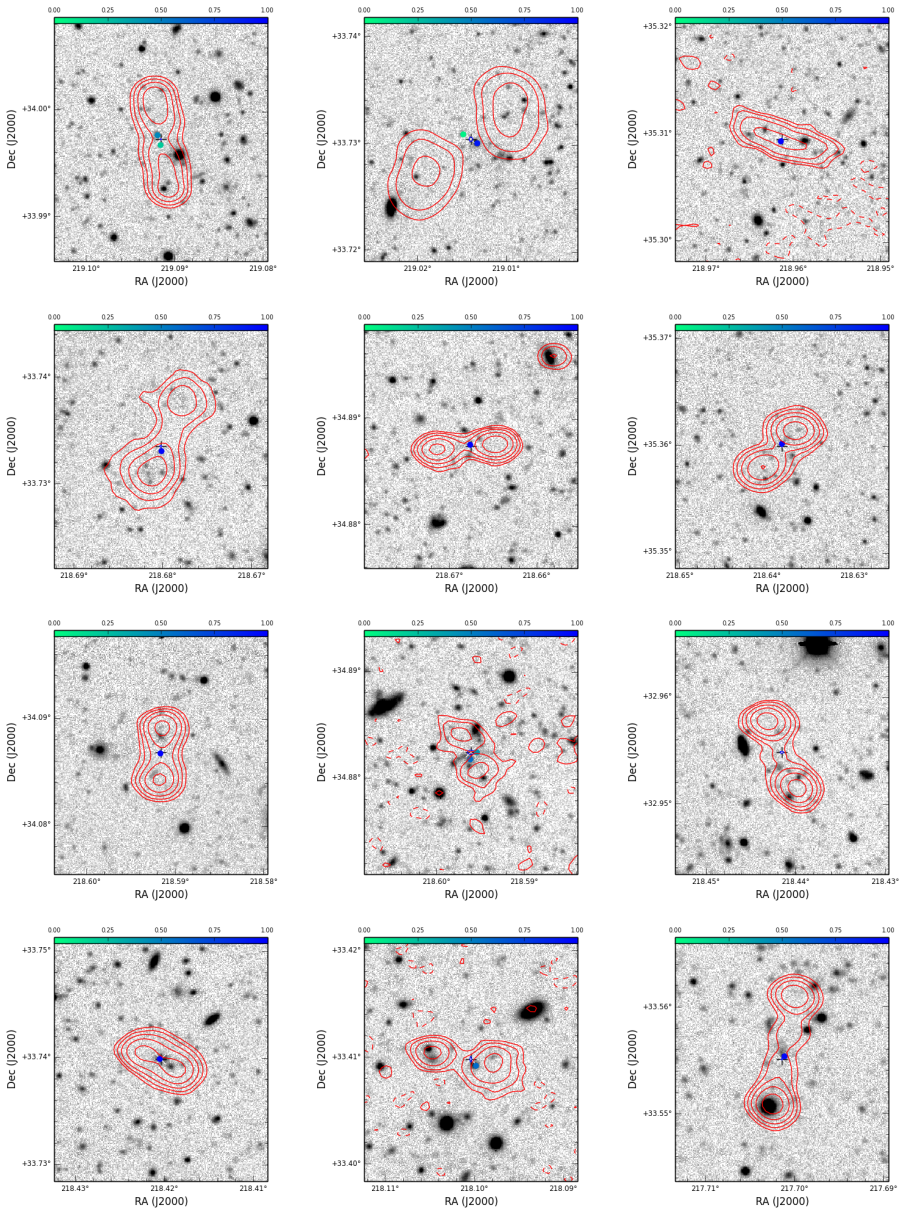


Figure 6.A.2: Examples of the radio-optical cross matches in Class 2. The greyscale image show the I-band NDWFS image. The red contours show the LOFAR $150\,\mathrm{MHz}$ image at levels of $3\sigma_{\mathrm{local}} \times [1, 1.4, 2, 2.8, \ldots]$ where σ_{local} is the local rms in the LOFAR map at the source position. The blue colorscale shows the LR probability of the matched optical source. Each image is $1.25\,\mathrm{arcmin}$ in diameter.

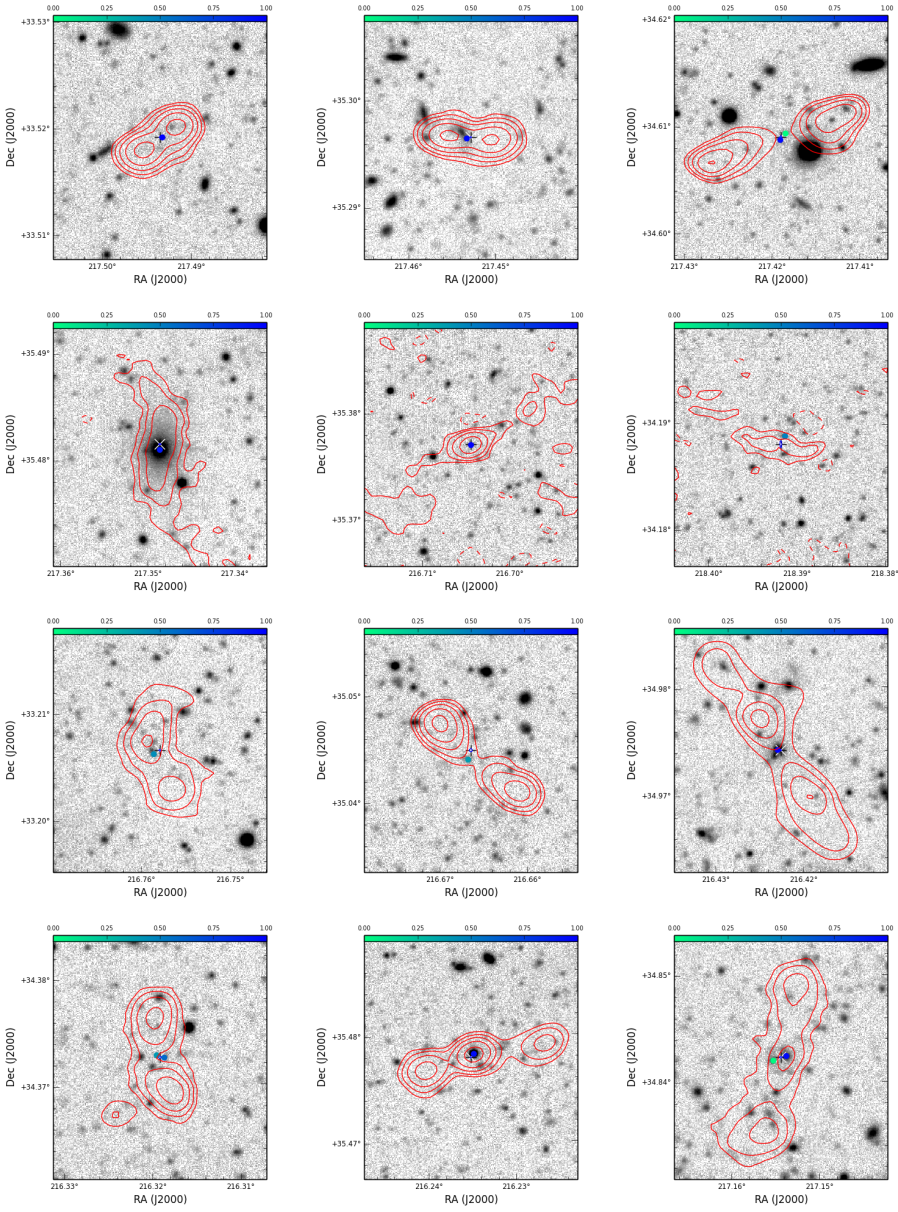


Figure 6.A.2: Cont.

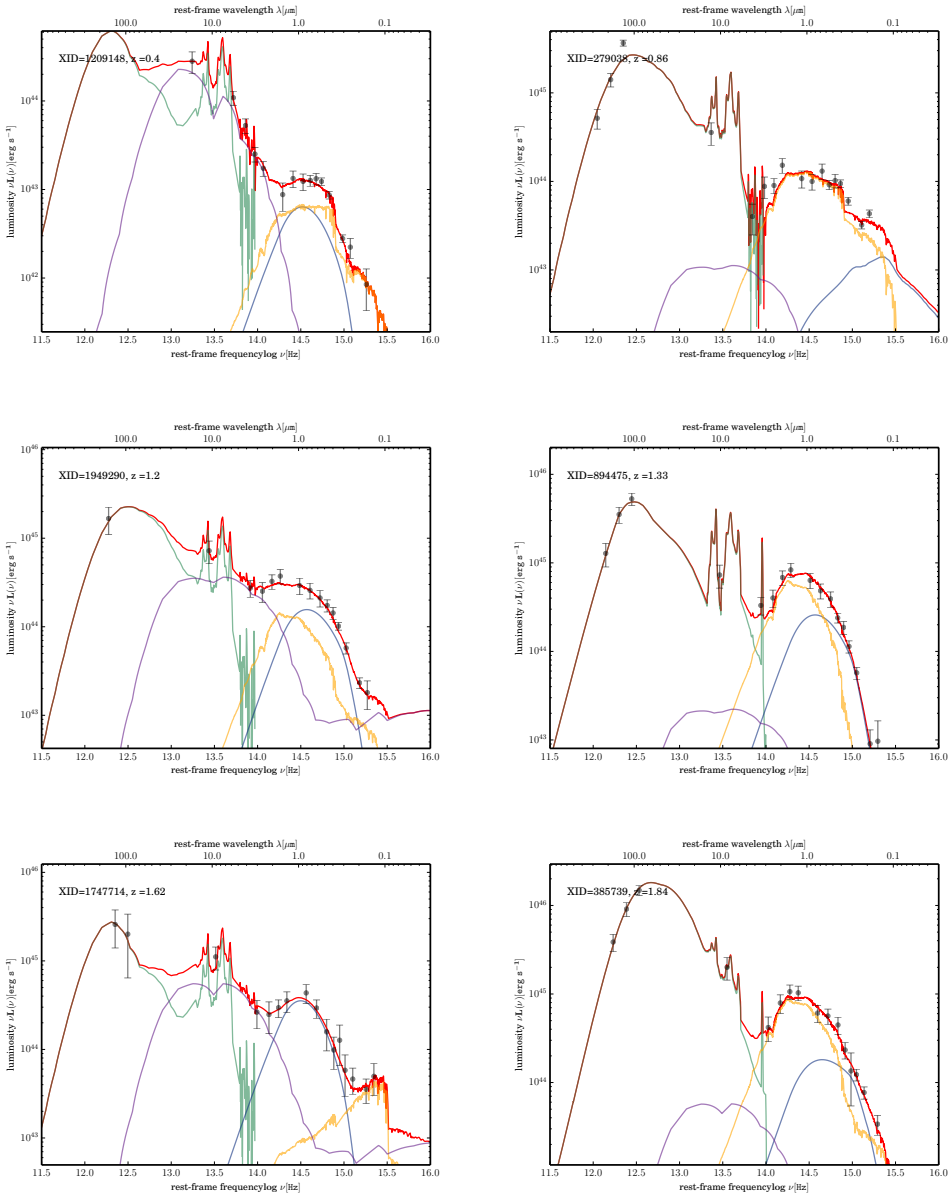


Figure 6.B.1: Examples of good quality SED Fits (with likelihood ≈ -1) with significant star formation contribution (high f_{SB} values) for *left* HERGs and *right* LERGs in the three redshift bins $0.5 < z \leqslant 1.0$ (*top*), $1.0 < z \leqslant 1.5$ (*middle*) and $1.5 < z \leqslant 2.0$ (*bottom*). In all cases the maximum likelihood realisation is plotted (red) and the fitted components are the AGN torus (purple), the starburst (green), the galaxy (yellow) and the blue bump (blue) with the total SED in red.

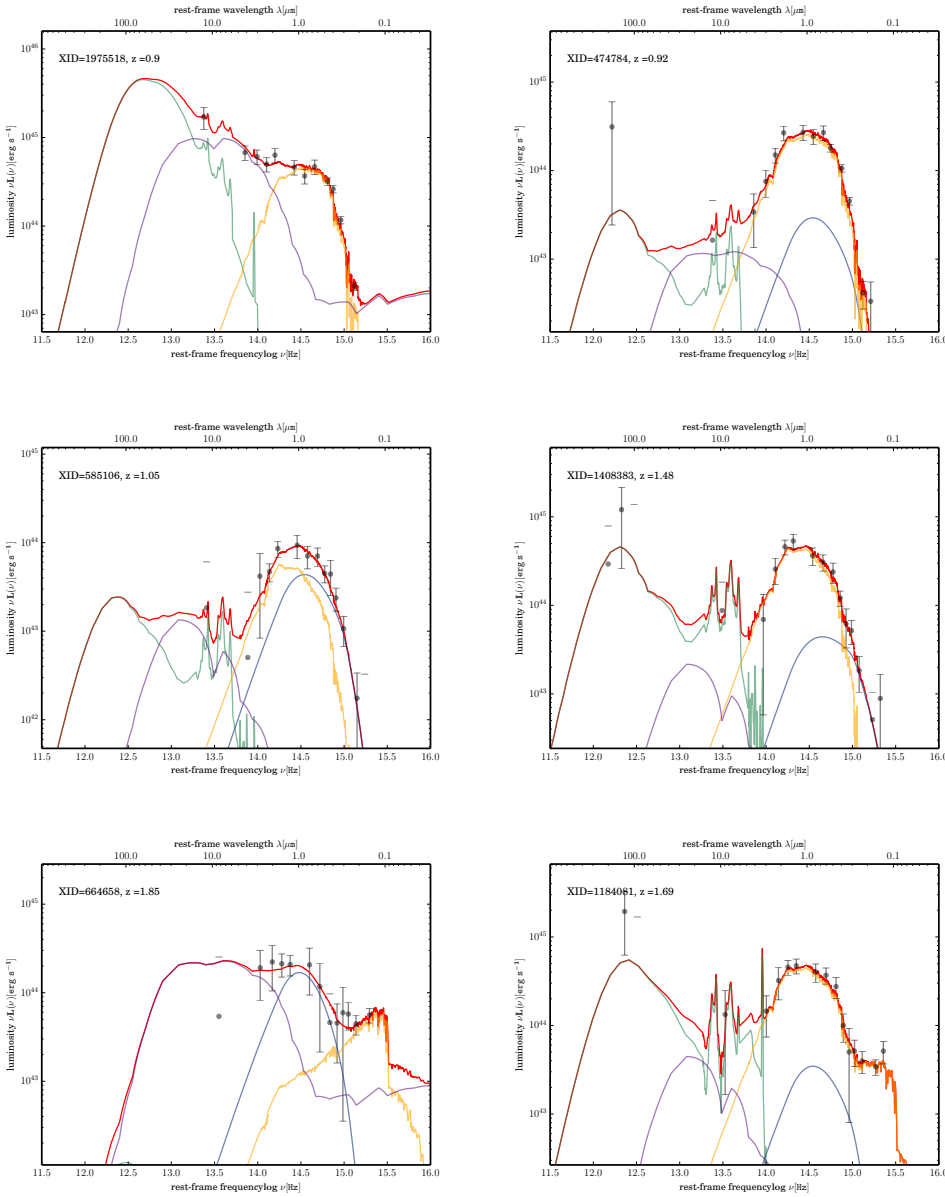


Figure 6.B.2: Examples of good quality SED Fits (with likelihood ≈ -1) with minimal star formation contribution (low f_{SB} values) for *left* HERGs and *right* LERGs in the three redshift bins $0.5 < z \leqslant 1.0$ (*top*), $1.0 < z \leqslant 1.5$ (*middle*) and $1.5 < z \leqslant 2.0$ (*bottom*). In all cases the maximum likelihood realisation is plotted (red) and the fitted components are the AGN torus (purple), the starburst (green), the galaxy (yellow) and the blue bump (blue) with the total SED in red.

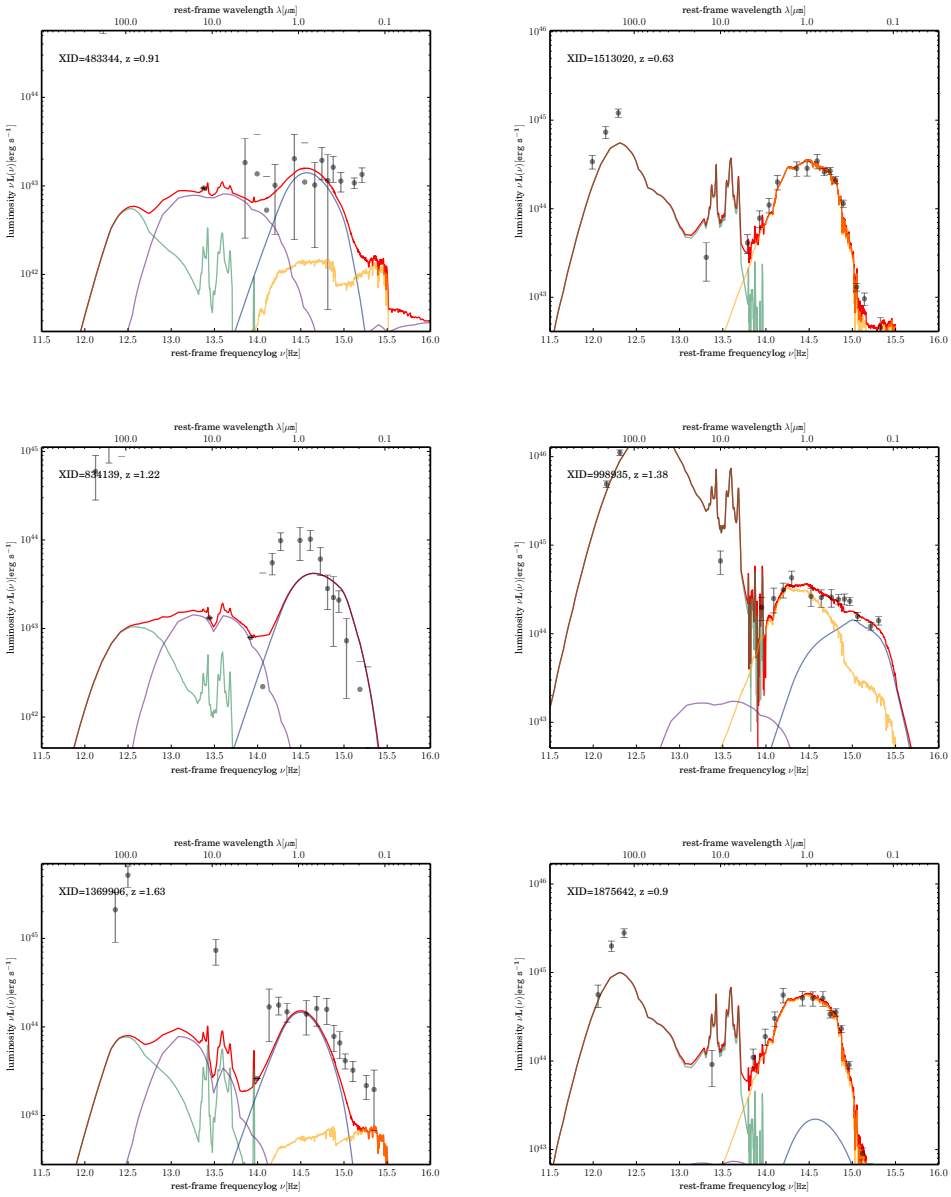


Figure 6.B.3: Examples of poorer SED Fits (with likelihood ≈ -20) for *left* HERGs and *right* LERGs in the three redshift bins $0.5 < z \leqslant 1.0$ (*top*), $1.0 < z \leqslant 1.5$ (*middle*) and $1.5 < z \leqslant 2.0$ (*bottom*). In all cases the maximum likelihood realisation is plotted (red) and the fitted components are the AGN torus (purple), the starburst (green), the galaxy (yellow) and the blue bump (blue) with the total SED in red.

Bibliography

Abazajian K. N., et al., 2009, ApJS, 182, 543

Ananthakrishnan S., 2005, International Cosmic Ray Conference, 10, 125

Antonucci R., 1993, ARA&A, 31, 473

Ashby M. L. N., et al., 2009, ApJ, 701, 428

Assef R. J., et al., 2008, ApJ, 676, 286

Assef R. J., et al., 2010, ApJ, 713, 970

Autry R. G., et al., 2003, in Iye M., Moorwood A. F. M., eds, Society of Photo-Optical Instrumentation Engineers (SPIE) Conference Series Vol. 4841, Instrument Design and Performance for Optical/Infrared Ground-based Telescopes. pp 525–539, doi:10.1117/12.460419

Baade W., Minkowski R., 1954, ApJ, 119, 206

Babbedge T. S. R., et al., 2004, MNRAS, 353, 654

Baldry I. K., Glazebrook K., Brinkmann J., Ivezić Ž., Lupton R. H., Nichol R. C., Szalay A. S., 2004, ApJ, 600, 681

Balogh M. L., Morris S. L., Yee H. K. C., Carlberg R. G., Ellingson E., 1999, ApJ, 527, 54

Barthel P. D., 1989, ApJ, 336, 606

Becker R. H., White R. L., Helfand D. J., 1995, ApJ, 450, 559

Benn C. R., 1983, The Observatory, 103, 150

Bennett A. S., 1962, MmRAS, 68, 163

Bertin E., Arnouts S., 1996, A&AS, 117, 393

Best P. N., 2009, Astronomische Nachrichten, 330, 184

Best P. N., Heckman T. M., 2012, MNRAS, 421, 1569

Best P. N., Carilli C. L., Garrington S. T., Longair M. S., Rottgering H. J. A., 1998, MNRAS, 299, 357

Best P. N., Arts J. N., Röttgering H. J. A., Rengelink R., Brookes M. H., Wall J., 2003, MNRAS, 346, 627

Best P. N., Kauffmann G., Heckman T. M., Ivezić Ž., 2005a, MNRAS, 362, 9

Best P. N., Kauffmann G., Heckman T. M., Brinchmann J., Charlot S., Ivezić Ž., White S. D. M., 2005b, MNRAS, 362, 25

Best P. N., Kaiser C. R., Heckman T. M., Kauffmann G., 2006, MNRAS, 368, L67

Best P. N., von der Linden A., Kauffmann G., Heckman T. M., Kaiser C. R., 2007, MNRAS, 379, 894

Best P. N., Ker L. M., Simpson C., Rigby E. E., Sabater J., 2014, MNRAS, 445, 955

Bhatnagar S., Cornwell T. J., Golap K., Uson J. M., 2008, A&A, 487, 419

Bian F., et al., 2013, ApJ, 774, 28

Bianchi L., Conti A., Shiao B., 2014, Advances in Space Research, 53, 900

Blanco V. M., Graham J. A., Lasker B. M., Osmer P. S., 1975, ApJ, 198, L63

Blandford R. D., Payne D. G., 1982, MNRAS, 199, 883

Blandford R. D., Znajek R. L., 1977, MNRAS, 179, 433

Blanton M. R., et al., 2003a, AJ, 125, 2348

Blanton M. R., et al., 2003b, ApJ, 592, 819

Blanton M. R., et al., 2003c, ApJ, 594, 186

Blumenthal G., Miley G., 1979, A&A, 80, 13
Blundell K. M., Rawlings S., Willott C. J., 1999, AJ, 117, 677
Bondi M., Ciliegi P., Schinnerer E., Smolčić V., Jahnke K., Carilli C., Zamorani G., 2008, ApJ, 681, 1129
Bongiorno A., et al., 2007, A&A, 472, 443
Bornancini C. G., O'Mill A. L., Gurovich S., Lambas D. G., 2010, MNRAS, 406, 197
Bower R. G., Benson A. J., Malbon R., Helly J. C., Frenk C. S., Baugh C. M., Cole S., Lacey C. G., 2006, MNRAS, 370, 645
Boyle B. J., Shanks T., Peterson B. A., 1988, MNRAS, 235, 935
Brammer G. B., van Dokkum P. G., Coppi P., 2008, ApJ, 686, 1503
Brand K., et al., 2006, ApJ, 641, 140
Braude S. Y., Rashkovsky S. L., Sidorchuk K. M., Sidorchuk M. A., Sokolov K. P., Sharykin N. K., Zakharenko S. M., 2002, Ap&SS, 280, 235
Bridle A. H., Schwab F. R., 1989, in Perley R. A., Schwab F. R., Bridle A. H., eds, Astronomical Society of the Pacific Conference Series Vol. 6, Synthesis Imaging in Radio Astronomy. p. 247
Bridle A. H., Davis M. M., Fomalont E. B., Lequeux J., 1972, AJ, 77, 405
Briggs D. S., 1995, in American Astronomical Society Meeting Abstracts. p. 112.02
Brinchmann J., Charlot S., White S. D. M., Tremonti C., Kauffmann G., Heckman T., Brinkmann J., 2004, MNRAS, 351, 1151
Brodwin M., et al., 2006, ApJ, 651, 791
Brookes M. H., Best P. N., Rengelink R., Röttgering H. J. A., 2006, MNRAS, 366, 1265
Brown M. J. I., Dey A., Jannuzi B. T., Brand K., Benson A. J., Brodwin M., Croton D. J., Eisenhardt P. R., 2007, ApJ, 654, 858
Brown M. J. I., et al., 2008, ApJ, 682, 937
Brown M. J. I., et al., 2014, ApJS, 212, 18
Bruzual G., Charlot S., 2003, MNRAS, 344, 1000
Calistro Rivera G., Lusso E., Hennawi J. H., Hogg D. W., 2015
Calzetti D., Armus L., Bohlin R. C., Kinney A. L., Koornneef J., Storchi-Bergmann T., 2000, ApJ, 533, 682
Capak P., et al., 2007, ApJS, 172, 99
Cattaneo A., Best P. N., 2009, MNRAS, 395, 518
Cattaneo A., et al., 2009, Nature, 460, 213
Cen R., Chisari N. E., 2011, ApJ, 731, 11
Chabrier G., 2003, PASP, 115, 763
Chambers K. C., Miley G. K., van Breugel W., 1987, Nature, 329, 604
Chandra P., Ray A., Bhatnagar S., 2004, ApJ, 612, 974
Ciliegi P., et al., 1999, MNRAS, 302, 222
Cimatti A., Daddi E., Renzini A., 2006, A&A, 453, L29
Ciotti L., Ostriker J. P., 1997, ApJ, 487, L105
Ciotti L., Ostriker J. P., Proga D., 2010, ApJ, 717, 708
Clemens M. S., Scaife A., Vega O., Bressan A., 2010, MNRAS, 405, 887
Cohen A. S., et al., 2003, ApJ, 591, 640
Cohen A. S., Röttgering H. J. A., Jarvis M. J., Kassim N. E., Lazio T. J. W., 2004, ApJS, 150, 417
Cohen A. S., Lane W. M., Cotton W. D., Kassim N. E., Lazio T. J. W., Perley R. A., Condon J. J., Erickson W. C., 2007, AJ, 134, 1245
Condon J. J., 1989, ApJ, 338, 13
Condon J. J., 1992, ARA&A, 30, 575
Condon J. J., 1997, PASP, 109, 166

Condon J. J., Cotton W. D., Greisen E. W., Yin Q. F., Perley R. A., Broderick J. J., 1994, in Crabtree D. R., Hanisch R. J., Barnes J., eds, Astronomical Society of the Pacific Conference Series Vol. 61, Astronomical Data Analysis Software and Systems III. p. 155

Condon J. J., Cotton W. D., Greisen E. W., Yin Q. F., Perley R. A., Taylor G. B., Broderick J. J., 1998, AJ, 115, 1693

Conway J. E., Cornwell T. J., Wilkinson P. N., 1990, MNRAS, 246, 490

Cool R. J., 2007, ApJS, 169, 21

Cool R. J., et al., 2012, ApJ, 748, 10

Coppejans R., Cseh D., Williams W. L., van Velzen S., Falcke H., 2015, MNRAS, 450, 1477

Cornwell T. J., 2008, IEEE Journal of Selected Topics in Signal Processing, 2, 793

Cornwell T. J., Perley R. A., 1992, A&A, 261, 353

Cornwell T., Braun R., Briggs D. S., 1999, in Taylor G. B., Carilli C. L., Perley R. A., eds, Astronomical Society of the Pacific Conference Series Vol. 180, Synthesis Imaging in Radio Astronomy II. p. 151

Cornwell T. J., Golap K., Bhatnagar S., 2005, in Shopbell P., Britton M., Ebert R., eds, Astronomical Society of the Pacific Conference Series Vol. 347, Astronomical Data Analysis Software and Systems XIV. p. 86

Cornwell T. J., Golap K., Bhatnagar S., 2008, IEEE Journal of Selected Topics in Signal Processing, 2, 647

Cotton W. D., 1999, in Taylor G. B., Carilli C. L., Perley R. A., eds, Astronomical Society of the Pacific Conference Series Vol. 180, Synthesis Imaging in Radio Astronomy II. p. 357

Cotton W. D., 2008, PASP, 120, 439

Cotton W. D., Uson J. M., 2008, A&A, 490, 455

Cotton W. D., Condon J. J., Perley R. A., Kassim N., Lazio J., Cohen A., Lane W., Erickson W. C., 2004, in Oschmann Jr. J. M., ed., Society of Photo-Optical Instrumentation Engineers (SPIE) Conference Series Vol. 5489, Ground-based Telescopes. pp 180–189, doi:10.1117/12.551298

Cowie L. L., Songaila A., Hu E. M., Cohen J. G., 1996, AJ, 112, 839

Croft S., et al., 2008, AJ, 135, 1793

Croft S., Bower G. C., Whysong D., 2013, ApJ, 762, 93

Croom S. M., et al., 2009, MNRAS, 399, 1755

Croston J. H., Hardcastle M. J., Mingo B., Evans D. A., Dicken D., Morganti R., Tadhunter C. N., 2011, ApJ, 734, L28

Croton D. J., et al., 2006, MNRAS, 365, 11

Cruz M. J., Jarvis M. J., Rawlings S., Blundell K. M., 2007, MNRAS, 375, 1349

Dalton G., et al., 2012, in Society of Photo-Optical Instrumentation Engineers (SPIE) Conference Series. p. 0, doi:10.1117/12.925950

David L. P., Durisen R. H., Cohn H. N., 1987, ApJ, 316, 505

De Breuck C., van Breugel W., Röttgering H. J. A., Miley G., 2000, A&AS, 143, 303

De Breuck C., van Breugel W., Stanford S. A., Röttgering H., Miley G., Stern D., 2002, AJ, 123, 637

Delain K. M., Rudnick L., 2006, Astronomische Nachrichten, 327, 561

Donley J. L., et al., 2012, ApJ, 748, 142

Dunlop J. S., Peacock J. A., 1990, MNRAS, 247, 19

Eales S. A., Rawlings S., 1990, MNRAS, 243, 1P

Eales S., Rawlings S., Law-Green D., Cotter G., Lacy M., 1997, MNRAS, 291, 593

Eddington A. S., 1913, MNRAS, 73, 359

Edge D. O., Shakeshaft J. R., McAdam W. B., Baldwin J. E., Archer S., 1959, MmRAS, 68, 37

Eisenhardt P. R., et al., 2004, ApJS, 154, 48

Elston R. J., et al., 2006, ApJ, 639, 816

Evans D. A., Worrall D. M., Hardcastle M. J., Kraft R. P., Birkinshaw M., 2006, ApJ, 642, 96

Fabian A. C., Celotti A., Erlund M. C., 2006, MNRAS, 373, L16

Fabricant D., et al., 2005, PASP, 117, 1411
Falcke H., 1996, ApJ, 464, L67
Fanaroff B. L., Riley J. M., 1974, MNRAS, 167, 31P
Feigelson E. D., Nelson P. I., 1985, ApJ, 293, 192
Fernandes C. A. C., et al., 2015, MNRAS, 447, 1184
Ferrarese L., Merritt D., 2000, ApJ, 539, L9
Fomalont E. B., Kellermann K. I., Cowie L. L., Capak P., Barger A. J., Partridge R. B., Windhorst R. A., Richards E. A., 2006, ApJS, 167, 103
Fontanot F., De Lucia G., Monaco P., Somerville R. S., Santini P., 2009, MNRAS, 397, 1776
Gaibler V., Khochfar S., Krause M., Silk J., 2012, MNRAS, 425, 438
Garn T., Green D. A., Hales S. E. G., Riley J. M., Alexander P., 2007, MNRAS, 376, 1251
Garn T., Green D. A., Riley J. M., Alexander P., 2008a, MNRAS, 383, 75
Garn T., Green D. A., Riley J. M., Alexander P., 2008b, MNRAS, 387, 1037
Gebhardt K., et al., 2000, ApJ, 539, L13
Gehrels N., 1986, ApJ, 303, 336
Gendre M. A., Best P. N., Wall J. V., 2010, MNRAS, 404, 1719
Gendre M. A., Best P. N., Wall J. V., Ker L. M., 2013, MNRAS, 430, 3086
Genzel R., et al., 2008, ApJ, 687, 59
George S. J., Stevens I. R., 2008, MNRAS, 390, 741
Ghosh A., Prasad J., Bharadwaj S., Ali S. S., Chengalur J. N., 2012, MNRAS, 426, 3295
Gower J. F. R., Scott P. F., Wills D., 1967, MmRAS, 71, 49
Granato G. L., De Zotti G., Silva L., Bressan A., Danese L., 2004, ApJ, 600, 580
Greisen E. W., 1998, in Albrecht R., Hook R. N., Bushouse H. A., eds, Astronomical Society of the Pacific Conference Series Vol. 145, Astronomical Data Analysis Software and Systems VII. p. 204
Griffin M. J., et al., 2010, A&A, 518, L3
Gruppioni C., et al., 1999, MNRAS, 305, 297
Gültekin K., et al., 2009, ApJ, 698, 198
Gürkan G., Hardcastle M. J., Jarvis M. J., 2014, MNRAS, 438, 1149
Hales S. E. G., Baldwin J. E., Warner P. J., 1988, MNRAS, 234, 919
Hales S. E. G., Waldram E. M., Rees N., Warner P. J., 1995, MNRAS, 274, 447
Hales S. E. G., Riley J. M., Waldram E. M., Warner P. J., Baldwin J. E., 2007, MNRAS, 382, 1639
Hamaker J. P., Bregman J. D., 1996, A&AS, 117, 161
Hardcastle M. J., Evans D. A., Croston J. H., 2006, MNRAS, 370, 1893
Hardcastle M. J., Evans D. A., Croston J. H., 2007, MNRAS, 376, 1849
Hardcastle M. J., et al., 2013, MNRAS, 429, 2407
Harrison C. M., et al., 2012, ApJ, 760, L15
Hasinger G., Miyaji T., Schmidt M., 2005, A&A, 441, 417
Haslam C. G. T., Salter C. J., Stoffel H., Wilson W. E., 1982, A&AS, 47, 1
Heald G., et al., 2010, in ISKAF2010 Science Meeting. p. 57
Heckman T. M., Best P. N., 2014, ARA&A, 52, 589
Hewett P. C., Foltz C. B., Chaffee F. H., 1993, ApJ, 406, L43
Heywood I., Blundell K. M., Rawlings S., 2007, MNRAS, 381, 1093
Heywood I., Jarvis M. J., Condon J. J., 2013, MNRAS, 432, 2625
Hickox R. C., et al., 2009, ApJ, 696, 891
Higdon J. L., et al., 2005, ApJ, 626, 58
Hine R. G., Longair M. S., 1979, MNRAS, 188, 111
Ho L. C., 2008, ARA&A, 46, 475

Hopkins A. M., Beacom J. F., 2006, ApJ, 651, 142
Hopkins A. M., Afonso J., Chan B., Cram L. E., Georgakakis A., Mobasher B., 2003, AJ, 125, 465
Hopkins P. F., Hernquist L., Cox T. J., Di Matteo T., Robertson B., Springel V., 2006, ApJS, 163, 1
Hopkins P. F., Richards G. T., Hernquist L., 2007, ApJ, 654, 731
Hopkins P. F., Hernquist L., Cox T. J., Kereš D., 2008, ApJS, 175, 356
Ilbert O., et al., 2009, ApJ, 690, 1236
Inskip K. J., Best P. N., Longair M. S., Röttgering H. J. A., 2005, MNRAS, 359, 1393
Intema H. T., 2014, preprint, (`arXiv:1402.4889`)
Intema H. T., van der Tol S., Cotton W. D., Cohen A. S., van Bemmel I. M., Röttgering H. J. A., 2009, A&A, 501, 1185
Intema H. T., van Weeren R. J., Röttgering H. J. A., Lal D. V., 2011, A&A, 535, A38
Ishwara-Chandra C. H., Marathe R., 2007, in Afonso J., Ferguson H. C., Mobasher B., Norris R., eds, Astronomical Society of the Pacific Conference Series Vol. 380, Deepest Astronomical Surveys. p. 237
Ishwara-Chandra C. H., Sirothia S. K., Wadadekar Y., Pal S., Windhorst R., 2010, MNRAS, 405, 436
Ivison R. J., et al., 2007, ApJ, 660, L77
Jackson N., Rawlings S., 1997, MNRAS, 286, 241
Jannuzi B. T., Dey A., 1999, in Weymann R., Storrie-Lombardi L., Sawicki M., Brunner R., eds, Astronomical Society of the Pacific Conference Series Vol. 191, Photometric Redshifts and the Detection of High Redshift Galaxies. p. 111
Jannuzi B. T., Dey A., NDWFS Team 1999, in American Astronomical Society Meeting Abstracts. p. 1392
Jannuzi B., et al., 2010, in American Astronomical Society Meeting Abstracts #215. p. 470.01
Jansky K. G., 1933, Nature, 132, 66
Janssen R. M. J., Röttgering H. J. A., Best P. N., Brinchmann J., 2012, A&A, 541, A62
Jarvis M. J., Rawlings S., 2004, New A Rev., 48, 1173
Jarvis M. J., et al., 2001, MNRAS, 326, 1563
Jarvis M. J., Teimourian H., Simpson C., Smith D. J. B., Rawlings S., Bonfield D., 2009, MNRAS, 398, L83
Johansson P. H., Burkert A., Naab T., 2009, ApJ, 707, L184
Johnston S., et al., 2007, PASA, 24, 174
Kalfountzou E., Jarvis M. J., Bonfield D. G., Hardcastle M. J., 2012, MNRAS, 427, 2401
Kapinska A. D., Hardcastle M., Jackson C., An T., Baan W., Jarvis M., 2015, Advancing Astrophysics with the Square Kilometre Array (AASKA14), p. 173
Kassim N. E., et al., 2007, ApJS, 172, 686
Kauffmann G., Haehnelt M., 2000, MNRAS, 311, 576
Kauffmann G., Heckman T. M., 2009, MNRAS, 397, 135
Kauffmann G., et al., 2003, MNRAS, 341, 33
Kauffmann G., Heckman T. M., Best P. N., 2008, MNRAS, 384, 953
Kazemi S., Yatawatta S., Zaroubi S., Lampropoulos P., de Bruyn A. G., Koopmans L. V. E., Noordam J., 2011, MNRAS, 414, 1656
Kellermann K. I., Fomalont E. B., Mainieri V., Padovani P., Rosati P., Shaver P., Tozzi P., Miller N., 2008, ApJS, 179, 71
Kenter A., et al., 2005, ApJS, 161, 9
Ker L. M., Best P. N., Rigby E. E., Röttgering H. J. A., Gendre M. A., 2012, MNRAS, 420, 2644
Kettenis M., van Langevelde H. J., Reynolds C., Cotton B., 2006, in Gabriel C., Arviset C., Ponz D., Enrique S., eds, Astronomical Society of the Pacific Conference Series Vol. 351, Astronomical Data Analysis Software and Systems XV. p. 497
Klamer I. J., Ekers R. D., Bryant J. J., Hunstead R. W., Sadler E. M., De Breuck C., 2006, MNRAS, 371, 852

Kochanek C. S., et al., 2012, ApJS, 200, 8
Kormendy J., Richstone D., 1995, ARA&A, 33, 581
Kovács A., Chapman S. C., Dowell C. D., Blain A. W., Ivison R. J., Smail I., Phillips T. G., 2006, ApJ, 650, 592
Kraft R. P., Vázquez S. E., Forman W. R., Jones C., Murray S. S., Hardcastle M. J., Worrall D. M., Churazov E., 2003, ApJ, 592, 129
Kriek M., van Dokkum P. G., Labbé I., Franx M., Illingworth G. D., Marchesini D., Quadri R. F., 2009, ApJ, 700, 221
Kunert-Bajraszewska M., Gawroński M. P., Labiano A., Siemiginowska A., 2010, MNRAS, 408, 2261
Lacy M., Rawlings S., Warner P. J., 1992, MNRAS, 256, 404
Laing R. A., Jenkins C. R., Wall J. V., Unger S. W., 1994, in Bicknell G. V., Dopita M. A., Quinn P. J., eds, Astronomical Society of the Pacific Conference Series Vol. 54, The Physics of Active Galaxies. p. 201
Lane W. M., Cotton W. D., van Velzen S., Clarke T. E., Kassim N. E., Helmboldt J. F., Lazio T. J. W., Cohen A. S., 2014, MNRAS, 440, 327
Larson R. B., 2010, Nature Physics, 6, 96
Larson R. B., Tinsley B. M., 1978, ApJ, 219, 46
Li C., Kauffmann G., Heckman T. M., White S. D. M., Jing Y. P., 2008, MNRAS, 385, 1915
Lilly S. J., et al., 2009, ApJS, 184, 218
Lilly S. J., Carollo C. M., Pipino A., Renzini A., Peng Y., 2013, ApJ, 772, 119
Lonsdale C. J., et al., 2009, IEEE Proceedings, 97, 1497
Madau P., Dickinson M., 2014, ARA&A, 52, 415
Magliocchetti M., Maddox S. J., Lahav O., Wall J. V., 1998, MNRAS, 300, 257
Magorrian J., et al., 1998, AJ, 115, 2285
Marconi A., Hunt L. K., 2003, ApJ, 589, L21
Martin C., et al., 2003, in Blades J. C., Siegmund O. H. W., eds, Society of Photo-Optical Instrumentation Engineers (SPIE) Conference Series Vol. 4854, Future EUV/UV and Visible Space Astrophysics Missions and Instrumentation.. pp 336–350, doi:10.1117/12.460034
Martin D. C., et al., 2005, ApJ, 619, L1
Mauch T., Klöckner H.-R., Rawlings S., Jarvis M., Hardcastle M. J., Obreschkow D., Saikia D. J., Thompson M. A., 2013, MNRAS, 435, 650
McCarthy P. J., van Breugel W., Spinrad H., Djorgovski S., 1987, ApJ, 321, L29
McCracken H. J., et al., 2012, A&A, 544, A156
McGilchrist M. M., Baldwin J. E., Riley J. M., Titterington D. J., Waldram E. M., Warner P. J., 1990, MNRAS, 246, 110
McLure R. J., Dunlop J. S., 2002, MNRAS, 331, 795
McMullin J. P., Waters B., Schiebel D., Young W., Golap K., 2007, in Shaw R. A., Hill F., Bell D. J., eds, Astronomical Society of the Pacific Conference Series Vol. 376, Astronomical Data Analysis Software and Systems XVI. p. 127
McNamara B. R., Nulsen P. E. J., 2012, New Journal of Physics, 14, 055023
Menci N., Rosati P., Gobat R., Strazzullo V., Rettura A., Mei S., Demarco R., 2008, ApJ, 685, 863
Merritt D., Ferrarese L., 2001, ApJ, 547, 140
Miley G., De Breuck C., 2008, A&A Rev., 15, 67
Mingo B., Hardcastle M. J., Croston J. H., Dicken D., Evans D. A., Morganti R., Tadhunter C., 2014, MNRAS, 440, 269
Miyaji T., Hasinger G., Schmidt M., 2000, A&A, 353, 25
Mobasher B., et al., 2004, ApJ, 600, L167
Mohan N., Rafferty D., 2015, PyBDSM: Python Blob Detection and Source Measurement, Astrophysics Source Code Library (ascl:1502.007)

Mohan R., Dwarakanath K. S., Srinivasan G., Chengalur J. N., 2001, Journal of Astrophysics and Astronomy, 22, 35
Morrissey P., et al., 2007, ApJS, 173, 682
Moster B. P., Somerville R. S., Newman J. A., Rix H.-W., 2011, ApJ, 731, 113
Murgia M., et al., 2011, A&A, 526, A148
Murray S. S., et al., 2005, ApJS, 161, 1
Muzzin A., et al., 2013a, ApJS, 206, 8
Muzzin A., et al., 2013b, ApJ, 777, 18
Narayan R., 2005, Ap&SS, 300, 177
Narayan R., Yi I., 1994, ApJ, 428, L13
Narayan R., Yi I., 1995, ApJ, 452, 710
Norman C., Scoville N., 1988, ApJ, 332, 124
Offringa A. R., de Bruyn A. G., Biehl M., Zaroubi S., Bernardi G., Pandey V. N., 2010, MNRAS, 405, 155
Offringa A. R., van de Gronde J. J., Roerdink J. B. T. M., 2012, A&A, 539, A95
Offringa A. R., et al., 2013, A&A, 549, A11
Ogle P., Whysong D., Antonucci R., 2006, ApJ, 647, 161
Oliver S. J., et al., 2012, MNRAS, 424, 1614
Osmer P. S., 1982, ApJ, 253, 28
Owen F. N., Morrison G. E., 2008, AJ, 136, 1889
Padovani P., Bonzini M., Kellermann K. I., Miller N., Mainieri V., Tozzi P., 2015, preprint, (`arXiv:1506.06554`)
Page M. J., et al., 2012, Nature, 485, 213
Pandey V. N., van Zwieten J. E., de Bruyn A. G., Nijboer R., 2009, in Saikia D. J., Green D. A., Gupta Y., Venturi T., eds, Astronomical Society of the Pacific Conference Series Vol. 407, The Low-Frequency Radio Universe. p. 384
Parma P., Murgia M., de Ruiter H. R., Fanti R., Mack K.-H., Govoni F., 2007, A&A, 470, 875
Peacock J. A., 1985, MNRAS, 217, 601
Pearson T. J., Readhead A. C. S., 1984, ARA&A, 22, 97
Perley R. A., 1989, in Perley R. A., Schwab F. R., Bridle A. H., eds, Astronomical Society of the Pacific Conference Series Vol. 6, Synthesis Imaging in Radio Astronomy. p. 287
Perley R. A., Taylor G. B., 1991, AJ, 101, 1623
Perley R. A., Napier P. J., Butler B. J., 2004, in Oschmann Jr. J. M., ed., Society of Photo-Optical Instrumentation Engineers (SPIE) Conference Series Vol. 5489, Ground-based Telescopes. pp 784–795, doi:10.1117/12.551557
Pilkington J. D. H., Scott J. F., 1965, MmRAS, 69, 183
Polatidis A. G., Conway J. E., 2003, PASA, 20, 69
Polko P., Meier D. L., Markoff S., 2010, ApJ, 723, 1343
Polletta M., et al., 2007, ApJ, 663, 81
Prandoni I., Gregorini L., Parma P., de Ruiter H. R., Vettolani G., Wieringa M. H., Ekers R. D., 2001, A&A, 365, 392
Prestage R. M., Peacock J. A., 1983, MNRAS, 204, 355
Quataert E., 2001, in Peterson B. M., Pogge R. W., Polidan R. S., eds, Astronomical Society of the Pacific Conference Series Vol. 224, Probing the Physics of Active Galactic Nuclei. p. 71
Rau U., Cornwell T. J., 2011, A&A, 532, A71
Reber G., 1940, ApJ, 91, 621
Rees M. J., 1978, Nature, 275, 516

Rees N., 1990, MNRAS, 244, 233
Reichard T. A., Heckman T. M., Rudnick G., Brinchmann J., Kauffmann G., Wild V., 2009, ApJ, 691, 1005
Rengelink R. B., Tang Y., de Bruyn A. G., Miley G. K., Bremer M. N., Roettgering H. J. A., Bremer M. A. R., 1997, A&AS, 124, 259
Richards E. A., 2000, ApJ, 533, 611
Richards G. T., et al., 2001, AJ, 122, 1151
Richter G. A., 1975, Astronomische Nachrichten, 296, 65
Rigby E. E., Best P. N., Brookes M. H., Peacock J. A., Dunlop J. S., Röttgering H. J. A., Wall J. V., Ker L., 2011, MNRAS, 416, 1900
Rigby E. E., et al., 2015
Roettgering H. J. A., van Ojik R., Miley G. K., Chambers K. C., van Breugel W. J. M., de Koff S., 1997, A&A, 326, 505
Roseboom I. G., et al., 2010, MNRAS, 409, 48
Rottgering H. J. A., 2010, in ISKAF2010 Science Meeting. p. 50
Rowan-Robinson M., et al., 2008, MNRAS, 386, 697
Russell H. R., McNamara B. R., Edge A. C., Hogan M. T., Main R. A., Vantyghem A. N., 2013, MNRAS, 432, 530
Rybicki G. B., Lightman A. P., 1979, Radiative processes in astrophysics
Ryle M., 1962, Nature, 194, 517
Ryle M., Vonberg D. D., 1946, Nature, 158, 339
Saikia D. J., Jamrozy M., 2009, Bulletin of the Astronomical Society of India, 37, 63
Salvato M., et al., 2009, ApJ, 690, 1250
Salvato M., et al., 2011, ApJ, 742, 61
Salvini S., Wijnholds S. J., 2014, A&A, 571, A97
Sandage A., 1965, ApJ, 141, 1560
Sandage A., 1972, ApJ, 178, 25
Sanders D. B., et al., 2007, ApJS, 172, 86
Scaife A. M. M., Heald G. H., 2012, MNRAS, 423, L30
Schilizzi R. T., 2005, in Gurvits L. I., Frey S., Rawlings S., eds, EAS Publications Series Vol. 15, EAS Publications Series. pp 445–463, doi:10.1051/eas:2005170
Schinnerer E., et al., 2004, AJ, 128, 1974
Schinnerer E., et al., 2007, ApJS, 172, 46
Schmidt M., 1963, Nature, 197, 1040
Schmidt M., 1968, ApJ, 151, 393
Schmidt M., Schneider D. P., Gunn J. E., 1988, in Osmer P., Phillips M. M., Green R., Foltz C., eds, Astronomical Society of the Pacific Conference Series Vol. 2, Optical Surveys for Quasars. pp 87–95
Schwab F. R., 1984, AJ, 89, 1076
Seymour N., et al., 2007, ApJS, 171, 353
Seymour N., et al., 2008, MNRAS, 386, 1695
Shakura N. I., Sunyaev R. A., 1973, A&A, 24, 337
Shankar F., Weinberg D. H., Miralda-Escudé J., 2009, ApJ, 690, 20
Sijacki D., Springel V., Haehnelt M. G., 2009, MNRAS, 400, 100
Silk J., Nusser A., 2010, ApJ, 725, 556
Silk J., Rees M. J., 1998, A&A, 331, L1
Simpson C., et al., 2006, MNRAS, 372, 741
Sirothia S. K., Saikia D. J., Ishwara-Chandra C. H., Kantharia N. G., 2009, MNRAS, 392, 1403

Smirnov O. M., 2011, A&A, 527, A107
Smirnov O. M., Tasse C., 2015, MNRAS, 449, 2668
Smith A. J., et al., 2012, MNRAS, 419, 377
Smolčić V., et al., 2009, ApJ, 696, 24
Snellen I. A. G., Mack K.-H., Schilizzi R. T., Tschager W., 2003, PASA, 20, 38
Sobral D., Smail I., Best P. N., Geach J. E., Matsuda Y., Stott J. P., Cirasuolo M., Kurk J., 2013, MNRAS, 428, 1128
Son D., Woo J.-H., Kim S. C., Fu H., Kawakatu N., Bennert V. N., Nagao T., Park D., 2012, ApJ, 757, 140
Springel V., Di Matteo T., Hernquist L., 2005, MNRAS, 361, 776
Stern D., et al., 2005, ApJ, 631, 163
Stern D., et al., 2012, ApJ, 753, 30
Strauss M. A., et al., 2002, AJ, 124, 1810
Sutherland W., Saunders W., 1992, MNRAS, 259, 413
Tasse C., et al., 2006, A&A, 456, 791
Tasse C., Röttgering H. J. A., Best P. N., Cohen A. S., Pierre M., Wilman R., 2007, A&A, 471, 1105
Tasse C., Le Borgne D., Röttgering H., Best P. N., Pierre M., Rocca-Volmerange B., 2008a, A&A, 490, 879
Tasse C., Best P. N., Röttgering H., Le Borgne D., 2008b, A&A, 490, 893
Tasse C., van der Tol S., van Zwieten J., van Diepen G., Bhatnagar S., 2013, A&A, 553, A105
Taylor G. B., 2007, Highlights of Astronomy, 14, 388
Taylor E. N., et al., 2009, ApJS, 183, 295
Taylor E. N., et al., 2011, MNRAS, 418, 1587
Tielens A. G. G. M., Miley G. K., Willis A. G., 1979, A&AS, 35, 153
Tingay S. J., et al., 2013, PASA, 30, 7
Urry C. M., Padovani P., 1995, PASP, 107, 803
Vernstrom T., et al., 2014, MNRAS, 440, 2791
Vlahakis N., Königl A., 2003, ApJ, 596, 1080
Wan L., Daly R. A., 1996, ApJ, 467, 145
Warren S. J., Hewett P. C., Osmer P. S., 1994, ApJ, 421, 412
Wayth R. B., et al., 2015, PASA, 32, 25
Werner N., et al., 2014, MNRAS, 439, 2291
White R. L., Becker R. H., Helfand D. J., Gregg M. D., 1997, ApJ, 475, 479
White G. J., et al., 2012, MNRAS, 427, 1830
Whysong D., Antonucci R., 2004, ApJ, 602, 116
Williams R. K., 1995, Phys. Rev. D, 51, 5387
Williams W. L., Röttgering H. J. A., 2015, MNRAS, 450, 1538
Williams W. L., Intema H. T., Röttgering H. J. A., 2013, A&A, 549, A55
Williams W. L., et al., 2015
Wilman R. J., et al., 2008, MNRAS, 388, 1335
Windhorst R. A., Miley G. K., Owen F. N., Kron R. G., Koo D. C., 1985, ApJ, 289, 494
Windhorst R., Mathis D., Neuschaefer L., 1990, in Kron R. G., ed., Astronomical Society of the Pacific Conference Series Vol. 10, Evolution of the Universe of Galaxies. pp 389–403
Windhorst R. A., Fomalont E. B., Partridge R. B., Lowenthal J. D., 1993, ApJ, 405, 498
Wolstencroft R. D., Savage A., Clowes R. G., MacGillivray H. T., Leggett S. K., Kalafi M., 1986, MNRAS, 223, 279
Yatawatta S., et al., 2013, A&A, 550, A136

York D. G., et al., 2000, AJ, 120, 1579
Zwart J. T. L., Santos M., Jarvis M. J., 2015, preprint, (arXiv:1503.02493)
de Gasperin F., Intema H. T., Williams W., Brüggen M., Murgia M., Beck R., Bonafede A., 2014, MNRAS, 440, 1542
de Vries W. H., Morganti R., Röttgering H. J. A., Vermeulen R., van Breugel W., Rengelink R., Jarvis M. J., 2002, AJ, 123, 1784
de Zotti G., Massardi M., Negrello M., Wall J., 2010, A&A Rev., 18, 1
van Breugel W., Filippenko A. V., Heckman T., Miley G., 1985, ApJ, 293, 83
van Haarlem M. P., et al., 2013, A&A, 556, A2
van Weeren R. J., in prep.
van Weeren R. J., Röttgering H. J. A., Brüggen M., Cohen A., 2009, A&A, 508, 75
van Weeren R. J., et al., 2012, A&A, 543, A43
van Weeren R. J., et al., 2014, ApJ, 793, 82
van der Tol S. ., Jeffs B. D., van der Veen A.-J. ., 2007, IEEE Transactions on Signal Processing, 55, 4497

Summary

Active Galactic Nuclei

Active Galactic Nuclei (AGN) are powered by gas falling into black holes with masses of millions to billions that of the Sun. Such supermassive black holes (SMBHs) lie at or near the centres of (probably) all galaxies. The observational characteristics of these AGN are diverse, from incredibly high luminosities, emission on very small scales, variability, broad and narrow emission lines, radio emission, to polarised emission. AGN play a crucial role in the evolution of galaxies and are necessary to produce the observed properties of galaxies in the contemporary Universe. To explain the observed co-evolution of black holes and their hosts, theoretical models invoke 'feedback' between the SMBH and the gas and dust within the host galaxy. This feedback allows the central black holes to control or terminate star formation in their host galaxies. It is important then to understand the fueling mechanisms of AGN and their feedback processes and how these evolve over cosmic time.

Radio continuum observations are an important means to find AGN. Radio-loud objects are notably important to our understanding of AGN. Despite the fact that they constitute only a small fraction of the overall population, it is during this phase that the impact of the AGN on their surrounding environment can be most directly observed and measured. The observed radio AGN population can be split in two categories, with the division between them based on their accretion rates (see Fig. 1). The populations are distinct in their SMBH and host galaxy properties. The first population is associated with radiatively efficient accretion via an accretion disc. These sources fit the paradigm of classic optical 'quasars', radiating across the electromagentic spectrum. This 'radiative mode' is characterised by strong optical emission lines and so are refered to as 'high-excitation' sources. High excitation radio galaxies (HERGs) are typically hosted by lower mass, bluer galaxies in less dense environments. This mode may be important in curtailing star formation at early times and creating the relationship between black hole and host galaxy masses that is observed in the nearby Universe. The second class of radio AGN was first noted by their lack of emission lines and are thought to occur when hot gas accretes directly onto the supermassive black hole in a radiatively inefficient manner. They lack any evidence of mid-infrared emission from dusty tori and accretion-related X-ray emission. These low excitation radio galaxies (LERGs) are hosted by galaxies that, in general, differ from those hosting HERGs: higher mass, redder and occurring in more dense environments. This 'jet mode' in particular provides a direct feedback connection between the AGN and its hot gas fuel supply in the manner of work done by the expanding radio lobes on the hot intra-cluster gas. It may be responsible for maintaining present-day elliptical galaxies as 'old, red and dead'.

Low Frequency Radio Astronomy

The radio emission from AGN is synchrotron radiation, which is caused by relativistic electrons spiraling around magnetic field lines, both of which likely originate near the central SMBH. This

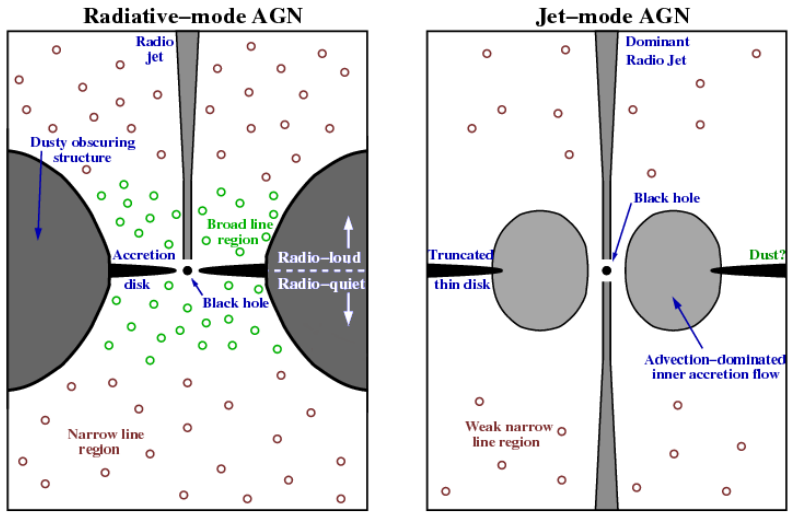


Figure 1: Schematic drawings of the central engines of AGN in the radiative mode (*left*) and jet mode (*right*). Radiative-mode AGN have a thin accretion disk that illuminates the broad- and narrow-line regions with UV radiation. At some viewing angles, a dusty, obscuring structure may inhibit the view of the accretion disk and broad-line region. While at other angles, these features are visible. A small fraction of these sources produce powerful radio jets. Jet-mode AGN lack the accretion disk and emission lines, but do have radio jets. (Image reproduced from Heckman & Best 2014).

emission has a characteristic power-law spectral shape, $S_\nu \propto \nu^\alpha$ over decades in frequency, where the spectral index, α, is typical negative. Radio observations of AGN can thus benefit from the increased brightness towards lower observing frequencies. The last decade has seen a substantial growth in the number and diversity of radio synthesis telescopes being constructed, as a lead up to the Square Kilometre Array (SKA), as well as a return to lower frquencies. In particular, the Low Frequency Array (LOFAR, see Fig. 2) is a new low frequency radio telescope in the Netherlands and surrounding European countries. Its revolutionary design makes use of phased arrays instead of the traditional and expensive dishes, which are joined electronically to imitate a dish. The array is composed of several 'stations' each containing a number of simple dipoles. LOFAR operates within the very high frequency (VHF) band that is commonly used for FM radio and television broadcasting, amateur radio, and marine and air traffic communications. There are two types of dipole antennas, one for the Low Band Array (LBA) operating at 10–80 MHz and one for the High Band Array (HBA) operating in the 110–240 MHz range. The Dutch array alone provides radio images of the sky with unprecedented resolution and sensitivity at these frequencies and allows large areas of the sky to be surveyed. The inclusion of the international stations allows for images of individual sources with resolutions a factor ten higher.

These telescopes bring both new scientific and new technical challenges. These challenges include developing new theories to describe instrumental and atmospheric effects, which were previously ignored and algorithms to solve the resulting equations. This requires a significant increase in the performance of these algorithms in order to produce the best possible sensitivity and contrast. Practically, the new instruments demand the ability to handle the large increase (of factors of hundreds or thousands) in data volume, which in turn requires high performance computing and faster calibration and imaging algorithms. In particular for low frequency ra-



Figure 2: The LOFAR superterp near Exloo, Netherlands, showing several stations with both HBA and LBA antennae (*left*). Individual LBA (*top right*) and HBA (*bottom right*). (credit LOFAR/ASTRON).

dio astronomy it is increasingly important to perform direction-dependent calibration, which corrects for the distorting effects of the ionosphere.

This Thesis

One of the most fundamental issues in understanding the role of AGN in galaxy formation is the need to accurately measure the accretion history of black holes, and to compare this with the growth of stars in galaxies: do black holes and their host galaxies grow coevally, or does one precede the other? Most of the growth of SMBHs and the stars in galaxies occured when the Universe was between 3 and 8 billion years old. Their present day growth is an order of magnitude lower than it was at that peak. To properly understand the detailed process of galaxy formation and evolution the physical processes involved in 'AGN feedback' need to be identified and quantified. Current radio and optical surveys have greatly increased our understanding of the contemporary population of AGN. To fully quantify the effect of AGN, it is necessary to extend such work back to earlier cosmic epochs where the AGN and star-formation activity of the Universe peaked. With the more powerful radio telescopes now available, it is now becoming possible to directly study the AGN population at these distant times. To this end, this thesis aims to answer the following:

1. How does the relationship between galaxy mass and radio AGN fraction, i.e. the radio source duty cycle, evolve over time?
2. How does the radio AGN population evolve over time?
3. What is relationship between host galaxy properties and radio AGN in the earlier Universe?

The main tool for these studies is deep, high-resolution, low frequency radio imaging of fields with excellent complementary data. The first part of this thesis (Chapters 2 to 4) uses the most advanced calibration techniques to provide low-frequency radio images using the GMRT and

LOFAR. The latter part of the thesis (Chapters 5 and 6) combine radio samples with optical data to study host galaxy properties of radio-loud AGN over cosmic time.

Chapter 2 presents 153 MHz GMRT observations of the NOAO Boötes field. This extragalactic deep field has been extensively studied at optical, ultraviolet and mid-infrared wavelengths. The low frequency radio data have been calibrated for direction-dependent ionospheric effects with the SPAM software package. The GMRT mosaic image, which combines seven observations, provides the largest and deepest low frequency image at the time. An important simple diagnostic of the radio source popoluation is the number of sources of different brightnes, or 'source counts'. The 1289 radio sources in the GMRT image were used to derive the low frequncy source counts.

In **Chapter 3** the first LOFAR LBA observations of the Boötes and 3C 295 fields at 34, 46, and 62 MHz are presented. The images are the deepest ever obtained in this frequency range and each image contains 300–400 radio sources. Source counts are again derived each frequency. The lowest frequency source counts show that the average spectral index of radio sources flattens towards lower frequencies, i.e. radio sources are not as bright as expected at lower frequencies. A sample of ultra-steep spectrum (USS) radio sources is selected in the Boötes field from the spectral indices computed between 62 MHz, 153 MHz and 1.4 GHz. These USS sources are of interest because they are likely to be associated with massive distant radio galaxies.

The first LOFAR, $130 - 169$ MHz, HBA deep field observations of the Boötes field are presented in **Chapter 4**. The 19 square degree image is an order of magnitude more sensitive and four times higher in resolution than that achieved with the GMRT observations in Chapter 2. Particular care is taken in the calibration of this data, making use of an advanced direction-dependent calibration scheme. The resulting radio source catalogue contains 5 652 sources. The source counts are are an order of magnitude lower in flux density than previously done at these frequencies. The counts show a flattening for the faintest sources, which is connected with the rise of the faint star forming galaxies.

Chapter 5 is a study of the evolution of the fraction of radio-loud AGN as a function of their host stellar mass and shows how the fraction of low mass galaxies hosting high power radio-loud AGN increases with cosmic time. This is done by combining radio and optical data for one sample in the local universe, and a second more distant sample. An increase of more than an order of magnitude in the fraction of lower mass galaxies hosting radio-loud AGN is observed in the distant sample. On the other hand the fraction of high mass galaxies hosting radio-loud AGN remains more or less constant. An increase in cold or radiative mode accretion with increasing cold gas supply at earlier cosmic time is argued to be responsible for the rising population of low mass radio-loud AGN.

In **Chapter 6** a further study of the redshift evolution of radio AGN as a function of the properties of their galaxy hosts is made. This uses the LOFAR data of the Boötes field from Chapter 4 combined with optical and infrared data. The optical-infrared data is used to compile a catalogue of galaxies with distances, stellar masses and intrinsic colours. We use this to study the host galaxies of strong distant radio sources. We also attempt to determine the mid-infrared AGN contribution to classify the radio-sources as HERGs and LERGs on the basis of photometry. We show that the fraction of HERGs and the fraction of blue radio AGN increases with redshift.

Future Prospects

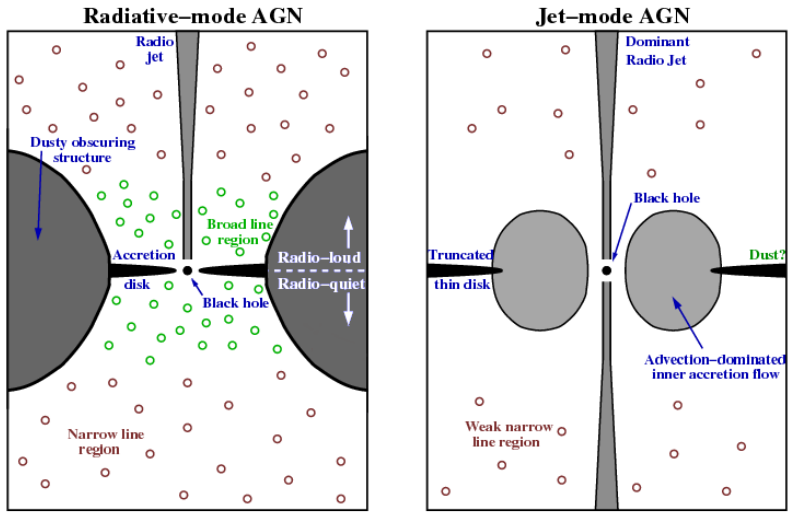
The future is bright for radio AGN evolution studies. The current LOFAR surveys are already providing larger, higher redshift samples, such as those presented in this thesis. Soon, other continuum surveys to be performed with new and upgraded instruments will provide complementary higher frequency. Deeper photometric surveys are also currenty underway or in planning. In particular, new optical instruments, will provide much larger samples of galaxies at high redshifts for the radio sources identified in the LOFAR surveys. Looking further ahead, the field is poised for another revolution, in terms of groundbreaking depth and area covered by future optical imaging and spectroscopic surveys. Finally, AGN and galaxy evolution studies are also an important part of the science case for the SKA, the next step forward in radio astronomy.

Samenvatting

Active Galactic Nuclei

De kernen van actieve sterrenstelsels *(Active Galactic Nuclei, of kortweg AGN)* worden aangedreven door gas dat instroomt in de relativistische gravitationele put rondom zwarte gaten. Deze zogenaamde *supermassive black holes (SMBHs)* van miljarden zonsmassa's bevinden zich in of nabij het centrum van (waarschijnlijk) alle sterrenstelsels. De waarneembare kenmerken van AGN lopen sterk uiteen, zoals een extreme lichtkracht, emissie vanaf zeer kleine schaal, variabel in tijd, brede en smalle emissielijnen, en (gepolariseerde) radiostraling. AGN spelen een cruciale rol in de evolutie van sterrenstelsels, en zijn een onmisbaar ingrediënt in de verklaring voor de waarneembare eigenschappen van sterrenstelsels in het nabije heelal. Theoretische modellen passen *terugkoppeling* toe tussen de SMBH en het gas en stof in de omringende sterrenstelsels, om zo de gekoppelde evolutie van zwarte gaten en sterrenstelsels te verklaren. Via terugkoppeling kan het zwarte gat de vorming van nieuwe sterren in het sterrenstelsel beïnvloeden of onderdrukken. Het is daarom zeer belangrijk om de processen van gastoevoer naar de AGN en terugkoppeling fysisch in detail te begrijpen, en om te bepalen hoe deze processen veranderen in de tijd.

Astronomische waarnemingen op radio-frequenties zijn een belangrijk hulpmiddel voor het vinden van AGN. Met name 'radio-luide' bronnen zijn belangrijk voor ons begrip van AGN. Ondanks dat het slechts een kleine fractie van alle AGN betreft, is het gedurende deze radio-luide fase dat de impact van de AGN op hun omgeving het best kan worden waargenomen en bestudeerd. De waargenomen groep radio AGN kan worden gesplitst in twee groepen, afhankelijk van de accretie snelheid en de eigenschappen van de SMBH en het omringende sterrenstelsel (zie figuur 1). Klassificatie van de eerste groep hangt samen met stralings-efficiënte accretie via een accretie-schijf. Deze klassieke 'optische quasars', zijn zichtbaar over vrijwel het gehele elektromagnetische spectrum. Deze *radiative mode* gaat gepaard met sterke optische emissielijnen, waardoor deze bronnen ook wel 'hoge excitatie' bronnen worden genoemd, of *high excitation radio galaxies (HERGs)*. Dit zijn relatief blauwe sterrenstelsels met een relatief lage massa, en bevinden zich in relatief dun-bevolkte omgevingen. Deze modus is mogelijk belangrijk in het onderdrukken van de vorming van sterren in vroeger tijden, en het ontstaan van de waargenomen samenhang tussen de massa's van het zwarte gat en het omringende sterrenstelsel in het nabije heelal. De tweede groep AGN werd oorspronkelijk opgemerkt vanwege de afwezigheid van emissielijnen. Men denkt dat dit komt door directe instroom van heet gas in het zwarte gat via een stralings-arm proces. Bij deze objecten wordt geen mid-infrarood straling van de stoftorus gedetecteerd, noch Röntgenstraling van de acrretieschijf. Deze zogenaamde *low excitation radio galaxies (LERGs)* zijn sterrenstelses die over het algemeen verschillen van HERGs door hun rode kleur en aanwezigheid in relatief dicht-bevolkte omgevingen. Specifiek deze *jet mode* voorziet in een directe link tussen de AGN en het instromende hete gas, vanwege de arbeid die de expanderende radio lobes verrichten in het hete gas tussen sterrenstelsels. Het is mogelijk de belangrijkste reden waarom nabije, eliptische sterrenstelsels 'oud, rood en dood' blijven.



Figuur 1: Schematisch overzicht van het centrum van AGN in de *radiative mode* en *jet mode*. Radiative-mode AGN hebben een dunne accretie-schijf die de nabij-gelegen breed- en smal-lijn regio's belicht met UV-straling. Afhankelijk van de waarneemhoek zijn de accretie-schijf en brede-lijn regio's zichtbaar, of liggen verscholen achter een band van stof. Een fractie van deze bronnen produceert krachtige radio jets. Jet-mode AGN hebben geen accretie-schijf en emissielijnen, maar wel radio jets. (Afbeelding overgenomen uit Heckman & Best 2014).

Lage-Frequentie Radio Sterrenkunde

De radiostraling van AGN is synchrotron-straling, gegenereerd door relativistische elektronen die rond magnetische veldlijnen cirkelen, beide waarschijnlijk afkomstig van dichtbij de centrale SMBH. Deze straling heeft een karakteristiek *power-law* spectrum ($S_\nu \propto \nu^\alpha$) over een zeer breed frequentiebereik, waarbij de waarde van de *spectral index* (α) meestal negatief is. Radio waarnemingen van AGN hebben het voordeel van toenemende helderheid bij lagere frequenties. In het afgelopen decennium heeft er een sterke groei plaatsgevonden in het aantal en soort nieuwe radio (interferometer) telescopen, onder andere als voorbereiding op de ontwikkeling van de *Square Kilometre Array (SKA)* inclusief een terugkeer naar lage frequenties. De Low-Frequency Array (LOFAR, zie figuur 2) is een nieuwe lage-frequentie radiotelescoop die zich voornamelijk in Nederland bevindt, maar ook in enkele omringende landen. Het revolutionaire ontwerp van LOFAR maakt gebruik van *phased arrays* in plaats van traditionele en dure schotels, welke elektronisch worden gekoppeld om een beweegbare schotel na te bootsen. De telescoop bestaat uit 'stations' die zijn opgebouwd uit simpele dipool-antennes. LOFAR werkt binnen de *Very High Frequency (VHF)* band die meestal gebruikt wordt voor de FM-radio en televisie-uitzendingen, amateur radio, marine- en luchtverkeers-communicatie. Er zijn twee soorten antennes, namelijk de *Low Band Array (LBA)* antennes voor waarnemingen tussen 10 en 80 MegaHertz (MHz), en de *High Band Array (HBA)* antennes voor waarneemfrequenties tussen 110 en 240 MHz. Met enkel de LOFAR stations in Nederland worden al ongekend hoge resolutie afbeeldingen geproduceerd. En toevoegen van internationale stations leidt tot resoluties die nog een factor tien hoger zijn.

Dit soort telescopen initiëren nieuwe wetenschappelijke èn technische uitdagingen. Dit laat-



Figuur 2: De LOFAR kern (de 'superterp') nabij Exloo (Drenthe), met daarop verschillende stations met HBA en LBA antennes (*links*). Individuele LBA (*boven rechts*) and HBA (*onder rechts*) antennes. (LOFAR/ASTRON).

ste omvat het ontwikkelen van nieuwe modellen ter beschrijving van instrumentele en atmosferische effecten die voorheen werden genegeerd, en het onwikkelen van algoritmes die deze modellen doorrekenen. Het vereist een sterke toename in de nauwkeurigheid algoritmes om optimale gevoeligheid en contrast te verkrijgen. In de praktijk leidt het gebruik van nieuwe instrumenten tot een sterke toename van de hoeveelheid gegenereerde data (een factor 100–1000). De gegevensbewerking vereist zeer krachtige computers en snelle algoritmes voor kalibratie en beeldvorming. Specifiek voor lage-frequentie radio waarnemingen is het belangrijk om richtingsafhankelijk te kalibreren, om zo de verstorende effecten van de ionosfeer teniet te doen.

Dit Proefschrift

Één van de meest fundamentele onderwerpen in het begrip van de rol van AGN in de formatie van sterrenstelsels is de noodzaak om nauwkeurig de accretie-geschiedenis van zwarte gaten te meten, en om deze te vergelijken met de opbouw van sterren in sterrenstelsels: groeien zwarte gaten en de omringende sterrenstelses tesamen, of gaan de één de ander voor? De meest dominante groei van SMBHs en de sterren in sterrenstelsels vindt plaats toen the heelal tussen de 3 en 8 miljard jaar oud was. De huidige groei is een orde van grootte langzamer dan op het maximum. Om het gedetailleerde proces van de formatie en evolutie van sterrenstelses goed te begrijpen is het nodig om de fysische processen van terugkoppeling van AGN te identificeren en te kwantificeren. Recente radio en optische surveys hebben ons begrip van de huidige populatie van AGN sterk doen toenemen. Om ten volle het effect van AGN te kwantificeren is het nodig om dit werk ook uit te voeren in vroeger tijden, toen de activiteit van AGN en stervorming in het heelal maximaal waren. Met de krachtigere radiotelescopen die nu beschikbaar zijn is het mogelijk om deze verre AGN direct te bestuderen. Om deze reden zijn in dit proefschrift de volgende onderzoeksvragen gedefiniëerd:

1. Hoe evolueert de relatie tussen de massa van sterrenstelsels en de fractie van radio AGN

(oftewel de relatieve duur van de radio-luide fase) met de tijd?

2. Hoe evolueert de populatie radio-luide AGN met de tijd?
3. Wat is het verband tussen de eigenschappen van radio-luide AGN en de omringende sterrenstelsels in vroeger tijden?

De belangrijkste gereedschappen om dit onderzoek te doen zijn zeer gevoelige, hoge-resolutie radiokaarten op lage frequenties, aangevuld met complementaire waarnemingen van andere type telescopen. Het eerste deel van dit proefschrift (hoofdstukken 2 t/m 4) beschrijft de productie van lage-frequentie radiokaarten uit GMRT en LOFAR waarnemingen, gebruikmakend van de meest geavanceerde kalibratie-technieken. In het tweede deel van het proefschrift (hoofdstukken 5 en 6) worden geselecteerde radiobronnen gecombineerd met optische waarnemingen ter bestudering van de eigenschappen van sterrenstelsels rondom radio-luide AGN als functie van tijd.

In **hoofdstuk 2** worden 153 MHz GMRT waarnemingen gepresenteerd van het zogenaamde *NOAO Boötes veld*. Dit extragalactische veld is uitgebreid bestudeerd met optische, ultraviolet- en infrarood-telescopen. De lage-frequentie radio data is gekalibreerd voor richtings-afhankelijke ionosferische effecten met behulp van het SPAM softwarepakket. De gecombineerde GMRT kaart, opgebouwd uit zeven afzonderlijke kaarten, is op het moment van publicatie de grootste en diepste van z'n soort, en bevat 1289 detecteerbare radiobronnen. Een belangrijke eigenschap bij het analyseren van de radiobronnen is het tellen van het aantal bronnen als functie van helderheid. Deze brontellingen zijn met behulp van de lage-frequentie GMRT kaart gedetailleerd uitgevoerd.

In **hoofdstuk 3** worden de eerste LOFAR LBA kaarten gepresenteerd van het Boötes veld en het veld rondom radiobron 3C 295 op 34, 46 en 62 MHz. Deze kaarten zijn de meest gevoelige kaarten ooit op deze frequenties, met elk tussen de 300 en 400 detecteerbare radiobronnen. Relatief lagere brontellingen op 34 MHz in vergelijking met 62 MHz suggereert een gemiddelde afvlakking van de spectral index van radiobronnen bij lagere frequenties. Een groep steil-spectrum (ultra-steep spectrum, or USS) bronnen is geïdentificeerd in het Boötes veld, gebruikmakend van de kaarten op 62, 153 en 1400 MHz. Deze USS bronnen zijn belangrijk omdat zij geassociëerd worden met zware, verre sterrenstelsels.

De eerste diepe LOFAR HBA waarnemingen (130 – 169 MHz) van het Boötes veld worden gepresenteerd in **hoofdstuk 4**. De kaart van 19 vierkante graden is een factor tien beter in gevoeligheid en een factor vier beter in resolutie dan de GMRT waarnemingen in hoofdstuk 2. Veel aandacht is besteed aan de kalibratie van deze data, gebruikmakend van een geavanceerde richtingsafhankelijke kalibratietechniek. De resulterende catalogus bevat 5 652 radiobronnen. De brontellingen gaan een factor tien dieper in gevoeligheid dan wat eerder is gedaan. De brontellingen vertonen een afvlakking voor de zwakste bronnen, welke samenvalt met de verwachte toename van aantallen (radio-zwakkere) sterrenstelsels met significante sterformatie.

Hoofdstuk 5 bevat een studie van de evolutie van de fractie radio-luide AGN als een functie van massa van het omringende sterrenstelsel, en toont hoe de fractie lage-massa sterrenstelsels met krachtige, radio-sterke AGN toeneemt met roodverschuiving. Dit is gerealiseerd door het kombineren van radio en optische waarnemingen voor zowel een groep sterrenstelsels in het nabije/huidige heelal alsmede in het verre/vroege heelal. Een toename van meer dan een factor tien is waargenomen in de fractie lage-massa sterrenstelsels met radio-luide AGN. Aan de andere kant blijft de fractie hoge-massa sterrenstelsels met een radio-luide AGN min of meer constant. Een toename in de *cold mode* of *radiative mode* accretie, als gevolg van een toenemende voorraad

koud gas in vroeger tijden, wordt opgevoerd als de reden voor het toenemende aantal lage-massa radio-luide AGN.

In **hoofdstuk 6** wordt de evolutie van radio AGN als functie van de eigenschappen van het omringende sterrenstelsel verder onderzocht. Hierbij wordt gebruik gemaakt van de LOFAR waarnemingen van het Boötes veld uit hoofdstuk 4. De gecombineerde optische en infrarood data is gebruikt om een catalogus van sterrenstelsels samen te stellen met daarin de intrinsieke optische kleuren, fotometrische metingen van afstand, en totale massa in sterren. Deze worden gebruikt voor het bestuderen van sterke verre radiobronnen. De infrarood-waarnemingen worden gebruikt om een eerste scheiding aan te brengen in de radiobronnen tussen de HERGs en LERGs. Aangetoond wordt dat de fractie HERGs èn de fractie van radio-luide AGN in blauwe sterrenstelsels toeneemt met roodverschuiving.

Toekomst Perspectief

De toekomst ziet er kleurrijk uit voor radio-studies van de evolutie van AGN. De huidige LOFAR surveys vinden nu al dergelijke objecten op hogere roodverschuiving, zoals in dit proefschrift is gepresenteerd. Binnen afzienbare tijd zullen complementaire continuüm surveys op hogere frequenties worden uitgevoerd met nieuwe en vernieuwde instrumenten. Diepere optische surveys worden momenteel gepland of reeds uitgevoerd. Nieuw geplande optische instrumenten zullen de belangrijkste bron van spectroscopische informatie worden voor de LOFAR surveys. Verder in de toekomst wordt een grotere vernieuwing van het onderzoeksveld verwacht in termen van ongekende diepte en hoeveelheid hemeloppervlak waargenomen in optische en spectroscopische surveys. Afsluitend, de studie van AGN en evolutie van sterrenstelsels is ook een belangrijk onderwerp in de wetenschappelijke onderbouwing van de SKA.

Publications

Refereed

Heald, G. H., et al. (including **Williams, W. L.**) 2015. *The LOFAR Multifrequency Snapshot Sky Survey (MSSS) I. Survey description and first results* A&A in press.

Williams, W. L., Röttgering, H. J. A. 2015. *Radio-AGN feedback: when the little ones were monsters.* MNRAS 450, 1538-1545.

Coppejans, R., Cseh, D., **Williams, W. L.**, van Velzen, S., Falcke, H. 2015. *Megahertz peaked-spectrum sources in the Boötes field I - a route towards finding high-redshift AGN.* MNRAS 450, 1477-1485.

van Weeren, R. J., **Williams, W. L.**, et al. 2014. *LOFAR Low-band Antenna Observations of the 3C 295 and Boötes Fields: Source Counts and Ultra-steep Spectrum Sources.* The AJ 793, 82.

Williams, W. L., Kraan-Korteweg, R. C., Woudt, P. A. 2014. *Deep NIR photometry of H I galaxies in the Zone of Avoidance.* MNRAS 443, 41-57.

de Gasperin, F., Intema, H. T., **Williams, W. L.**, Brüggen, M., Murgia, M., Beck, R., Bonafede, A. 2014. *The diffuse radio emission around NGC 5580 and NGC 5588.* MNRAS 440, 1542-1550.

Williams, W. L., Intema, H. T., Röttgering, H. J. A. 2013. *T-RaMiSu: the Two-meter Radio Mini Survey. I. The Boötes Field.* A&A 549, A55.

Non-refereed

Williams, W. L., Röttgering, H. J. A. 2015. *LOFAR and Radio-Loud AGN.* IAU Symposium 309, 137-140.

Williams, W. L., Röttgering, H., van Weeren, R. 2014. *LOFAR and Radio Loud AGN.* IAU Symposium 304, 86-92.

Williams, W. L., Woudt, P. A., Kraan-Korteweg, R. C. 2011. *Deep NIR Photometry of HI Galaxies Behind the Milky Way.* in 'Ten years of Infrared Survey Facility and the Future', eds. Nagayama, T., Sato, S., and Wakamatsu, K.

Curriculum Vitae

I was born on August 16, 1986 in Edenvale, Gauteng, South Africa. I attended Eastleigh Primary School for the first 4 years of primary school, before moving to Sunnyridge Primary School and then on to Dawnview High School where I matriculated with distinction in 2004. From an early age I was fascinated by the stars and planned to pursue a career in Astronomy. My interest in science was fostered by public lecture demonstrations and Open nights held by a University of the Witwatersrand Physics professor at the old Royal Observatory in Johannesburg.

In January 2005 I moved to Cape Town and enrolled in the Science Faculty of the University of Cape Town for a degree in Physics and Astrophysics. As part of my first year Astronomy course I made my first of many trips to the South African Astronomical Observatory site in Sutherland. I completed my BSc degree with distinction in 2007 and in 2008 I completed the BSc Honours course as part of the National Astrophysics and Space Science Programme.

In 2009 I started a research Master's degree in Astronomy at the University of Cape Town under Prof. R. Kraan-Korteweg. During this time I studied the cosmic flow fields in the Zone of Avoidance, where dust in our Galaxy obscures the galaxies beyond. This multiwavelength project had a dual approach including near-infrared galaxy photometry, for which I spent many nights observing on the Japanese InfraRed Survey Telescope situated in Sutherland, and radio HI spectral line observations, for which I had the opportunity to observe at the Parkes Radio Telescope. I was awarded my MSc degree in Astronomy with distiction in 2011.

Also in 2011, I moved to Leiden Observatory, where I started my PhD position with Prof. H. Röttgering. My thesis work focussed on using low frequency radio observations to understand how active galactic nuclei evolve over cosmic time and how this interplays with the formation and evolution of galaxies. As part of this I have reduced data from the newly comissioned LOw Frequency ARray (LOFAR) located in the Netherlands, and been actively involved in the LOFAR Surveys team. During my time in Leiden, I assisted in organising the conference "Astronomy, Radio Sources and Society", and I was a teaching assistant for the Master's course "Detection of Light", for which I was awarded a prize for the Best Teaching Assistant of the Semester. During my PhD, I have presented my work at conferences in Bonn (Germany), Groningen (the Netherlands), Yerevan (Armenia), Vienna (Austria), Tempe (USA), and Cape Town (South Africa).

In the next three years I will continue my career in Astronomy as a postdoctoral researcher at the Centre for Astrophysics Research at the University of Hertfordshire in the United Kingdom.

Acknowledgements

This thesis would not have been possible without the friendship, help, guidance, and support of family, friends and colleagues. This list cannot fully capture my gratitude and is likely to be incomplete.

Firstly, on a practical note, I owe my thanks to the Leiden computer group, particularly for your support on the para cluster, and to the administrative staff at the Observatory for keeping things running smoothly. I am grateful also for the support of the staff at ASTRON, in particular to those in Science Support.

I would not have made it to starting a PhD without some people in my early academic career. In particular my thanks go to my B.Sc (Hons) and M.Sc supervisors Patrick Woudt and Renée Kraan-Korteweg. I am grateful for the continued support of the South African government to the development of Astronomy in general and which has in particular benefited me through the National Astrophysics and Space Science Programme and the South African SKA project.

Several people played a very key role in the work I have done over the past few years. Huib, Reinout, and Cyril, I have learned most of what I know about Radio interferometry from you. Philip Best, George Miley, thank you for your advice and guidance. For the useful discussions on AGN: Renier, Gaby, and Jarle Brinchmann. Thanks also to my collaborators, Mike Brown for the Boötes photometry and Ivo Labbe, for the advice on SED fitting. I have been fortunate to be a part of a dynamic research group. So my thanks go to those in the Leiden LOFAR group, which has over the years evolved from technical discussions to more science: Aayush, Andra, Bas, David, Duy, Edwin, Joris, and Raymond. I have been fortunate, also, to be a part of the larger LOFAR Surveys group: Francesco, George H., Ilse, Jon, Liz, Martin, and Pepe. I owe my thanks also to those other Leiden colleagues: Berenice, Renske, and Steven. A special note of thanks goes to Xander Tielens for helping me through the final lap.

Over the years in Leiden I have had the pleasure to count some wonderful people in the Observatory as friends. To the postdocs in our group, Emma and Tim, you have not only added guided me, but you have been good friends. Leah, you made Leiden so much better when you joined our Group. I have learned a lot from you. Your enthusiasm is inspiring.

I have been privileged to meet some incredible friends in Leiden. Annalize, I could not have asked for a better flatmate. I look forward to one day eating excellent food and drinking cocktails with you again on the Mediterranean. Bruha Holly, I'm not going to forget you any time soon! To Dan and Sam and your beautiful family, it was a pleasure to share your time in Leiden. And to Dan, thank you for your support at the Observatory and interesting discussions. To my friends I met in Leiden: Abby, Alina, Amy, Ben, Daniëlle, Hanna, Jérôme, Joshua, Liza, Lydia, Marie, and Paulina, one day I hope to visit you in your places all over the world.

To my fellow South Africans and very special friends now in Nijmegen, Deanne, Rocco, and Sally, thank you for all the times I have been able to step away from work and laugh and have some fun with you. Kosma, my friend so far away, your words of encouragement gave me the strength to endure. You open my mind. And to immortalise it in writing: "JDB – You are Awesome!"

Most importantly, my thanks go to my family. Despite being a continent away, your love and support have seen me through some hard times and I would not be where I am today without you. Mom, you may not know exactly what a tutorial or a journal paper is, but you have always encouraged me. Angie, your love of Physics and Astronomy has inspired me to get to this point. Veronica and Heather, my two very different big sisters, you have both guided me in your own way and stood with me.